Electrochemical study of the etching of III-V semiconductors

Please check the document version of this publication:

• A submitted manuscript is the version of the article upon submission and before peer-review. There can be important differences between the submitted version and the official published version of record. People interested in the research are advised to contact the author for the final version of the publication, or visit the DOI to the publisher's website.
• The final author version and the galley proof are versions of the publication after peer review.
• The final published version features the final layout of the paper including the volume, issue and page numbers.

[Link to publication](#)

Electrochemical study of the etching of III-V semiconductors

P.H.L. Notten
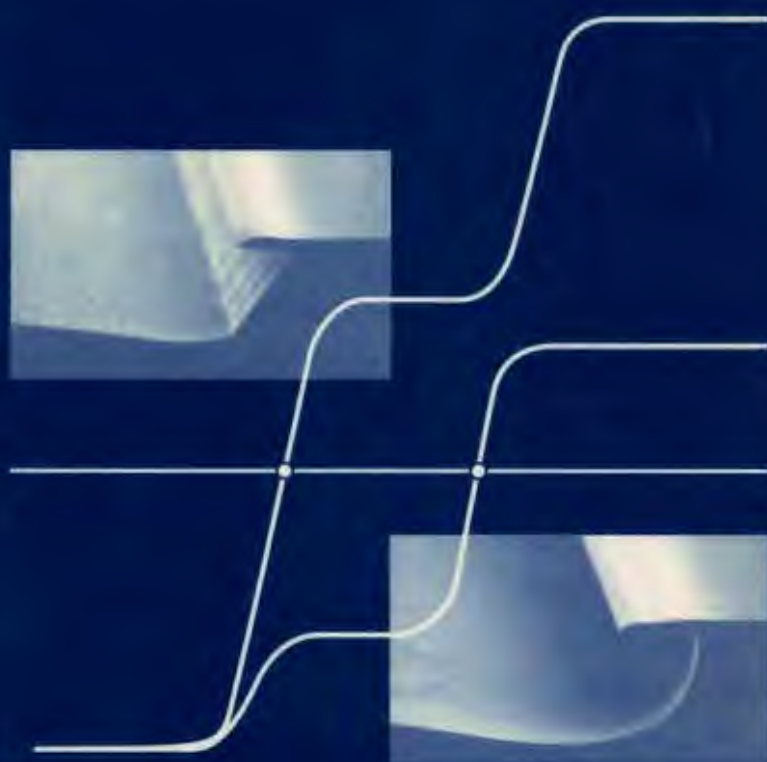
The front cover shows how electrochemical measurements can be used to predict the shape of etched profiles in monocrystalline semiconducting materials near resist edges.

Electrochemical study of the etching of III-V semiconductors

Proefschrift

Petrus Henricus Laurentius Notten

geboren op 7 juni 1952 te Eindhoven

Dit proefschrift is goedgekeurd door de promotoren:

Prof. E. Barendrecht
Prof. dr. J.J. Kelly

aan Pascalle,
    Brechtje en Roel

Contents

Chapter 1

Introduction

Semiconductors play an indispensable role in many aspects of present-day life. This is clear when one considers the enormous importance of silicon integrated-circuit technology. Interest in other semiconductors, however, continues to grow. III-V compounds, composed of group III and group V elements of the Periodic Table, have become important for various applications in the last decade. For example, semiconductor lasers and light emitting diodes are essential for the registration and read-out of information, stored in Compact Discs and digital optical recording systems [1,2]. Such devices are also required in optical telecommunication systems [3]. Furthermore, field effect transistors based on GaAs are of great interest since they can operate faster than corresponding silicon devices as a result of the higher electron mobility in GaAs [4,5].

For these applications, multilayer structures of different III-V semiconductors are grown epitaxially from either the liquid phase or the gas phase on a III-V substrate, with techniques such as liquid phase epitaxy (LPE) or metal-organic vapour-phase epitaxy (MO-VPE) [6]. To obtain the required high device performance, perfect monocrystalline multilayer structures must be grown. Besides crystal growth, etching also plays an essential role in various steps of device fabrication. Both dry and wet etching methods can, in principle, be employed. However, in contrast to silicon technology, wet chemical etching plays a far more important role in the III-V field. The applications of wet etching can be divided into four main categories:

(i)   Polishing: Polishing etchants are widely used to obtain wafers with perfectly smooth surfaces, which can serve as high-quality substrates for epitaxial growth [7].

(ii) Defect-revealing: Crystallographic imperfections in the multilayer structures determine the performance and life-time of III-V devices. To investigate the quality of the substrate and of the various epitaxial layers, etchants are used to reveal crystallographic defects. Photoetching sys-

tems are often employed to obtain the required defect selectivity [8,9].

(iii) Selective etching: For various applications it is frequently necessary to etch epitaxial layers selectively with respect to other layers [10]. It is important to note that the various layers are usually very similar in chemical composition so that high demands are made on the etching technology.

(iv) Profile etching: Etching of special predetermined forms is essential for insulating and defining accurately the active region in III-V devices. For example, in the case of InP lasers used in optical telecommunication systems, laser light with a wavelength in the infrared is generated in the active layer. The width of this layer is defined laterally by two symmetrical rounded grooves which are etched with the aid of a resist. In the case of GaAs lasers applied in Compact Disc players, light is generated in the visible or in the near-infrared part of the spectrum. In contrast to InP lasers, faceted V-grooves are required to define the light-generating region in the active layer.

It is obvious that the etching solutions needed for these various applications must meet quite different but very stringent requirements.

In recent years much work has been done on the etching of III-V semiconductors. However, the approach has been largely empirical and there is a considerable need for a more fundamental understanding of the processes involved. The main aims of the work described in this thesis are the elucidation of both the etching mechanisms and etching kinetics, and the application of this knowledge to practical etching systems. The thesis can be divided into two parts:

– In the first part, fundamental aspects of different etching systems are considered. It has long been recognized that, as in the case of metals, the dissolution of semiconductors in etchants containing an oxidizing agent can be described and characterized by electrochemical methods [11,12]. Such an electrochemical approach forms the basis of the work described in chapters 2-7. Since, for technological applications, GaAs and InP are by far the most important substrate materials, the study is restricted to these compounds. In addition, macroscopic etching experiments were performed. As a result of these investigations a classification of the etching systems according to mechanism and kinetics is presented.

– In the second part (chapter 8) the results from the fundamental study are used for a consideration of practical etching systems. The classification, referred to in the previous paragraph, forms the basis of this part of the work. Although the four application areas of wet chemical etching, listed above, will be considered at various points in this thesis, the main em-

phasis in chapter 8 will be on the factors which determine the shape of etching profiles at resist edges.

The first part of the thesis is organized as follows. The basic principles of semiconductor electrochemistry, essential for understanding the etching behaviour of these materials, are described in chapter 2. In particular, the various etching mechanisms and the factors which determine etching kinetics are considered. In the experimental chapter 3 electrochemical methods employed in this work are described together with the experimental set-up used for the etching experiments. From chapter 2 it follows that the dissolution of semiconductors is often determined by the kinetics of anodic oxidation. The factors important for the anodic oxidation of GaAs are described in chapter 4. Chapters 5 and 6 are devoted to electrochemical studies of GaAs and InP in solutions containing a variety of redox systems. The results of these studies are summarized in chapter 7 and classified in an etching table. This table presents conclusions regarding the dissolution mechanism and macroscopic etching kinetics of GaAs and InP in the various etchants.

The etching table serves as an introduction to the investigation of the influence of both the dissolution mechanism and kinetics on the shape of profiles etched at resist edges, described in chapter 8. Crystallographic properties of the monocrystalline semiconductors are important in determining etched shapes [13] and are therefore considered. Finally the main conclusions of the thesis are summarized in chapter 9.

References

[1] J.C.J. Flinck, H.J.M. van der Laak and J.T. Schrama, *Philips Techn. Rev.*, **39**, 37, (1980).

[2] G.E. Thomas, *Philips Techn. Rev.*, **44**, 51, (1988).

[3] G.A. Acket, *Editor of special issue on Semiconductor Lasers, IEEE J. Quant. Electron*, **QE-19**, page 897 et. seq., june, (1983).

[4] C.E. Timmering, J.M. Lagemaat, C.T. Foxon and J.J. Harris, *Semicond. Sci. Technol.*, **3**, 1139, (1988).

[5] A.S. Grove, *'Physics and Technology of Semiconductor Devices'*, Table 4.1, page 102, J. Wiley and Sons, New York, (1976).

[6] *'Advanced Crystal Growth'*, Eds. P.M. Dryburgh, B. Coekayne and K.G. Barraclough, Prentice Hall Int., New York, (1987).

[7] J.S. Basi, *U.S. Patent* 3,738,882.

[8] J.L. Weyher and J. van de Ven, *J. Cryst. Growth*, **78**, 191, (1986).

[9]   J.J. Kelly, J.E.A.M. van den Meerakker and P.H.L. Notten, *'Grund-lagen von Elektrodenreaktionen'*, Dechema-Monographien, Band 102, page 453, VCH-Verlagsgesellschaft, Ed. J.W. Schultze, Frankfurt am Main, (1986).

[10] R.P. Tijburg and T. van Dongen, *J. Electrochem. Soc.*, **123**, 687, (1976).

[11] S.R. Morrison, *'Electrochemistry at Semiconductor and Oxidized Metal Electrodes'*, Plenum Press, New York, (1980).

[12] R. Memming, *'Electroanalytical Chemistry. A Series of Advances'*, Ed. A.J. Bard, vol. 11, pages 1-84, Dekker, New York, (1979).

[13] D.W. Shaw, *J. Cryst. Growth*, **47**, 509, (1979).

Chapter 2

Basic principles of semiconductor electrochemistry

2.1. Introduction

In this chapter some essential aspects of semiconductor electrochemistry [1] will be briefly described and differences with the electrochemistry at metal electrodes will be considered. This chapter is intended as an introduction to the principles which form the basis of the work described in later chapters of this thesis.

Characteristic of semiconductors is the separation of the valence and conduction bands by a forbidden energy zone, called the band-gap (E_g). For example, the band-gap of GaAs is 1.43 eV while that of InP amounts to 1.35 V (pages 218 and 281 of [2]). The position of the Fermi level, the chemical potential of electrons in a semiconductor, depends strongly on the doping level. For an intrinsic semiconductor the Fermi level (E_F) is located at the middle of the band-gap. When a semiconductor is doped with atoms acting as electron donors, with energy levels at the top of the band-gap (e.g. Si in GaAs) an n-type semiconductor is obtained. The Fermi level is, in this case, close to the conduction band (CB) edge and is related to the CB electron concentration in the bulk of the semiconductor (n_o) by

$$n_o = N_c \cdot \exp\left\{ \frac{-(E_c - E_F)}{kT} \right\}, \qquad (2.1)$$

where N_c is the effective density of states in the CB, E_c is the energy level of the lower edge of the CB, k is the Boltzmann constant and T is the absolute temperature (page 6 of [1]). On the other hand, a p-type semiconductor is obtained when acceptor levels are present close to the valence band (VB) edge. Such levels can accept electrons from the VB, thereby giving rise to holes in this band. For a zinc-doped III-V semiconductor, where

zinc acts as such an electron acceptor, the Fermi level is close to the VB-edge and the hole concentration (p_o) is given by

$$p_o = N_v \cdot \exp\left\{ \frac{-(E_F - E_v)}{kT} \right\}, \qquad (2.2)$$

where N_v is the effective density of states in the VB and E_v is the upper edge of the VB.

The doping level for III-V semiconductors used in the device technology, and also used in this work, is generally between 10^{15} and 5×10^{18} cm^{-3}. Due to these low concentrations, the potential distribution at the semiconductor/ solution interface is different from that at a metal/solution interface. This is reflected in the electrochemical behaviour of the solids. Therefore, the potential distribution at the semiconductor/solution interface is described in some detail and contrasted with that at a metal/solution interface in section 2.2. A large part of this thesis is devoted to the electrochemical behaviour of a wide variety of redox systems at III-V semiconductor electrodes. Moreover, as we will show, etching processes can often be considered as electrochemical reactions in which mobile charge carriers are exchanged between the solid and solution. To understand such charge transfer processes it is necessary to consider the energy levels of redox systems in solution. This is described in section 2.3 together with the conditions necessary for charge transfer to occur. Since we are primarily interested in etching of III-V semiconductors, which is generally an electrochemical process, the basic principles of anodic dissolution of these materials are discussed briefly in section 2.4. 'Electroless' etching, in which an oxidizing agent is used to dissolve the solid electrochemically, is described in section 2.5. It will be shown that the Mixed Potential Theory can be applied to electroless etching of semiconductors. As in the case of metals, dissolution can be considered in terms of two separate reactions occurring at the same surface, viz. the oxidative dissolution of the semiconductor and the reduction of the oxidizing agent. A second, less well-known class of etchants is denoted by the term 'chemical' etchants. The special features of these systems are emphasized in section 2.6. Finally in section 2.7 some aspects of etching kinetics of semiconductors in both electroless and chemical etchants are considered.

2.2. Charge and potential distribution at the semiconductor/ electrolyte interface

When a semiconductor is immersed in an electrolyte a redistribution of charge occurs at the semiconductor/electrolyte interface. The charge distribution at this interface and the consequences with regard to the potential distribution will be discussed in this section. It will be illustrated with an n-type semiconductor for two different cases: an electrode in equilibrium with the electrolyte and an electrode under applied potential. Obviously, similar considerations can be made for p-type semiconductors.

Equilibrium

In Fig. 2.1.A an energy diagram is shown for an n-type semiconductor. Energy is plotted vertically and distance from the interface is plotted horizontally. The ionized immobile donor atoms are indicated as positive

A. *non-equilibrium*   B. *equilibrium*
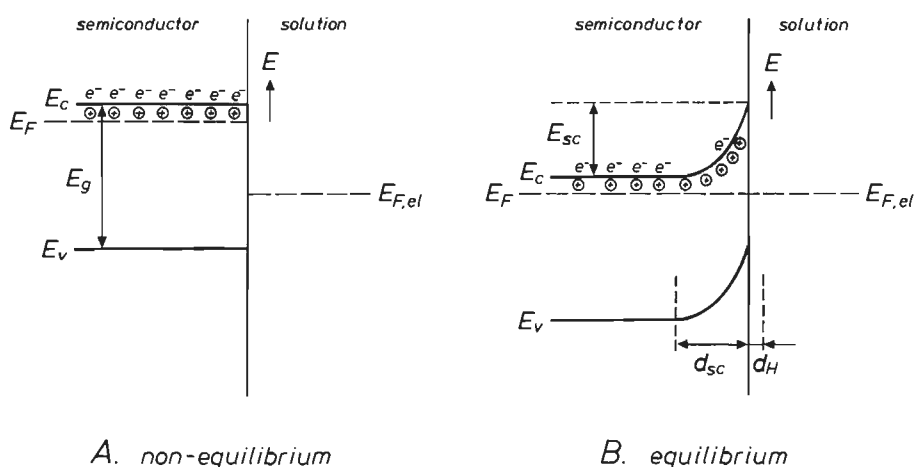
Fig. 2.1. Schematic representation of a semiconductor/electrolyte interface. The energy band model is shown for an n-type semiconductor with band-gap E_g in contact with an electrolyte which is characterized by the Fermi level $E_{F,el}$:
A) for the case in which the semiconductor and solution are not in equilibrium $(E_F \neq E_{F,el})$.
B) for the case in which the semiconductor is in equilibrium with the electrolyte. At equilibrium the Fermi level in the semiconductor (E_F) is equal to $E_{F,el}$. As a consequence, a space-charge layer with thickness d_{sc} is established within the solid over which an energy drop E_{sc} occurs. The immobile ionized donors are indicated by $\oplus$ and the mobile electrons in the CB by e^-. The thickness of the Helmholtz layer is represented by d_H.

charges ($\oplus$) close to the conduction band-edge while the mobile electrons, supplied by the donors, are shown as negative charges (e^-) in the CB. The distance between E_F and E_c is related to the doping level as given by eq. (2.1). It is assumed that all donors are ionized, which is likely to be the case for the types of doping elements considered in this work (section 4.2 of [3]). The same holds for the ionization of acceptors in the case of p-type electrodes.

The Fermi level in solution is determined by redox systems in the solution as will be shown in section 4.3. Here, a Fermi level in the electrolyte ($E_{F,el}$) will be assumed as indicated in Fig. 2.1.A. Because of the difference in Fermi level between the solid and solution (see Fig. 2.1.A), electrons are transferred to solution and a space-charge layer consisting of uncompensated immobile ionized donors is formed within the semiconductor (see Fig. 2.1.B). At equilibrium, the Fermi levels in both phases are the same

$$E_F = E_{F,el}. \tag{2.3}$$

The thickness of the space-charge layer in Fig. 2.1.B is denoted by d_{sc}. The space-charge layer capacitance C_{sc} can be defined as

$$C_{sc} = \frac{\delta Q_{sc}}{\delta V_{sc}}, \tag{2.4}$$

where Q_{sc} is the charge in the space-charge layer and V_{sc} is the potential drop over this layer. According to the Boltzmann equation the electron concentration in the CB at the semiconductor surface (n_s) is related to the band bending E_{sc} ($= e \cdot V_{sc}$) by

$$n_s = n_0 \cdot \exp\left\{ - \frac{e V_{sc}}{kT} \right\}, \tag{2.5}$$

where n_0 is the bulk concentration of electrons in the CB and e is the electronic charge. Similarly the surface hole concentration (p_s) in the VB depends on V_{sc}:

$$p_s = p_0 \cdot \exp\left\{ \frac{e V_{sc}}{kT} \right\}, \tag{2.6}$$

where p_0 is the bulk concentration of holes in the VB.
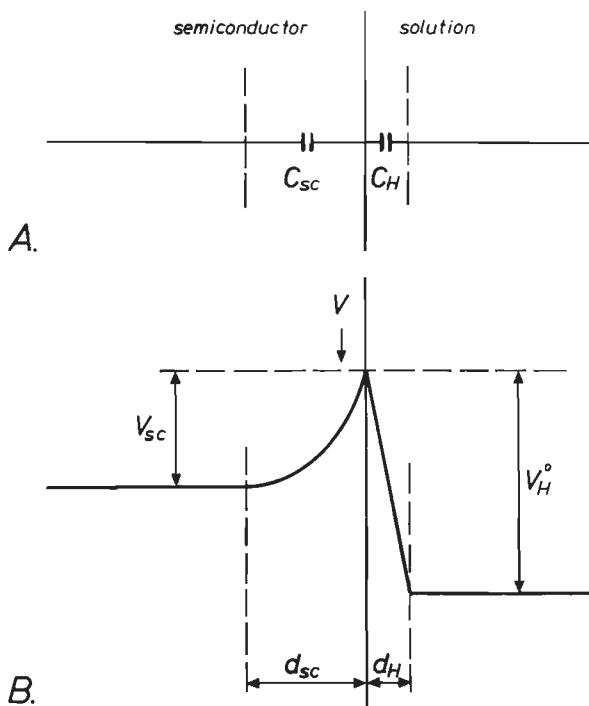
Fig. 2.2. Schematic representation of a semiconductor/electrolyte interface.
A) a simple equivalent circuit for the semiconductor/solution interface is charac-
terized by two capacitances in series, the space-charge capacitance (C_{sc}) of the solid
and the Helmholtz capacitance (C_H) of the solution.
B) the potential distribution at the interface occurs in the solid over the space-
charge layer (V_{sc}) and in solution over the Helmholtz layer (V_H^o). The thicknesses
of both layers, which are indicated by d_{sc} and d_H respectively, are not given on the
same scale. d_H is in general much smaller than d_{sc}.

Charge transfer also results in an electrical double layer in the solution.
As in the case of metals, the double layer in solution consists of the compact
double layer (the Helmholtz layer) and the diffuse double layer. It can be
shown that in electrolyte solutions with ionic concentrations larger than
0.1 mole $\cdot$ l^{-1}, the diffuse double layer can be disregarded so that one need
only consider the Helmholtz layer with capacitance C_H. This capacitance can
also be represented as

$$C_H = \frac{\delta Q_H}{\delta V_H^o}, \tag{2.7}$$

where Q_H is the charge at either side of the compact double layer and V_H^o is the potential drop over this layer. For semiconductor electrodes it is obvious from the discussion above that one has to take into account two capacitors in series, C_{sc} and C_H, as shown in Fig. 2.2.A. The total capacitance (C_t) can then be represented as

$$\frac{1}{C_t} = \frac{1}{C_{sc}} + \frac{1}{C_H}. \tag{2.8}$$

From electrostatic theory using the Poisson equation [4,5], the potential in the solid can be calculated as a function of the distance from the surface. This results in a smooth potential drop over the space-charge layer (V_{sc}) as shown in Fig. 2.2.B. A linear potential drop (V_H^o) over the Helmholtz layer is assumed. The thickness of the Helmholtz layer (d_H) is much smaller $(d_H \approx 0.2\text{-}0.5 \text{ nm})$ than that of the space-charge layer (d_{sc}), which can vary under depletion conditions in the range of $10\text{-}100$ nm. It should be noted that d_H and d_{sc} in Figs. 2.1 and 2.2 are not drawn to scale.

For metals with much higher carrier densities (about 10^{22} cm^{-3}), the charge is located directly at the metal surface and a space-charge layer is not established within the solid. Consequently, a potential drop at a metal/solution interface only occurs over the Helmholtz layer. This is in contrast to semiconductor electrodes.

Applied potential

In this paragraph we consider what happens to the potential distribution at the interface when an overpotential (η) is applied to the electrode and the semiconductor is no longer in equilibrium with the solution. The Fermi level in the solid changes with respect to that in solution by an amount determined by the overpotential according to

$$E_F - E_{F,el} = e \cdot \eta. \tag{2.9}$$

In principle, the applied overpotential can be distributed over both the space-charge and Helmholtz layers. This results in a change with respect to equilibrium of the potential over the two layers, δV_{sc} and δV_H, according to

$$\eta = \delta V_{sc} + \delta V_H. \tag{2.10}$$

A change of the electrode potential results in changes of the charge densities in both the space-charge layer (δQ_{sc}) and the Helmholtz layer (δQ_H).

Since $\delta Q_{sc} = -\delta Q_H$ it can be shown from eqs. (2.4) and (2.7) that

$$\frac{\delta V_{sc}}{-\delta V_H} = \frac{C_H}{C_{sc}}. \qquad (2.11)$$

It is clear from eq. (2.11) that the potential distribution between the semiconductor and the solution depends strongly on the relative magnitudes of C_{sc} and C_H.

A rather complex general relation between C_{sc} and the potential drop over the space-charge layer can be derived (pages 126-130 of [1]). A schematic representation of this equation is given for an n-type semiconductor in Fig. 2.3. Three potential ranges can be distinguished. In the intermediate potential range, depletion of electrons in the space-charge layer occurs, i.e. $n_s < n_o$ (see eq. (2.5)). This is the case shown in Fig. 2.1.B; C_{sc} is very small (of the order of $(0.01-1) \times 10^{-6}$ F·cm^{-2} [4]) compared to the Helmholtz capacitance (C_H is assumed to be in the range of $(10-30 \times 10^{-6}$ F·cm^{-2} (page 64 of [6], [7]). As a consequence the measured electrode capacitance C_t in eq. (2.8) actually corresponds to the space-charge layer
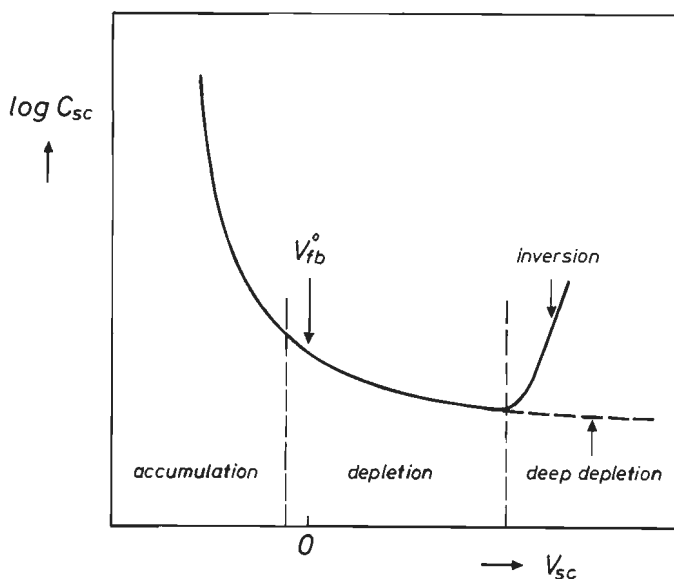
Fig. 2.3. Schematic representation of the space-charge capacitance (C_{sc}) as a function of the band bending (V_{sc}) for an n-type semiconductor. Three potential ranges can be distinguished: accumulation, depletion and inversion. Inversion (solid line) can in certain cases be replaced by deep depletion (dashed line).

C. accumulation   B. flat-band   A. depletion
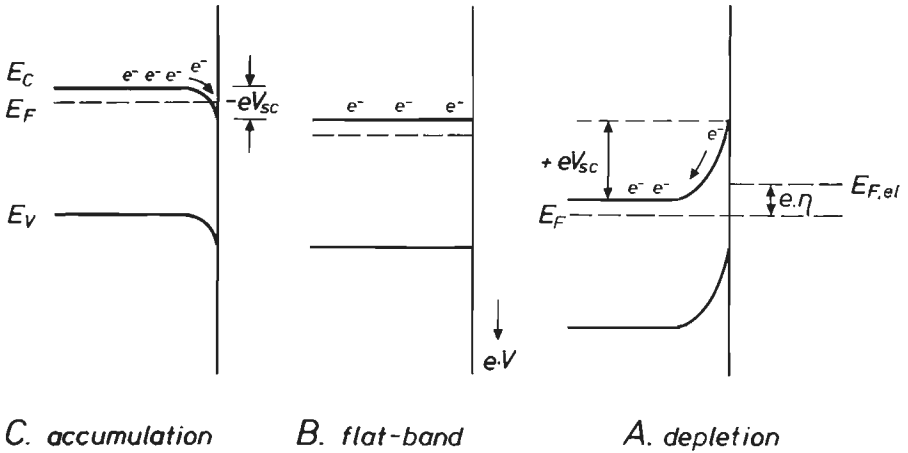
Fig. 2.4. Band bending at the electrode surface for an n-type electrode as a function of applied overpotential (η).
A) represents the depletion condition where $n_s < n_o$ (compare with the equilibrium situation of Fig. 2.1.),
B) is the flat-band situation where $n_s = n_o$ and
C) shows accumulation of majority charge carriers in the space-charge layer ($n_s > n_o$).

capacitance C_{sc}. It also follows from eq. (2.11) that a change of the electrode potential occurs almost completely over the space-charge layer within the solid. In this case the Helmholtz potential can be regarded as a constant ($\delta V_H = 0$), equal to V_H^o as defined for the equilibrium situation. This means that the conduction and valence band-edges at the semiconductor surface in this potential range are fixed and do not depend on the electrode potential. Again, the difference with metal electrodes is clear where a potential change only occurs over the Helmholtz layer ($\eta = \delta V_H$). In Fig. 2.4.A the energy band model of an n-type semiconductor is shown when a positive overpotential is applied to the electrode. This results in a larger upward band bending at the semiconductor surface compared to that at equilibrium. The change of the potential drop over the space-charge layer is equal to the applied overpotential. According to eq. (2.5) n_s is smaller than in the equilibrium case. Under such depletion conditions the expression for the space-charge capacitance can be considerably simplified to the Mott-Schottky equation [4]:

$$C_{sc} = \left\{ \frac{\varepsilon\varepsilon_o N_D e}{2} \right\}^{\frac{1}{2}} \cdot \left\{ V_{sc} - \frac{kT}{e} \right\}^{-\frac{1}{2}}, \qquad (2.12)$$

where ε is the dielectric constant of the semiconductor, ε_o is the permittivity of free space, N_D is the donor concentration and V_{sc} represents the potential drop within the solid as indicated in Fig. 2.4.A. In the case of a p-type electrode N_D must be replaced by the acceptor concentration N_A. It is obvious from eq. (2.12) that when the applied potential becomes more positive, i.e. when V_{sc} increases, the space-charge capacitance decreases as is shown in the depletion potential range of Fig. 2.3.

When the applied potential is made more negative the potential drop over the space-charge layer decreases. At the flat-band potential (V_{fb}^o) the semiconductor band-edges are flat up to the surface, i.e. there is no potential drop $(V_{sc} = 0)$ and thus no space-charge within the solid (see Fig. 2.4.B). The V_{fb}^o value is an important reference potential for semiconductor electrochemistry. The potential drop over the space-charge layer (V_{sc}) can now be defined with respect to V_{fb}^o as follows. As discussed in relation with Fig. 2.2.B, the applied electrode potential (V) which is in general measured with respect to a reference electrode, is distributed over the Helmholtz layer (V_H^o) and the space-charge layer (V_{sc}). When the constant potential drop (φ) occurring at the interface of the reference electrode and the electrolyte is also taken into account, the applied electrode potential can be represented as [4]

$$V = V_{sc} + V_H^o + \varphi. \tag{2.13}$$

Since the flat-band potential is defined at $V_{sc} = 0$, it follows that

$$V_{fb}^o = V_H^o + \varphi. \tag{2.14}$$

Substitution of eq. (2.14) into eq. (2.13) gives

$$V_{sc} = V - V_{fb}^o. \tag{2.15}$$

From the above considerations it is clear that the determination of V_{fb}^o is very important. This is possible when C_{sc} is measured under depletion conditions as a function of the applied electrode potential. Substituting eq. (2.15) into eq. (2.12) gives, after rearrangement

$$\frac{1}{C_{sc}^2} = \frac{2}{\varepsilon \varepsilon_o N_D e} \cdot \left\{ V - V_{fb}^o - \frac{kT}{e} \right\}. \tag{2.16}$$

Accordingly a plot of $1/C_{sc}^2$ versus V yields a straight line as shown in Fig. 2.5 for a GaAs electrode. Curve (a) represents the Mott-Schottky plot obtained with n-GaAs and (b) with p-GaAs in a solution of $pH = 0$. From eq. (2.16) it follows that if $1/C_{sc}^2 = 0$, then $V - V_{fb}^o = kT/e$; since kT/e is approximately 25 mV at room temperature this means that the band bending is very slight. Thus, on taking this very small potential difference into account V_{fb}^o is obtained from the intercept on the potential axis. Since V_{fb}^o is actually a measure for the position of the Fermi level in the semiconductor at flat-band situation, it is evident that the difference between V_{fb}^o values of p- and n-type electrodes should be approximately equal to the band-gap of the semiconductor $\left(E_g \approx \left(e \cdot \{V_{fb}^o(p) - V_{fb}^o(n)\}\right)\right)$. For GaAs, a difference in V_{fb}^o values close to the band-gap is found, as expected (see Fig. 2.5). In this
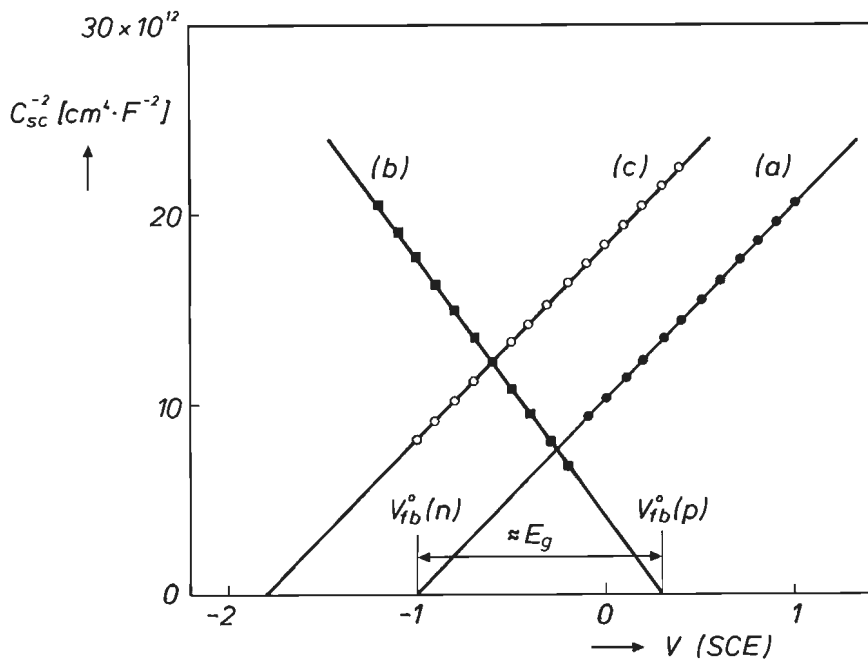
Fig. 2.5. Mott-Schottky plots obtained at n-GaAs ($N_D = 1.0 \times 10^{18}$ cm^{-3}) in a solution of 0.5 M H_2SO_4 (curve (a)) and in a solution of 0.1 M NaOH (curve (c)). Curve (b) gives the Mott-Schottky plot of a p-type GaAs electrode ($N_A = 8.4 \times 10^{17}$ cm^{-3}) in a solution of 0.5 M H_2SO_4. For the experimental details see chapter 3. The difference between the flat-band potentials of p-type GaAs ($V_{fb}^o(p)$) and n-type GaAs ($V_{fb}^o(n)$) in the same electrolyte is slightly smaller than the band-gap (E_g) of GaAs $\left(E_g \approx e \cdot \{V_{fb}^o(p) - V_{fb}^o(n)\}\right)$.

example the potentials are measured with respect to a Saturated Calomel Electrode (SCE) as reference. This potential scale can be related to an energy scale with respect to vacuum [4] as

$$E = -\left\{4.75 \text{ eV} + e \cdot V(\text{SCE})\right\}, \qquad (2.17)$$

where V is given versus (SCE). The donor (N_D) or acceptor (N_A) concentration in the bulk of the semiconductor can be calculated from the slope of the Mott-Schottky plots according to eq. (2.16).

It is known that the Helmholtz potential is affected by specific adsorption of ions from solution (page 62 of [1]). An example is the adsorption of OH^- ions on GaAs when the pH of the solution is raised. It can be shown, that the change in V_H^o is 60 mV per unit change in pH (page 62 of [1], [8]). According to eq. (2.14) V_{fb}^o depends on changes in V_H^o. Consequently, specific adsorption should influence the V_{fb}^o value. This effect is shown in curve (c) of Fig. 2.5 for an n-type electrode in a solution of $pH = 13$. The Mott-Schottky plot is shifted some 780 mV to negative potentials with respect to that at $pH = 0$, as expected for a pH difference of 13. A similar dependence is, of course, also found for p-type electrodes (this is not shown in Fig. 2.5).

In addition to the charge in the space-charge layer of the semiconductor, charge (Q_{ss}) may also be stored in surface states. This may also lead to a change of the potential drop over the Helmholtz layer [4]. This effect will be discussed in more detail in later chapters.

So far, the important intermediate depletion range of Fig. 2.3 has been discussed. If the potential at an n-type electrode is made negative with respect to V_{fb}^o the bands bend downwards (as in case C of Fig. 2.4) and the electron concentration at the surface, given by eq. (2.5), is higher than in the bulk of the semiconductor ($n_s > n_o$). This accumulation of majority charge carriers at the surface is accompanied by a considerable increase in the space-charge capacitance as Fig. 2.3 shows. It can be shown that C_{sc} is no longer much smaller than the Helmholtz capacitance. Consequently, under accumulation conditions the potential drop occurs not only over the space-charge layer but also over the Helmholtz layer (see eq. (2.11)), i.e. δV_H can no longer be regarded as zero. Under strong accumulation the Fermi level may intersect the CB-edge near the surface. The semiconductor becomes degenerate and shows quasi-metallic behaviour, e.g. the potential drop occurs almost exclusively over the Helmholtz layer [4].

On the other hand, at large upward band bending when V_{sc} is very large, n_s may become even smaller than p_s and an inversion layer is formed.

This also results in a large C_{sc} value (see solid line in Fig. 2.3). However, with large band-gap semiconductors, such as GaAs and InP, inversion is generally not established at moderate overpotentials ($V - V_{fb}^o < 2$ V). A build-up of minority charge carriers at the semiconductor surface does not occur due to the fact that they are easily transferred to the solution via electrochemical reactions. Instead of inversion, a deep depletion condition is established, as indicated by the dashed line in Fig. 2.3. The δV_H is also slight under deep depletion.

So far, the band bending for n-type semiconductors has been discussed. Of course, a similar argument also holds for p-type electrodes. However, the potential dependence of the surface hole concentration is reversed; a depletion layer is formed at negative potentials whereas an accumulation layer is formed at potentials positive with respect to V_{fb}^o.

2.3. Charge transfer reactions

Since charge transfer between a semiconductor electrode and a redox system in solution can only occur between levels of equal energy [4], it is necessary to know the energy levels of the oxidized (Ox) and reduced (Red) states of redox systems with respect to the energy levels of the semiconductor. Therefore, the energy levels in solution will be described first and, after that, the conditions that must be fulfilled for charge transfer to occur and the parameters that determine the rate of these reactions.

Energy levels in solution

A redox couple in solution is characterized by its Fermi level ($E_{F,el}$). As in solids, the energy states of a redox system can be either empty or occupied by electrons. The position of these energy states for oxidized and reduced species can differ considerably, owing to the strong interaction of the ions of the redox couple with the solvent. Solvation of the ions depends on their size and charge. When an electron is transferred from the reduced component (Red) of a redox system to the oxidized component (Ox) a rearrangement of the solvation shell must take place in order to produce solvation shell characteristic of the oxidized component. This has the result that the energy levels of the reduced and oxidized components, E_{red} and E_{ox}, each differ from the Fermi level $E_{F,el}$ of the redox system by an energy λ which is called the reorientation energy (see Fig. 2.6.A and B). The energy states are, however, not two discrete levels but are distributed over a certain energy range owing to the fluctuations of the solvation shell (Fig. 2.6.C).
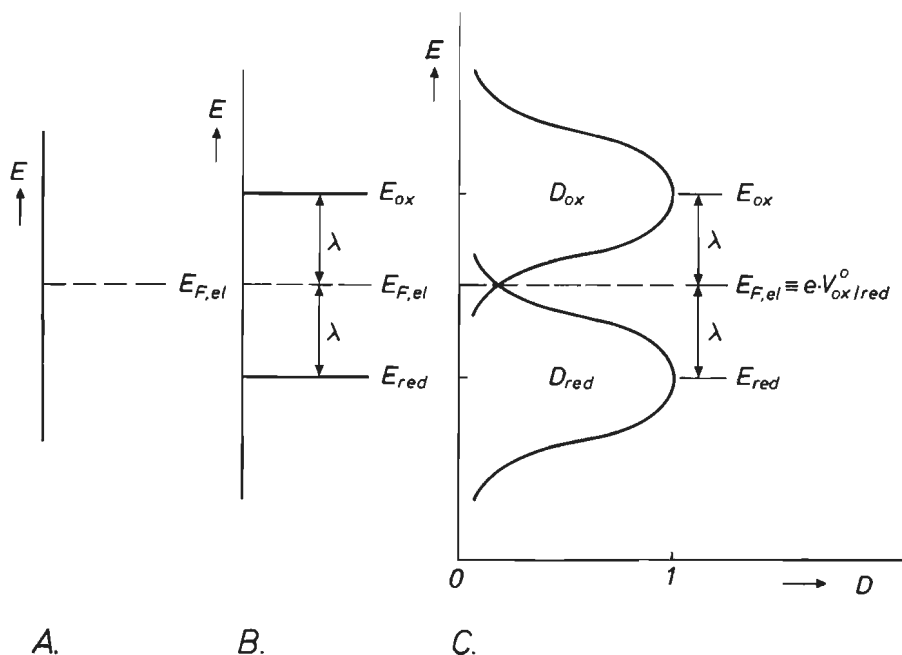
Fig. 2.6.A) a redox couple in solution is characterized by its Fermi level $E_{F,el}$ where $E_{F,el} = e \cdot V^o_{ox/red}$.

B) *Ox* and *Red* have different energy levels, E_{ox} and E_{red} respectively, due to the different solvation shells. λ is the reorientation energy for the solvation shell relaxation.

C) energy distribution functions D_{ox} and D_{red} of the same redox couple as in A and B when the fluctuation of the solvation shells are taken into account.

The corresponding energy distribution functions D_{ox} and D_{red} for the density of energy states of *Ox* and *Red*, respectively, are given by

$$D_{ox} = \exp\left\{\frac{-(E - E_{F,el} + \lambda)^2}{4kT\lambda}\right\}, \qquad (2.18)$$

and

$$D_{red} = \exp\left\{\frac{-(E - E_{F,el} - \lambda)^2}{4kT\lambda}\right\}. \qquad (2.19)$$

The Fermi level $E_{F,el}$ is related to the standard redox potential ($V^o_{ox/red}$) of the redox couple according to eq. (2.17) by

$$E_{F,el} = -(4.75 \text{ eV} + e \cdot V^o_{ox/red}), \qquad (2.20)$$

where $V^o_{ox/red}$ is given with respect to SCE [9]. The distribution functions of eqs. (2.18) and (2.19) have maxima at $(E - E_{F,el}) = \pm\lambda$, and thus the energy levels of a redox couple are distributed around $e \cdot V^o_{ox/red}$. It is found that λ can vary within a broad range between 0.3 and 1.6 eV [10,11]. It is generally assumed that the λ of Ox and that of Red of a redox system are equal. Since it has been shown in section 2.2 that the energy levels of a
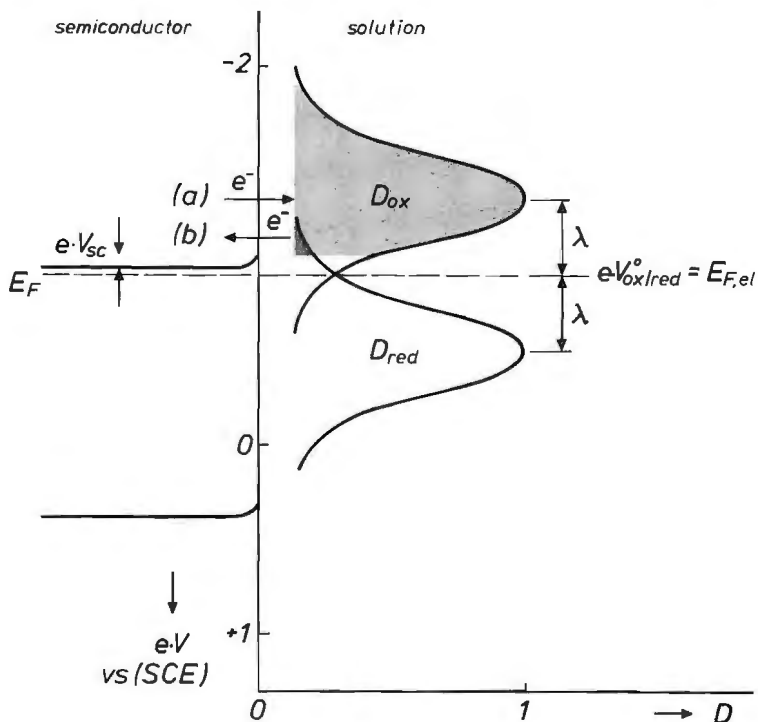
Fig. 2.7. Band model of an n-type GaAs electrode in equilibrium with a solution of $pH = 0$ containing a redox system with a standard redox potential $V^o_{ox/red} = -0.9$ V(SCE) and $\lambda = 0.4$ eV. The Ox and Red components of this redox system have energy levels which can be described with distribution functions D_{ox} and D_{red} respectively (see also eqs. (2.18) and (2.19)). The energy levels in both the solid and the solution are given on a voltage scale with respect to a Saturated Calomel Electrode (SCE). The light shaded and dark shaded areas of D_{ox} and D_{red} function respectively, indicate the correspondence of energy levels in solution with those in the CB. At equilibrium ($E_F = E_{F,el}$) the rate of Ox reduction by means of electron transfer from the CB to Ox (arrow (a)) is equal to the rate of Red oxidation (= the rate of electron injection into the CB by Red, represented by arrow (b)).

semiconductor can also be considered on a potential scale (see eq. (2.17)), the energy levels of both the redox couple and the semiconductor can be directly compared. This is shown in Fig. 2.7 for an n-type GaAs electrode in a solution of $pH = 0$ containing a redox couple having a relatively nega-tive $V^o_{ox/red}$. From the Mott-Schottky measurements in curves (a) and (b) of Fig. 2.5 and eqs. (2.1) and (2.2), it is estimated that the band-edges of GaAs at $pH = 0$ are situated at -1.0 and $+0.3$ V versus SCE. The relative po-sitions of D_{ox} and D_{red} in this example, with a $\lambda = 0.4$ eV, are chosen so that D_{ox} overlaps very well, and D_{red} very poorly with the conduction band as indicated by the light-shaded and dark-shaded areas, respectively. As dis-cussed above, the Fermi level in the electrolyte at equilibrium is equal to that in the semiconductor (eq. (2.3)). This results, for this example, in a slight band bending (e $\cdot V_{sc}$) in the semiconductor.

Charge transfer

The reduction of an oxidizing agent (Ox^+) in solution can take place either by electron transfer (e^-) via the conduction band

$$Ox^+ + e^-(CB) \rightarrow Red, \qquad (2.21)$$
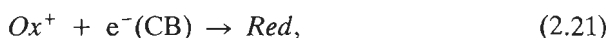
or by hole transfer (h^+) from the oxidizing agent into the valence band

$$Ox^+ \rightarrow Red + h^+(VB). \qquad (2.22)$$
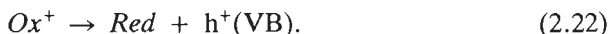
For simplicity it is assumed that one electron is involved in the reduction reaction. It is clear that the rate of the former reaction (eq. (2.21)) can be expressed as a cathodic current density (i^c_{cb}) and will depend on the electron concentration at the electrode surface (n_s) and on the density of Ox^+ states in solution with energy levels corresponding to the CB (see the lightly shaded area of D_{ox} in Fig. 2.7). That the current density is cathodic is in-dicated by the superscript c, while the subscript cb denotes a CB reaction. i^c_{cb} is given by

$$i^c_{cb} = F\varkappa^c_{cb}[Ox^+], \qquad (2.23)$$

where F is the Faraday constant, $[Ox^+]$ is the concentration of Ox^+ species in solution, and $\varkappa^c_{cb}$, the rate constant of the electrochemical reduction reac-tion, is given by

$$\varkappa^c_{cb} \propto \int_{E_c}^{\infty} n_s D_{ox}(E)\, dE. \qquad (2.24)$$

The energy levels of Ox^+ species corresponding to those of the CB is reflected by the integral of eq. (2.24). When the band-edges at the semiconductor surface are fixed ($\delta V_H = 0$), then $\int D_{ox}(E)\,dE$ can be regarded as a constant independent of the applied electrode potential. This constant will be denoted as k_{cb}^c. Eq. (2.24) can then be represented as

$$\varkappa_{cb}^c = k_{cb}^c \cdot n_s. \tag{2.25}$$

When eq. (2.25) is inserted into eq. (2.23) and eq. (2.5) is taken into account, equation (2.23) can be rewritten as

$$i_{cb}^c = F k_{cb}^c [Ox^+] n_0 \cdot \exp\left\{\frac{-e V_{sc}}{kT}\right\}. \tag{2.26}$$

From this equation it follows that i_{cb}^c depends strongly on the applied electrode potential via n_s. The reduction rate of reaction (2.21) for the equilibrium situation of Fig. 2.7 is schematically represented by the length of arrow (a).

The reduction rate of Ox^+ via the valence band (eq. (2.22)) depends, of course, also on $D_{ox}(E)$ states, now corresponding to energy levels of the VB, and on the density of filled states (N_v) in the VB into which holes can be injected by the oxidizing agent. The rate constant for the reduction of Ox^+ via the VB ($\varkappa_{vb}^c$) is given by

$$\varkappa_{vb}^c \propto \int_{-\infty}^{E_v} N_v D_{ox}(E)\,dE. \tag{2.27}$$

As the number of states in the VB is very high and the band-edges are fixed ($\delta V_H = 0$), $\varkappa_{vb}^c$ can be regarded as a constant (k_{vb}^c) which is independent of the applied potential. Therefore, the reduction current density (i_{vb}^c) can be expressed as

$$i_{vb}^c = F k_{vb}^c [Ox^+], \tag{2.28}$$

and is independent of the applied electrode potential. The subscript vb in i_{vb}^c refers to a VB reaction. In fact the overlap of the D_{ox} function with the VB determines the reduction rate. For the example of Fig. 2.7, it is obvious that hole injection into the VB cannot take place for this reason.

The oxidation of *Red* species can be described in a similar way. The

anodic current density via the CB (i_{cb}^a) is determined by $\varkappa_{cb}^a$, the rate constant of the oxidation reaction,

$$\varkappa_{cb}^a \propto \int_{E_c}^{\infty} N_c D_{red}(E)\, \mathrm{d}E. \tag{2.29}$$

On the basis of an analogy with eq. (2.27), $\varkappa_{cb}^a$ is a constant (k_{cb}^a) independent of the applied electrode potential. The oxidation current density, which can be represented as

$$i_{cb}^a = F k_{cb}^a [Red], \tag{2.30}$$

is therefore also independent of the electrode potential. i_{cb}^a is determined by the overlap of the D_{red} function with the CB under the conditions that $\delta V_H = 0$ (the overlap between D_{red} and the CB is indicated for the example of Fig. 2.7 by the dark shaded area).

On the other hand, oxidation can occur by hole transfer from the VB to *Red* in solution. $\varkappa_{vb}^a$ is given by

$$\varkappa_{vb}^a \propto \int_{-\infty}^{E_v} p_s D_{red}(E)\, \mathrm{d}E. \tag{2.31}$$

which consists of a potential-dependent term (p_s) and a potential independent term. The latter is denoted as k_{vb}^a, with

$$k_{vb}^a = \int_{-\infty}^{E_v} D_{red}(E)\, \mathrm{d}E. \tag{2.32}$$

The anodic current density (i_{vb}^a) becomes

$$i_{vb}^a = F k_{vb}^a [Red] p_o \cdot \exp\left\{ \frac{e \cdot V_{sc}}{kT} \right\}, \tag{2.33}$$

when eq. (2.6) is taken into account. i_{vb}^a is clearly potential-dependent via p_s. Since D_{red} in Fig. 2.7 only overlaps with the CB, only the potential-independent injection reaction, as described by eq. (2.30), is possible. However, the oxidation rate will be low due to the poor overlap, i.e. the oxidation rate will be kinetically controlled. The electron injection rate is represented by arrow (b) in Fig. 2.7. It is obvious that at equilibrium the rate
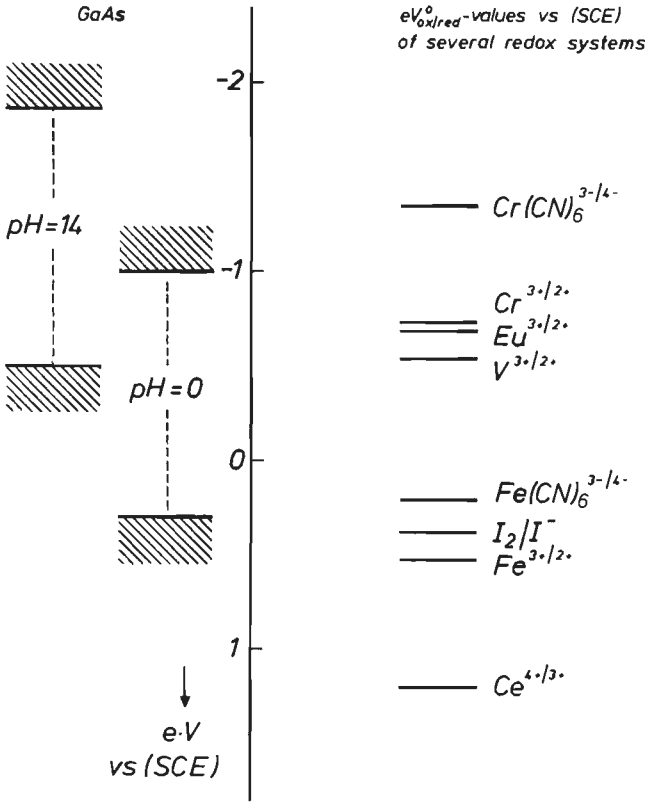
Fig. 2.8. The energy levels of GaAs in two different solutions, $pH = 0$ and $pH = 14$, are schematically represented on a voltage scale with respect to SCE (see eq. (2.17)) together with the standard potentials ($V_{ox/red}^o$) of various redox systems also with respect to SCE.

of oxidation ($i_{cb}^a + i_{vb}^a$) is equal to the rate of reduction ($i_{cb}^c + i_{vb}^c$). In the example of Fig. 2.7 the reduction and oxidation only occur via the conduction band and $i_{cb}^c = i_{cb}^a$, at equilibrium.

It should be emphasized that for the cases in which the rate of electron or hole injection is kinetically controlled, a potential-independent reduction or oxidation current is found (eqs. (2.28) and (2.30)). This contrasts with kinetically controlled redox reactions at metal electrodes which are, in general, potential-dependent. This difference is due to the fact that the applied overpotential changes V_H^o at the metal/solution interface, thereby lowering the activation energy of the electrochemical reactions (chapter 3 of [6]).

Finally it should be emphasized that the energy level diagram of GaAs in Fig. 2.7 is shown for a solution of $pH = 0$. The position of the band-edges depends strongly on the pH of the solution as was shown in the previous section. This can significantly change both the mechanism and kinetics of charge transfer reactions. For example at $pH = 14$ the band-edges of GaAs are shifted 840 mV upwards, towards negative potentials as illustrated in Fig. 2.8. Consequently, D_{red} of the example in Fig. 2.7 overlaps no longer with the CB but its energy levels correspond now to those of the VB; herewith the $V^o_{ox/red}$ is assumed to be pH-independent. At $pH = 14$, *Red* can therefore be oxidized by hole capture from the VB, which is a potential-dependent reaction (see eq. (2.33)), instead of the potential-independent oxidation in the case of a CB reaction (eq. (2.30)).

It is evident that the mechanism and kinetics of the charge transfer reaction are also influenced by the value of the standard redox potential $V^o_{ox/red}$ of the redox system in solution. On the right-hand side of Fig. 2.8, e · $V^o_{ox/red}$ values for several redox systems are given ranging from very negative potentials to very positive potentials for the strong oxidizing agents.

2.4. Anodic dissolution of III-V semiconductors

Etching of semiconductor materials is generally an electrochemical process. Insight into the anodic dissolution of these materials can contribute to the elucidation of the etching processes. Since many studies were made with GaAs, the anodic dissolution of this material will, in particular, be considered. The dissolution mechanism of GaAs is rather complex. Therefore, only a simplified representation will be given to indicate the conditions necessary for dissolution of III-V semiconductors. It should be emphasized that this section is not meant as a review of the various dissolution models.

III-V semiconductor single crystals, such as GaAs and InP, have the zinc-blende structure (page 144 of [2]). In this type of solid most of the surface atoms are triply bonded to three underlying atoms by means of valence electrons. The bonding states form the valence band of the semiconductor [12]. When such a crystal is dissolved the bonding electrons have to be removed from the semiconductor surface. The presence of a hole (h^+) in a localized surface bond means that one of the electrons in a bonding orbital has been removed. As suggested by Gerischer [12], this hole trapping at the semiconductor surface can, in the simplest case, be represented by the following reaction:

$$\overset{\displaystyle |}{-}\text{Ga} - \text{As} - \quad + \quad h^+ \quad + \quad X^- \quad \xrightarrow{\quad k_1^a \quad} \quad \overset{\displaystyle \overset{X}{|}}{-}\text{Ga} \quad \bullet \text{As} - , \quad (2.34)$$
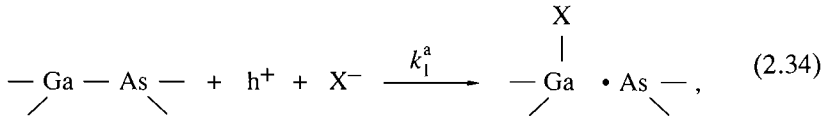
in which a nucleophilic agent (X^-) reacts with one of the positively charged surface atoms from which an electron is removed. The rate constant of this oxidation reaction is given by k_1^a. The remaining unpaired electron is no longer in a valence band state but has an energy level in the band-gap [12]. The following step in the dissolution process could be electron excitation into the CB or hole capture from the VB. However, Gerischer has argued that, since energy levels of the surface states are closer to the VB, the capture of a second hole is more likely [12]. Continuing the notation of eq. (2.34) gives [12,13]

$$\overset{\displaystyle \overset{X}{|}}{-}\text{Ga} \quad \bullet \text{As} - \quad + \quad h^+ \quad + \quad X^- \quad \xrightarrow{\quad k_2^a \quad} \quad \overset{\displaystyle \overset{X \quad X}{| \quad |}}{-}\text{Ga} \quad \text{As} - . \quad (2.35)$$
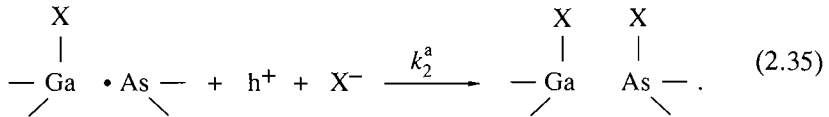
It has been determined that four more holes are needed to dissolve one GaAs entity according to

$$\overset{\displaystyle \overset{X \quad X}{| \quad |}}{-}\text{Ga} \quad \text{As} - \quad + \quad 4h^+ \quad \longrightarrow \quad \text{Ga}^{III} \quad + \quad \text{As}^{III} . \quad (2.36)$$
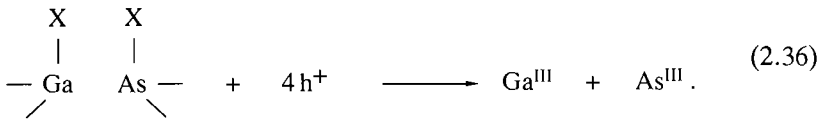
In total, 6 charge carriers are involved and trivalent species are formed in solution (eq. (2.36)). The precise nature of these oxidized products depends on the pH of the solution but this is not important in the present context. It is obvious, from the discussion above, that for the anodic dissolution of III-V semiconductors holes are required at the electrode surface. For p-type materials holes are present in the VB and anodic dissolution can indeed occur when holes are available at the electrode surface. Fig. 2.9.A shows a

▷

Fig. 2.9. Typical current-potential curves of GaAs electrodes in a solution of 0.5 M H_2SO_4.
A) p-GaAs: Curve (a) shows the current response in the dark; the anodic current density at positive potentials is due to anodic dissolution of GaAs. Curve (b) shows the potential dependence under illumination. Two energy band models of GaAs under illumination are given in insert (d) and (e) at -0.7 V and 0 V, respectively.
B) n-GaAs: Anodic dissolution cannot occur in the dark due to the lack of holes in the VB (curve (a)). Curve (b) shows the photoanodic dissolution at positive potentials. Inserts (f) and (g) correspond to energy band models at -0.7 V and $+0.1$ V, respectively.
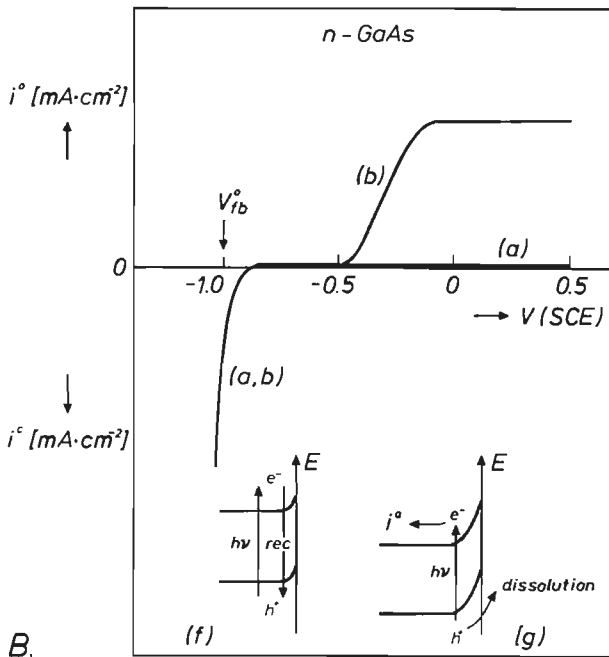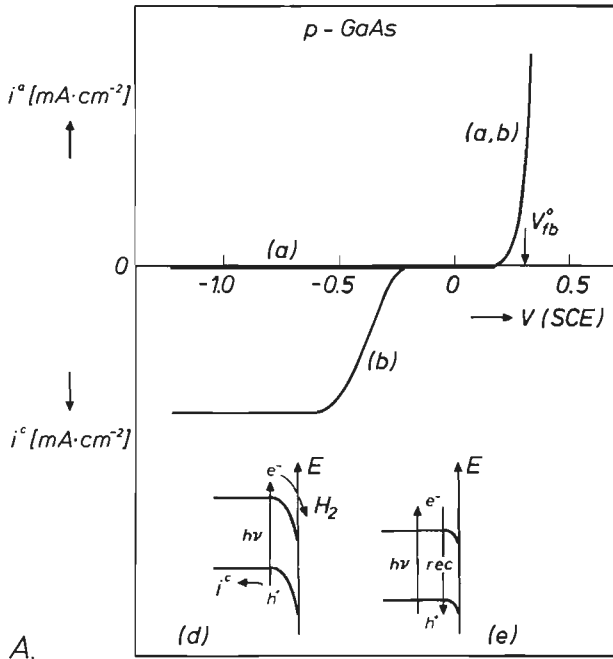
current-potential curve of a p-GaAs electrode in an inert solution of $pH = 0$. In the dark (curve (a)) the current is low at cathodic potentials at which the holes are depleted from the electrode surface. Due to hole accumulation at the surface, anodic dissolution starts close to the flat-band potential and the current increases exponentially at more positive potentials. If the various steps in the above reaction scheme are irreversible, then the steady-state current in the dark i_d^a is given by

$$i_d^a = 6Fk_1^a p_s[X^-]_s, \qquad (2.37)$$

where $[X^-]_s$ is the surface concentration of the nucleophilic agent. According to eq. (2.6) p_s is an exponential function of the applied potential. This should explain the exponential increase of the anodic current at positive potentials. However, it is experimentally found that the potential dependence of the current is not always 60 mV/current decade as expected from eq. (2.6). This may be due to the fact that V_H^o can no longer be considered as a constant in this potential range, as near V_{fb}^o accumulation of majority charge carriers occurs. Moreover, the Helmholtz layer can be significantly changed by specific adsorption of X^- ions which are involved in the dissolution reaction, and by hole trapping at the surface. Consequently, a change of the Helmholtz potential is very likely to influence V_{sc} in eq. (2.13) and thus p_s in eq. (2.6). Although the exact value of p_s cannot be predicted for these reasons, it is generally found that the anodic current density increases exponentially with V.

When the electrode is illuminated with light of a wavelength corresponding to the band-gap of the semiconductor, electron-hole pairs are created. For p-type electrodes this means that electrons are generated in the CB. Due to the large band bending at cathodic potentials these electrons accumulate at the electrode surface and are subsequently transferred to H_3O^+ at low pH or H_2O at high pH. This reduction leads to the formation of hydrogen gas. This photo process at cathodic potentials is schematically shown in the insert (d) of Fig. 2.9.A. The holes, which provides for the electrical conductivity in a p-type semiconductor, are carried to the back side of the electrode and a cathodic photocurrent is measured. The plateau current in curve (b) is determined by the light intensity. At a potential about 800 mV negative with respect to V_{fb}^o the current decreases and becomes very low at more positive values. In this potential range the hole concentration at the surface is relatively high due to the smaller band bending. As a result, recombination of electrons and holes competes effectively with H_2 evolution. (see insert (e) of Fig. 2.9.A). This well-known phenomenon in semiconductor electrochemistry has been extensively studied [14].

For n-type electrodes holes are not present in the VB and these electrodes cannot be dissolved anodically in inert electrolytes in the dark. Negligibly low anodic currents are indeed found at n-GaAs in a solution of $pH = 0$, as curve (a) of Fig. 2.9.B shows. The cathodic dark current starting in the vicinity of V_{fb}^o is due to H_2 evolution via the conduction band. The current increases when the potential becomes more negative, i.e. when n_s increases according to eq. (2.5). Hydrogen evolution occurs in the dark since majority charge carriers are now involved in the reduction reaction. To dissolve n-GaAs anodically the electrode has to be illuminated to create holes in the VB. Dissolution starts approximately 500 mV positive with respect to V_{fb}^o (curve (b)) and becomes independent of the applied electrode potential at more positive values. The plateau photocurrent is again determined by the light intensity. In this potential range corresponding to a large band bending all photo-generated holes in the VB migrate to the semiconductor surface and are used to dissolve GaAs. The electrons in the CB provide for anodic current flow (see insert (g) of Fig. 2.9.B). That the photoanodic dissolution starts at such a positive potential with respect to V_{fb}^o is again due to recombination of electrons and holes at moderate band bending [15] (see insert (f) of Fig. 2.9.B).

2.5. Principle of electroless dissolution

From the previous section it is clear that anodic dissolution depends on the availability of holes at the electrode surface and is strongly influenced by an externally applied electrode potential. Another way of dissolving a semiconductor is to make use of an oxidizing agent in the solution. Dissolution of the semiconductor can be considered at open-circuit (no potential is applied to the electrode) as two separate electrochemical reactions, reduction of the oxidizing agent and oxidation of the semiconductor, taking place simultaneously on the same surface. This type of dissolution is termed 'electroless' dissolution and can be described by the Mixed Potential Theory (chapter 5 of [16]). It will be shown in this section by means of current-potential curves that two separate partial reactions are indeed involved in this type of dissolution process.

According to eqs. (2.21) and (2.22) Ox^+ can be reduced either via the CB or via the VB. For the example in this section an oxidizing agent with a very positive $V_{ox/red}^o$ is considered. As a result the D_{ox} function overlaps very well with the VB of the semiconductor. The rate constant for reduction of Ox^+ by hole injection (k_{vb}^c in eq. (2.28)) is so high that the rate is controlled

by diffusion of Ox^+-species from the bulk of the solution to the electrode surface. Consequently, the reduction rate is independent of the applied electrode potential in a broad potential range, as shown in the current-potential curves of both p- and n-type GaAs in a solution of $pH = 0$ (dashed curves (a) of Fig. 2.10). According to eqs. (2.34)-(2.36) the injected holes can be used to dissolve GaAs. However, as was shown in Fig. 2.9, the rate strongly depends on the applied electrode potential. The partial anodic curve of p-GaAs in Fig. 2.9.A is once again shown as a dashed line in curve (b) of fig. 2.10.A. According to the Mixed Potential Theory the total measured current-potential curve (solid line of curve (c)) can be simply deduced from a summation of the partial curves (curve (a) + curve (b)). Herewith it is assumed that both partial reactions do not influence each other. During electroless etching under open-circuit conditions a mixed potential (V_r) is established at which the reduction and oxidation reactions occur at the same rate. At V_r the partial current densities, represented by i^+ and i^-, must be equal $(i^+ = i^-)$, as indicated in Fig. 2.10. In the case of a one electron transfer to the oxidizing agent the overall reaction can be represented as

$$GaAs + 6\,Ox^+ \rightarrow Ga^{III} + As^{III} + 6\,Red. \tag{2.38}$$

The electroless etch rate (v_e) at V_r, which in this example is determined by diffusion of Ox^+-species in solution, is related to i^- and can be obtained via the Faraday equation (page 8 of [16]) as follows:

$$v_e = \frac{i^- M_s 10^4}{6F\varrho_s} = \frac{i^+ M_s 10^4}{6F\varrho_s}, \tag{2.39}$$

where M_s and ϱ_s are semiconductor constants, molecular weight and density respectively, and 6 is the number of charge carriers required to dissolve one GaAs entity. The factor 10^4 is needed for the adjustment of the dimensions.

▷

Fig. 2.10. Typical current-potential curves of p-type (A) and n-type (B) GaAs electrodes in the dark in a solution of pH = 0 containing a strong oxidizing agent having a positive $V_{ox/red}^o$ with respect to the VB (see also Fig. 2.8). The dashed lines of curves (a) and (b) show the partial current densities for reduction of the oxidizing agent and the anodic dissolution of GaAs, respectively. Curves (c) show the current-potential curves which are actually measured; (curve (a) + curve (b)). The energy band models shown in inserts (d) and (f) correspond to −0.3 V and −0.6 V, respectively. Inserts (e) and (g) refer to the open-circuit potential (V_r) at which $i^+ = i^-$.
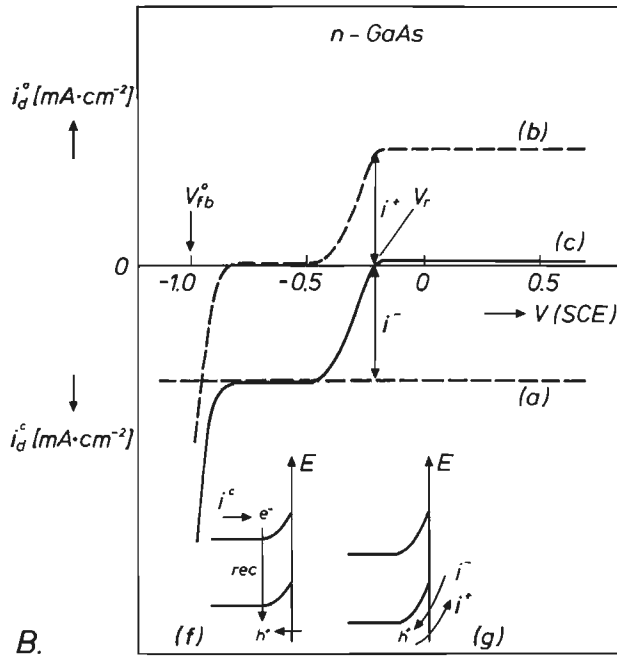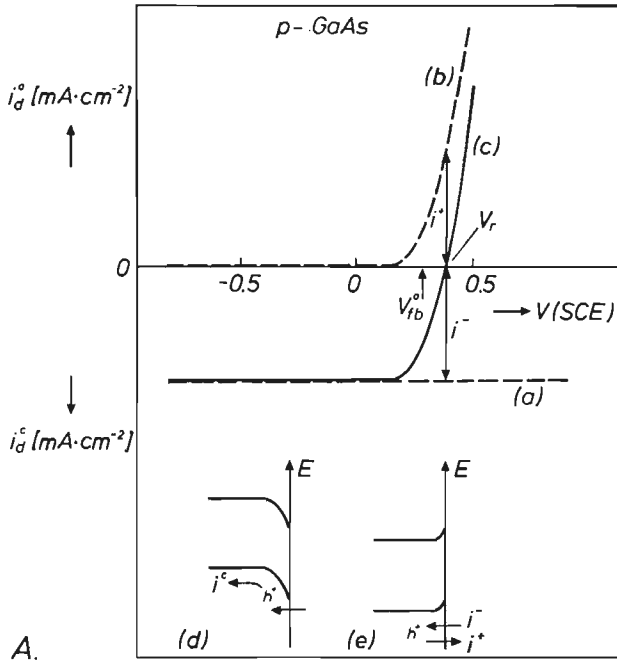
For n-type GaAs the electroless mechanism is somewhat more complex since the injected holes are now minority charge carriers. As at p-type electrodes, the hole injection rate is diffusion-controlled (see the partial reduction current in the dashed curve (a) of Fig. 2.10.B). The potential dependence of the photoanodic dissolution of n-GaAs was discussed in the previous section. In this case, however, the holes are not created by light but are injected by the oxidizing agent. It is clear that at positive potentials $(V > -0.2$ V) the injected holes are held at the electrode surface due to the large band bending (see insert (g) of Fig. 2.10.B). The holes are used to oxidize GaAs in the dark. Consequently, a low net current is expected over a broad potential range (curve (c) of Fig. 2.10.B). The diffusion-controlled cathodic current in curve (c) at moderate band bending, between -0.85 and -0.5 V, is due to recombination of injected holes with electrons from the CB near the electrode surface (see insert (f) of Fig. 2.10.B). The potential range in which recombination occurs corresponds to that found with an illuminated n-GaAs electrode in a solution without an oxidizing agent (see Fig. 2.9.B). However, in the present case recombination results in a cathodic current because CB electrons, which are majority carriers, are supplied from the bulk to the space-charge region to maintain the recombination reaction. This recombination reaction at the cathodic current plateau will be used in one of the following chapters in order to discriminate between charge transfer reactions via the VB and CB [15]. The increase of the cathodic current at negative potentials is again due to hydrogen evolution.

During electroless dissolution a stable and reproducible open-circuit potential (V_r) is established (see Fig. 2.10.B) at which the partial current densities are equal $(i^+ = i^-)$. This would not be expected when the rate of hole injection is exactly balanced by the rate at which holes are used to oxidize GaAs; in such a case, the net current should be zero over a broad potential range and the open-circuit potential would be poorly defined. However, a small anodic current is, in fact, always found at positive potentials (curve (c) of Fig. 2.10.B). Gerischer attributed this to electron exitation into the CB from intermediates of the dissolution process [12] (see eq. (2.34)). At GaAs it was found [17] that only approximately 0.1% of the dissolution reaction is due to this electron step. For the stability of the rest potential this small anodic current is of essential importance. The low rate of electron exitation into the CB of GaAs confirms the suggestion of Gerischer that the successive steps in the dissolution process (eqs. (2.35) and (2.36)) are almost exclusively hole capture steps and that the electron injection can, indeed, be disregarded.

Etching with an oxidizing agent which injects holes into the VB can ob-

viously occur in the dark. For the case in which the D_{ox} function of the oxidizing agent overlaps with the CB, illumination is always necessary to etch the semiconductor crystal via an electroless mechanism at open-circuit. For n-type electrodes no holes are present in the VB and the semiconductor cannot be dissolved in the dark; when the electrode is illuminated, then dissolution should be possible. For p-type semiconductors holes are present in the VB in the dark. However, to reduce the oxidizing agent electrons must be created in the CB by light. With these CB redox systems it is only possible to *photoetch* III-V semiconductor crystals [18]. For several applications this photoetching can be a great advantage [19]. In this work, the main interest is not photoselectivity but etching systems which can dissolve both semiconductor types in the dark. This thesis will therefore concentrate on redox systems whose D_{ox} functions overlap with the valence band of the semiconductor.

2.6. Principle of chemical dissolution

According to the Mixed Potential Theory the electroless etching of semiconductors in solutions containing oxidizing agents can be described by the partial anodic and cathodic current-potential curves. The dissolution rate can be changed by means of an externally applied potential. This has been shown for many etching systems [20,21].

Gerischer and co-workers [22] found the etch rate of n-type Ge in an acidic H_2O_2 solution to be potential-independent in a potential range in which Ge is not anodically dissolved. They proposed a distinction between an 'electroless' and a 'chemical' mechanism for the dissolution of Ge. They also found similar potential-independent etching of GaAs in bromine solutions [23]. For the chemical dissolution of GaAs in these solutions they proposed a coordinated reaction sequence involving the rupture of Ga − As and Br − Br bonds and the simultaneous formation of Ga − Br and As − Br bonds [12,23]. This can be represented as follows

$$
\begin{array}{ccc}
& & \begin{array}{cc} \text{Br} & \text{Br} \\ | & | \end{array} \\
\begin{array}{c} \diagup \end{array}\!\!\text{Ga}-\text{As}\!\!\begin{array}{c} \diagdown \end{array} \quad + \quad \begin{array}{c} \text{Br} \\ | \\ \text{Br} \end{array} \quad \longrightarrow \quad \begin{array}{c} \diagup \end{array}\!\!\text{Ga} \quad \text{As}\!\!\begin{array}{c} \diagdown \end{array} . & & (2.40)
\end{array}
$$
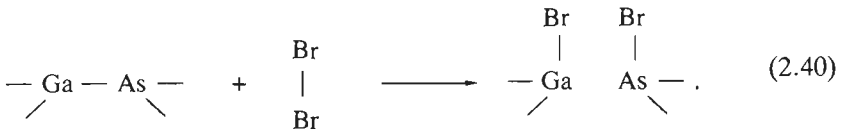
They suggested that symmetrical bifunctional oxidizing agents, such as bromine or H_2O_2, are needed for the chemical dissolution of semiconductors; the bifunctional molecules are capable of forming two new bonds with the semiconductor surface more or less simultaneously.

Most of their experimental results were obtained with n-type semiconductors, which do not always allow unequivocal conclusions to be drawn. Since it may be expected that results with p-type electrodes can be interpreted more unequivocally, the dependence of the etch rate on the electrode potential is studied in this work for p-type semiconductors in a number of cases [24-26]. Recently, Kelly and Reijnders showed that GaAs is also etched by a chemical mechanism in alkaline H_2O_2 solutions [27]. As Fig. 2.11, curve (b) shows, p-type GaAs is indeed etched at a potential-in-
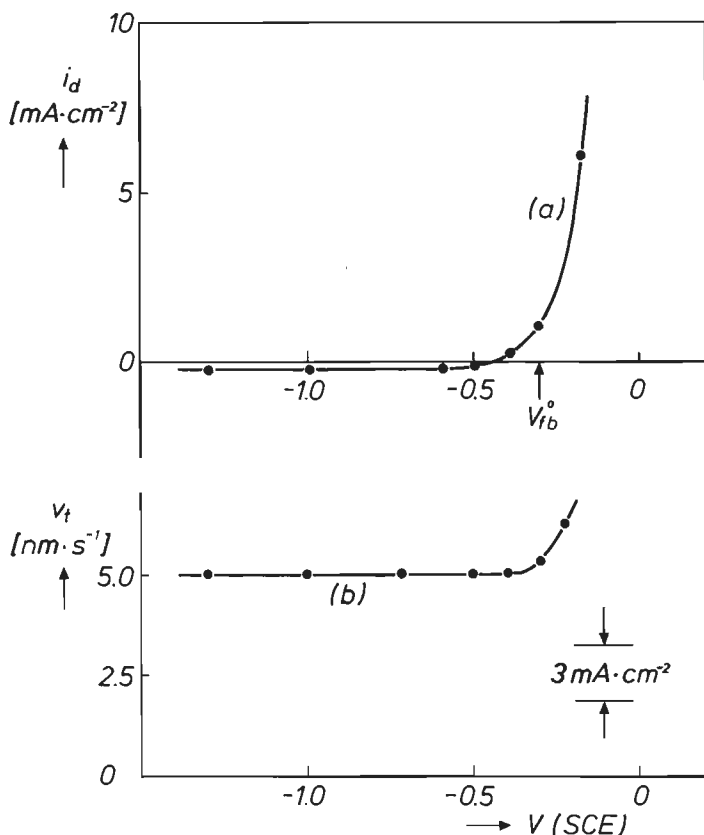
Fig. 2.11. Current density (curve (a)) and etch rate (curve (b)) as a function of the applied electrode potential for a p-type GaAs electrode in the dark in a solution containing 0.2 mole $\cdot$ l^{-1} H_2O_2 at $pH = 10.5$. A potential-independent etch rate, found over a broad potential range in curve (b), cannot be attributed to anodic dissolution of GaAs as the current-potential curve (a) shows. The dissolution of GaAs at cathodic potentials must be attributed to 'chemical' etching of GaAs by H_2O_2 (from [27]).

dependent rate of $5.0 \ nm \cdot s^{-1}$, even at potentials considerably cathodic with respect to that at which GaAs is dissolved anodically (see curve (a)). This behaviour is typical of a chemical etchant. Van den Meerakker [28] showed that both p- and n-type GaAs are dissolved chemically in a solution of I_2, again a symmetrical bifunctional chemical etching species.

It can be concluded that chemical etchants are more important in dissolving semiconductors than has so far been assumed. It should be emphasized that the term 'chemical' etching is often confused in the literature with 'electroless' etching.

2.7. Kinetic considerations in etching reactions

As shown in section 2.5, the electroless etch rate of a semiconductor in a solution containing an oxidizing agent is determined by the rate at which the oxidizing agent injects holes into the VB (eq. (2.22)). When the overlap between D_{ox} and the VB is poor, the hole injection rate is kinetically controlled and can be described by the reduction rate constant (k_{vb}^c) which is given by eq. (2.28). For a purely kinetically controlled reaction the concentration of the oxidizing agent at the semiconductor surface is the same as that in the bulk of the solution $[Ox^{n+}]_s = [Ox^{n+}]_b$ and agitation of the solution does not affect the reaction rate. When the D_{ox} function overlaps very well with the VB, the reduction rate can become so high that the supply of etching species in solution becomes rate-determining, i.e. the reduction rate has become diffusion-controlled. As a consequence the concentration of the oxidizing agent at the electrode surface is almost zero in the steady-state. When one-dimensional diffusion with a linear concentration gradient is assumed, the current corresponding to a diffusion-controlled reduction reaction (i_{lim}^c) can be expressed as

$$i_{lim}^c = \frac{nF\mathscr{D}_{ox}[Ox^{n+}]_b}{\partial},$$
(2.41)

where n is the number of charge carriers to reduce one Ox^{n+}-species, $\mathscr{D}_{ox}$ is the diffusion coefficient of Ox^{n+} in solution, $[Ox^{n+}]_b$ is the Ox^{n+} concentration in the bulk of the solution and ∂ is the diffusion layer thickness. It is clear that ∂ is sensitive to solution agitation caused by density or temperature gradients in the electrolyte which may occur during the etching process. The diffusion-controlled reduction current density is therefore not very stable in non-stirred solutions (page 48 of [29]).

A well-defined diffusion layer is obtained when the electrode, RDE or RRDE, is rotated in the electrolyte [30]. The limiting diffusion current density (i_{lim}^c) depends on the square root of the electrode rotation rate and is given by the 'Levich' equation (chapter 2 of [30])

$$i_{lim}^c = 0.62nF[Ox^{n+}]_b \mathcal{D}_{ox}^{\frac{2}{3}} \nu^{-\frac{1}{6}} \omega^{\frac{1}{2}}, \tag{2.42}$$

where ν is the kinematic viscosity of the solution and ω is the angular velocity of the electrode ($\omega = 2\pi f$ where f is the number of electrode revolutions per second). A plot of i_{lim}^c versus $\omega^{\frac{1}{2}}$ yields a straight line which, when extrapolated, passes through the origin. The diffusion coefficient of the Ox^{n+} species can be obtained from the slope. It is obvious that when the etch rate is determined by the diffusion of Ox^{n+} in solution the etch rate of the semiconductor at the mixed potential also depends on ω.

As already described in the beginning of this section, a rotation-independent current is found for a kinetically controlled reduction reaction. In the intermediate range the reduction can be under mixed kinetic/diffusion control. When the reduction reaction is irreversible a mathematical expression is obtained in which the kinetic and diffusion terms can be recognized (page 291 of [31]):

$$\frac{1}{i_{vb}^c} = \frac{1}{nFk_{vb}^c[Ox^{n+}]_b} + \frac{1}{0.62nF[Ox^{n+}]_b \mathcal{D}_{ox}^{\frac{2}{3}} \nu^{-\frac{1}{6}} \omega^{\frac{1}{2}}}. \tag{2.43}$$

A plot of i^{-1} versus $\omega^{-\frac{1}{2}}$ gives a straight line. Again $\mathcal{D}_{ox}$ can be obtained from the slope. The rate constant k_{vb}^c can be deduced from the intercept on the Y-axis. Indeed, for the two limiting cases one obtains the simplified equations; when the reaction rate constant is very high, eq. (2.43) becomes eq. (2.42) as for a diffusion-controlled reaction; when the electrode rotation rate is high so that mass-transport is not a limitation, the second term of eq. (2.43) can be disregarded and the reduction rate is kinetically controlled:

$$i_{vb}^c = nFk_{vb}^c[Ox^{n+}]_b. \tag{2.44}$$

This equation is similar to eq. (2.28). According to eq. (2.39) the etch rate for electroless systems can be obtained when i^- is known.

The kinetic and diffusion considerations can also be applied to a chemical reaction. Assuming an irreversible first-order reaction, an equation very similar to that reported in eq. (2.43) for the reduction of an oxidizing agent can be derived as is shown in the Appendix of this chapter. The result is

shown in eq. (2.45). The rotation rate dependence of the chemical etch rate (v_{ch}) of a semiconductor crystal can be represented in the steady-state as

$$\frac{1}{v_{ch}} = \frac{\varrho_s}{10^4 k_{ch}[Ch]_b M_s} + \frac{p\varrho_s}{0.62 \times 10^4 [Ch]_b \mathfrak{D}_{ch}^{\frac{2}{3}} v^{-\frac{1}{6}} M_s \omega^{\frac{1}{2}}}, \qquad (2.45)$$

where k_{ch} is the rate constant of the overall chemical dissolution reaction, $[Ch]_b$ is the concentration of the chemical species (Ch) in the bulk of solution, M_s is the molecular weight of the semiconductor, $\mathfrak{D}_{ch}$ is the diffusion coefficient of Ch-species in solution and p gives the number of chemical-species needed to dissolve one III-V 'molecule'. Again, the first term at the right side of the equation represents the rotation-independent etch rate for a kinetically controlled reaction. The second term represents the rotation dependence of a diffusion-controlled chemical etch reaction. From the latter the diffusion coefficient of the chemical-species in solution can be obtained.

When a crystal is not rotated in solution then it is clear that for a kinetically controlled reaction the first term of eq. (2.45) can also be used to obtain the rate constant of the chemical reaction. For a purely diffusion-controlled reaction on the analogy of eq. (2.41) the diffusion layer thickness (∂) has to be considered. The chemical etch rate of a semiconductor crystal can be expressed as

$$v_{ch} = \frac{10^4 [Ch]_b \mathfrak{D}_{ch} M_s}{p\varrho_s \partial}, \qquad (2.46)$$

when one dimensional diffusion with a linear concentration gradient is assumed (see also the right-hand term of eq. (A.11) in the Appendix).

With the set of equations presented in this section the macroscopic steady-state etch rate of III-V semiconductors in either electroless or chemical etchants can be obtained.

Appendix

Derivation of the dependence of the chemical etch rate on the rotation rate of semiconductor crystals

The procedure that will be followed is similar to that applied by Albery (page 51 et seq. of [29]) for the derivation of the rotation rate dependence of the rate of reduction or oxidation of an electroactive species in solution.

In the case of electrochemical reduction of an oxidizing agent this resulted in a relation which was presented in eq. (2.43).

Consider an irreversible chemical dissolution reaction of a solid S and assume this reaction to be of first order in chemical etching-species (Ch). The overall reaction can be represented as

$$S + pCh \xrightarrow{\quad k_{ch} \quad} \text{dissolution products,} \qquad (A.1)$$
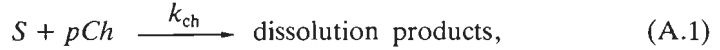
where p gives the number of Ch in solution required to dissolve one 'molecule' S and k_{ch} is the rate constant of the chemical reaction. Furthermore, it is assumed that the dissolution products are directly soluble and thus oxide formation at the solid/solution interface, which might influence the dissolution kinetics, does not occur. The kinetics of the dissolution reaction (eq. (A.1)) normalized per unit area can then be described by

$$-\frac{\delta S}{\delta t} = 10^{-3} A k_{ch}[Ch]_s, \qquad (A.2)$$

and

$$-\frac{\delta Ch}{\delta t} = 10^{-3} A p k_{ch}[Ch]_s, \qquad (A.3)$$

where A is the surface area of the solid in contact with the etchant, k_{ch} of the first order reaction is expressed as $(cm \cdot s^{-1})$ and $[Ch]_s$ is the concentration of the Ch-species at the surface of the solid. To adjust the dimensions the factor 10^{-3} in the numerator of eqs. (A.2) and (A.3) is introduced. The chemical etch rate (v_{ch}) for S is given by

$$v_{ch} = \frac{10^7 M_s}{A \varrho_s} \cdot \left| \frac{\delta S}{\delta t} \right|, \qquad (A.4)$$

where M_s and ϱ_s are again material constants of the solid. The term 10^7 is used to express v_{ch} in $[nm \cdot s^{-1}]$. Inserting eq. (A.2) into eq. (A.4) yields

$$v_{ch} = \frac{10^4 k_{ch}[Ch]_s M_s}{\varrho_s}. \qquad (A.5)$$

It is obvious that the supply of Ch from the bulk of the etching solution to the solid surface must be provided by diffusion. The flux of Ch-species

to the surface is described by Fick's First Law of Diffusion (page 130 of [31])

$$\frac{\delta Ch}{\delta t} = 10^{-3} A \mathcal{D}_{ch} \cdot \frac{\delta [Ch]}{\delta y},$$ (A.6)

where $\frac{\delta [Ch]}{\delta y}$ is the concentration gradient of Ch in solution; y is the normal distance to the solid/solution interface. When a linear concentration gradient of Ch-species in the solution is assumed (page 132 of [6]), eq. (A.6) can be rewritten as

$$\frac{\delta Ch}{\delta t} = 10^{-3} A \mathcal{D}_{ch} \cdot \frac{[Ch]_b - [Ch]_s}{\partial},$$ (A.7)

where $[Ch]_b$ is the concentration of Ch in the bulk of the etchant and ∂ is the diffusion layer thickness. The rate of the surface reaction must, of course, be equal to the flux of the dissolution products from the solid/solution interface into solution, i.e.

$$|eq. (A.3)| = eq. (A.7).$$ (A.8)

Inserting eq. (A.3) and eq. (A.7) into eq. (A.8) yields an expression for the surface concentration of the chemical etching-species, $[Ch]_s$:

$$[Ch]_s = \frac{\mathcal{D}_{ch} [Ch]_b}{p k_{ch} \partial + \mathcal{D}_{ch}}.$$ (A.9)

$[Ch]_s$ can now be eliminated from the relation of the chemical etch rate which was given in eq. (A.5):

$$v_{ch} = \frac{10^4 k_{ch} \mathcal{D}_{ch} [Ch]_b M_s}{p \varrho_s \partial k_{ch} + \varrho_s \mathcal{D}_{ch}}.$$ (A.10)

Rearranging eq. (A.10) gives

$$\frac{1}{v_{ch}} = \frac{\varrho_s}{10^4 k_{ch} [Ch]_b M_s} + \frac{p \varrho_s \partial}{10^4 [Ch]_b \mathcal{D}_{ch} M_s}.$$ (A.11)

When the etching process is fully characterized, the only parameter in eq. (A.11) is the diffusion layer thickness (∂). The dependence of the diffusion layer thickness on the electrode rotation rate is derived by Levich (page 168 of [29]) and is given by

$$\partial = 1.61 \, \mathcal{D}_{ch}^{\frac{1}{3}} \nu^{\frac{1}{6}} \omega^{-\frac{1}{2}}. \qquad (A.12)$$

Eliminating ∂ in eq. (A.11) with eq. (A.12) ultimately yields the rotation rate dependence of the chemical etch rate:

$$\frac{1}{v_{ch}} = \frac{\varrho_s}{10^4 k_{ch}[Ch]_b M_s} + \frac{p\varrho_s}{0.62 \times 10^4 [Ch]_b \mathcal{D}_{ch}^{\frac{2}{3}} \nu^{-\frac{1}{6}} M_s \omega^{\frac{1}{2}}}. \qquad (A.13)$$

The result of this derivation (eq. (A.13)) was already presented as eq. (2.45) in section 2.7.

References

[1]   S.R. Morrison, *'Electrochemistry at Semiconductor and Oxidized Metal Electrodes'*, Plenum Press, New York, (1980).

[2]   *'Landolt-Börnstein, Numerical Data and Functional Relationships in Science and Technology'*, New Series Group III, vol. 17, subvol. a, Springer Verlag, Berlin, (1982).

[3]   A.S. Grove, *'Physics and Technology of Semiconductor Devices'*, J. Wiley and Sons, New York, (1967).

[4]   R. Memming, *'Electroanalytical Chemistry. A Series of Advances'*, editor A.J. Bard, Vol. 11, p. 1-84, Dekker, New York, (1979).

[5]   M.M. Faktor, T. Ambridge, C.R. Elliott and J.C. Regnault, *'Current Topics in Materials Science'*, Editor E. Kaldis, Vol. 6, p. 1, (1980).

[6]   J.O'M. Bockris and D. Drazic, *'Electrochemical Science'*, Taylor and Francis Ltd., London, (1972).

[7]   J.J. Kelly and P.H.L. Notten, *J. Electrochem. Soc.*, **130**, 2452, (1983).

[8]   H. Gerischer, *'Physical Chemistry, An Advanced Treatise'*, Editor H. Eyring, D. Henderson and W. Jost, Vol. IX A, p. 463-542, Academic Press, New York, (1970).

[9]   R. Memming, *Philips Tech. Rev.*, **38**, 160, (1978/1979).

[10] K.W. Frese, Jr., *J. Phys. Chem.*, **85**, 3911, (1981).

[11] R. Memming and F. Möllers, *Ber. Bunsenges. Phys. Chem.*, **76**, 475, (1972).

[12] H. Gerischer and W. Mindt, *Electrochem. Acta*, **13**, 1329, (1968).

[13] K.W. Frese, M.J. Madou and S.R. Morrison, *J. Phys. Chem.*, **84**, 3172, (1980).

[14] J.J. Kelly and R. Memming, *J. Electrochem. Soc.*, **129**, 730, (1982).

[15] J.E.A.M. v.d. Meerakker, J.J. Kelly and P.H.L. Notten, *J. Electrochem. Soc.*, **132**, 638, (1985).

[16] K.J. Vetter, *'Electrochemical Kinetics'*, Academic Press, London, (1967).

[17] D. Vanmaekelbergh and J.J. Kelly, Extended Abstract No. 6.53, 38th ISE Meeting, Maastricht, sept., (1987).

[18] J.J. Kelly, J.E.A.M. v.d. Meerakker and P.H.L. Notten, in *'Grundlagen von Elektrodenreaktionen'*, Dechema Monographien Band 102, page 453, Frankfurt, (1986).

[19] D.V. Podlesnik, H.H. Gilgen and R.M. Osgood, Jr., *Appl. Phys. Lett.*, **45**, 563, (1965).

[20] P.H.L. Notten, *Electrochim. Acta*, **32**, 575, (1987).

[21] P.H.L. Notten, J.J. Kelly and H.K. Kuiken, *J. Electrochem. Soc.*, **133**, 1226, (1986).

[22] H. Gerischer and W. Mindt, *Surf. Sci.*, **4**, 440, (1966).

[23] H. Gerischer and I. Wallem-Mattes, *Z. Phys. Chem. N.F.*, **64**, 187, (1969).

[24] P.H.L. Notten, *J. Electrochem. Soc.*, **131**, 2641, (1984).

[25] P.H.L. Notten and A.A.J.M. Damen, *Appl. Surf. Sci.*, **28**, 331, (1987).

[26] P.H.L. Notten, *J. Electroanal. Chem.*, **224**, 211, (1987).

[27] J.J. Kelly and A.C. Reijnders, *Appl. Surf. Sci.*, **29**, 149, (1987).

[28] J.E.A.M. van den Meerakker, *Electrochim. Acta*, **30**, 435, (1985).

[29] J. Albery, *'Electrode Kinetics'*, Oxford University Series, Clarendon Press, Oxford, (1975).

[30] W.J. Albery and M.L. Hitchman, *'Ring-Disc Electrodes'*, Clarendon Press, Oxford, (1971).

[31] A.J. Bard and L.R. Faulkner, *'Electrochemical Methods, Fundamentals and Applications'*, J. Wiley and Sons, New York, (1980).

Chapter 3

Experimental considerations

3.1. Introduction

As described in the general introduction of chapter 1, the work in this thesis can be divided into two parts: the electrochemical study of semiconductor materials in solutions containing either oxidizing agents or chemical etching agents and etching experiments on semiconductor crystals in these solutions. The experimental approach is, in each case, quite different. Therefore, the same distinction is maintained in this chapter; the electrochemical set-up and experiments are first described in section 3.2 and the etching experiments in section 3.3.

3.2. Electrochemical measurements

3.2.1. Electrode preparation

The GaAs single-crystal wafers used in this work were obtained from MCP Electronics, Ltd., England. The crystals were Zn-doped in the case of p-type and Si-doped in the case of n-type GaAs and had a doping level in the range of $8 \times 10^{16} - 2 \times 10^{18}$ cm^{-3}. Different crystal orientations were used, such as (001), (111)Ga and (111)As faces. Before use, the slices were mechano-chemically polished in a 0.1 M NaOCl, 0.1 M Na$_2$CO$_3$ solution of pH = 13 [1]. The zinc-doped InP (p-type) slices were obtained from liquid-encapsulated Czochralski material which was grown at the Philips Research Laboratories, Eindhoven. The carrier concentration was in the range of 1 - 2×10^{18} cm^{-3}. The InP crystals were mechano-chemically polished in a methanol solution containing 0.1 M Br$_2$ [2]. Two different crystal orientations, (001) and (111)In, were used. Unless otherwise stated, the (001) surface of GaAs and InP was used in both the electrochemical and etching experiments.

For electrochemical measurements ohmic contacts at the back side of the semiconductor crystal are essential. Au-Ge-Ni (83-13-4 wt %) layers about 100 nm thick were sputtered onto the back side of both n-type GaAs and InP crystals. For p-type crystals a zinc diffusion was performed from the vapour phase, before 100 nm thick Pt layers were sputtered. The contacts became ohmic after annealing for 15 minutes at a temperature of 400 °C under argon.
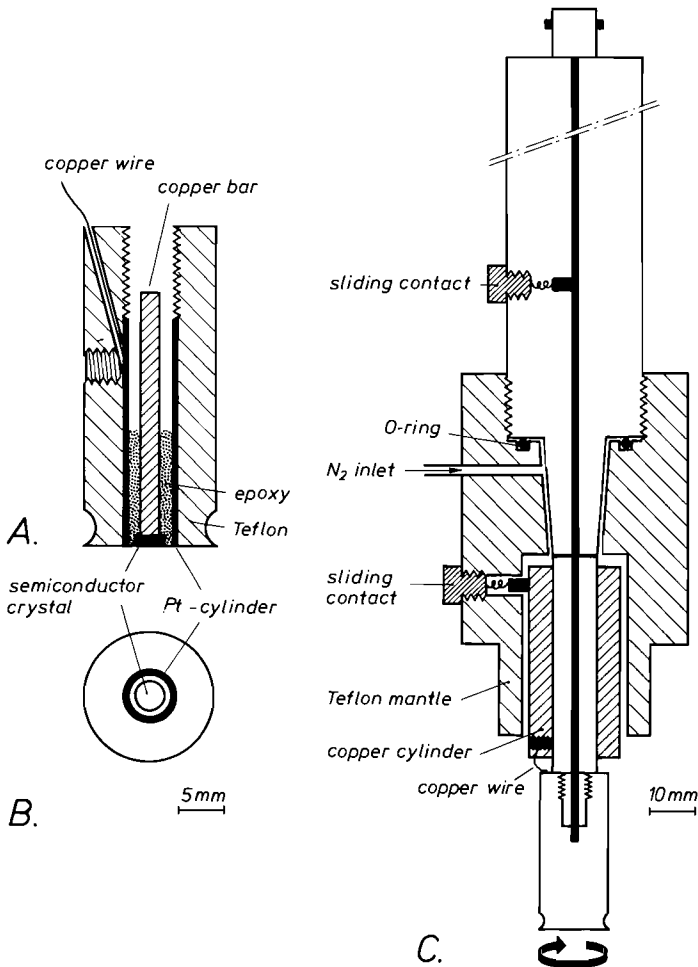
Fig. 3.1. In (A) a cross-section and in (B) a top-view of a rotating Pt-ring/III-V disk electrode (RRDE) are shown. C) shows the adapted Tacussel motor with the second sliding contact in contact with the Pt-ring electrode.

Rotating disk (RDE) or rotating ring/disk (RRDE) electrodes were mainly used for the electrochemical measurements. The aim was to make rotating electrodes which were readily interchangeable. For this purpose, disks with a diameter of 4.00 mm were cut from wafers approximately 400 μm thick. Fig. 3.1.A shows how the electrodes were made. A copper bar was fixed to the ohmic contact on the back side of the electrode using a conducting resin (E-solder no 3021 from ACME). The electrode was centered with respect to a Teflon holder using a spacer. Both the electrode and the holder were then mounted on double-sided adhesive tape fixed to a flat surface. The empty space between the disk electrode and the Teflon holder was filled with Araldite. This is a two-component epoxy resin (mixture of 17 wt % HY-956 and 83 wt % DRL) which is chemically inert in a wide variety of solutions. After hardening of the resin, the electrode was removed from the tape and was cleaned in n-hexane. The flatness of the surface was examined afterwards with an optical microscope. In the case of Pt-ring/III-V-disk electrodes a Pt-cylinder was pressed into the Teflon holder before the disk electrode was mounted. A copper wire, connected to the Pt-cylinder through the Teflon holder, served as a contact for the ring electrode. The inner and outer diameters of the Pt-cylinder were 4.50 and 5.00 mm, respectively. A top-view of a ring/disk electrode is shown in Fig. 3.1.B. According to Albery and Hitchman (pages 17-28 of ref. [3]) a theoretical collection factor (γ) can be calculated when the geometric parameters are known. For the RRDE with r_1 = 2.00 mm, r_2 = 2.25 mm and r_3 = 2.50 mm a collection factor of 0.23 is determined. In order to check the accuracy of the ring/disk electrodes, γ of each RRDE was measured and compared with the theoretical value.

The rotating disk electrodes could be directly fitted to a Tacussel ED-I motor. A spring mechanism was used for making contact between the copper bar and the sliding contact of the motor. For the rotating ring/disk electrodes this motor had to be adapted to make a second external contact for the Pt-ring electrode. Fig. 3.1.C shows schematically how a Teflon mantle, containing a second sliding contact, was fitted to the stationary part of the motor. An O-ring ensured a gas-tight seal. A copper cylinder was attached to the rotating part of the motor. The cylinder was connected electrically via the sliding contact to the copper wire from the Pt-cylinder. The rotation rate of the motor could be varied accurately up to 5000 revolutions per minute (rpm) with a control unit, 'Controvit', from Tacussel.

3.2.2. Instrumentation

The rotating electrode could be mounted in a conventional electrochemical cell as is shown in Fig. 3.2. As reference, a Saturated Calomel Electrode (SCE) was used. To reduce the ohmic drop between the working electrode and the reference electrode a Luggin capillary was located close to the working electrode. All potentials in this thesis are given with respect to SCE on a voltage scale and are indicated by V(SCE). A large-area Pt counter electrode was placed in a separate compartment to prevent O_2-gas, evolved at the counter electrode, from diffusing into the electrolyte of the working electrode compartment. Electrical contact between the two compartments was provided by a salt bridge (3.5 M KCl in 4 wt % agar-agar/water solution).

All solutions were prepared with reagent grade chemicals. The following concentrated solutions were supplied by Merck: HCl ($37\% \approx 12$ molar), HBr ($47\% \approx 9$ molar), H_2O_2 ($30\% \approx 10$ molar), acetic acid (100%) and Br_2 ($100\% \approx 20$ molar). NaOCl was obtained from BDH Chemicals (Poole, En-
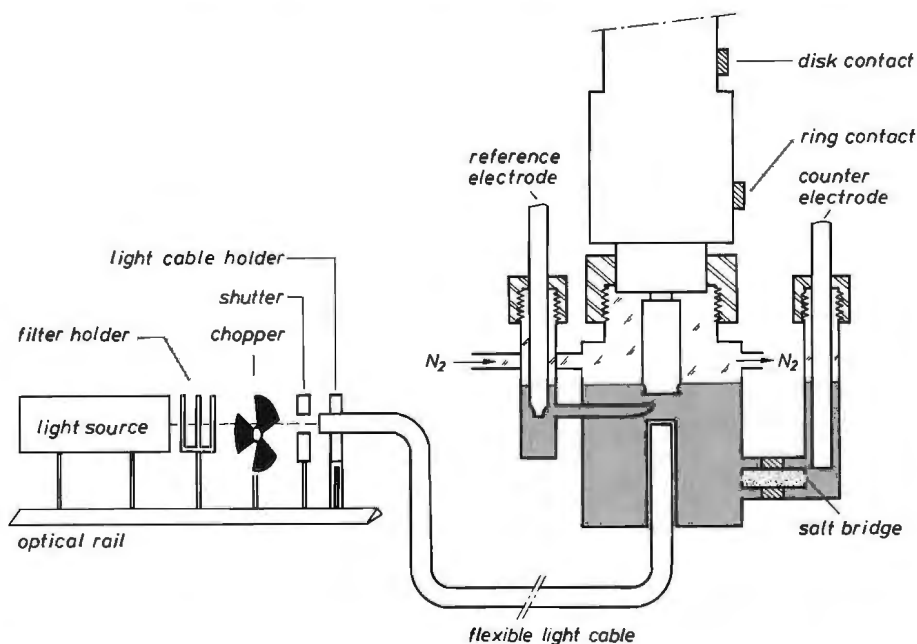
Fig. 3.2. The gas-tight electrochemical cell containing the RRDE, the reference electrode and counter electrode and the equipment used for illuminating the working electrode.

gland) as an approximately 0.5 M solution in 0.1 M NaOH. Chemical analysis showed that more than 96% of the chlorine species in the stock solution was available as OCl^- ions. EDTA is used here to denote the disodium salt of ethylenediamine tetraacetic acid and (Oxa) to denote potassium oxalate. For some experiments buffered solutions supplied by Merck were used: citrate buffers in the pH range 3 - 6, a phosphate buffer at $pH = 7$ and borate buffers in the pH range 8 - 11. For the electrochemical measurements the solutions were purged of oxygen before use by bubbling N_2 through the solution and the experiments were performed at room temperature unless otherwise stated.

The illumination equipment is schematically shown on the left side of Fig. 3.2. As light sources either He-Ne lasers (wavelength 632.8 nm) from Spectra Physics (Model 133 with 1 mW output, Model 120 with 5 mW output and Model 133 with 15 mW output) or white light sources (150 Watt Schott halogenlamp, KL 150 B or KL 1500) were used. In one experiment a high power (4W) multi-line argon ion laser from Spectra Physics (Model 166) was used; for this experiment only light with a wavelength of 350 nm was selected. The light intensity could be varied stepwise with the Schott lamps and in the case of the He-Ne and Ar-ion lasers with neutral density filters. As a relative measure of the light intensity, the limiting photocurrent of an n-GaAs electrode in 0.5 M H_2SO_4 was used (at the anodic plateau of curve (b) in Fig. 2.9.B). In this electrolyte no inhibition effects were found. A photon density ϕ with arbitrary unit (a.u.) = 1 corresponds to a limiting photocurrent density of 1 $mA \cdot cm^{-2}$. All light intensities in this thesis are given in a.u. All light sources were used in combination with a glass fibre light cable which could be brought close to the working electrode (see Fig. 3.2).

To modulate the light beam, a chopper (frequency programmable light chopper MK1 from Rofin Ltd.) and a shutter controlled by a timer (Uniblitz, Model 310B) were used. The rise time of the shutter was less than 0.25 ms. The absolute light intensity was measured using a callibrated Laser Power Meter (Model 460-1-A) with a Si-detector (Model 460-2) in combination with an attenuator (Model 550-11Q) from EG and G Electro-Optics. To prevent interference from daylight the cell was placed in a lightproof box.

Fig. 3.3 shows schematically the set-up for the electrochemical measurements. The basic element is the potentiostat which is connected to the three or four electrodes of the electrochemical cell. In the case of a three-electrode system a Wenking potentiostat was used (Model LB 75 H or POS 73). For the ring-disk experiments a BIPAD 2 bipotentiostat from Tacussel was used.
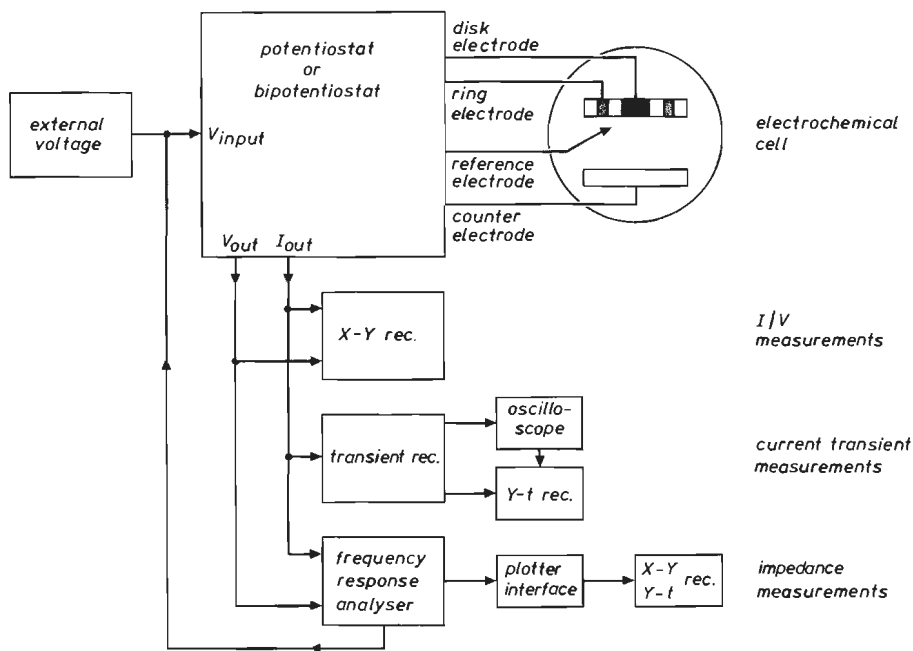
Fig. 3.3. Block scheme of the equipment for electrochemical measurements with the three electrochemical techniques applied.

An additional external voltage could be applied to the voltage input of all potentiostats. The three types of electrochemical techniques used in this work can be distinguished in Fig. 3.3. For the potentiostatically or potentiodynamically measured current-potential curves the external voltage was supplied by a Voltage Scan Generator from Wenking (Model VSG 72). The potential and current were directly recorded by an X-Y recorder (Philips PM 8141). The current transient measurements were performed using a potential step generated by a Chemical Electronics WG 01 modular waveform generator (Birtley Ltd.). The resulting signal was detected by a Datalab DL 901 transient recorder in combination with a Philips PM 3310 oscilloscope and was recorded on a Philips Y-t recorder (combination of PM 8141 and PM 9884). For the impedance measurements a Solartron 1186 Electrochemical Interface was used as potentiostat together with a 1174 Frequency Response Analyser and a 1180 Plotter Interface both from Solartron (Schlumberger). For the potentiodynamically measured Mott-Schottky plots a 10 mV rms signal was applied to the working electrode at a frequency of 10 kHz. To analyse impedance behaviour of electrodes, the frequency of the

applied a.c. potential was varied between 0.5 and 30 kHz and the imaginary and real components of the impedance were measured.

3.2.3. Flow-cell measurements

In chapter 2 chemical etching has been discussed [4,5]. An important feature of chemical dissolution is the high etch rate of the semiconductor electrode even at very negative potentials where the surface hole concentration is extremely low (see Fig. 2.11). An elegant way to distinguish between chemical and electroless mechanisms is to measure the dissolution rate as a function of the applied potential in a broad potential range and to correlate this etch rate with the measured current density.

Ambridge et al. [6] described a micro-electrochemical flow-cell which accommodates all three electrodes used in a conventional electrochemical cell, but which also allows electrolyte to be pumped continuously past the electrode. Haroutiounian et al. [7] developed this concept by measuring automatically the gallium ion concentration in the solution, due to the dissolution of GaAs, directly after the electrolyte has left the cell. This method makes a direct correlation of the etch rate with the measured current density possible. In fact, it can be considered as an 'in situ' measurement. This design was used to make a micro-electrochemical flow-cell from glass, a material inert in the concentrated aggressive solutions used in the present work. This is shown in Fig. 3.4. In the upper half of the figure a photograph is shown of the complete cell (A). The micro-electrochemical compartment is situated at the bottom and is surrounded by a waterjacket for temperature control. In the waterjacket different supply tubes can be clearly distinguished. In the lower part (B) of Fig. 3.4 an enlargement of the electrochemical cell compartment is schematically presented. In a solid glass block several cylindrical holes were mechanically bored as indicated, one for the supply of electrolyte, one for the removal of electrolyte and one to accommodate a flexible light cable for illumination of the working electrode. To detect accurately low etch rates with small electrode areas, it was necessary to reduce the volume of the working electrode compartment so that the product concentrations to be detected were not too low. Therefore a small cavity, about 2 mm high, was made at the bottom to form the working electrode compartment. A PMMA (PolyMethylMethAcrylate) holder containing the semiconductor electrode could be screwed into the bottom of the glass part of the cell. An O-ring was used as seal between the two parts.

For these experiments the stationary working electrode was prepared in a somewhat different manner from that already described for the rotating

A.

B.
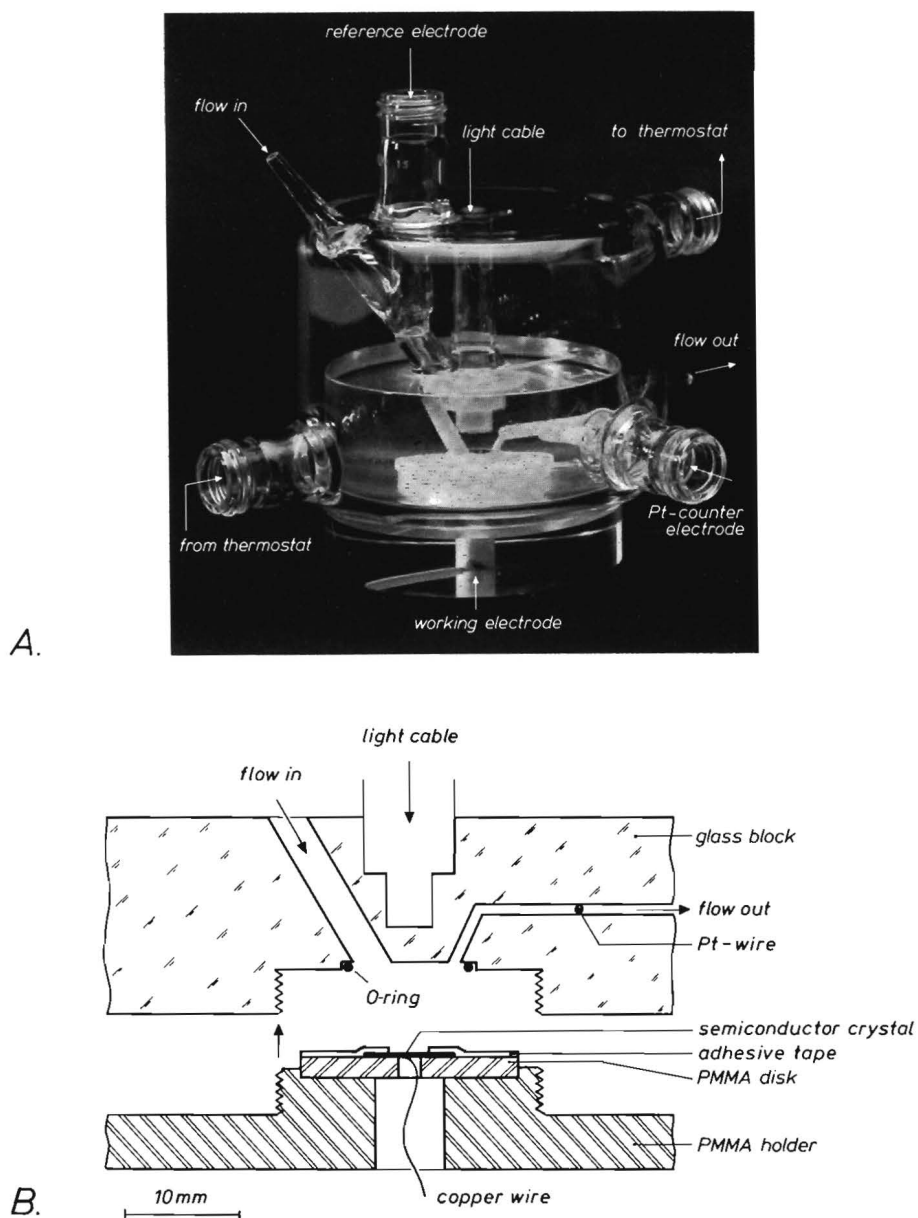
Fig. 3.4.A) photograph of the micro-electrochemical flow-cell made from glass.
B) shows schematically how the stationary working electrode is mounted in the small
working electrode compartment. Also shown are the supply and outlet tubes for the
electrolyte flow and the light cable holder.

electrodes. The semiconductor crystal was mounted on a PMMA disk with adhesive tape (Macal 8100-series), in which a 3 mm diameter hole was pre-perforated thus leaving the centre of the crystal surface uncovered. A well-defined electrode area of 0.07 cm² was obtained in this way. At the back side a copper wire was fixed through a hole in the PMMA disk to the ohmic contact of the semiconductor crystal with the conducting resin.

The SCE reference electrode was placed in the tube through which the electrolyte was supplied (see photo). The counter electrode, a Pt wire, could be screwed into the electrolyte outlet tube. This location is of essential importance because gas evolution occurs at the Pt counter electrode. The gas bubbles are, in this way, carried off directly without disturbing the electrolyte flow in the working and reference electrode compartments. The electrolyte solution was pumped through the cell with an LKB Varioperpex peristaltic pump. The flow rate could be varied accurately in the range of 0.001 to 0.040 ml·s⁻¹. The flow of the electrolyte in the cell was checked with a coloured solution and it was found that turbulence could be avoided with a relatively broad inlet tube, as expected. The small outlet tube prevents the back flow of the electrolyte containing the dissolution products. The electrolyte was collected at the exit of the flow-cell in fractions of 1 ml in test tubes. These flow-cell experiments were performed under potentiostatic control. On changing the applied potential it was found experimentally that it took a few minutes, depending on the flow rate, before a new steady-state is established and the concentration of products in the solution does not change. Only the solutions obtained after the establishment of a steady-state were used for the analyses. Measurements were made in the dark in a light-proof box and under illumination using the various light sources.

The dissolution rate of GaAs and InP electrodes at various potentials was determined by measuring analytically the gallium and indium concentration, respectively, in the etching solution by Inductively-Coupled-Plasma (ICP) emission spectrometry. Concentrations as low as 5×10^{-6} mole·l⁻¹ could be determined with a relative accuracy of about 5%. The flow-rate of the electrolyte was determined mainly by the lower limit of the gallium and indium detection. When the gallium concentration is analysed in the electrolyte the total etch rate (v_t) of the semiconductor electrode can be simply calculated according to

$$v_t = \frac{10^4 [\text{Ga}^{\text{III}}] v_{\text{sol}} M_{\text{GaAs}}}{\varrho_{\text{GaAs}} \cdot A},$$

(3.1)

where $[\text{Ga}^{\text{III}}]$ is the measured gallium ion concentration in the solution ex-

pressed as (mole·l^{-1}), v_{sol} in the flow-rate of the solution (ml·s^{-1}), $M_{GaAs} = 144.6$ is the molecular weight of GaAs, ϱ_s is the density of GaAs ($\varrho_{GaAs} = 5.32$ [8]) expressed as (g·cm^{-3}) and A is the electrode area in cm^2. The 10^4 term in the numerator is needed for the adjustment of the etch rate to (nm·s^{-1}). To correlate the etch rate directly with the measured current density it is convenient to express the etch rate as a current density. The following equation can be used,

$$i = \frac{6F[Ga^{III}]v_{sol}}{A} \qquad (3.2)$$

where 6 is the number of holes needed for the dissolution of one GaAs entity and F is the Faraday constant. The current density in eq. (3.2) is expressed as (mA·cm^{-2}). The two equations above refer to the dissolution of GaAs but they can also be used with different constants for the dissolution of InP: $M_{InP} = 145.8$ and $\varrho_{InP} = 4.81$ g·cm^{-3} [8].

3.3. Etching experiments

3.3.1. Mask preparation and orientation

Both GaAs and InP have a zinc-blende structure [9]. In this type of crystal the gallium and arsenic atoms, in the case of GaAs, alternately occupy the available sites according to an ordered pattern. It will be clear that the crystal surface and the orientation of the resist pattern are important when the shape of the etched profiles near resist edges in III-V semiconductor crystals has to be investigated. Since only (001) surfaces are used in the solid state laser technology most of the etching experiments, and also the electrochemical experiments, were made with these surfaces. The resist patterns were oriented in two directions as shown in Fig. 3.5, perpendicular to the two planes which can be very easily cleaved, i.e. the (110) and ($\bar{1}$10) planes [2].

Two different resist patterns were used. For one series of experiments we covered only one half of the crystal surface with resist which we denote as the semi-infinite case. For another series, a masking pattern of variable width (a) was used (see Fig. 3.5). The widths used were $a = 1, 3, 10, 30, 100, 300$ to 1000 μm. In most cases an SiO$_2$ layer with a thickness (d_r) of about 100 nm was used as mask. The SiO$_2$ masks were produced with conventional CVD equipment at an operating temperature of 400 °C. In certain
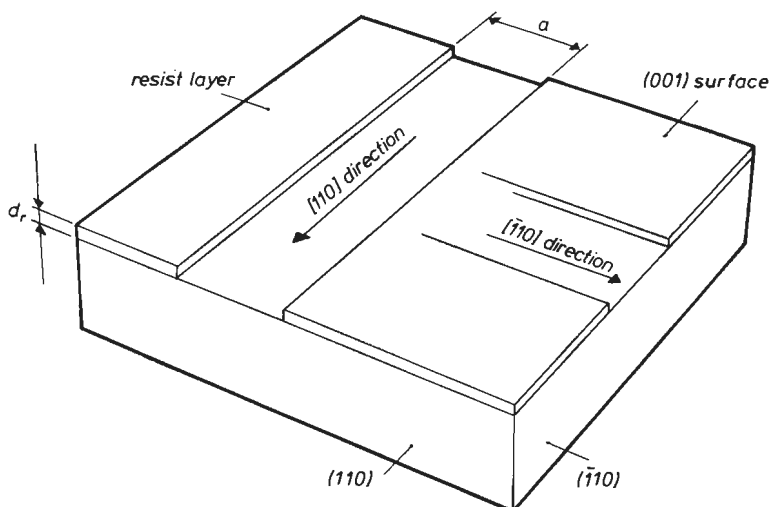
Fig. 3.5. Resist orientation in two directions at right angles on a (001) semiconductor surface. The resist edges are aligned either in the [110] or [$\bar{1}$10] direction, perpendicular to the (110) and ($\bar{1}$10) cleave facets, respectively. The resist thickness is represented by d_r and the slit width by a. The width is varied between 1 μm and semi-infinite.

cases photoresists (HNR-999 or HPR-204 from Shipley) were also used. Thin photoresist layers at the surface were obtained by spinning the wafers at 6000 revolutions per minute at room temperature. The resist patterns were produced by standard photolithographic techniques. The produced structures are finally backed during 30 minutes at a temperature of 120 °C (HPR) or 135 °C (HNR-photoresist). The mask preparation procedures were performed in a 'clean room'. The orientation accuracy was determined by a microscope and was better than 0.05°. The samples were about 6 × 6 mm large and were mounted on a glass plate before etching.

3.3.2. Etching conditions

The glass plate with the sample was placed either horizontally or vertically in a closed glass vessel containing the etching solution. The vessel was surrounded by a waterjacket to allow the etching solution to be thermostated at different temperatures (accuracy, ± 0.5 °C). The temperature range at which the etching experiments were performed was generally between −10 and +40 °C. To cool down the etchants a cryostat (PBC-4 Bath Cooler from

Neslab Instruments Inc.) was used in combination with the thermostat. Unless otherwise stated, etching experiments were performed in the dark at 20 °C. After etching, the slices were cleaved perpendicular to the resist edge and the etched profiles were examined in a Scanning Electron Microscope (SEM) or with an optical microscope. In some cases the etch depth relatively far away from the resist edge was measured with a Leitz Michelson interferometer after the resist had been removed from the crystal surface.

Some remarks should be made about two etching systems used in chapters 5 and 8. It is clear from the standard redox potentials of the OCl^-/Cl_2 and H_2O_2/H_2O redox couples ($V^o_{OCl^-/Cl_2}$ = 1.38 V(SCE) and $V^o_{H_2O_2/H_2O}$ = 1.53 V(SCE), respectively [10]) that solutions of OCl^- or H_2O_2 with HCl are unstable since chloride can be oxidized to chlorine ($V^o_{Cl_2/Cl^-}$ = 1.11 V(SCE)). Gas evolution in HCl/H_2O_2 etchants begins rather slowly, and a slight yellowish coloration of the solution indicates some Cl_2 formation. However, the rate of this reaction is limited, and H_2O_2 is the active component in the etching bath. Etching was performed, in this case, immediately after the solution components were mixed. When hypochlorite and HCl are mixed, chlorine is instantaneously formed according to the following overall reaction

$$OCl^- + Cl^- + 2H^+ \rightarrow Cl_2 + H_2O. \tag{3.3}$$
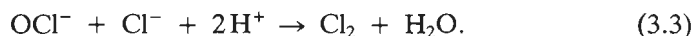
However, the relative concentration of the starting solutions determines whether chlorine gas is evolved or not. When concentrated solutions are mixed, a very vigorous Cl_2 evolution is immediately observed. This subsides after some minutes. The etching experiments with this bath were performed 3 minutes after mixing, when only a very slight gas evolution occurred. The Cl_2 concentration in the solution is determined by its solubility and is 0.10 molar at 20 °C [11]. When a solution of low OCl^- concentration is mixed with HCl, Cl_2 is also immediately formed in solution. However, since the Cl_2 solution is now lower than 0.10 molar, no Cl_2 evolution is observed in this case and the solution is relatively stable in time. For both H_2O_2 and NaOCl-based etchants, a fresh solution was prepared for each electrochemical and etching experiment.

As a result of the dissolution of InP in concentrated HCl and HBr solutions gas is evolved at the crystal surface. This gas was analysed qualitively using the colour detector tube method ('Dräger' tube), which gave, in this case, a characteristic colour reaction for phosphine. A gas burette was used for the quantitative gas analysis.

References

[1] J.S. Basi, *U.S. Patent 3,738,882*.

[2] Y. Tarui, Y. Komiya and Y Harada, *J. Electrochem. Soc.*, **118**, 118, (1971).

[3] W.J. Albery and M.L. Hitchman, *'Ring-disc electrodes'*, Clarendon Press, Oxford, (1971).

[4] H. Gerischer and W. Mindt, *Electrochim. Acta*, **13**, 1329, (1968).

[5] H. Gerischer and I. Wallem-Mattes, *Z. Phys. Chem. N.F.*, **64**, 187, (1969).

[6] T. Ambridge, C.R. Elliott and M.M. Factor, *J. Applied Electrochem.* **3**, 1, (1973).

[7] E. Haroutiounian, J. Sandino, P. Clechet, D. Lamouche and J. Martin, *J. Electrochem. Soc.*, **131**, 27, (1984).

[8] *'Landolt-Börnstein, 'Numerical Data and Functional Relationships in Science and Technology'*, New Series Group III, vol. 17, subvol. a, Springer Verlag, Berlin, (1982).

[9] C. Kittel, *'Introduction to Solid State Physics'*, 5th edition, New York, (1976), Wiley and Sons Inc.

[10] *'Handbook of Chemistry and Physics'*, 51st edition, Ed. R.C. Weast, The Chemical Rubber Co., (1970).

[11] *'Handbook of Chemistry and Physics'*, 37th edition, Ed. C. Hodgeman, The Chemical Rubber Co., (1955).

Chapter 4

Anodic dissolution of GaAs

4.1. Introduction

The kinetics of anodic oxidation of semiconductors are important both for anodic etching and polishing applications. In electroless systems oxidation of the solid is also important since it constitutes the anodic partial reaction. In addition, this process may influence indirectly the kinetics of the cathodic reaction; hole injection from the oxidizing agent. In this chapter, certain factors will be considered which influence the oxidation kinetics. The consequences of these results for the kinetics of electroless dissolution of GaAs will be dealt with in chapter 5.

The rate of (photo)anodic dissolution of GaAs clearly depends on the pH of the electrolyte [1-4]. High rates are observed both at low and high pH values [5]. In the intermediate pH range, dissolution rates are greatly reduced; this is due to passivation caused by film formation on the electrode [6,7]. These trends are in general agreement with what one expects on the basis of simplified Pourbaix diagrams for GaAs in aqueous media [1,3]. For etching applications the neutral pH range is generally not interesting and will not be further considered in this work.

There are indications in the literature that the anodic dissolution of GaAs even at high pH can be determined, to some extent, by film formation. Decker has shown the importance of oxide formation for n-GaAs at a pH of 11.5 [8]. In the introduction to anodic dissolution in section 2.4, it was suggested that charged intermediates might be formed during oxidation of the solid [9-13]. A build-up of positive charge at the surface should influence the potential distribution over the semiconductor/electrolyte interface. This could, in turn, affect the position of the band-edges at the surface and consequently, the kinetics of hole injection. It would be expected that such effects are accentuated when dissolution is accompanied by film-formation.

The aim of the work described in this chapter is, therefore, two-fold:

– in the first place, the influence of the pH and film formation on the kinetics of anodic dissolution of GaAs was investigated (section 4.2). Measurements were performed in two pH ranges: 0 - 6 and 10 - 14. To compare electrodes with and without surface oxide, layer formation was 'artificially' stimulated in acidic medium by working with an oxide-promoting reagent, EDTA [1].

– in the second place, to obtain information on surface charging effects and potential redistribution, impedance measurements were performed. Such experiments are described with electrodes under oxide-free conditions in section 4.3. Under oxide-forming conditions the charge and potential distribution has to be considered, not only in the Helmholtz and space-charge layers, but also in the oxide layer. This is described in section 4.4. It turned out that the photoanodic dissolution of n-GaAs in EDTA solutions is a suitable model system for the impedance study.

In section 4.5 a summary is given of the kinetic results and potential distribution at the electrode / electrolyte interface. Since the hole injection kinetics of an oxidizing agent strongly depend on this potential distribution (see section 2.3) its importance for etching systems is obvious. Implications of these results for practical electroless etching systems are given. This chapter will be concluded with some remarks about the practical importance of anodic dissolution of III-V semiconductors.

4.2. Kinetics of anodic dissolution

4.2.1. Introduction

In order to investigate the factors that determine the kinetics of anodic dissolution of GaAs, potentiodynamic current-potential curves were measured at p-GaAs RDEs in the dark and at n-GaAs RDEs under illumination in both alkaline and acidic solutions. On the basis of a systematic study in the pH range 11 - 14 a model for the anodic dissolution of GaAs will be presented which takes into account the importance of oxide formation. To study the initial stages of oxide formation, photo-current transient measurements were also made under potentiostatic control at n-GaAs in an EDTA-containing solution of pH $= 5$. Oxide formation is initiated in this solution even at low light intensities. Finally, processes which are essential in the anodic dissolution of oxide-covered GaAs are discussed.

4.2.2. Results

Two potentiodynamic current-potential curves of a p-type GaAs RDE measured in the dark in solutions of different pH are shown in Fig. 4.1. In curve (a), for a H_2SO_4 solution of $pH = 0$, the current density is low at negative potentials and begins to increase at $+0.20$ V, which is near the flat-band potential at this pH ($V_{fb}^o(pH = 0) = 0.30$ V(SCE)). As expected, the dissolution rate increases exponentially with the applied potential (section 2.4). Anodic dissolution in an NaOH solution of $pH = 14$ starts at more negative potentials (curve (b)), since the flat-band value in this solution ($V_{fb}^o(pH = 14) = -0.54$ V) is shifted 840 mV in the negative direction (section 2.2). The increase of the anodic current density is, however, in both solutions very similar and anodic current densities of more than 100 mA·cm^{-2} can be obtained in both cases. These results, in which the dissolution of GaAs is not hindered by oxide formation, are in agreement with thermodynamic calculations [1,4]: the reaction products are soluble in strongly acidic and alkaline solutions.
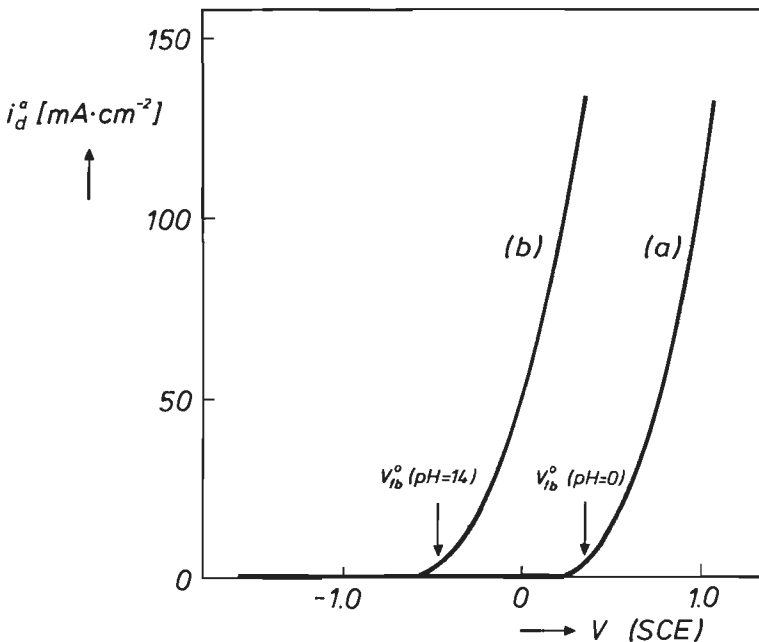
Fig. 4.1. Potentiodynamically (200 mV·s^{-1}) measured current-potential curves for a p-GaAs RDE (500 rpm) in the dark in a solution of 0.5 M H_2SO_4 (curve (a)) and 1 M NaOH (curve (b)).

Fig. 4.2. Potentiodynamically (20 mV·s^{-1}) measured current-potential curves for a p-GaAs RDE (100 rpm) in the dark in NaOH solutions of $pH = 12.5$ (curve (a)), $pH = 13.0$ (curve (b)), $pH = 13.5$ (curve (c)). The insert shows the dependence of the anodic plateau current density (i_{max}^a) on the square root of the electrode rotation rate ($\omega^{\frac{1}{2}}$) for p-GaAs in the dark ('Levich' equation (4.12)) at $+1.00$ V(SCE) in a NaOH solution of $pH = 11.5$.

This contrasts with the situation in more dilute NaOH solutions as Fig. 4.2 shows. Here, anodic dissolution curves, again for a p-type GaAs electrode in the dark, are given for three solutions of different pH in the range 11-14. Dissolution starts in the vicinity of the flat-band potential for the given pH and the rate increases at more positive potentials. After a certain potential the anodic current levels off and becomes constant at more positive values. In this potential range the dissolution reaction is clearly inhibited. The maximum anodic current density in the plateau range, which will be defined as i_{max}^a, depends on the pH of the solution as curves (a)-(c) show. In Fig. 4.3 it can be seen that a plot of the logarithm of i_{max}^a for a p-type electrode (filled circles) versus pH gives a straight line of unit slope.
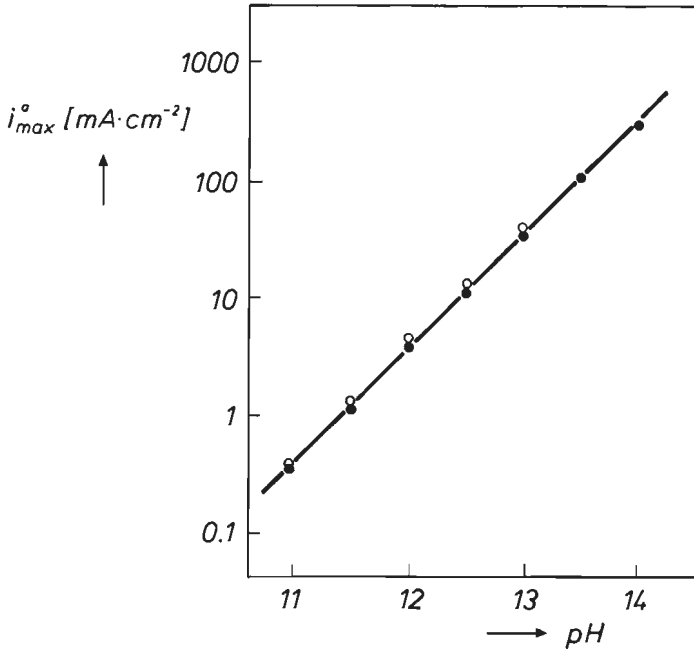
Fig. 4.3. Anodic plateau current density (i^a_{max}) as a function of the *p*H of NaOH solutions for a p-GaAs RDE (100 rpm) in the dark (filled circles) and for an n-GaAs RDE (100 rpm) under illumination (open circles). White light source: Schott lamp.

Furthermore, i^a_{max} depends on the square root of the electrode rotation rate for all solutions. One example of this dependence at $pH = 11.5$ is shown in the insert of Fig. 4.2. From these results it is clear that dissolution of p-GaAs at anodic potentials is determined by diffusion of OH^- ions in alkaline solutions.

A similar result was found for the photoanodic dissolution of an n-GaAs RDE (100 rpm) in a 0.1 M NaOH solution shown in Fig. 4.4. Due to recombination, anodic dissolution only starts at about 500 mV positive with respect to the flat-band potential. The photocurrent reaches a limiting value at more positive potentials. At low intensities the anodic plateau current density (i^a_{hv}) depends linearly on the photon flux (ϕ), as Fig. 4.5 shows (filled circles). Curve (a) of this figure shows that at an electrode rotation rate of 100 rpm, i^a_{hv} in the anodic current plateau range becomes independent of ϕ at higher light intensities. This limiting value is caused by the maximum dissolution rate of GaAs (i^a_{max}). The same dependence of i^a_{max} on the *p*H of the solution was found both for n-GaAs under illumination and p-GaAs in
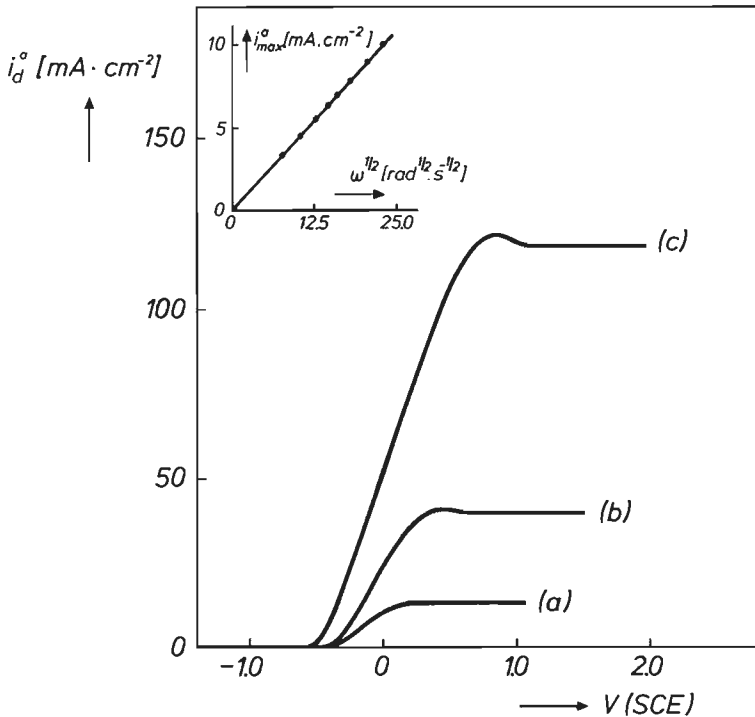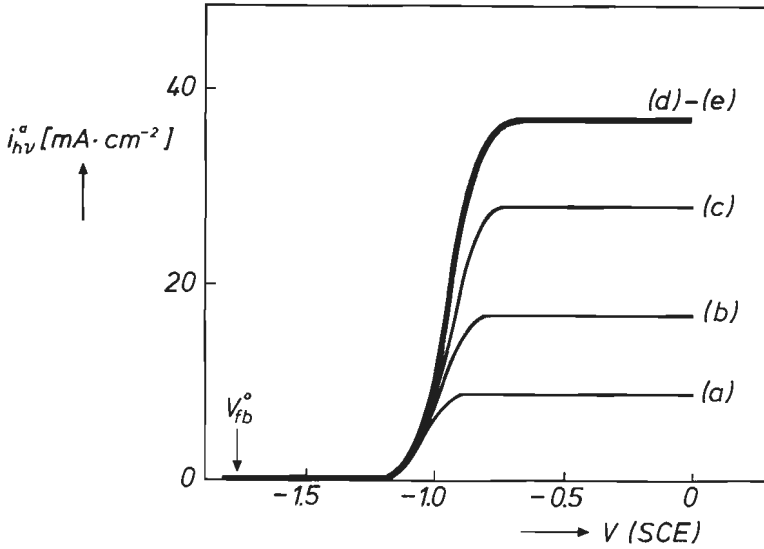
Fig. 4.4. Potentiodynamically (20 mV·s^{-1}) measured current-potential curves for an n-GaAs RDE (100 rpm) in a solution of 0.1 M NaOH under illumination: the photon density $\phi = 8.8$ (curve (a)); 16 (curve (b)); 28 (curve (c)); 63 (curve (d)) and 89 a.u. (curve (e)). White light source: Schott lamp.

the dark, as the open circles in Fig. 4.3 show. In this intensity range the current-potential curves do not change further with increasing intensity, as curves (d) and (e) of Fig. 4.4 reveal. However, when the electrode rotation rate was increased to 5000 rpm the plateau current responded rapidly to give higher dissolution rates, and a linear dependence of i_{hv}^a on the light intensity was found in the entire photon density range (see open circles of curve (b) in Fig. 4.5). So, it can be concluded that the photoanodic dissolution rate of n-GaAs at positive potentials is determined by the light intensity ($i_{hv}^a = e \cdot \phi$) when

$$e \cdot \phi < i_{max}^a. \tag{4.1}$$

When the photon flux exceeds the maximum dissolution rate

$$e \cdot \phi > i_{max}^a, \tag{4.2}$$

the dissolution rate is determined by OH$^-$ diffusion in the solution and the anodic photocurrent (i_{hv}^a) is equal to i_{max}^a in the steady-state. A transition
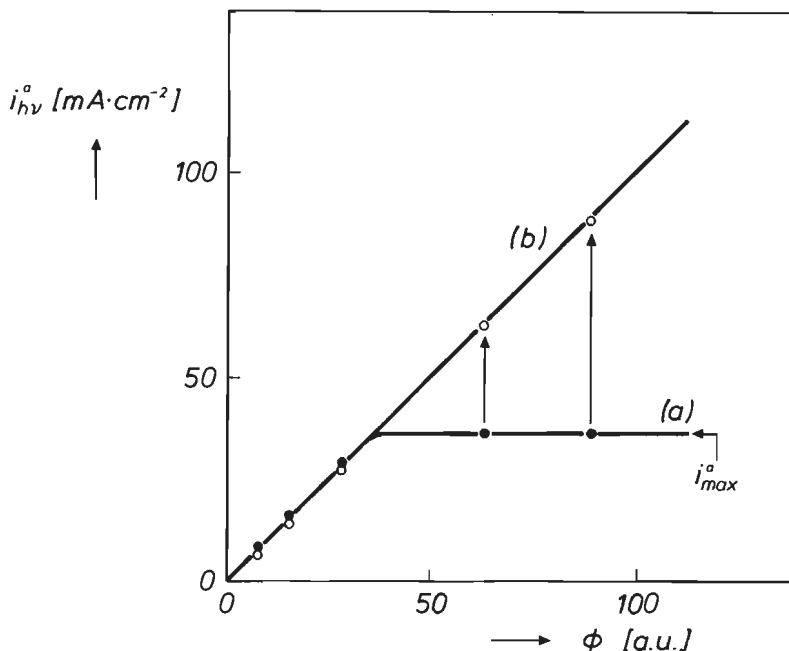
Fig. 4.5. Steady-state photocurrent ($i_{h\nu}^a$) in the anodic current plateau range of an n-GaAs RDE under potentiostatic control (0.00 V(SCE)) in a solution of 0.1 M NaOH as a function of the photon density (ϕ). The electrode rotation rate is 100 rpm in curve (a) (filled circles) and 5000 rpm in curve (b) (open circles). White light source: Schott lamp.

from the condition expressed in eq. (4.1) to that of eq. (4.2) can be simply achieved by changing the electrode rotation rate and thus by changing the supply of OH$^-$ ions to the electrode surface. When the condition given by eq. (4.2) is fulfilled, the same dependence of i_{max}^a on the pH is found as for p-GaAs (compare open and filled circles in Fig. 4.3).

So far, results have been presented which show that the anodic dissolution kinetics of GaAs are inhibited under certain conditions and can depend on the transport of OH$^-$ ions in solution. Such inhibition is generally not found in acidic solutions (Fig. 4.1). However, this effect can also be obtained in EDTA-containing solutions of pH = 5 [14,15]. Therefore, the photoanodic dissolution of n-GaAs was also investigated in these solutions. To ensure conductivity a supporting electrolyte of 0.1 M NaClO$_4$ was used. This solution, without EDTA, was also used as a reference electrolyte. The shape of the photocurrent-potential curve (not shown) of a stationary n-GaAs elec-

trode in 0.1 M Na_2EDTA, 0.1 M $NaClO_4$ solution of $pH = 5$ is similar to
that found in $NaClO_4$ solutions without EDTA: in both cases the onset po-
tential for the photocurrent flow is -0.8 V and the current reaches its lim-
iting value at approximately -0.6 V. The current-potential curves resemble
those found in alkaline solutions in Fig. 4.4 when the different flat-band po-
tentials are taken into account. Although the limiting photocurrent is poten-
tial-independent in both $NaClO_4$ electrolytes, the presence of EDTA in the
solution has a considerable influence on the magnitude of this current. This
effect is illustrated in Fig. 4.6 where the steady-state limiting photocurrent
was measured under potentiostatic control as a function of the light inten-
sity. Curve (a) shows that the photocurrent is proportional to the light in-
tensity in a solution of 0.1 M $NaClO_4$, as expected (open circles). In the
case of an EDTA-containing solution the photocurrent is only proportional
to the photon flux at low intensities (filled circles). At higher intensities the
steady-state photocurrent is essentially independent of the photon flux, as
curve (b) shows. The inhibition of the photocurrent can be prevented by
adding to the electrolyte a reducing agent (0.1 M $Fe^{II}(EDTA)$) capable of
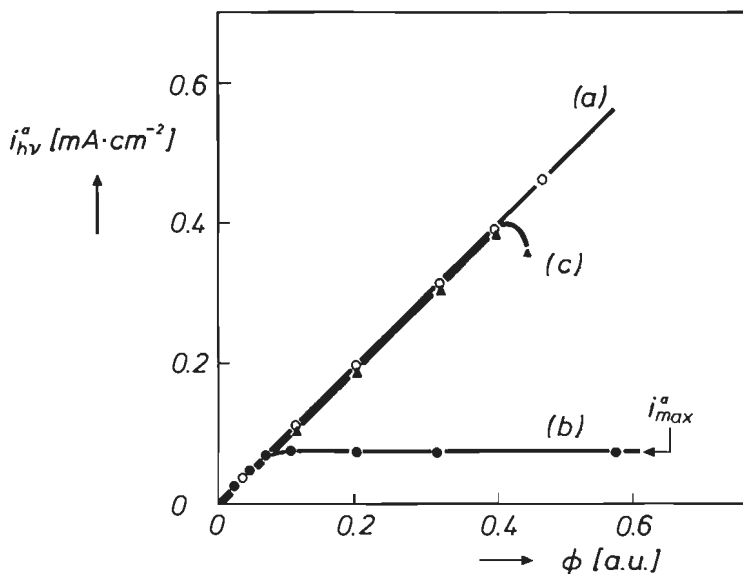
Fig. 4.6. Steady-state photocurrent (i_{hv}^a) in the anodic current plateau range of a
stationary n-GaAs electrode under potentiostatic control ($+0.50$ V(SCE)) as a func-
tion of the photon density (ϕ) in $pH = 5$ solutions containing: 0.1 M $NaClO_4$
(curve (a)); 0.1 M Na_2EDTA and 0.1 M $NaClO_4$ (curve (b)); 0.1 M Na_2EDTA,
0.1 M $NaClO_4$ and 0.1 M $Fe^{II}(EDTA)$ (curve (c)). Light source: 1 mW He-Ne laser.

competing with the GaAs dissolution [16] (triangles in curve (c) of Fig. 4.6). The photo-generated holes at the electrode surface are transferred very effectively to $Fe^{II}(EDTA)$ in solution; the D_{red} function of $Fe^{II}(EDTA)$ overlaps very well with the VB of GaAs ($V^o_{Fe^{II/III}}(EDTA) = -0.12$ V(SCE) whereas the VB edge is positioned at 0 V(SCE)). The competing VB reaction can be represented as

$$Fe^{II}(EDTA) + h^+(VB) \rightarrow Fe^{III}(EDTA). \tag{4.3}$$

At higher light intensities the competition is incomplete and photocurrent decay is eventually observed, as curve (c) shows.

These results clearly show that the dissolution of n-GaAs in EDTA-containing solutions is considerably hindered. i^a_{max} is exceeded even at relatively low light intensities, as a comparison of the values with those obtained under similar conditions in alkaline solutions shows (compare i^a_{max} values in Figs. 4.5 and 4.6). The suggestion made in the literature, that oxide forma-
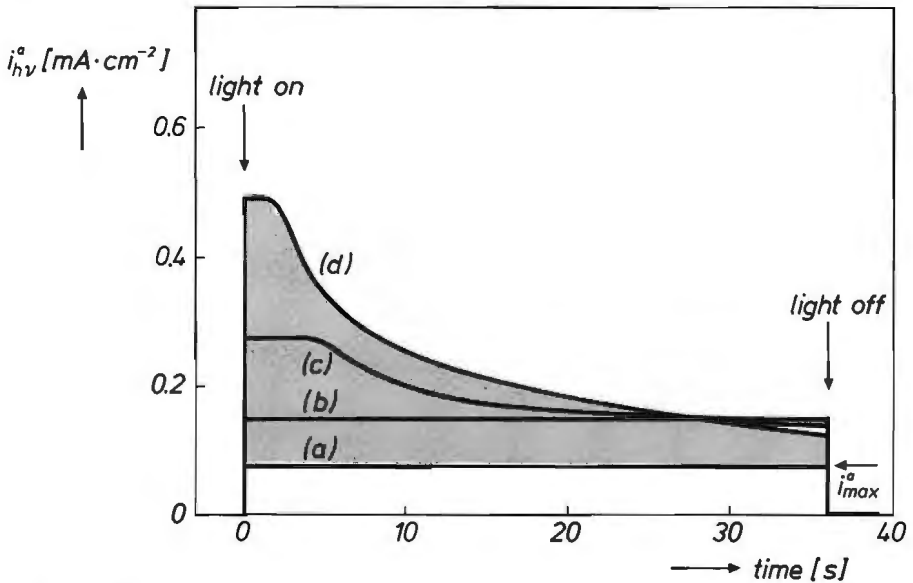
Fig. 4.7. Photocurrent transients for a stationary n-GaAs electrode under potentiostatic control (+0.50 V(SCE)) in a 0.1 M Na_2EDTA, 0.1 M $NaClO_4$ solution of $pH = 5$ at photon densities $\phi = 0.075$ (curve (a)); 0.15 (curve (b)); 0.28 (curve (c)) and 0.49 a.u. (curve (d)). Light source: 1 mW He-Ne laser. The maximum dissolution rate in the steady-state is given by i^a_{max}. The charge to build up an oxide layer is indicated by the shaded area for curve (d) ($= \int_0^t (i^a_{hv} - i^a_{max})dt$).

tion is induced in EDTA-containing solutions [15], is confirmed by photo-
current transient measurements which are shown in Fig. 4.7. At low light in-
tensity, the anodic photocurrent measured at constant potential in
0.1 M EDTA, 0.1 M NaClO$_4$ solution of $pH = 5$ is constant in time
(curve (a) of Fig. 4.7) and is proportional to the photon density. This cor-
responds to the lower part of curve (b) of Fig. 4.6. At higher light intensities
the photocurrent observed initially, when the light is switched on, is also
proportional to the photon density and is the same as that found under
steady-state conditions in solutions without EDTA (curve (a), Fig. 4.6). This
current, however, decayed after an induction period. The induction time de-
creased as the light intensity was increased (curves (b)-(d) in Fig. 4.7). The
steady-state photocurrent corresponds to that found in curve (b) of Fig. 4.6
and was independent of the light intensity. Similar transient effects were ob-
served by Elliott and Regnault [15]. They worked, however, at much higher
potentials and considerably thicker oxide films were formed.
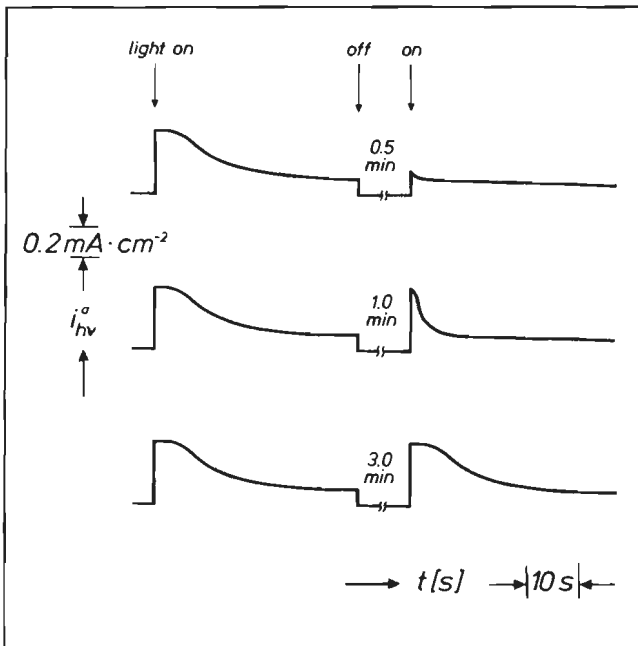
Fig. 4.8. Recovery of the photocurrent at a stationary n-GaAs electrode after film
formation at +0.50 V(SCE) in the same solution as used in Fig. 4.7. The photocur-
rent transient was recorded until a steady-state current was obtained. The light was
switched off and the electrode was kept at +0.50 V in the dark for the time shown,
before illumination was recommenced ($\phi = 0.5$ a.u.). Light source: 1 mW He-Ne
laser.

Since the original photocurrent transient could be reproduced after film formation by maintaining the electrode at the same potential in the dark (see Fig. 4.8), it is clear that the surface film dissolves chemically in the electrolyte. This figure shows that the oxide layer is completely removed after approximately 3 minutes. Under steady-state conditions, the rate of chemical dissolution determines the magnitude of the photocurrent. This explains why the current in the limiting photocurrent range is independent of the light intensity and applied potential in the same way as found above for the photoanodic dissolution of n-GaAs in alkaline solutions (see e.g. curve (e) in Fig. 4.4). On the basis of this constant photocurrent and the time required to dissolve the surface film in the dark, and assuming a molecular weight and density typical of a GaAs oxide [17], thicknesses of the order of 1.5 - 5.0 nm are calculated (equation (2.39)) for various oxide layers which are formed under different experimental conditions.

4.2.3. Discussion

From the results presented in the above section it is clear that the kinetics of anodic dissolution of GaAs can be divided into two regions, depending on whether the anodic oxidation at positive potentials is inhibited or not. A generalized mechanism of anodic dissolution of GaAs will be used to account for the results obtained both in alkaline and acidic solutions.

The oxidation of a III-V material can be represented in the simplest possible way as a series of irreversible electrochemical steps each involving the localization of a VB hole in a surface bond [18-21]. The charged intermediate, formed in each of these reactions, is subsequently neutralized by a reaction with a nucleophilic species from solution. In the alkaline solutions of the present study, OH^- ions must be the nucleophilic species. The reactions in which a surface bond is attacked can be schematically represented in four successive steps as follows:

$$-\overset{\diagup}{Ga} \cdot\cdot \overset{\diagdown}{As}- \quad + \quad h^+ \quad \xrightarrow{\;k_1^a\;} \quad -\overset{\diagup}{Ga}^{\oplus} \cdot \overset{\diagdown}{As}- \qquad (4.4)$$

$$-\overset{\diagup}{Ga}^{\oplus} \cdot \overset{\diagdown}{As}- \quad + \quad OH^- \quad \xrightarrow{\;k_2^a\;} \quad -\overset{\diagup}{Ga} \cdot \overset{\diagdown}{As}- \qquad (4.5)$$

$$\begin{array}{c} \text{OH} \\ | \\ -\!\!\text{Ga} \quad \cdot\text{As}\!-\!\! \\ \diagup \qquad\quad \diagdown \end{array} \quad + \quad \text{h}^+ \quad \xrightarrow{\;k_3^a\;} \quad \begin{array}{c} \text{OH} \\ | \\ -\!\!\text{Ga} \quad ^\oplus\!\text{As}\!-\!\! \\ \diagup \qquad\quad \diagdown \end{array} \qquad (4.6)$$

$$\begin{array}{c} \text{OH} \\ | \\ -\!\!\text{Ga} \quad ^\oplus\!\text{As}\!-\!\! \\ \diagup \qquad\quad \diagdown \end{array} \quad + \quad \text{OH}^- \quad \xrightarrow{\;k_4^a\;} \quad \begin{array}{c} \text{OH} \quad\;\; \text{OH} \\ | \qquad\quad | \\ -\!\!\text{Ga} \quad\;\; \text{As}\!-\!\! \\ \diagup \qquad\quad\;\; \diagdown \end{array} \qquad (4.7)$$
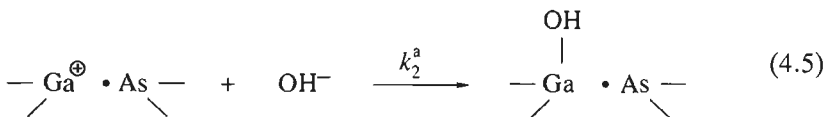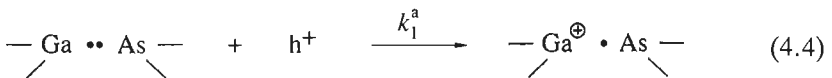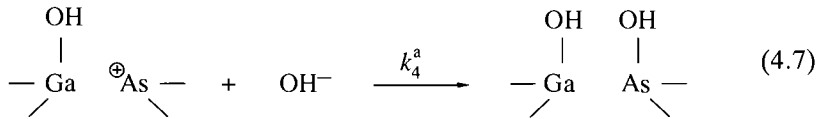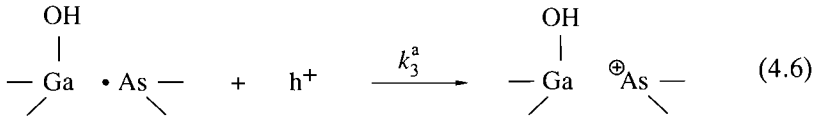
where k_1^a, k_2^a etc. represents the rate constants of the various reactions. The surface produced in this way corresponds to the oxidized form. As discussed in chapter 2, four more holes have to be supplied to the surface to dissolve one GaAs entity. Rupture of the first Ga — As bond is generally considered to be the rate-determining step [13,22]. The results found with p-type electrodes show two distinct cases:

– first, when the supply of OH$^-$ to the electrode surface is sufficient to ensure that the OH$^-$ is not depleted at the electrode surface, then dissolution depends on the surface hole concentration p_s; the rate of the anodic oxidation of GaAs in the dark is given by

$$i_d^a = 6F k_1^a p_s. \qquad (4.8)$$

– in the second case, observed at positive potentials for which the surface hole concentration is high, the dissolution rate is determined by OH$^-$ diffusion in the solution. From the Levich dependence of the limiting anodic dissolution current density it is clear that i_{max}^a depends not only on the pH of the solution (Fig. 4.3) but also on the electrode rotation rate (insert in Fig. 4.2).

For n-type electrodes the same two cases can be distinguished. However, for these electrodes p_s is determined both by the applied potential and by the light intensity (eqs. (4.1) and (4.2)).

On the basis of a photo-electrochemical study of n-GaAs, Decker [8] has shown that, when the anodic dissolution rate is limited an oxide layer is formed which is dissolved by OH$^-$ ions. Continuing the notation of eq. (4.7) ultimately yields the formation of an oxide film. The overall reaction of this oxide formation can be represented as follows:

$$\text{GaAs} + 6\text{OH}^- + 6\text{h}^+ \rightarrow \tfrac{1}{2}\text{Ga}_2\text{O}_3 + \tfrac{1}{2}\text{As}_2\text{O}_3 + 3\text{H}_2\text{O}. \qquad (4.9)$$
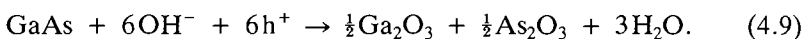
Surface analysis measurements (XPS, Auger) have, indeed, shown the presence of mixed gallium and arsenic oxides in anodically grown oxide films at GaAs [7,23]. The exact nature of these oxides is not important for the present discussion. Chemical dissolution of the oxide by OH^- proceeds according to reaction (4.10):

$$\tfrac{1}{2}Ga_2O_3 + \tfrac{1}{2}As_2O_3 + 6\,OH^- \rightarrow GaO_3^{3-} + AsO_3^{3-} + 3\,H_2O, \quad (4.10)$$
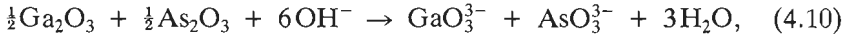
where GaO_3^{3-} and AsO_3^{3-} are products soluble in alkaline solutions. Under this condition the OH^- consumption is diffusion-controlled and an approximately linear concentration gradient of OH^- ions in solution is established. The ultimate dissolution rate of GaAs is determined by the rate at which the oxide is dissolved in the electrolyte (eq. (4.10)). The chemical dissolution rate is represented by eq. (2.45). In the steady-state the chemical dissolution rate of the oxide (v_{ch}) is equal to the oxidation rate of GaAs ($v_e = v_{ch}$). Using eq. (2.39), which describes the rate of oxidation, the dependence of i_{max}^a on the electrode rotation rate can, in general, be represented by

$$\frac{1}{i_{max}^a} = \frac{1}{6\,Fk_{ch}[Ch]_b} + \frac{p}{0.62 \times 6\,F[Ch]_b \mathcal{D}_{ch}^{\frac{2}{3}} v^{-\frac{1}{6}} \omega^{\frac{1}{2}}}. \quad (4.11)$$

Since the dissolution rate of the oxide in the present alkaline solutions is controlled by diffusion of OH^- ions, only the diffusion term of eq. (4.11) has to be considered ($k_{ch} \rightarrow \infty$). Eq. (4.11) can, under these conditions, be simplified to

$$i_{max}^a = \frac{0.62 \times 6\,F[OH^-]_b \mathcal{D}_{OH^-}^{\frac{2}{3}} v^{-\frac{1}{6}} \omega^{\frac{1}{2}}}{p}. \quad (4.12)$$

It can be concluded that when the anodic dark current density at p-GaAs (i_d^a) or the photoanodic current density at n-GaAs (i_{hv}^a) is less than i_{max}^a,

$$i_d^a, \; i_{hv}^a < i_{max}^a, \quad (4.13)$$

oxide is not formed to any extent on the electrode surface. When, however,

$$i_d^a, \; i_{hv}^a > i_{max}^a, \quad (4.14)$$

an oxide is formed which can be dissolved by OH^- ions. The dissolution rate of GaAs under the latter condition is clearly inhibited and is determined by the rate at which the oxide layer is dissolved chemically ($= i_{max}^a$ in the steady-state).

In acid solutions the anodic dissolution of GaAs is, in general, not inhibited and high dissolution rates can be obtained (see curve (a) of Fig. 4.1). The rate of oxidation depends, as in alkaline solutions, on the surface hole concentration. It is obvious that in acidic solutions anions other than OH^- ions must be the nucleophilic species which neutralize the positively charged intermediates in eqs. (4.5) and (4.7). Moreover, it is proposed [24] that water molecules can accomplish this role. As a result, oxide films are not formed in these solutions under normal conditions. However, by comparing the results obtained in $NaClO_4$ solutions with those in EDTA-containing solutions, it has been shown that oxide formation can be promoted during the photoanodic dissolution of n-GaAs. (Figs. 4.6 and 4.7) [14,15]. From the current transient measurements in Fig. 4.7 it is clear that, because $i_{hv}^a > i_{max}^a$, an oxide film is formed at the electrode surface in the initial stages of the photoanodic oxidation of n-GaAs. In the steady-state the rate at which the oxide is formed is equal to the rate of oxide dissolution at the oxide/electrolyte interface ($i_{hv}^a = i_{max}^a$). As a consequence of the oxide formation the photocurrent decayed after a certain period. By integrating the photocurrent used to build-up the oxide layer from $t = 0$ to the time at which a steady-state photocurrent is established ($i_{hv}^a - i_{max}^a$, as indicated as an example for curve (d) in Fig. 4.7 by the shaded area), an oxide film thickness of the same order of magnitude is calculated as that previously deduced from the dissolution time of this layer in the dark (see Fig. 4.8). Decker [8] recently studied the oxide formation at n-GaAs in an alkaline solution of $pH = 11.5$ with current transient measurements and found results which closely resemble the present transient results obtained in EDTA solutions (Fig. 4.7). He also concluded that a thin oxide layer with a thickness of the order of 1.0-2.0 nm is formed during the photoanodic oxidation of n-GaAs.

When the photoanodic dissolution of n-GaAs is inhibited by oxide formation, only some of the minority charge carriers created by light, are used to dissolve GaAs and, as a result, an excess of holes is created in the semiconductor beneath the oxide layer. It is assumed that light can easily penetrate the oxide films which is very likely to be the case with these thin films. In the steady-state the excess holes cannot be maintained and they consequently recombine with conduction band electrons at the same rate at which they are generated by light.

From the foregoing discussion it is clear that when eq. (4.14) is fulfilled
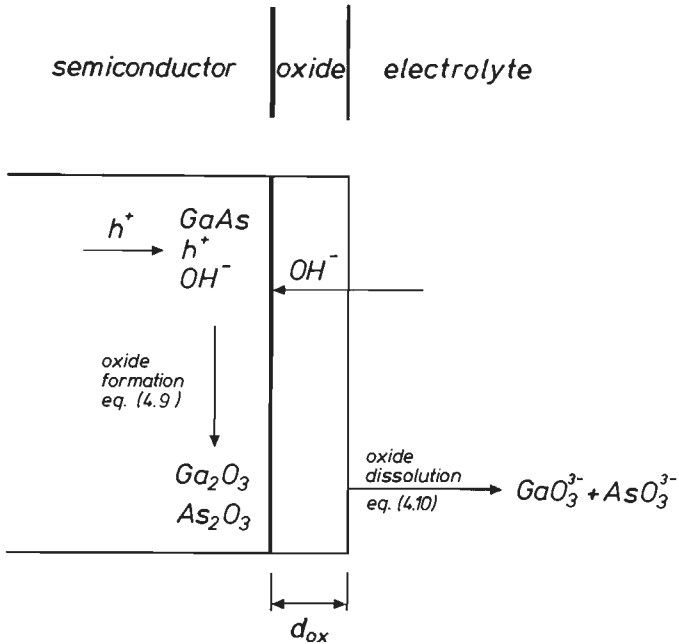
Fig. 4.9. Scheme showing processes occurring during the anodic oxidation of an oxide-covered electrode when; i_d^a, $i_{hv}^a > i_{max}^a$ (eq. (4.14)). This figure refers to the anodic dissolution of p-GaAs in the dark in alkaline solutions. The various steps described in the text are indicated, including ionic transport through the oxide layer. The thickness of the oxide layer is indicated by d_{ox}. Similar processes occur at n-type electrodes. However, in this type of electrodes holes must be generated by light within the semiconductor.

for both alkaline and EDTA-containing acidic solutions, film formation occurs at positive potentials during the anodic oxidation of GaAs. Steady-state oxide films up to a few nm thick are found. The processes which are essential in the formation and dissolution of such oxide covered electrodes will now briefly be considered (page 698 et seq. of [25]). In Fig. 4.9 the steady-state of an oxide covered GaAs electrode is shown schematically. During polarization at anodic potentials the gallium and arsenic atoms at the semiconductor/oxide interface are oxidized. The required holes are delivered from the bulk of the semiconductor in the case of a p-type electrode or must be generated by light in the case of n-type electrodes. In order to maintain a steady-state oxide layer, ionic conductivity in the oxide layer is essential. This phenomenon is well-known and has been extensively re-

viewed by Vetter [25]. As a result of an electric field, which is maintained across the oxidized interface (eqs. (4.4)-(4.7)), both cations (gallium and/or arsenic ions) and anions (X^-) from solution can, in principle, migrate through the oxide film. Which species dominates the ionic transport depends on the relative mobility. The situation shown in Fig. 4.9 refers to the anodic dissolution of p-GaAs in alkaline solutions. It is likely that, in these solutions, the anion transport in the solid is provided by OH^- ions. For simplicity, it is assumed that the mobility of anions is higher than that of cations, so that migration of these latter is neglected. As a consequence of this simplification, oxide formation occurs, in this example at the semiconductor/oxide interface. According to eq. (4.9), H_2O is also formed during the formation reaction. This probably leads to the formation of an hydrated oxide at the interface. A similar mechanism as proposed above for GaAs was prooved to take place during the anodic oxidation of Si [26,27]. Schmidt and Ashner [26] have shown, using tritium tracer techniques, that ionic conductivity in anodic SiO_2 layers, formed under relatively high field strengths, is dominated by the inward migration of OH^- ions. They also concluded that this leads to the formation of hydrated SiO_2 at the silicon/oxide interface.

It is likely that oxide growth occurs via a field-dependent mechanism [28,29], i.e. the rate of formation (i^a_{form}) is determined by the migration of ions under the influence of the electric field over the oxide. This dependence is represented by

$$i^a_{form} = i^o \cdot \exp\left\{ B \cdot \frac{V_{ox}}{d_{ox}} \right\}, \tag{4.15}$$

where d_{ox} is the thickness of the oxide film and i^o and B are constants. At the same time the oxide layer is chemically dissolved at the oxide/electrolyte interface (eq. (4.10)). In the steady-state the rates of oxide formation and dissolution are, of course, equal and a constant value of d_{ox} is established (eq. (4.15)). The successive steps of the dissolution of GaAs in alkaline solutions as presented in eqs. (4.9) and (4.10) can be recognized in Fig. 4.9. Similarly, oxide formation in other media can be represented when migration of other ions is taken into account.

It is obvious from the above discussion that during the initial stages of oxide formation a build-up of charge, which are intermediates in the dissolution reaction of GaAs (eqs. (4.4)-(4.7)), occurs at the semiconductor/oxide interface. It is therefore expected that the combination of interface charge and oxide formation at the surface will significantly influence the potential distribution at the complex surface structure.

4.2.4. Conclusions

It has been shown that the kinetics of (photo)anodic dissolution of GaAs can be divided into two regions which are related to oxide formation at the electrode surface. When the condition expressed in eq. (4.13) is valid, oxide formation does not occur as the maximum dissolution rate of the oxide film is high compared to the rate of oxide formation. Dissolution is not inhibited and is determined by kinetic factors such as the surface hole concentration. When, on the other hand, the rate of oxide formation exceeds the maximum dissolution rate of the oxide (eq. (4.14)), dissolution of GaAs is inhibited by an oxide film. The dissolution rate is then independent of the electrode potential and light intensity, and is determined by the rate at which the oxide film is chemically dissolved in the electrolyte.

The maximum dissolution rate (i_{max}^a) is shown to be strongly dependent on the nature of the anion and its concentration in the solution. In alkaline solutions i_{max}^a is found to be proportional to the OH^- concentration; the dissolution rate of the oxide is diffusion-controlled. A generalized mechanism for the anodic oxidation of GaAs in these solutions was used to account for the dissolution under both oxide-free and oxide-forming conditions. In acid solutions oxide formation does not, in general, occur. However, this can be artificially stimulated by so-called oxide promoting agents. EDTA is found to be a good example of such an agent in which i_{max}^a of GaAs is considerably lowered which results in very low dissolution rates.

4.3. Surface charging under oxide-free conditions

4.3.1. Introduction

This section is devoted to an impedance study of charging effects during (photo)anodic dissolution under the condition given by eq. (4.13): i_d^a, $i_{h\nu}^a < i_{max}^a$, where no oxide was found to be present at the semiconductor surface. These charging effects can be most easily followed under majority carrier depletion conditions. As was shown in section 2.2, the space-charge capacitance is then very small (see Fig. 2.3) and a well-defined relationship between C_{sc} and V exists (eq. (2.12)). This means that a change in the impedance behaviour due to charging can be simply measured.

Photoanodic dissolution of n-type electrodes occurs under depletion conditions, so impedance can be measured in the steady-state and the effect of charging due to oxidation can be studied by comparing results obtained in the dark and under illumination. On the other hand, anodic oxidation of p-

type electrodes occurs close to or positive with respect to the flat-band po-
tential, i.e. under accumulation conditions. Interpretation of the steady-state
impedance results under these conditions is therefore much more complex.
For that reason a different approach was adapted. Immediately after pre-
polarization at anodic potentials, transient impedance measurements were
performed in the depletion potential range. The prepolarization potential
was chosen so that an anodic current flows, i.e. the electrode dissolves at
a certain rate. Relaxation of the electrode impedance at negative potentials
gives, in this indirect way, information about charging effects at positive po-
tentials at p-type electrodes.

In the previous section the dissolution kinetics in acidic and alkaline so-
lutions were reported. In this section charging effects in both pH regions
will be considered. First, results will be presented for p-GaAs electrodes in
the dark in acid solutions with different ionic composition. The impedance
behaviour during the photoanodic dissolution of n-GaAs will then be con-
sidered in alkaline solutions. The influence of the light intensity on this be-
haviour will be described.

4.3.2. Results

p-GaAs in acid solutions

Mott-Schottky plots measured under steady-state conditions in a potential
range where no dissolution occurs were compared with those obtained in the
same range immediately after anodic prepolarization of a stationary p-GaAs
electrode in the dark. For the results shown in Fig. 4.10 with a buffered so-
lution of $pH = 5$, the electrode was held for one minute at a fixed anodic
potential of 0.00 V. At this potential the anodic dissolution current density
i_d^a was 1.4 mA·cm^{-2}. At $t = 0$, the potential was stepped to different
cathodic values. In each case $1/\omega_f C_t$ was measured as a function of time,
where C_t is the total series cell capacitance, and the angular frequency ω_f
is defined by $\omega_f = 2\pi f$, where f is the frequency of the a.c. signal, in this
case 10 kHz. Immediately after application of the potential step, $1/\omega_f C_t$ ex-
ceeds the steady-state value at the cathodic potential but decreases gradually
to this value (see insert of Fig. 4.10). In curve (b), the C_t-value at $t = 0$ is
plotted in the Mott-Schottky form as a function of the cathodic potential.
It is clear that anodic prepolarization of the electrode gives a positive dis-
placement with respect to the steady-state Mott-Schottky curve (a). Similar
effects were also observed with a solution of $pH = 5$ containing 0.01 M
EDTA, with a 0.5 M H$_2$SO$_4$ solution and with a 1 M HCl solution. It should
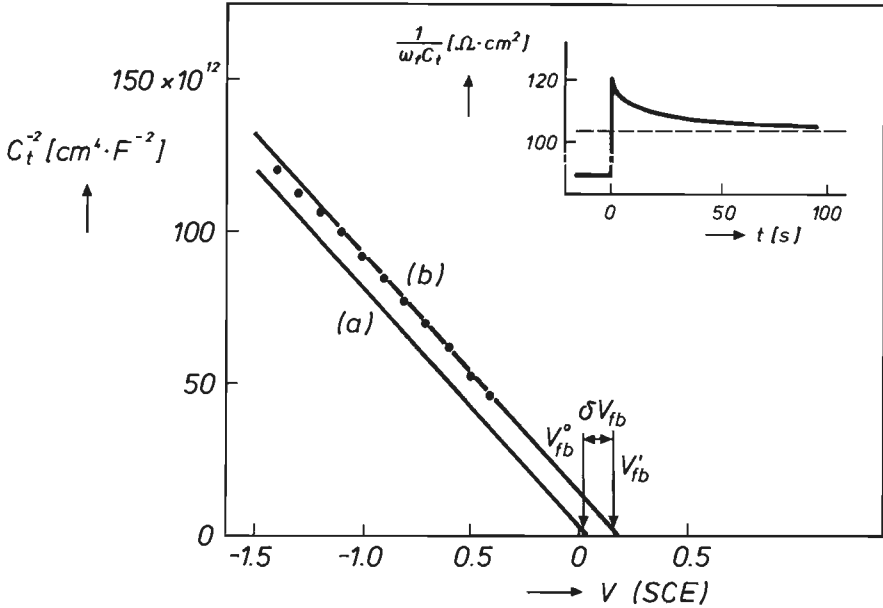
Fig. 4.10. Mott-Schottky plots for a stationary p-GaAs ($N_A = 1.0 \times 10^{17}\,\mathrm{cm}^{-3}$) electrode in a citrate/NaOH buffer solution of $pH = 5$ in the dark. The solid line (a) is the steady-state plot. Curve (b) was obtained by first holding the electrode for 1 minute at 0.00 V before measuring the imaginary part of the impedance at $t = 0$ immediately after stepping the potential to the value shown. The flat-band potential obtained under standard conditions at $pH = 5$ is denoted by V_{fb}^{o}, that obtained immediately after prepolarization by V_{fb}'. The shift of the flat-band potential $\delta V_{fb} = V_{fb}^{o} - V_{fb}'$. In the insert, an example is given of the change in $1/\omega_f C_t$ as a function of time after a potential step from 0.00 V to -0.50 V.

be noted that the anodic dissolution current density was always well below that at which oxide formation occurs. In all cases, a positive shift in the apparent flat-band potential was found in the range of 50 - 150 mV. These values may represent a lower limit, as the time-response of the impedance measuring system was limited to $t > 0.25$ s. The relaxation of the impedance after the potential step was slower in HCl solution than in other systems.

Fig. 4.11 shows, as an example, the effect of stepping the potential in 0.5 M H_2SO_4 from various values of the anodic potential V_a to a fixed cathodic potential of -0.30 V. The shift in the apparent flat-band potential (δV_{fb}), measured at $t = 0$ (see Fig. 4.10), is plotted as a function of the anodic prepolarization potential. It is clear that a displacement of the Mott-
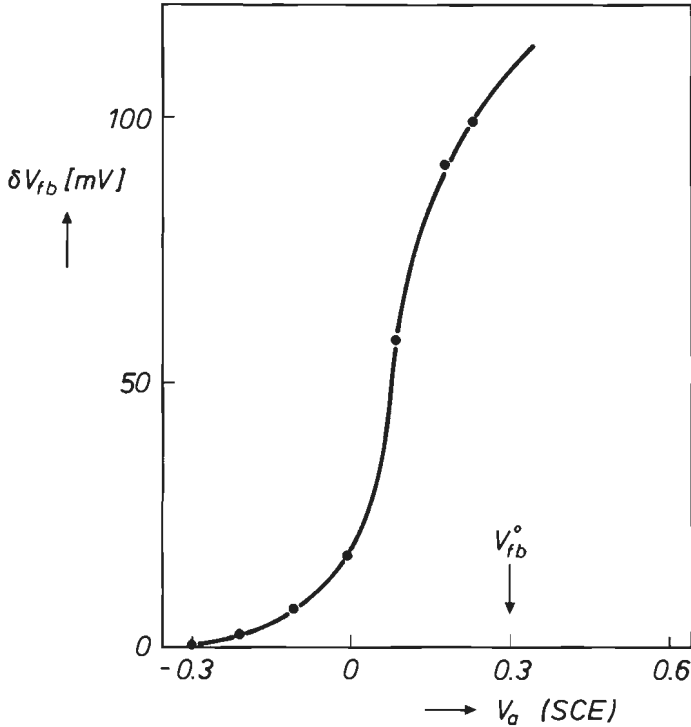
Fig. 4.11. The shift in apparent flat-band value (δV_{fb}) of a stationary p-GaAs electrode in 0.5 M H_2SO_4 in the dark, measured immediately after application of a potential step from an initial potential V_a to a fixed cathodic value (-0.30 V), as a function of V_a.

Schottky curve is only observed as V_a approaches the steady-state V_{fb}^o value at which dissolution of GaAs starts.

n-GaAs in alkaline solutions

The impedance results for a rotating n-GaAs electrode in a solution of 0.1 M NaOH are presented again in Mott-Schottky form in Fig. 4.12. A V_{fb}^o value of -1.78 V (curve (a)) is found in the dark, as expected. When the electrode was illuminated with white light the Mott-Schottky plots were shifted to positive potentials with respect to the dark curve (a). The displacement becomes larger with increasing light intensity (curves (b)-(h)). It is striking that even at extremely high light intensities an almost parallel displacement of up to 800 mV is found. The slope of the Mott-Schottky plots
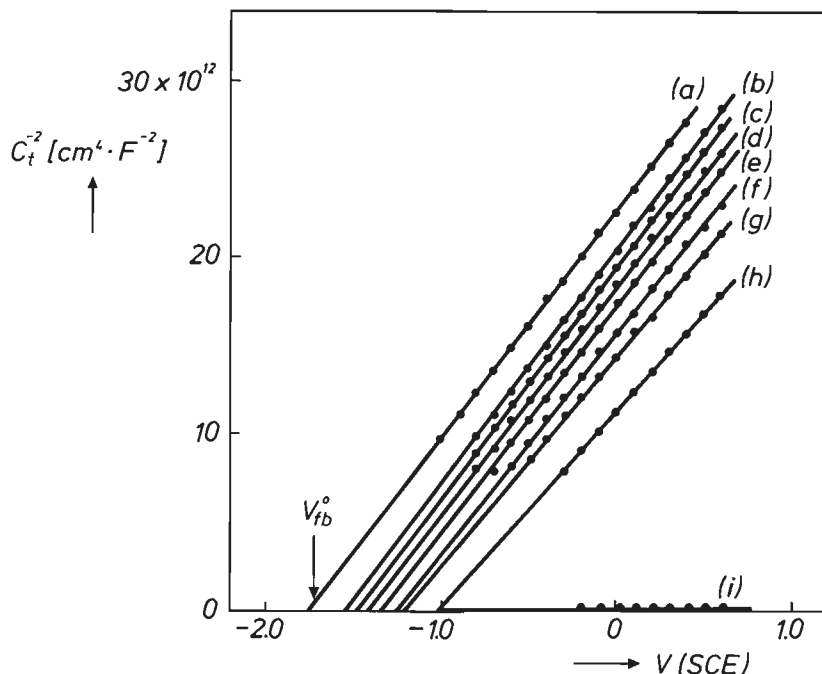
Fig. 4.12. Mott-Schottky plots obtained at an n-type ($N_D = 1.0 \times 10^{18}$ cm^{-3}) GaAs RDE (500 rpm) in a solution of 0.1 M NaOH in the dark (curve (a)) and under illumination. The photon density ranges from: $\phi = 7.1$ (curve (b)); 11.1 (curve (c)); 18.6 (curve d)); 25.9 (curve (e)); 34.9 (curve (f)); 42.9 (curve (g)); 61.9 (curve (h)); 88.6 a.u. (curve (i)). White light source: Schott lamp.

decreases slightly at the highest light intensities. This is probably caused by an increase of the electrode area as a result of surface roughening at these extreme dissolution rates. The light intensities' used in curves (b)-(h) of Fig. 4.12 are indeed lower than i_{max}^a, as can be deduced from the kinetic results obtained in the previous section ($i_{max}^a = 67$ mA·cm^{-2} at 500 rpm in a solution of $pH = 13$). The parallel displacement was reproducible and was also observed in 1 M NaOH solution and when the electrode was illuminated with an argon ion laser. In Fig. 4.13 the flat-band potentials, measured under various conditions, are shown as a function of the light intensity. A linear relation is found over most of the intensity range. At very low light intensities the relative shift of V_{fb} is even more pronounced. This is in agreement with the results which Allongue and Cachet [30] recently obtained for the anodic photodissolution of n-GaAs at low light intensities, also in alkaline solutions.
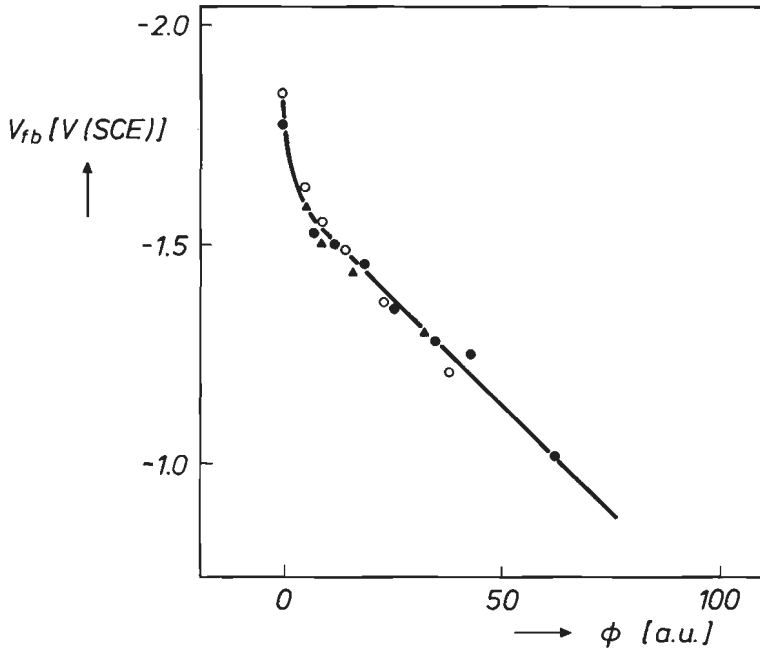
Fig. 4.13. Flat-band potential of an n-type ($N_D = 1.0 \times 10^{18}$ cm^{-3}) GaAs RDE (500 rpm) as a function of the photon density (ϕ): ($\bullet$) in 0.1 M NaOH, white light (Schott lamp); ($\blacktriangle$) in 1.0 M NaOH, white light (Schott lamp); ($\circ$) in 0.1 M NaOH, Argon ion laser.

When the light intensity exceeds i^a_{max} an oxide layer is formed at the electrode surface which results in a dramatic decrease of C_t^{-2}, as curve (i) of Fig. 4.12 shows. This situation will be considered in more detail in section 4.4.

4.3.3. Discussion

The results obtained at p-GaAs in acidic solutions will first be discussed. From the parallel displacement of the Mott-Schottky curve in the transient impedance measurements (Fig. 4.10) it follows that anodic prepolarization must cause a change in the Helmholtz potential. The new potential drop over this layer, which is denoted by V_H', can be defined with respect to the V_H^o under standard conditions as

$$V_H' = V_H^o + \delta V_H. \tag{4.16}$$

It is obvious that the δV_H, which was assumed to be zero under normal depletion conditions (see eq. (2.16)), can no longer be neglected under these conditions. On the basis of an analogy with eq. (2.13), the applied electrode potential can be represented as

$$V = V_{sc} + V_H' + \varphi. \tag{4.17}$$

Using eq. (4.16), V_H' can be eliminated in eq. (4.17). This leads to

$$V = V_{sc} + V_H^o + \varphi + \delta V_H. \tag{4.18}$$

Taking the flat-band potential under standard conditions into account (eq. (2.14)), yields the following expression for V_{sc}

$$V_{sc} = V - V_{fb}^o - \delta V_H. \tag{4.19}$$

A modified Mott-Schottky expression for a p-type electrode, which also involves changes in the Helmholtz potential, can now be obtained by inserting V_{sc} from eq. (4.19) into the Mott-Schottky equation (2.12). It follows that

$$\frac{1}{C_{sc}^2} = \frac{2}{\varepsilon \varepsilon_o N_A e} \cdot \left\{ V - V_{fb}^o - \delta V_H - \frac{kT}{e} \right\}. \tag{4.20}$$

When $1/C_{sc}^2 = 0$, this results in

$$V - V_{fb}^o - \delta V_H = \frac{kT}{e}, \tag{4.21}$$

(see also eq. (2.16) and further). Since V_{fb}^o is known under normal depletion conditions from curve (a) of Fig. 4.10 ($V_{fb}^o = +0.03$ V) it follows from eq. (4.21) and curve (b) of this figure that anodic prepolarization results in a positive change of the Helmholtz potential of $\delta V_H = +0.15$ V. The positive shift in the apparent flat-band potential corresponds to a downward displacement of the semiconductor band-edges at the surface.

Since the relaxation of an accumulation layer, after stepping of the electrode potential from anodic to cathodic values, should be fast [31,32], it is obvious from Fig. 4.11 that the changes in the Helmholtz layer, which are most pronounced at anodic potentials, are connected with the process of oxidative dissolution. It therefore seems reasonable to suggest a form of hole trapping to account for changes of the Helmholtz potential. In chap-

ter 2 (section 2.2) it was noted that charge can be stored in surface states at the semiconductor electrode. This charge is compensated by anions in the Helmholtz layer ($Q_{ss} = -\delta Q_H$). As a result the potential drop over this layer will change according to

$$\delta V_H = \delta V_{fb} = \frac{Q_{ss}}{C_H}, \tag{4.22}$$

where Q_{ss} is the surface state charge density. If the Helmholtz capacitance is assumed to be 20×10^{-6} F·cm^{-2} [33], then a positive change of the Helmholtz potential in the range of 50 - 150 mV corresponds to a positive charge density (Q_{ss}/e) of the order of 10^{13} cm^{-2}. We suggest that this positive charge is related to the intermediates in the dissolution reaction of GaAs as proposed in the previous section in eqs. (4.4) - (4.7). Whether the charge responsible for the change in potential is discrete (eqs. (4.4), (4.6)) or due to surface dipoles, resulting from reaction of anions with these charged intermediates (eqs. (4.5) and (4.7)), is not clear from these results.

The transient impedance measurements of Fig. 4.10 show that the lifetime of intermediates after prepolarization is relatively long (approximately 1 minute in a solution of pH $= 5$). That this is not exceptional can be seen from the results obtained with germanium, for which lifetimes of 5 min. are reported [34]. Our results in HCl show that the electrolyte may influence the life-time drastically. Specific adsorption of anions, such as chloride which could compete with hydroxide ions, obviously gives a better stabilization of surface-trapped holes.

Charging effects are also observed during the dissolution of n-GaAs. To dissolve n-type electrodes, the electrode has to be illuminated with light of a wavelength corresponding to the band-gap of the semiconductor. As a result, electron-hole pairs are created within the semiconductor. The penetration depth of light (L) is determined by the absorption coefficient (α) and depends strongly on the wavelength of the light. For GaAs the penetration depth of visible light ranges from approximately 0.05 μm for wavelengths near the UV to 1 μm for a wavelength of 800 nm (page 538 of [35]). At positive potentials a charge separation occurs and the photo-generated holes migrate under the influence of the electric field to the electrode surface [36]. Holes trapped in localized surface bonds are used to dissolve n-GaAs (see eqs. (4.4) and (4.6)). Since the penetration depth of light is small compared with the diffusion length of minority charge carriers in the solid, it is generally assumed that at positive potentials each photo-generated hole reaches the electrode surface of n-GaAs and participates in the dissolution reaction when $i_{hv}^a < i_{max}^a$ [9,36].

The Mott-Schottky plots of Fig. 4.12 were obtained in the potential range in which the dissolution of GaAs takes place (compare with the photocurrent-potential curves at n-GaAs in Fig. 4.4). The photoanodic dissolution of n-GaAs causes a shift of the Mott-Schottky plots which clearly depends on the light intensity (Fig. 4.13). The increase of the potential drop over the Helmholtz layer ($\delta V_H \neq 0$) with increasing intensity can be directly deduced from the parallel displacement of the Mott-Schottky plots using eq. (4.20) in which N_A is replaced by N_D. This increase results from the build-up of positive charge at the semiconductor. Fig. 4.13 shows that two regions can clearly be distinguished: a sharp increase of δV_H at relatively low light intensity and a more moderate linear dependence of δV_H on ϕ at higher light intensities. This result suggests that two different processes contribute to δV_H. The sharp change of the Helmholtz potential at low light intensities ($\delta V_H \leqslant 200$ mV) is in good agreement with the values reported by other authors at GaAs in various electrolytes, using similar photon densities [37,38]. The magnitude of the shift is also very similar to that found at p-GaAs in the dark after anodic prepolarization, when the (photo)dissolution rates of both type of electrodes are taken into account. It therefore seems very likely that at these relatively low dissolution rates the same intermediates of the (photo)dissolution reaction (eqs. (4.4)-(4.7)) are responsible for the change of the Helmholtz potential at both p- and n-type electrodes. The reported saturation of δV_{fb} at higher light intensities [37,38] would correspond to our moderate dependence at higher ϕ in Fig. 4.13. From the present results at the highest light intensity at which oxide formation does not yet occur (curve (h) of Fig. 4.12) a large change of V_H of 0.76 V is obtained. This value agrees with that found when the results of Allongue and Cachet [30] are extrapolated to the high dissolution rates used here. According to eq. (4.22), such a large shift should correspond with a very large charge density at the semiconductor. From the results presented so far, it is not clear whether this is only due to the much higher dissolution rates of n-GaAs ($i_{hv}^a \leqslant 62$ mA·cm^{-2}) with respect to those at p-GaAs ($i_d^a \leqslant 1.6$ mA·cm^{-2} in Fig. 4.11) or that illuminating the electrode contribute to these extreme parallel displacements. It should be noted that as a result of illumination electron-hole pairs are generated within the space-charge region over a certain penetration depth. It is possible that besides the charged intermediates located at the electrode surface, there will be a certain steady-state concentration of minority charge carriers in the space-charge layer which becomes more pronounced at higher photon densities. These two different charging phenomena would account for the two regions in Fig. 4.13. We will return to this point in subsection 5.3.3 where the effects of ex-

tremely high dissolution rates on the impedance behaviour of n-GaAs in the dark will be discussed. The use of an oxidizing agent to dissolve n-GaAs in the dark allows steady-state impedance measurements to be made in the depletion potential range during the dissolution reaction. Studying charging effects in the dark in these solutions is therefore interesting in order to compare with the present photoresults at high light intensity (see section 5.3).

4.3.4. Conclusions

Using steady-state impedance measurements in the case of n-GaAs under illumination and transient impedance measurements in the case of p-GaAs in the dark, it has been shown that during the (photo)anodic dissolution of GaAs, positive charge is trapped at the electrode surface. In this section the discussion is restricted to the situation covered by eq. (4.13) in which the kinetics of anodic dissolution are not inhibited by oxide formation. As a result of surface charging under oxide-free conditions, the potential drop over the Helmholtz layer changes. The degree of charging is found to be clearly dependent on the rate at which GaAs is dissolved, for both p-and n-type electrodes. We suggest that this positive charge is related to the intermediates in the dissolution reaction of GaAs as proposed in eqs. (4.4)-(4.7). An important conclusion is that during (photo)anodic dissolution the semiconductor band-edges are not fixed but are shifted downwards, towards positive potentials.

4.4. Interface charging under oxide-forming conditions

4.4.1. Introduction

From the previous sections it has become clear that when oxide is not present during the (photo)anodic dissolution of GaAs the intermediates in the dissolution reaction act as positively charged surface states. This surface charging results in a change of the potential drop over the Helmholtz layer. When the anodic dark current density of p-GaAs or the anodic photocurrent density of n-GaAs exceeds the limiting anodic current density, an oxide film is formed at the electrode surface (eq. (4.14)). The oxide film inhibits the dissolution rate of GaAs, as has been shown in section 4.2.

In this section we will consider the effects of positively charged intermediates (eqs. (4.4)-(4.7)), formed during the oxidation process at the semiconductor/oxide interface (see Fig. 4.9), on the potential distribution at the more complex Electrolyte/Oxide/Semiconductor (EOS) structure. Since

steady-state impedance measurements during the anodic dissolution can only be obtained at n-type electrodes, these measurements were performed on n-GaAs in two electrolytes, already described in section 4.2; viz. in an alkaline solution of $pH = 12$ which has a high value of i_{max}^a, and an EDTA-containing solution of $pH = 5$ in which oxide formation occurs even at very low light intensities (i_{max}^a is very low). In order to elucidate the charge and potential distribution at the electrode surface, frequency-dependent impedance measurements were also performed at various light intensities. In addition, transient impedance measurements were carried out to study the effect of interface charge in the initial stages of the oxide formation. Finally on the basis of these results an (EOS) model is described which can account for the observed features.

4.4.2. Results

The Mott-Schottky plot for a stationary n-GaAs electrode measured in the steady-state in the dark in EDTA solution at $pH = 5$ (curve (a) in Fig. 4.14)
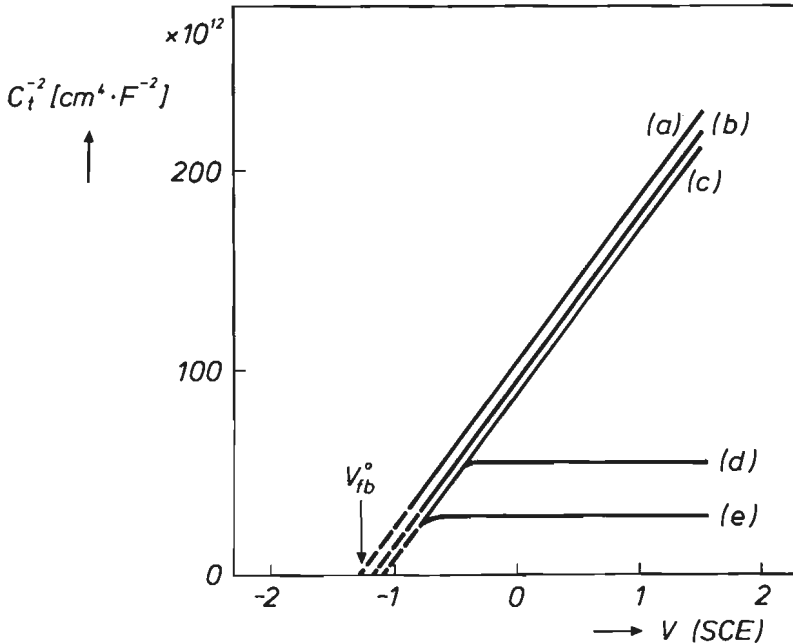
Fig. 4.14. Mott-Schottky results for a stationary n-type ($N_D = 8.6 \times 10^{16}$ cm^{-3}) GaAs electrode in a 0.1 M Na$_2$EDTA, 0.1 M NaClO$_4$ solution of $pH = 5$ in the dark (curve (a)) and under illumination : $\phi = 0.035$ (curve (b)); 0.065 (curve (c)); 0.20 (curve (d)) and 0.32 a.u. (curve (e)). Light source: 1 mW He-Ne laser.

is identical with that found in a citrate/NaOH buffer solution of the same pH; C_t is again the total series cell capacitance measured at a frequency of 10 kHz. In the dark, oxide is not present on the GaAs electrode. Since the capacitance of the Helmholtz layer is much greater than that of the depletion layer (section 2.2), the change of the applied potential V is concentrated in the space-charge region of the semiconductor, and the electrode behaves like a Schottky barrier (eq. (2.12)), as expected.

When the electrode is exposed to a low light intensity, a linear plot is again observed (curve (b)) but displaced with respect to the dark curve (a). An increase in light intensity, to a value still not sufficient to cause film formation (compare with curve (b) of Fig. 4.6), gives a further shift in the curve (curve (c)). Such parallel displacements of the Mott-Schottky plots are similar to those reported in the previous section; in both cases oxide is not present at the surface. The displacement corresponds to a change of the Helmholtz potential (δV_H).

The presence of an oxide film has a dramatic effect on the impedance of the illuminated electrode. This is shown in curve (d) of Fig. 4.14 for a photon density capable of maintaining a stable film. The steady-state C_t value at 10 kHz has become almost independent of the applied potential in a wide range. C_t increases with increasing photon density as is shown in curve (e). That these effects are connected with the presence of the surface film can be deduced from transient measurements at 10 kHz, shown in Fig. 4.15. During the period of film formation the photocurrent density (i_{hv}^a) decreases to a steady-state value, as was shown before in Fig. 4.7, curve (d). Such a photocurrent transient is again represented in curve (a) of Fig. 4.15. During the initial stages of oxide formation, the imaginary part of the cell impedance $(Z_{im} = (j\omega_f C_t)^{-1})$ decreased somewhat with respect to its dark value (Fig. 4.15, curve (b)). This change corresponds to the parallel shift in the Mott-Schottky curve of Fig. 4.14. Z_{im}, however, decreased markedly as the photocurrent decayed to its steady-state value. A corresponding change was also observed in the real part of the impedance (Z_{re}) in Fig. 4.15, curve (c). Similar behaviour is also found at other light intensities, with Z_{re} and Z_{im} following the photocurrent changes closely. It should be noted that, although the surface film dissolves only slowly in the dark, as shown in Fig. 4.8, both Z_{im} and Z_{re} relaxed 'rapidly' to the dark values when the light was switched off (see curves (b) and (c) of Fig. 4.15).

Further evidence that the anodic film formed in EDTA solution is responsible for the impedance results in curves (d) and (e) of Fig. 4.14 is provided by measurements in an EDTA-free electrolyte at $pH = 5$. As already described in section 4.2, the photocurrent in the absence of EDTA is stable
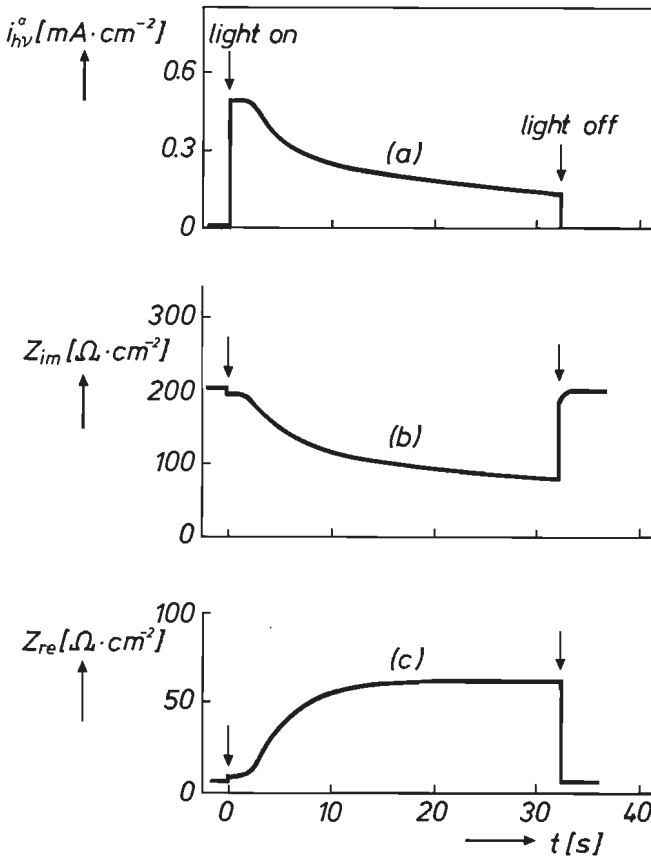
Fig. 4.15. The influence of light ($\phi = 0.5$ a.u.) on the photo-current (curve (a)) and the imaginary and real components of the impedance (curves (b) and (c), respectively) of a stationary n-GaAs electrode at +0.50 V(SCE) in a 0.1 M Na_2EDTA, 0.1 M $NaClO_4$ solution of $pH = 5$. Light source: 1 mW He-Ne laser.

and directly proportional to light intensity up to the highest values used (curve (a) in Fig. 4.6). In this case, illumination also gives a shift in the Mott-Schottky curve similar to that shown in curves (b) and (c) of Fig. 4.14. However, the displaced curve remained parallel to the dark curve up to the highest photon density ($i_{hv}^a \leqslant 1.1$ mA·cm^{-2}): the change in the flat-band potential tended to level off at higher light intensity ($\delta V_H \approx 0.22$ V). Although much lower light intensities were used in these experiments, the results are in agreement with those obtained with n-GaAs under oxide-free conditions shown in the previous section.
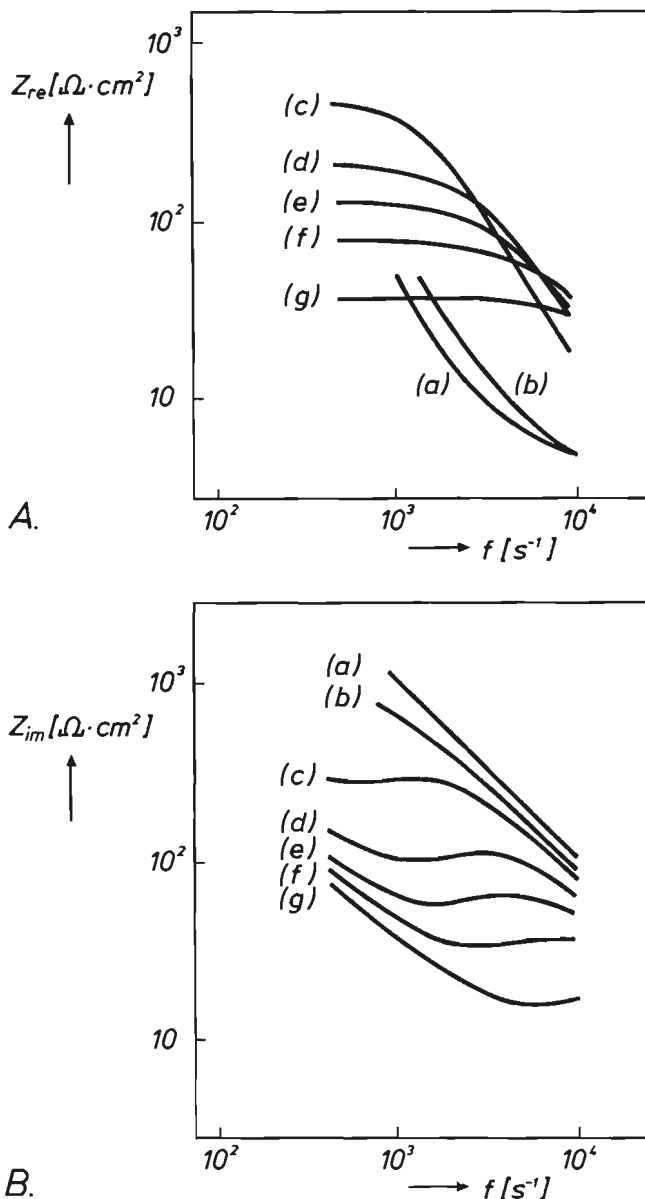
Fig. 4.16. The frequency dependence of the real (A) and imaginary (B) components of the impedance of a stationary n-GaAs electrode at +0.50 V(SCE) in a 0.1 M Na_2EDTA, 0.1 M $NaClO_4$ solution of $pH = 5$ in the dark (curves (a)). The remaining curves (b)-(g) refer to an illuminated (1 mW He-Ne laser) electrode at increasing light intensity. ϕ values are given in Table I.

If the capacitance of the film-covered electrode, measured under illumination, is due mainly to the space-charge layer of the semiconductor, then the potential-independent C_t values in curves (d) and (e) of Fig. 4.14 imply a considerably reduced but almost fixed band bending. A similar behaviour was also found in alkaline solutions at much higher light intensities (curve (i) of Fig. 4.12). Such a pinning of the Fermi level could result from a build-up of charge at the GaAs/oxide interface. A fast decay of this interface charge due to recombination of trapped minority charge carriers and majority charge carriers at the interface, would account for the rapid relaxation of the electrode impedance when the light is switched off.

In order to test the applicability of the oxide model, the frequency dependence of the electrode impedance was measured at various light intensities. It has been shown [39] that such measurements yield information about the recombination processes which take place in the space-charge region. The real and imaginary components of the impedance, Z_{re} and Z_{im} respectively, are plotted in Fig. 4.16 in the frequency range of 500 Hz - 10 kHz, for an electrode without a surface film in the dark and at low light intensity (curves (a) and (b), respectively), and at increasing light intensity for an electrode with an anodic oxide film in curves (c) - (g) (compare the steady-state photocurrent densities, which are tabulated in Table I, with those in

Table I

Influence of the photon density ϕ on the parameters R_{rec}, C_{sc}, δV_{sc} $(= -V_{ox})$ and V_{sc} measured at +0.50 V(SCE).

Case	ϕ^*[a.u.]	R_{rec} [$\Omega \cdot cm^2$]	C_{sc} [F$\cdot$cm^{-2}]	δV_{sc} [V] $(= -V_{ox})$	V_{sc} [V]
a	dark	35,000	0.082×10^{-6}	0.00	1.80
b	0.035	28,000	0.085×10^{-6}	0.10**	1.70
c	0.11	838	0.114×10^{-6}	0.88	0.92
d	0.20	338	0.129×10^{-6}	1.08	0.72
e	0.32	195	0.142×10^{-6}	1.21	0.59
f	0.57	109	0.150×10^{-6}	1.27	0.53
g	1.14	52	0.156×10^{-6}	1.31	0.49

* 1 a.u. corresponds to a limiting photocurrent density of 1 mA·cm^{-2} (see experimental chapter 3).

** Note: an anodic oxide film is not formed ($\delta V_{sc} = -\delta V_H$)

Fig. 4.6). The light intensity has a significant effect on the impedance of the film-covered electrode. These results will be further processed in the discussion.

Frequency-dependent steady-state impedance measurements were also performed on an n-GaAs RDE (100 rpm) in a 0.01 M NaOH solution at light intensities at which oxide formation also occurs (see Fig. 4.3). Although much higher light intensities are needed to form an oxide film ($i_{max}^a = 4.3$ mA·cm^{-2} at 100 rpm), results were found very similar to those for EDTA shown in Fig. 4.16. Up to current densities of 4.3 mA·cm^{-2} ($= i_{max}^a$ at pH $= 12$) the impedance spectra do not change very much with respect to the dark case (see Fig. 4.16, curves (a) and (b)). However, when i_{max}^a was exceeded by a very small amount ($4.3 < \phi < 4.4$ a.u.) a dramatic effect on both the real and imaginary parts of the impedance was observed, similar to that shown in curves (c) to (g) of Fig. 4.16. When the light intensity was further raised ($\phi > 4.4$ a.u.) the imaginary part of the impedance decreased to extremely low values similar to those found for the pH $= 13$ solution in curve (i) of Fig. 4.12. By simply increasing the electrode rotation rate from 100 to 5000 rpm, the rate of oxide dissolution is increased due to the improved supply of OH$^-$ ions to the electrode surface. At this high electrode rotation rate, the impedance spectrum changed dramatically to that found in the dark and at low light intensities for the oxide-free case (see curves (a) and (b) of Fig. 4.16 where also $i_{hv}^a < i_{max}^a$). This shows again that the striking changes in the impedance behaviour are related to oxide formation at the electrode surface.

4.4.3. Discussion

The behaviour of the electrode with photoanodic oxide film, described above, resembles, in certain respects, that of the illuminated Metal/Oxide/Semiconductor (MOS) transistor [40-42]. In order to discuss our results, we shall therefore use an analogous Electrolyte/Oxide/Semiconductor (EOS) model, which includes hole trapping in interface (if) states at the semiconductor/oxide interface. In Fig. 4.17.A an energy band model is presented of an oxide-covered semiconductor electrode. A similar approach has been used qualitatively by Morrison and co-workers [43,44] for photoanodic reactions at n-type Si electrodes.

The complex equivalent circuit of such an oxide model can be considerably simplified to that shown in Fig. 4.17.B [45], (see also page 124 of [46]). The following elements are considered. In the semiconductor, a space-charge layer is established whose capacitance is given by C_{sc}. C_{if} describes
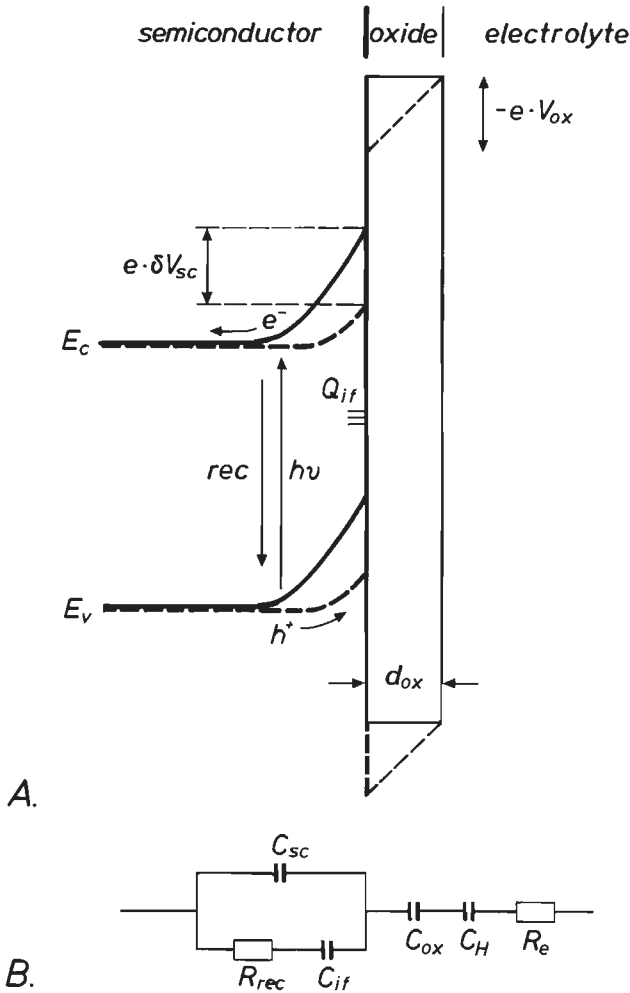
Fig. 4.17. Schematic representation of an oxide-covered n-type GaAs electrode during photoanodic dissolution.

A) energy band model of a Semiconductor/Oxide/Electrolyte (EOS) surface structure. E_c and E_v (solid lines) refer to conduction and valence bands in the dark. As a result of illumination, a positive charge density Q_{if} is built up at the GaAs/oxide interface. Consequently, the semiconductor band-edges shift to more positive potentials; the semiconductor band bending is reduced by δV_{sc} and a corresponding potential drop V_{ox} appears over the surface film (dashed lines). As a consequence of the inhibited dissolution of GaAs, recombination is important. The recombination reaction is represented by rec.

B) equivalent circuit for an illuminated n-GaAs electrode with surface film (EOS surface structure).

the storage capacitance of the photo-generated minority carriers in the interface region, for the case in which the carriers are in quasi-equilibrium with the bulk of the semiconductor. Since the excess minority charge carriers in the semiconductor must inevitably recombine with conduction band electrons in the space-charge layer, a recombination resistance R_{rec} must be taken into account. At the semiconductor surface an oxide film is formed whose capacitance is represented by C_{ox}. Finally, C_H and R_e refer to the Helmholtz capacitance and to the combined resistance of the bulk semiconductor and electrolyte, respectively.

In the present EDTA case, a small direct current ($= i_{max}^a$) flows during illumination (see Fig. 4.6). This means that the space-charge, the oxide film and the Helmholtz capacitances must be shunted by a large parallel resistance. The resistance, which could be deduced from measurements at low frequencies, has a value in excess of 500 kΩ. For simplicity, it has been omitted from Fig. 4.17.B as it is not important for the impedance measurements at higher frequencies discussed here. A further simplification is achieved when C_H is disregarded in the circuit. ($C_{ox} < C_H$, see also eq. (2.8)). We will return to this assumption later in the discussion.

An analysis of the equivalent circuit of Fig. 4.17.B yields the following two equations;

$$\frac{1}{Z_{re} - R_e} = (R_{rec}C_{sc}^2)\omega_f^2 + \frac{(C_{if} + C_{sc})^2}{R_{rec}C_{if}^2}, \qquad (4.23)$$

and

$$\frac{-\omega_f Z_{im}}{Z_{re} - R_e} = \left\{ \frac{R_{rec}C_{sc}(C_{sc} + C_{ox})}{C_{ox}} \right\} \omega_f^2 + \left\{ \frac{(C_{if} + C_{sc})(C_{if} + C_{sc} + C_{ox})}{R_{rec}C_{ox}C_{if}^2} \right\}. \qquad (4.24)$$

R_e can be obtained from the high frequency limit of Z_{re} in the dark. It follows from these equations that plots of $\cdot\dfrac{1}{Z_{re} - R_e}$ and $\dfrac{-\omega_f Z_{im}}{Z_{re} - R_e}$ as a function of ω_f^2 should give straight lines.

In Fig. 4.18 the second of these functions is plotted for a film-covered electrode in EDTA solution at a photon density of $\phi = 0.20$ a.u. which corresponds to the impedance results of curves (d) in Fig. 4.16. Excellent linearity is observed over a range of two orders of magnitude. This is also the case for eq. (4.23) and with other light intensities. Some deviation from the ideal behaviour is only found for eq. (4.23) at lower frequencies ($f < 2$ kHz) at the highest light intensities.
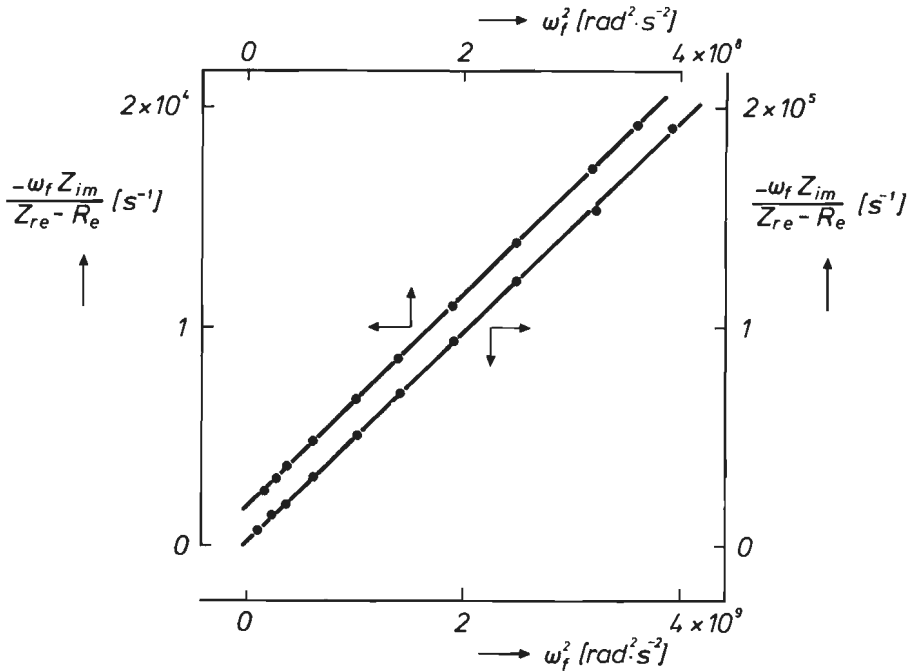
Fig. 4.18. The results shown in curves (d) of Fig. 4.16 plotted according to eq. (4.24), as described in the text.

It is not possible to obtain the four unknown circuit elements of Fig. 4.17.B directly from eqs. (4.23) and (4.24). In order to get an estimate of various parameters it is assumed that $C_{if} \gg C_{sc}$. This condition is subsequently used to calculate a self-consistent set of impedance parameters. The intercept and slope of the plot of eq. (4.23) yield R_{rec} and C_{sc}, and C_{ox} can then be obtained from eq. (4.24). The most striking aspect of this analysis is the very significant decrease of the recombination resistance R_{rec} and the gradual increase in C_{sc} with increasing photon density (ϕ) as Table I shows. Since C_{sc} is related to V_{sc} via the Mott-Schottky equation (2.12), the latter result supports the suggestion made before that illumination decreases the band bending (see the last column in Table I). This is also found with the illuminated MOS device [40]. We further note a dependence of R_{rec} on the light intensity

$$R_{rec} \propto \phi^q, \tag{4.25}$$

where q is a constant equal to -1.1, a value similar to that found for the silicon MOS transistor [41,42]. In the MOS case, this dependence has been accounted for theoretically by the Shockley-Read recombination model [41].

The recombination resistance used above has a wider relevance in semiconductor electrochemistry. This is clear when one studies in oxide-free systems the electrode impedance in the potential range in which the current due to minority carrier transfer is dominated by recombination (see sections 2.4 and 2.5). In chapter 2 it has been pointed out that minority carriers generated by light or injected from an oxidizing agent in solution, recombine in a small potential range (see Figs. 2.9.B and 2.10.B). In both cases an equivalent circuit similar to that shown in Fig. 4.17 accounts for the impedance results and a characteristic recombination resistance is also obtained with a relationship similar to that of eq. (4.25) and with q also equal to -1.1. To these recombination measurements at n-GaAs under oxide-free conditions will be returned in section 5.4 where oxidizing agents are used to supply the minority charge carriers.

Table II shows that, at constant light intensity, C_{sc} and R_{rec} change only slightly with applied potential in the limiting photocurrent range. The oxide-film capacitance C_{ox}, however, decreases significantly with increasing potential. This might be expected for electric field dependent film growth (eq. (4.15)) [8,29]. Since the oxide film can be considered as a parallel plate capacitor whose capacitance is given by

$$C_{ox} = \frac{\varepsilon_{ox}\varepsilon_o \cdot 10^7}{d_{ox}}, \tag{4.26}$$

where ε_{ox} is the dielectric constant of the oxide and d_{ox} is the oxide layer thickness, it is clear that when the oxide layer thickness increases at positive

Table II

Influence of the electrode potential on the impedance parameters measured at $\phi = 1.1$ a.u.

V(SCE)	0.00	0.50	1.00
$R_{rec}[\Omega \cdot cm^2]$	54	55	54
$C_{sc}[F \cdot cm^{-2}]$	0.156×10^{-6}	0.156×10^{-6}	0.155×10^{-6}
$C_{ox}[F \cdot cm^{-2}]$	$4{,}51 \times 10^{-6}$	$2{,}68 \times 10^{-6}$	$1{,}97 \times 10^{-6}$
$d_{ox}[nm]$	1.6	2.6	3.6

potentials C_{ox} decreases. For anodic films on GaAs, a proportionality constant in the range of $B = 1.4 - 4.0$ nm·V^{-1} is reported for the potential dependence of the film thickness (see eq. (4.15)) [8,47]. In the extreme case at very positive potentials, very thick oxide films with a thickness of the order of hundreds of Ångstroms are reported in EDTA-containing solutions [15]. If a dielectric constant of 8 for the oxide film is assumed [47], the measured C_{ox} values indicate in the present case oxide layer thicknesses ranging from 1.6 to 3.6 nm (Table II). These values are in good agreement with those already estimated from the kinetic experiments in section 4.2 in EDTA-containing solutions (see Figs. 4.7 and 4.8) and also in alkaline solutions [8]. A proportionality constant of 2.0 nm·V^{-1} is obtained from Table II, which agrees well with that found in the literature [47].

For the analysis of the impedance results two assumptions have been made. In the first place it was assumed that $C_{if} \gg C_{sc}$. Comparing the values of C_{sc} in Tables I and II with the estimated C_{if} values which are of the order of 15×10^{-6} F·cm^{-2} under similar conditions [45], it is clear that this condition is, indeed, amply fulfilled. In the second place, the Helmholtz capacitance was not taken into account in the mathematical description of the equivalent circuit. It was assumed that $C_{ox} < C_H$ and that C_H could therefore be omitted. From Table II it follows that, except at low potential, C_{ox} is approximately an order of magnitude smaller than the generally accepted values of the Helmholtz capacitance; omitting C_H involves, however, some error in the determination of C_{ox}.

For electrolytes without EDTA the impedance spectra of the electrode illuminated up to the highest intensity ($\phi \leq 1.1$ a.u.) resemble those of the EDTA system in the dark or at very low light intensity (curves (a) and (b) of Fig. 4.16). The Z_{im} versus f plots are linear, when plotted on a double logarithmic scale between 1 and 10 kHz, with a slope of -1.0. The equivalent R_{rec} term is, as in the dark case, very large and decreases only slightly on illumination, in contrast to the considerable decrease in the EDTA case when oxide formation occurs (Table I). In the absence of an anodic film, recombination is not important as hole transfer to the solution remains effective at positive potentials even at high photon density. Under these oxide-free conditions the equivalent circuit of Fig. 4.17.B can therefore be reduced to two series capacitors, C_{sc} and C_H, in series with the electrolyte/semiconductor bulk resistance R_e. Since during the anodic oxidation of GaAs positively charged intermediates of the dissolution reaction are formed (see section 4.3), acting now as surface states (SS) instead of interface states, a capacitor C_{ss} parallel to C_{sc} must be taken into account under illumination (page 119 et seq. of [46]). It can then be shown, again omitting

C_H from the circuit, that the imaginary part of the impedance is given by:

$$Z_{im} = -\frac{1}{2\pi f(C_{sc} + C_{ss})}.$$ (4.27)

Since C_{sc} and C_{ss} are constant at fixed potential and light intensity, this explains the slope of the Z_{im} versus f plots (a) and (b) of Fig. 4.16.B. It is obvious that in the dark the electrode does not dissolve; C_{ss} can then also be disregarded and the equivalent circuit is further simplified to that of Fig. 2.2.A when R_e is included.

By using the results of the above impedance analysis and following a procedure very similar to that adapted by Frese and Morrison [47], information can be obtained concerning the potential and charge distribution at the semiconductor/oxide/electrolyte surface structure. For the oxide-free case it was argued in the previous section that an applied potential is distributed over both the space-charge and Helmholtz layers (eq. (4.19)). Very often the latter can be disregarded ($\delta V_H = 0$) when $C_{sc} \ll C_H$. When an oxide layer is formed at the electrode surface, a potential change over the oxide film must also be considered. The potential drop over the space-charge layer (V_{sc}) will, of course, diminish when part of the potential drop occurs over the oxide layer (V_{ox}). Eq. (4.19) can be rewritten for the case when an oxide is formed at the electrode surface, as

$$V_{sc} = V - V_{fb}^o - \delta V_H - V_{ox}.$$ (4.28)

As C_{ox} is in most cases an order of magnitude smaller than C_H, the potential drop will mainly occur over the oxide layer. We will therefore consider, for the moment, that $\delta V_H = 0$. The potential drop across the depletion layer V_{sc} can be calculated from the measured value of C_{sc} (see Table I) via the Mott-Schottky relation (eq. (2.12)). Since V_{fb}^o is defined as the value of V at which $V_{sc} = V_{ox} = 0$ (dark case of Fig. 4.14 curve (a)), V_{ox} can be calculated as a function of the light intensity using eq. (4.28). Values for the change in band bending (δV_{sc}), which results from illumination, are given in Table I and confirm the trend that the band bending decreases with increasing light intensity. The decrease in V_{sc} is, of course, compensated by an increase in V_{ox} ($\delta V_{sc} = -V_{ox}$ when $\delta V_H = 0$) as is schematically shown in Fig. 4.17.A.

At constant light intensity, C_{sc} is nearly constant with applied electrode potential in the limiting anodic current plateau range (see Table II). According to the Mott-Schottky equation (2.12) this results in a constant V_{sc}. Con-

sequently, V_{ox} increases with applied potential (eq. (4.28)). Since in the steady-state the rate of oxide formation (i_{form}^a) is equal to the rate of oxide dissolution and since the rate of the latter reaction is potential-independent, this implies that i_{form}^a is constant. From the mechanism of a field-dependent growth of oxide layers [28,29], described by eq. (4.15), it is obvious that when V_{ox} increases at constant i_{form}^a, the oxide layer thickness must increase with potential. This results, of course, in a decrease of C_{ox} (eq. (4.26)), as found experimentally (see Table II). Summarizing, we note that when the electrode potential is increased in the anodic potential range that the potential drop over the space-charge layer remains constant whereas the potential drop over the oxide layer increases. Consequently, to accommodate a larger potential drop, the oxide layer thickness increases and a continuous shift of the semiconductor band-edges toward positive potentials results with increasing electrode potential (see Fig. 4.17.A). The potential-independent values of C_t^{-2} in curves (d) and (e) of Fig. 4.14 and also in curve (i) of Fig. 4.12 can be understood in this way.

The charge distribution at the semiconductor/oxide interface can also be obtained from the impedance results. If the charge density in the depletion region of the semiconductor is denoted by Q_{sc} and that at the interface by Q_{if}, then

$$Q_{sc} + Q_{if} = -Q_{ox}, \qquad (4.29)$$

where Q_{ox} is the charge density of ions of opposite sign at the outer surface of the oxide film. Q_{sc} can be estimated for a given value of V_{sc} from an integrated form of eq. (2.12):

$$Q_{sc} = \left\{ \frac{2\varepsilon\varepsilon_0 N_D}{e} \right\}^{\frac{1}{2}} \cdot \left\{ V_{sc} - \frac{kT}{e} \right\}. \qquad (4.30)$$

Since C_{ox} and V_{ox} are known, Q_{ox} can be obtained when a linear film capacitance, $C_{ox} = Q_{ox}/V_{ox}$, is assumed [47]. Subsequently, the charge density stored at the interface can be calculated according to eq. (4.29). The values of Q_{if}/e range from approximately 5×10^{12} cm^{-2} to 3×10^{13} cm^{-2} at the highest light intensity for the film-covered electrode.

It should be emphasized that when the light is switched off, both the real and imaginary parts of the impedance of an oxide-covered electrode respond immediately, to give values which are characteristic of the dark case (Fig. 4.15, curves (b) and (c)), although the electrode is still covered with an oxide; it has been shown in Fig. 4.8 that the dissolution of an oxide film

formed at $+0.50$ V takes approximately three minutes. This result can be understood in the following way. When the light is switched off, the generation of minority charge carriers stops instantaneously, but the recombination continues and the interface states are quickly discharged. This result shows that the interface states are responsible for maintaining the potential drop over the oxide layer. The semiconductor band-edges immediately shift back to their original dark position once the occupancy of interface states drops when the light is switched off (compare dashed and solid lines in the energy band model of Fig. 4.17.A).

In the steady-state under oxide-forming conditions a certain interface charge density is established at the semiconductor/oxide interface. This results in a potential drop over the oxide layer and consequently in a decrease of the potential drop over the space-charge layer ($\delta V_{sc} = -V_{ox}$). This latter condition must be fulfilled for the following reason: more minority charge carriers are generated by light than are needed to maintain the oxide film; to enable the excess of holes to recombine with electrons at a sufficient rate, the electron concentration in the space-charge layer must increase, i.e. according to the Boltzmann equation (2.5) V_{sc} must decrease. The potential drop over the oxide layer increases at higher light intensities (Table I) because the electron concentration near the interface must be larger to maintain a higher recombination rate (see Fig. 2.9.B).

In the absence of an oxide film at lower light intensity ($e \cdot \phi < i^a_{max}$), the density of charged surface states can be calculated directly from eq. (4.20), using eq. (4.22) and the parallel displacement of the Mott-Schottky plots (curves (b) and (c) of Fig. 4.14). In this case a change of V_{sc} must, of course, be compensated by a change in the Helmholtz potential ($\delta V_{sc} = -\delta V_H$, see Table I), as has been pointed out in the previous section. A limiting value of Q_{ss}/e for a photon density just below that required to form an oxide film, of the order of 3×10^{13} cm^{-2}, is calculated when C_H is again assumed to be 20×10^{-6} F·cm^{-2}. These surface state densities are quite similar to the interface state densities found under oxide-forming conditions. It is therefore very likely that the same intermediate states are involved in the dissolution mechanisms. This is in agreement with the dissolution models presented in section 4.2 in which the common intermediates are assumed in eqs. (4.4)-(4.7).

So far, only the results in EDTA-containing solutions, having a low i^a_{max} value, has been discussed. However, the same trends are also found under oxide-forming conditions during the photoanodic dissolution of n-GaAs in a 0.01 M NaOH solution having a much higher i^a_{max} than the EDTA solutions.

4.4.4. Conclusions

In this section it has been shown that an EOS model can be used to describe the semiconductor/oxide/electrolyte interface at n-GaAs. Impedance measurements were found to be useful in determining the parameters which are involved in this model. It was shown that under oxide-forming conditions ($e \cdot \phi > i_{max}^a$), high charge densities are located at the semiconductor/oxide interface and that this charge can be attributed to intermediates of the dissolution reaction of n-GaAs under illumination. For the results in EDTA-containing solutions charge densities of up to 3×10^{13} cm^{-2} were found, very similar to those found under oxide-free conditions at low light intensity. In the latter case the holes are readily removed from the surface region by the dissolution reaction and the change of the Helmholtz potential is attributed to the same intermediates, now acting as positively charged surface states.

The presence of an anodic film, as found at higher light intensity, has two important effects. In the first place, dissolution is inhibited so that holes generated by light cannot escape to the solution at a sufficient rate. The excess photogenerated minority charge carriers recombine with conduction band electrons, which results in a dramatic decrease of the recombination resistance with increasing light intensity, as expected [45]. In the second place, as C_{ox} is considerably smaller than C_H, the surface film can accommodate a more substantial rearrangement of the surface potential. This implies that the semiconductor band-edges shift considerably with respect to the solution, thereby reducing V_{sc} over the space-charge layer. This latter effect is necessary in order to increase the electron concentration at the electrode surface to supply the recombination reaction in the space-charge layer. Shifts of the semiconductor band-edges of more than 1.3 V were found.

In this section conclusions are drawn for n-type semiconductors because steady-state impedance measurements during photoanodic dissolution can only be measured on this type of electrode. However, a similar reasoning can be given for the anodic dissolution of p-type electrodes in the dark under oxide-forming conditions. When, in the initial stages of oxidation of p-GaAs, the anodic dark current density is larger than i_{max}^a (eq. (4.14)) an oxide film is formed at the electrode surface. In the steady-state the rate of oxidation at the semiconductor/oxide interface is equal to the rate of oxide dissolution at the surface ($i_d^a = i_{max}^a$). Again, as in the case of n-GaAs at positive potentials, i_{max}^a is independent of the applied electrode potential (see Fig. 4.2). Consequently, i_d^a is constant in this potential range. According to eq. (4.8), i_d^a depends only on p_s for a given solution. Since p_s is related

to V_{sc} via the Boltzmann equation (2.6), it is clear that the band bending over the space-charge layer is determined by the maximum dissolution rate (i^a_{max}) and is independent of the applied potential. Consequently, the remaining potential drop occurs over the oxide layer. As found at n-GaAs, V_{ox} increases with applied potential, in this case to reduce the rate of oxidation in the dark. It should be noted that recombination is not important at p-type electrodes because only majority charge carriers are involved in the dissolution reaction.

4.5. Summary

It has been shown that oxide-formation plays a very important role in the (photo)anodic dissolution of both p- and n-type GaAs, not only with regard to the dissolution kinetics but also with regard to the charge and potential distribution at the electrode surface. These phenomena were investigated at GaAs electrodes. It seems likely that similar basic ideas can also be applied to the dissolution of other III-V semiconductors.

When the oxidation rate of GaAs (i^a_d, i^a_{hv}) is lower than the rate at which the surface oxide can dissolve in the electrolyte (i^a_{max}), then oxide is not present at the electrode surface during (photo)anodic dissolution. A generalized working model has been presented with which the successive steps of the oxidative dissolution of GaAs can be described. From this model it is clear that positively charged intermediates, formed during the dissolution reaction, can act as surface states. These surface states can account for the change in the potential drop over the Helmholtz layer as found with impedance measurements. This results in a downward displacement by 50 to 200 mV of the semiconductor band-edges during the anodic dissolution of GaAs at relatively low dissolution rates. When n-GaAs is photoanodically dissolved at a high rate, much larger shifts were found ($\delta V_H \leq 800$ mV) and were attributed to additional charge generated within the space-charge layer under strong illumination.

On the other hand, when the rate of GaAs oxidation is higher than the maximum dissolution rate, an oxide film is formed at the electrode surface. In the steady-state, the dissolution rate of the semiconductor is ultimately determined by the rate at which the oxide can be dissolved in the electrolyte. Oxide layer thicknesses estimated from kinetic measurements are in good agreement with values obtained from impedance measurements. A model was considered which can account for the diffusion-controlled dissolution rate of the oxide (i^a_{max}) by OH^- ions in solution. It has also been

shown that i_{max}^a can be considerably lowered by 'oxide-promoting' reagents such as EDTA. From the model of oxide formation it is clear that GaAs is oxidized at the semiconductor/oxide interface and that the same intermediates in the oxidation reaction are involved as in the case of oxide-free dissolution. However, these intermediates, now acting as interface states, have a much more drastic effect on the potential distribution at the semiconductor/oxide/electrolyte surface structure. As found with impedance measurements, the oxide layer can accommodate a large potential drop which is determined by the capacitance of the oxide layer and the density of interface states. In the initial stages of oxide formation the build-up of interface charge continues until a steady-state value is reached, such that the potential distribution between the space-charge and oxide layers is most favourable for the inhibited dissolution of GaAs. As a result, during the photo(anodic) dissolution of GaAs under oxide-forming conditions, the magnitude of the shift of the semiconductor band-edges is in general much larger than in the case of oxide-free dissolution of GaAs. Values of more than 1.3 V are found.

Finally, this chapter will be concluded with some remarks about the implications these results may have on the electroless etching systems to be described in the following chapters, and about the practical importance of anodic dissolution.

In chapter 2 it was shown that the electroless etch rate of III-V semiconductors in solutions containing an oxidizing agent is determined by the hole injection kinetics, which are related to the overlap of the distribution function of the oxidizing agent (D_{ox}) in solution and the valence band of the semiconductor. It is clear from the results of the present chapter that the band-edges at the semiconductor surface are not fixed during anodic dissolution. This can seriously affect the hole injection kinetics and consequently the dissolution rate of the semiconductor in these solutions. We shall return to this point in the following chapter.

Although for technological applications it is often inconvenient to etch semiconductors anodically with an externally applied potential, this method can be used when other methods fail. For example, it is possible to etch selectively p- or n-type regions of multilayer structures commonly used in devices. The p-type material can be dissolved by maintaining the p-n junction in the dark at a potential close to the flat-band value for a p-type electrode. The n-type material does not dissolve in the dark. Selective etching of the n-type region can be achieved photoanodically at a potential which is sufficiently negative so that the p-type region remains immune. For polishing applications of rough semiconductor surfaces, use is made of oxide

formation during the anodic dissolution. Under oxide-forming conditions, smooth, mirror-like surfaces are obtained since the oxide film prevents preferential local dissolution [1,15]. On the other hand, under oxide-free conditions, defects which are always present in monocrystalline semiconductor crystals can be revealed during the (photo)anodic dissolution of the semiconductors [14,48].

Finally, it should be noted that the macroscopic etch rate of the semiconductor, either kinetically controlled or diffusion controlled, can be obtained from the anodic (photo)current density by means of eq. (2.39).

References

[1]   M.M. Faktor, T. Ambridge, C.R. Elliott and J.C. Regnault, 'Current Topics in Materials Science', 6, 1, (1980), Ed. E. Kaldis.

[2]   R. Memming, J. Electrochem. Soc., 125, 117, (1978).

[3]   W.W. Harvey, J. Electrochem. Soc., 114, 472, (1967).

[4]   S. Park and M.E. Barber, J. Electroanal. Chem., 99, 67, (1979).

[5]   S. Menezes and B. Miller, J. Vac. Sci. Technology, B, 1, 48, (1983).

[6]   W.W. Harvey and J. Kruger, Electrochim. Acta, 16, 2017, (1971).

[7]   C.C. Chang, B. Schwartz and S.P. Murarka, J. Electrochem. Soc., 124, 922, (1977).

[8]   F. Decker, Electrochim. Acta, 30, 301, (1985).

[9]   R. Memming and J.J. Kelly, 'Photochemical Conversion and Storage of Solar Energy', Ed. J.S. Connolly, chapter 9, Academic Press, New York, (1981).

[10] Y. Nakato, A. Tsumura and H. Tsubomura, J. Electrochem. Soc., 128, 1300, (1981).

[11] H. Gerischer, Faraday Spec. Discuss. Chem. Soc., No. 70, 137/258, (1980).

[12] J.J. Kelly and P.H.L. Notten, Extended Abstract No. IV C12, 33rd ISE Meeting, Lyon, Sept. (1982).

[13] H. Gerischer and W. Mindt, Electrochim. Acta, 13, 1329, (1968).

[14] M.M. Faktor and J.L. Stevenson, J. Electrochem. Soc., 125, 621, (1978).

[15] C.R. Elliott and J.C. Regnault, J. Electrochem. Soc., 127, 1557, (1980).

[16] K.W. Frese, M.J. Madou and S.R. Morrison, J. Phys. Chem., 84, 3172, (1980).

[17] *'Handbook of Chemistry and Physics'*, 51st edition, Ed. R.C. Weast, The Chemical Rubber Co., (1970).

[18] H. Gerischer and I. Mattes, *Z. Phys. Chem.*, **49**, 112, (1966).

[19] H. Gerischer, *Surf. Sci.*, **13**, 265, (1969).

[20] R. Memming and G. Neumann, *J. Electroanal. Chem.*, **21**, 295, (1969).

[21] H. Gerischer and W. Mindt, *Surf. Sci.*, **4**, 440, (1966).

[22] K.W. Frese, M.J. Madou and S.R. Morrison, *J. Electrochem. Soc.*, **128**, 1527, (1981).

[23] C.W. Wilmsen, *'Physics and Chemistry of III-V Compound Semiconductor Interfaces'*, chapter 7, page 403, Ed. C.W. Wilmsen, Plenum Press, New York, (1985).

[24] S. Lingier, D. Vanmaekelbergh and W.P. Gomes, *J. Electroanal. Chem.*, **228**, 77, (1987).

[25] K.J. Vetter, *'Electrochemical Kinetics'*, Academic Press, London, (1967).

[26] P.F. Schmidt and J.D. Ashner, *J. Electrochem. Soc.*, **118**, 325, (1971).

[27] E.D. Palik, J.W. Faust, Jr., H.F. Gray and R.F. Greene, *J. Electrochem. Soc.*, **129**, 2051, (1982).

[28] J.W. Diggle, T.C. Downie and C.W. Goulding, *Chem. Rev.*, **69**, 365, (1969).

[29] J.J. Kelly, *Electrochim. Acta*, **24**, 1273, (1979).

[30] P. Allongue and H. Cachet, *J. Electrochem. Soc.*, **132**, 45, (1985).

[31] Y. Nakato, A. Tsumura and H. Tsubomura, *'Photoeffects at Semiconductor-Electrolyte Interfaces'*, Ed. A.J. Nozik, p. 145, A.C.S. Symp., Houston, March, (1980).

[32] J.J. Kelly and P.H.L. Notten, *J. Electrochem. Soc.*, **130**, 2452, (1983).

[33] R. Memming, *'Photoelectrochemistry, Photocatalysis and Photoreactors'*, Ed. M. Schiavello, Nato Ser. C., Vol. 146, p. 107, D. Reidel, Dordrecht, (1984).

[34] R. Memming and G. Neumann, *Surf. Sci.*, **10**, 1, (1968).

[35] *'Landolt-Börnstein, Numerical Data and Functional Relationships in Science and Technology'*, New Series Group III, vol. 17, subvol. a, Springer Verlag, Berlin, (1982).

[36] W.W. Gärtner, *Phys. Rev.*, **116**, 84, (1959).

[37] J.J. Kelly and R. Memming, *J. Electrochem. Soc.*, **129**, 730, (1982).

[38] K. Schröder and R. Memming, *Ber. Bunsenges. Phys. Chem.*, **89**, 385, (1985).

[39] D. Vanmaekelbergh, W.P. Gomes and F. Cardon, *Ber. Bunsenges. Phys. Chem.*, **90**, 431, (1986).

[40] J. Crosvalet and C. Jund, *IEEE Trans. Electron Devices*, **ed-14**, 777, (1967).

[41] R.F. Pierret and C.T. Sah, *Solid-State Electron.*, **13**, 269, (1970).

[42] R.F. Pierret and C.T. Sah, *Solid-State Electron.*, **13**, 289, (1970).

[43] B.H. Loo, K.W. Frese and S.R. Morrison, *Surf. Sci.*, **109**, 75, (1981).

[44] M.J. Madou, K.W. Frese and S.R. Morrison, *J. Phys. Chem.*, **84**, 3423, (1980).

[45] J.E.A.M. van den Meerakker, J.J. Kelly and P.H.L. Notten, *J. Electrochem. Soc.*, **132**, 638, (1985).

[46] S.R. Morrison, *'Electrochemistry at Semiconductor and Oxidized Metal Electrodes'*, Plenum Press, New York, (1980).

[47] K.W. Frese and S.R. Morrison, *J. Electrochem. Soc.*, **126**, 1235, (1979).

[48] K. Nagato, S. Komiya, A. Shibatomi and S. Ohkawa, *J. Electrochem. Soc.*, **128**, 2247, (1981).

Chapter 5

Redox reactions at GaAs electrodes

5.1. Introduction

In this chapter, the electrochemical behaviour of a number of oxidizing agents at GaAs electrodes will be considered. We will restrict ourselves to oxidizing agents with standard redox potentials close to or positive with respect to the valence band-edge of GaAs, i.e. to systems with an overlap between the VB and the distribution function of the oxidizing agent. Since the degree of overlap determines the hole injection rate constant (eq. (2.27)) and thus the hole injection rate, it is expected that these agents can inject holes into the VB.

In the previous chapter it was concluded that considerable shifts of the semiconductor band-edges can occur due to the dissolution of GaAs, even under oxide-free conditions (section 4.3). As a result, the overlap between the VB and the distribution functions is expected to change. This should influence the hole injection kinetics during dissolution of the semiconductor [1]. Redox systems whose D_{ox} function have a very good overlap with the VB, such as Ce^{4+} in acidic solutions and $Fe(CN)_6^{3-}$ in alkaline solutions (see Fig. 2.8), are not suitable for detecting such effects because the reduction rate under these conditions is very likely determined by diffusion of the oxidizing agent in solution. In order to study the effects of surface charging on the hole injection rate, several redox systems based on Fe^{3+}, which have a moderate overlap with the VB, were investigated and compared with systems having a good overlap. This is described in section 5.2.

In section 4.3 it has been shown that when an oxide is formed at the electrode surface during the dissolution of GaAs, the shifts of the semiconductor bands are very pronounced. To study the effect of oxide formation on the hole injection kinetics, simple oxidizing agents having an excellent overlap with the VB are very suitable. In section 5.3, $Fe(CN)_6^{3-}$ is used as a strong oxidizing agent for this purpose. The electrochemical results during the dis-

solution of GaAs in alkaline $Fe(CN)_6^{3-}$ solutions obtained under oxide-forming conditions are compared with those obtained under oxide-free conditions.

In sections 5.4 and 5.5 the behaviour of more complicated redox systems, such as various halogens and hypochlorite, at GaAs are described.

The kinetics of the various oxidizing agents were investigated at both p- and n-type GaAs RDEs and RRDEs. Impedance measurements were also employed in these solutions to study charging effects at the solid/solution interface. It is obvious that the interplay between the reduction of the oxidizing agent and the anodic dissolution of GaAs as mentioned above, can occur in the dark. However, to elucidate the complex reduction mechanisms the effect of illumination on the reaction can give useful information and will therefore also be considered in the experiments.

The minority carrier recombination resistance allows a distinction to be drawn between valence band and conduction band processes [2]. This method was employed in some cases to determine the rate of hole injection by an oxidizing agent at n-GaAs electrodes.

To determine the etching mechanism of GaAs in solutions containing the various oxidizing agents two main routes can be followed: in the first place the products of the reduction reaction can be analyzed at the Pt-ring of an RRDE. When the collection factor of the ring-disk response is taken into account, the partial reduction current due to the reduction of the oxidizing agent at the disk can be deduced. A correlation between this partial reduction current and the measured current of the GaAs-disk electrode yields information about the etching behaviour of GaAs [3]. In the second place the macroscopic etch rate can be measured directly as a function of the applied electrode potential with the flow-cell (see experimental chapter 3). These etching results can then be correlated with the potentiostatically measured disk current [4]. Both methods have been employed in the present work. In addition, etching experiments were also performed with GaAs crystals at open-circuit potential in some cases.

At the end of each section the relevance of the electrochemistry of the oxidizing agents to the macroscopic etching behaviour in these solutions will be briefly discussed.

The results obtained in this chapter will be summarized separately in chapter 7.

5.2. Reduction of Fe^{3+} and its complexes

5.2.1. Introduction

It was shown in section 4.3 that anodic prepolarization of a p-type GaAs electrode causes a change in the potential drop over the Helmholtz layer. During anodic dissolution of GaAs the semiconductor band-edges are shifted downwards by $50 - 150$ mV (compare dashed and solid lines in Fig. 5.1). These shifts are observed in inert electrolytes under oxide-free dissolution conditions. The aim of the work described in the present section was to investigate the effect of anodic prepolarization of p-GaAs RRDEs on the kinetics of hole injection under oxide-free conditions.
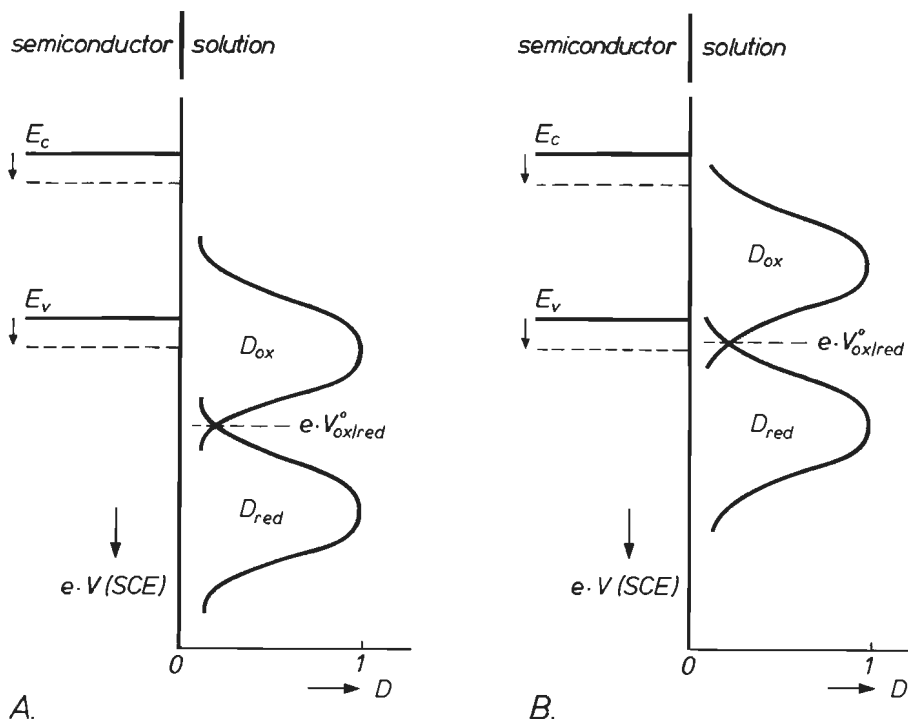
Fig. 5.1. Energy scheme showing the distribution functions (D_{ox} and D_{red}) of a redox system with respect to the band-edges (E_c and E_v) of GaAs (solid lines). During anodic dissolution the band-edges are shifted towards positive potentials (dashed lines). Two different redox systems are shown:
A) D_{ox} shows a good overlap with the valence band.
B) the overlap in this case is less favourable for hole injection.

Table III

Standard redox potentials $V^o_{ox/red}$ of various redox systems considered in this section and flat-band potentials V^o_{fb} of p-GaAs in inert electrolytes of different pH.

Group	Redox system	$V^o_{ox/red}$ V(SCE)	pH	$V^o_{fb}(p)$ V(SCE)	$V = V^o_{ox/red} - V^o_{fb}(p)$
A	$Ce^{4+/3+}$	$+1.20$	0	$+0.30$	$+0.90$
	$Fe(CN)_6^{3-/4-}$	$+0.22$	14	-0.55	$+0.77$
B	$Fe(CN)_6^{3-/4-}$	$+0.22$	4	$+0.05$	$+0.17$
	$Fe(CN)_6^{3-/4-}$	$+0.22$	5	0.00	$+0.22$
	*$Fe^{III}(EDTA)$	-0.12	5	0.00	-0.12
	**$Fe^{III}(Oxa)$	-0.24	5	0.00	-0.24
	$Fe^{3+/2+}$	$+0.53$	0	$+0.30$	$+0.23$
	$Fe^{3+/2+}$	$+0.53$	1.5	$+0.20$	$+0.33$

The working solutions contained:

*0.05 M Fe^{III} and 0.055 M EDTA
**0.05 M Fe^{III} and 0.165 M potassium oxalate (Oxa)

It is clear that, in order to detect a displacement of the band-edges, an oxidizing agent such as that represented in Fig. 5.1.A is unsuitable. The overlap with the valence band is so favourable that the rate constant for reduction is likely to be high and the rate of reduction is expected to be restricted by mass-transport in solution. The rate constant for hole injection from a system with a more negative redox potential (Fig. 5.1.B) should be much smaller; in this case, the rate of reduction may be sensitive to changes in the position of the band-edges resulting from a change in the Helmholtz layer. The kinetics of hole injection into the VB of p-GaAs, both in the dark and under illumination, can be followed experimentally using cyclic voltammetry and potential step measurements.

In table III a survey is given of the redox systems and the experimental conditions used. The flat-band potential $V^o_{fb}(p)$, as obtained from Mott-Schottky plots at p-type GaAs electrodes, is shown for the various pH values and can be seen in relation to the standard redox potential $V^o_{ox/red}$ of the redox systems. On the basis of these values, two groups can be defined which will be denoted as (A) and (B):

Group (A); the $V^o_{ox/red}$ value is significantly positive with respect to $V^o_{fb}(p)$. This corresponds to the situation shown in Fig. 5.1.A for which the distribution function overlaps very well the valence band of GaAs.

Group (B); $V^o_{ox/red}$ is close to $V^o_{fb}(p)$ so that the correspondence between valence band and distribution function is much less favourable (Fig. 5.1.B).

The redox systems in Table III are, with one exception, all based on Fe^{3+}; Ce^{4+} was also used because the $Ce^{4+/3+}$ redox system is simple and has been widely studied at GaAs [3,5]. It can therefore be considered as a reference redox system.

5.2.2. Results

Rate studies in the dark

In Fig. 5.2 results are presented for the reduction of an A-group oxidizing agent, Ce^{4+} at $pH = 0$, whose D_{ox} function shows a good overlap with the VB of GaAs (Table III). These cyclic voltammograms are also typical of $Fe(CN)_6^{3-}$ at $pH = 14$ when the different flat-band potential at the higher pH is taken into account. The limiting cathodic current, measured at the GaAs disk (curve (a)) is directly proportional to the square root of the electrode rotation rate, as expected for a reaction determined solely by mass-transport in solution (eq. (2.42)).

Due to the very positive $V^o_{ox/red}$ value of the $Ce^{4+/3+}$ redox system it is impossible to detect at the Pt-ring Ce^{3+} ions which are produced at the GaAs disk (H_2O is more easily oxidized). Therefore the Pt-ring was used in the shielding mode ([5] and page 22 of [6]) to detect the decrease in Ce^{4+}, concentration due to the reaction at the disk. In the case of $Fe(CN)_6^{3-}$, with a $V^o_{ox/red}$ more negative than that of Ce^{4+}, both the shielding and collecting modes can be applied (see experimental chapter 3). The latter method was used for the detection of $Fe(CN)_6^{4-}$ (see following section).

From the potential-independent current, measured at the Pt-ring (curve (b) in Fig. 5.2), it can be concluded that the Ce^{4+} reduction rate is not affected by the anodic dissolution of the GaAs at more positive potentials. No hysteresis in the current-potential curves is observed. This behaviour contrasts strongly with that of systems having a poorer overlap of the valence band and D_{ox} function. Fig. 5.3 shows cyclic voltammograms for Fe^{3+} reduction in 0.5 M H_2SO_4. The limiting cathodic current at the GaAs

disk (curves (a) and (b)) is similar to that shown in Fig. 5.2 for Ce^{4+} reduction. In the Fe^{3+} case, however, the anodic limit of the potential scan has a pronounced effect on the results. While the current-potential curve (a) measured to +0.20 V is independent of the scan direction, a considerable hysteresis is observed when the anodic limit is extended to more positive values (+0.40 V in curve (b)); the reduction current measured during the cathodic sweep is significantly lower than that found in the return sweep and both branches of the curve are displaced with respect to curve (a). Curves (c) and (d) of Fig. 5.3 show that the Pt-ring current, due to oxidation of Fe^{2+} species produced at the disk, follows the corresponding disk current closely. As in curve (b), a considerable hysteresis is observed in the equivalent curve (d). It is striking that reduction of Fe^{3+} ions at the p-GaAs disk

Fig. 5.2. Current-potential curves for a Pt/p-GaAs RRDE (5000 rpm) in 0.05 M Ce^{4+}, 0.5 M H_2SO_4 solution in the dark at 50 mV·s^{-1}. Curve (a), disk current; curve (b), ring current measured in the shielding mode under potentiostatic control (0.00 V). V_r represents the open-circuit potential. Similar results are also obtained in a 0.05 M $Fe(CN)_6^{3-}$, $pH = 14$ solution.

stops completely at about 0.25 V, although the redox potential is > 0.50 V in this case, and reduction at a Pt electrode continues up to the redox potential.

Further evidence for this type of inhibition of the cathodic reduction current is provided by potential step measurements (Fig. 5.4). The GaAs-RDE was held at a potential V_a close to V_{fb}^o. The current, which at this potential is determined by dissolution of the semiconductor and reduction of the oxidizing agent, was recorded as a function of time. At $t = 0$, the potential was switched to a more negative value V_c, at which only the reduction reaction is possible. The resultant current transient was recorded. The results

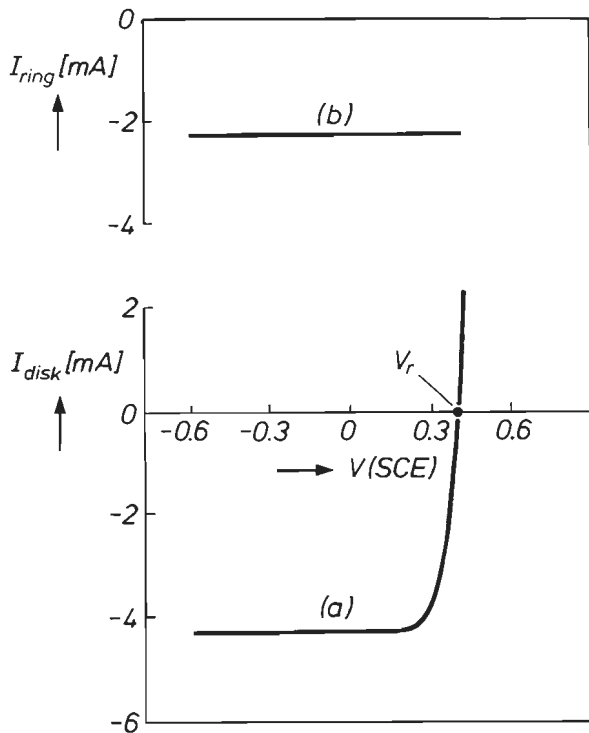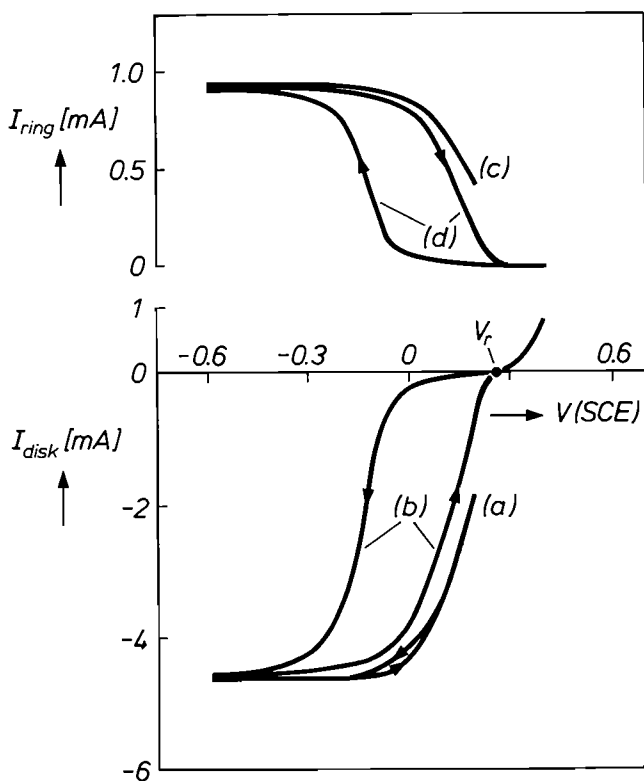**Fig. 5.3.** Current-potential curves for a Pt/p-GaAs RRDE (5000 rpm) in 0.05 M Fe^{3+}, 0.5 M H_2SO_4 solution in the dark at 50 mV·s^{-1}. Curves (a) and (b) show the disk current for two different limits of the anodic scan. Curves (c) and (d) refer to the corresponding ring current measured in the collection mode under potentiostatic control ($+1.10$ V). V_r represents the open-circuit potential.
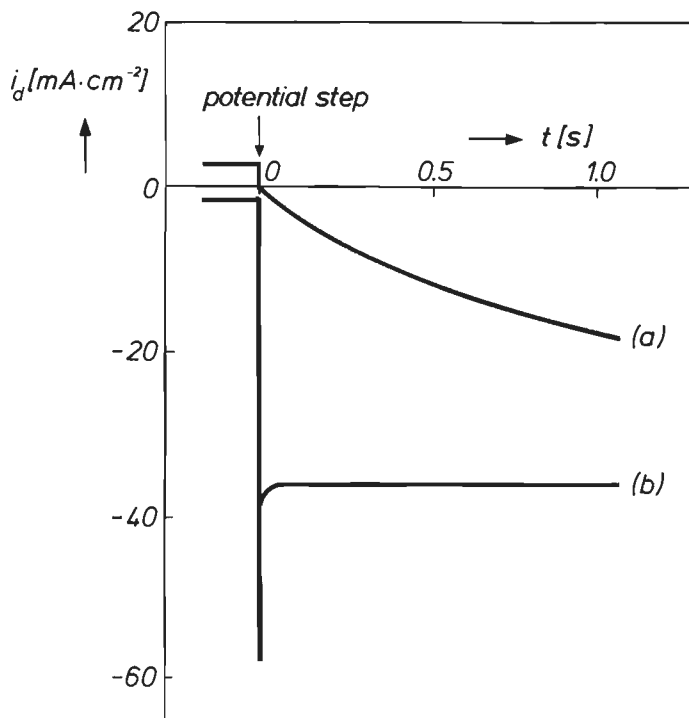
Fig. 5.4. Potential step measurements for a p-GaAs RDE (5000 rpm) in the dark in 0.05 M Fe^{3+}, 0.5 M H_2SO_4 solution. At $t = 0$, the potential was decreased to a V_c value of -0.30 V from an anodic value of $V_a = +0.40$ V (curve (a)) and from $V_a = +0.20$ V (curve (b)).

shown in Fig. 5.4 refer again to the Fe^{3+} system in 0.5 M H_2SO_4. The reduction current measured at -0.30 V ($t \geq 0$), after a 1 min. prepolarization at $+0.40$ V, is initially very low (curve (a)), but increases to a steady-state value of 36 mA·cm^{-2} within approximately 60 s. From curve (b) it is clear that the initial cathodic current at -0.30 V is much higher when the anodic potential V_a is made more negative ($+0.20$ V in this case). This is further illustrated in Fig. 5.5 which shows that the cathodic current at $t = 0$ ($i_d^c(t = 0)$) increases significantly as V_a is decreased. The current spike in curve (b) of Fig. 5.4 confirms that the reduction rate of Fe^{3+} ions at $+0.20$ V is lower than the mass-transport limited value (see Fig. 5.4). The enhanced reduction current at $t = 0$ results from a higher surface concentration of the oxidizing agent at the moment the potential step is applied. The subsequent decrease to the steady-state value is due to depletion of electroactive species at the electrode surface. In contrast, a current spike is
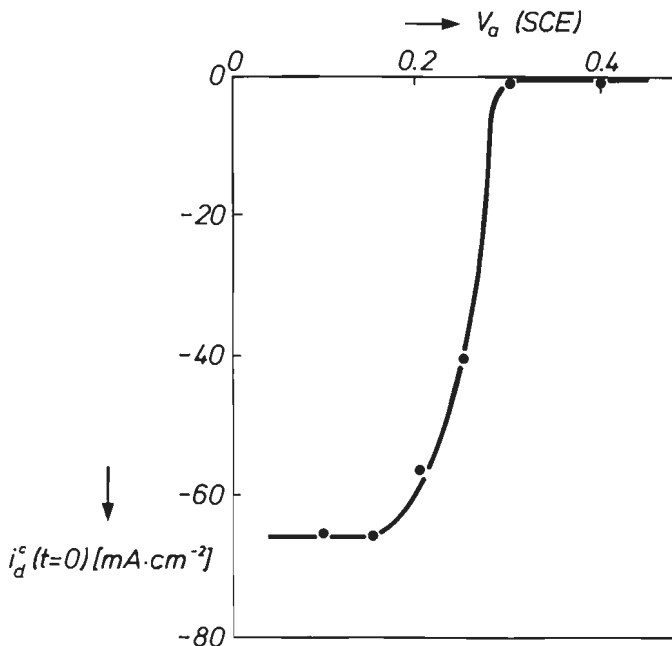
Fig. 5.5. The cathodic dark current density (i_d^c), recorded at $t = 0$ after application of a potential step to $V_c = -0.30$ V, as a function of initial anodic potential V_a. The experimental conditions were the same as in Fig. 5.4.

not found in similar step measurements with the Ce^{4+} ($pH = 0$) or $Fe(CN)_6^{3-}$ ($pH = 14$) systems. A steady-state involving mass-transport limited reduction of the oxidizing agent exists at all values of the anodic potential prior to application of the potential step.

Results, similar to those shown for the Fe^{3+}/H_2SO_4 system in Figs. 5.3 - 5.5 were found for all B-group oxidizing agents. General trends, expected on the basis of the $V_{fb}^o(p)$ and $V_{ox/red}^o$ values, are observed with these systems. At $pH = 5$, for example, both the initial and the steady-state cathodic currents, measured after potential step application (see Fig. 5.4), increase as the standard redox potential becomes more positive (see Table III), i.e. in the sequence:

$$Fe(CN)_6^{3-} > Fe^{III}(EDTA) > Fe^{III}(Oxa). \tag{5.1}$$
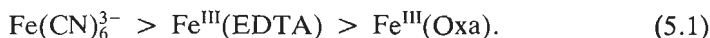
This results from a better overlap of D_{ox} with the valence band. For a given oxidizing agent, an increase in pH gives rise to relatively higher cathodic currents, as $V_{fb}^o(p)$ and consequently the position of the valence band-edge

is shifted upward by 60 mV per unit increase in pH, i.e. ($V^o_{ox/red} - V^o_{fb}(p)$) becomes more positive. Somewhat exceptional behaviour is observed with $FeCl_3$ in 1 M HCl solution. Although the standard redox potential should be similar to that in H_2SO_4, the steady-state reduction currents found in HCl solution are substantially lower than those shown in Fig. 5.4 and recovery of the current after the potential step was slower. This is probably due to specific adsorption of Cl^- ions at the electrode surface which results in a better stabilization of the positively charged dissolution intermediates. A similar effect was discussed before in section 4.3 for the impedance relaxation after anodic prepolarization of a p-GaAs electrode in HCl solutions without oxidizing agent. As expected from the data of Table III, reduction via hole injection from B-group systems is most favourable in the case of Fe^{3+} at $pH = 1.5$. However, despite the differences in the absolute magnitude of the cathodic current for these different redox systems, in all cases prepolarization of the electrode at potentials close to $V^o_{fb}(p)$ was found to inhibit the hole injection rate at more negative potentials.

It should be emphasized that in the above experiments care was taken to avoid high anodic potentials which might lead to excessively high dissolution rates and film formation on the electrode. This is especially important for $Fe(CN)^{3-}_6$ solutions at lower pH in which mixed ferri/ferrocyanide solid films can be formed [7] and in EDTA containing solutions in which oxide formation can occur at higher current densities, as described in the previous chapter.

Influence of illumination on the reaction rates

From the results in the dark described so far, it can be concluded that prepolarization of p-GaAs at anodic potentials inhibited the rate of hole injection from B-group oxidizing agents. Illumination of the electrode was found to counteract this effect, enhancing the reduced cathodic current in all cases. Although some hysteresis in the cyclic voltammetric curves similar to the dark case is still observed, illumination decreases considerably the 'overpotential' for reduction of Fe^{3+} species. In the sub-limiting current range, higher cathodic currents are observed during exposure. Since it is difficult to distinguish between photo-effects and dark-effects using cyclic voltammetry, potentiostatic transient current measurements were made to investigate the role of light. The cathodic potentials chosen for these measurements were such that hydrogen evolution during illumination was negligible.

Fig. 5.6 shows the effect of illumination on the reduction of Fe^{3+} ions in 0.5 M H_2SO_4. In each case the electrode was held at +0.40 V for 1 minute prior to stepping to a potential of -0.30 V at $t = 0$. The increase in

cathodic current with time in the dark is shown as a dashed reference curve
in each case. The difference in time scale in the four figures (5.6.A - 5.6.D)
should be noted. The change in the current transients caused by switching
on the light (first arrow) after a short dark period at the cathodic potential
is shown in the solid lines. The exposure time was increased from 20 ms to
20 s, as shown. The considerable increase in cathodic current, resulting from
illumination, can be separated into two parts: a photocurrent which decays
rapidly when the light is switched off (second arrow) and a 'dark' current
component whose magnitude depends on the previous period of exposure.
When this background dark current is large, the corresponding photocurrent
is small (compare 20 ms and 20 s exposures). Experiments with the RRDE
using a chopped light source at longer times showed clearly that both the
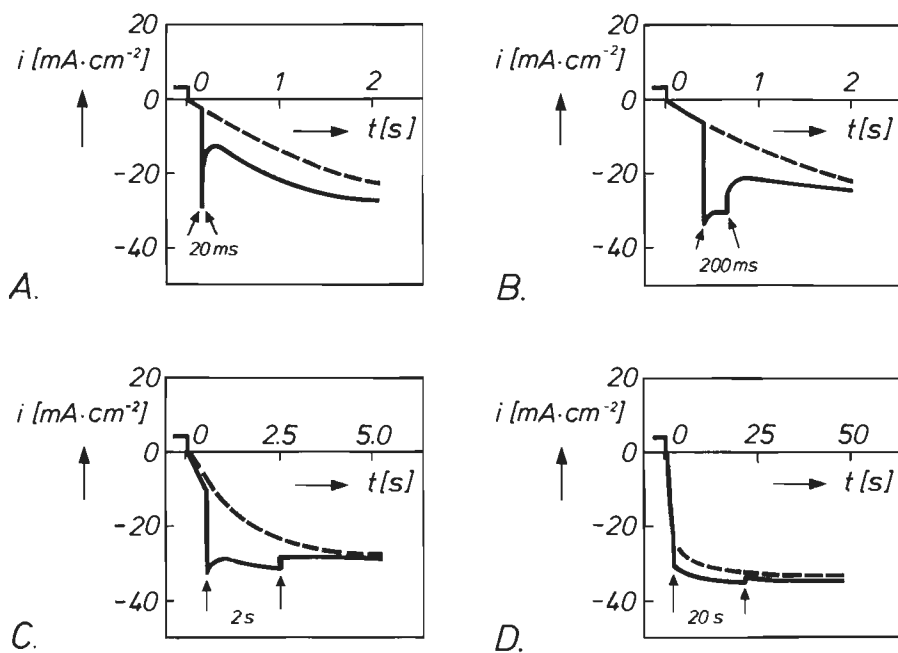
Fig. 5.6. Current transients for a p-GaAs RDE (5000 rpm) in 0.05 M Fe^{3+},
0.5 M H_2SO_4 solution. At $t = 0$, the potential was stepped from +0.40 to −0.30 V.
The dashed lines show the subsequent increase of the cathodic current in the dark.
The solid lines show the influence of illumination. After a short period in the dark
at −0.30 V, the light was switched on (first arrow) for a fixed period and then
switched off (second arrow). Photon density ϕ = 25 a.u. (He-Ne laser). The expo-
sure periods used were: A) 20 ms; B) 200 ms; C) 2 s; D) 20 s.

enhanced dark current after illumination and the (total) current during il-
lumination must be attributed to reduction of Fe^{3+} species.

The effect of very short illumination periods on the current transients for
$Fe(CN)_6^{3-}$ reduction at $pH = 4$ is shown in Fig. 5.7. In this case the elec-
trode was held for 1 min. at 0.00 V before the potential was changed to
-0.60 V. After anodic prepolarization, the dark current at the cathodic po-
tential is low and increases with time. In the very short time scale of Fig. 5.7
this dark current, which is shown again as a dashed line, is essentially con-
stant. When the light was switched on (at $t = 0$), the cathodic current rose
sharply (photocurrent component) and then continued to rise more slowly
(contribution of the enhanced dark current). When the light was switched
off, an abrupt decrease in current was observed, after which the current re-
mained relatively constant. The rise and decay times of the photocurrent
shown in Fig. 5.7 were determined by the shutter speed. The photocurrent,
measured as the abrupt drop in the cathodic current on terminating expo-
sure, decreases somewhat with increasing exposure time and the values are
always smaller than that measured from the sharp current rise at the start
of illumination. Saturation of the dark current is achieved after an exposure
time of approximately 20 ms for the case shown in Fig. 5.7. At lower light
intensities a longer exposure time is required to 'saturate' the dark current.

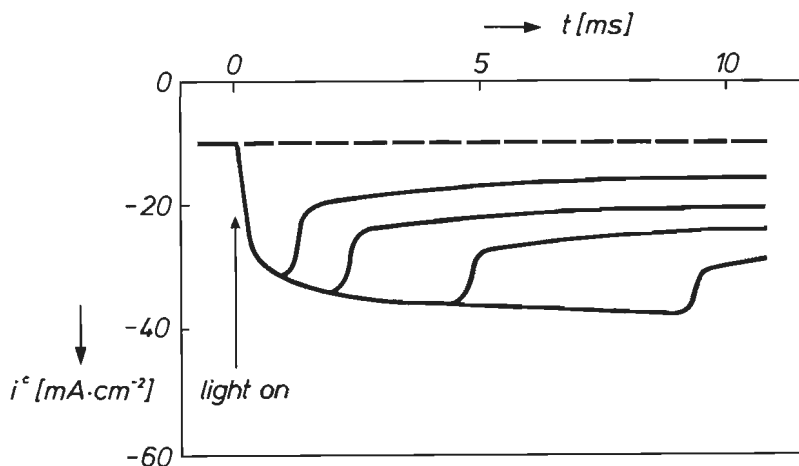**Fig. 5.7.** Current transients for a p-GaAs RDE (5000 rpm) in a 0.05 M $Fe(CN)_6^{3-}$
solution of $pH = 4$. In all cases the potential was held at 0.00 V for 1 min. and then
stepped to -0.60 V. The cathodic dark current at this potential is shown at $t < 0$.
At $t = 0$, the electrode was illuminated ($\phi = 20$ a.u.) for four different periods be-
fore the light was switched off (He-Ne laser).

Etching results

As an example of an etchant based on an A-group oxidizing agent, a
0.1 M $Fe(CN)_6^{3-}$ solution of $pH = 14$ was used (Table III). A GaAs(001)
crystal was partly covered with a photoresist layer and was etched at the
open-circuit potential in this solution for 5 minutes in the dark. The etch
depth was examined with an interferometer after removal of the resist layer.
The etch depth was strongly enhanced near the resist edge. This characteris-
tic shape will be discussed in chapter 8. A uniform etch depth was obtained
further away from the masked edge. A macroscopic etch rate of approxi-
mately 1.3 $nm·s^{-1}$ was found in this region.

On the other hand, the etch rate of GaAs crystals in solutions containing
B-group oxidizing agents was so low that much longer etching times had to
be used in order to obtain significant etch depths. As an example of a B-
group system a 0.05 M Fe^{3+} solution of 0.5 M H_2SO_4 (see Table III) was
used. After etching for 2 hours in the dark an etch depth of 250 nm was
found; this corresponds to a macroscopic etch rate of 0.035 $nm·s^{-1}$. The etch
rate of GaAs in a 0.05 M $Fe^{III}(EDTA)$ solution of $pH = 5$, also a B-group
redox system (Table III), is much lower, viz. 0.003 $nm·s^{-1}$. In contrast to
A-group etchants the etch depth for B-group etchants is uniform, i.e. the
etch rate is not enhanced near the resist edge.

5.2.3. Discussion

As concluded in section 4.3.4, anodic prepolarization causes a change in
the Helmholtz potential which was attributed to intermediates in the disso-
lution reaction. This change corresponds to a downwards displacement of
the semiconductor band-edges at the surface (see dashed lines in Fig. 5.1)
and is therefore consistent with the reduced rate of hole injection from B-
group oxidizing agents in the dark (Figs. 5.3 and 5.4). The increase in δV_{fb}
with increasing anodic potential observed in Fig. 4.11 of chapter 4 explains
the corresponding decrease in the cathodic dark current, measured after ap-
plication of the potential step (Fig. 5.5). The resemblance between these two
figures is very close. Both effects, the changes in the electrode capacitance
(Fig. 4.11) and hole injection rate (Fig. 5.5) point to the localization of posi-
tive charge at the electrode surface [8,9] which can be attributed to the dis-
solution of GaAs. The relaxation time of the semiconductor band-edges in
the dark after anodic prepolarization as observed with impedance measure-
ments in Fig. 4.10 is in good agreement with that obtained from the current
transient measurements (Fig. 5.4). With both independent methods a relax-
ation time of approximately 60 s is found in Fe^{3+}/H_2SO_4 solution.

Two effects are found on illuminating the p-GaAs electrode at cathodic potentials (Figs. 5.6 and 5.7). In the first place, a photocurrent due to reduction of the oxidizing agent is observed, despite the fact that the standard potentials of the redox systems used here are close to the valence band of the semiconductor. Kelly and Memming [10] have reported similar effects with p-type III-V electrodes and suggested that, in certain cases, reduction occurs by a surface state mechanism as well as a conduction band mechanism; electrons created by light can be transferred via surface states in the band-gap to the oxidizing agent in solution. This mechanism will be discussed in more detail in section 5.5. In addition to the photocurrent, illumination increases the rate at which holes are injected into the valence band; this enhanced dark current is obvious when the light is switched off. Continuing the line of reasoning above, the influence of light on the dark cathodic current can be ascribed to the discharge by photo-electrons of positive charge localized at the surface during anodic prepolarization. Before this explanation is justified, however, two other possibilities should be discussed;

(i) Inhibition of the cathodic current in the dark might be due to oxide-formation at anodic potentials, while the effect of illumination could be attributed to oxide reduction by means of photo-electrons. This seems unlikely for three reasons:

  – the photoeffect is quite pronounced, not only at $pH = 4$ and 5 but also in H_2SO_4 and HCl solutions after anodic polarization at potentials $(V < V_{fb}^o)$ at which GaAs dissolution is negligible. Under these conditions oxide formation should be very limited (see section 4.2);

  – redox systems showing a good overlap with the valence band give high cathodic currents, limited only by mass-transport in solution (Fig. 5.2);

  – very low values of the absorbed photon density are sufficient to raise the hole injection rate markedly. For example, an exposure of approximately 1 ms doubled the dark cathodic current of Fig. 5.7. If the photocurrent in this case is attributed completely to oxide reduction, then the charge involved corresponds to approximately 0.02 of an monolayer which cannot account for the significant increase of the dark current. Similar results are found with other redox systems.

(ii) In the work cited above on a photocurrent process via a surface state mechanism, electron trapping at the surface accompanied by an upward displacement of the band-edges during illumination was proposed [10]. Such an effect would, of course, improve the position of the D_{ox} function with respect to the VB (Fig. 5.1.B) and consequently favour hole injection. Again a number of indications suggest that this is not the primary effect of light:

- the fraction of surface states, occupied by electrons, only becomes considerable when surface recombination can be disregarded. This occurs in the potential range in which hydrogen begins to be evolved under influence of light [10], i.e. at potentials more negative than those used here;
- since B-group oxidizing agents can very likely scavenge electrons trapped in surface states (thus giving photocurrent) [10], the occupancy of such states with electrons should be even lower than in an indifferent electrolyte. It will be shown that this mechanism is realistic and indeed occurs during the reduction of hypochlorite at p-GaAs under illumination in a following section;
- if trapped electrons can react with the oxidizing agent in solution or recombine with holes, then a fast decay of the enhanced hole injection rate would be expected. This is not the case.

For these reasons it is clear that electron trapping at the surface can be disregarded in the present discussion.

It seems likely therefore that the main effect of photo-electrons is the reduction of positively charged surface states (eqs. (4.4)-(4.7)) formed during anodic prepolarization. This results in an upwards shift of the semiconductor band-edges to their original position (solid lines of Fig. 5.1).

An indication of the effect of a change in the Helmholtz potential on the kinetics of hole injection can be obtained by considering the energy-dependence of the distribution function D_{ox} of the redox system given in eq. (2.18) of chapter 2. The rate constant for the reduction reaction is determined by the magnitude of the overlap of this function and the VB of the semiconductor and is expressed by the integral of eq. (2.27). However, since the D_{ox} function is an exponential function of E, the rate constant will be mainly determined by the magnitude of this function at $E = E_v$, the valence band-edge. According to eq. (2.18) this depends on the reorientation energy λ and on the standard potential of the redox system. As an example of a B-group agent, we take Fe^{3+} at $pH = 0$ with a $\lambda = 1.15$ eV [1]. A downward displacement of the band-edges amounting to $0.05 - 0.15$ eV decreases D_{ox} (at $E = E_v$) by a factor of between 2 and 15. This would account for the considerable decrease in the hole injection rate. In section 4.3 it was calculated that such a change in the Helmholtz potential corresponds to a positive charge density of approximately 10^{13} cm^{-2}.

An analogous effect on the kinetics of redox reactions at an n-GaAs electrode has been reported [3,5]. Reduction of similar B-group oxidizing agents in the dark was observed by RRDE measurements in the potential range before photoanodic dissolution. However, at potentials more positive than

the value for anodic photocurrent onset, the rate of reduction of the oxidizing agent in the dark decreases abruptly. As in the present case with p-GaAs, it was found that A-group oxidizing agents do not show this effect. The mass-transport limited reduction rate is maintained to high positive potentials. Electroluminescence measurements lead Decker et al. [5] to conclude that reduction of Ce^{4+} (an A-group agent) at n-GaAs occurs by hole injection into the valence band of GaAs. This is in agreement with the present results at p-GaAs in the dark (Fig. 5.2). However, for the reduction of Fe^{3+} in H_2SO_4 solution, Decker suggests that reduction of Fe^{3+} proceeds via conduction band electrons and that hole injection only becomes important when the formation of an accumulation layer near the flat-band potential gives an upward shift of the band-edges. Our results show that injection from Fe^{3+} ions can occur at a significant rate on p-GaAs in the dark. In this case a conduction band process is excluded. Reduction of the oxidizing agent becomes inhibited at potentials approaching the value (V_{fb}^{o}) at which the electrode begins to dissolve. These results show that hole injection at n-GaAs should also be possible and that the decrease in the reduction current at potentials near the photocurrent-onset value must be attributed to changes in the Helmholtz layer. In recent work Schröder and Memming [11] clearly showed by means of recombination resistance measurements, that reduction of Fe^{3+} at n-GaAs in H_2SO_4 solutions is indeed a valence band process.

Macroscopic etching

From the electrochemical results it is clear that the dark etch rate of GaAs at open-circuit potential (V_r) in solutions containing A-group oxidizing agents should differ considerably from that found in B-group etchants (see V_r in Figs. 5.2 and 5.3, respectively, and the corresponding ring response at V_r). The etching experiments indeed confirm these electrochemical measurements. According to eq. (2.39) the electroless etch rate (v_e) in these etchants can be calculated when the hole injection rate ($i_{vb}^{c} = i^{-}$) at the rest potential is known. Since for A-group oxidizing agents the hole injection rate is diffusion-controlled and is independent of the applied electrode potential (see ring response of Fig. 5.2), i_{vb}^{c} obtained at cathodic potentials can be used for this calculation. However, i_{vb}^{c} was not found to be very stable under diffusion-controlled conditions at a stationary GaAs electrode and ranges from 2 to 4 mA·cm^{-2} in a 0.1 M $Fe(CN)_6^{3-}$ solution of $pH = 14$. These fluctuations are due to the fact that the diffusion layer thickness near a stationary electrode is sensitive to solution agitation (see also section 2.7). Taking $i_{vb}^{c} = 3$ mA·cm^{-2} as an average diffusion-controlled hole injection rate at the

rest potential, then according to eq. (2.39), an etch rate of 1.4 nm·s^{-1} is cal-
culated which is in good agreement with the value obtained from the etching
experiments (1.3 nm·s^{-1}). It is concluded that the etch rate of GaAs in so-
lutions containing A-group oxidizing agents is controlled by transport of the
oxidizing agent and that shifts of the semiconductor band-edges do not in-
fluence the etching kinetics of GaAs. The enhanced etch rate near the resist
edge confirms this conclusion (see Fig. 8.5).

On the other hand, very low etch rates are found with B-group redox sys-
tems. In 0.05 M Fe^{3+} solution of pH = 0 the etch rate is 0.035 nm·s^{-1} and
this value is much lower than that expected on the basis of the diffusion-
controlled hole injection rate at cathodic potentials. This agrees with the ob-
servation that during electroless dissolution at V_r the semiconductor band-
edges are shifted downwards, thereby inhibiting the hole injection rate. As
a result, the etch rate becomes kinetically controlled in the steady-state. It
is obvious that in this case the cathodic current measured at the disk elec-
trode at negative potentials cannot be used to calculate the etch rate at V_r.
The even lower etch rate in Fe^{III}(EDTA) solution is in agreement with the
poorer overlap of the valence band and the D_{ox} function of Fe^{III}(EDTA)
(see Table III).

5.2.4. Conclusions

A redistribution of the potential between the Helmholtz and space-charge
layers of a GaAs electrode explains the effect of anodic polarization on the
rate of hole injection from oxidizing agents in solution. It is shown that the
resulting downward displacement of the semiconductor band-edges which
has also been observed independently in impedance measurements (sec-
tion 4.3), is related to the mechanism of oxidative dissolution. Results of il-
lumination experiments involving very low photon densities indicate that
ion-radical intermediates which are formed due to hole trapping at the elec-
trode surface at anodic potentials can be reduced by photo-electrons. As a
result, the semiconductor band-edges rapidly shift back to their original dark
positions, thereby increasing significantly the reduction rate at cathodic po-
tentials.

These results have obvious consequences for electroless dissolution of
GaAs in the dark, a reaction requiring valence band reduction of the oxidiz-
ing agent. Hole injection from redox systems, whose standard potential is
close to the valence band-edge of p-GaAs, is kinetically inhibited at poten-
tials near the flat-band value. Because overlap of the D_{ox} function and the
valence band of the solid is critical, the formation of an oxidized surface

with ion-radical type surface states, as represented in eqs. (4.4)-(4.7), re-
duces the rate of hole injection. In fact, this is a self-inhibiting mechanism:
during the initial stages of electroless etching of a GaAs crystal in these
electrolytes, the injected holes, supplied initially at a high rate by the oxidiz-
ing agent, are used to oxidize the GaAs surface; this results in a reduction
of the hole injection rate to low values. Systems with a more positive redox
potential do not show this effect. Here, the rate constants for hole injection
are so high that the diffusion limited reduction current is not affected by
changes in the Helmholtz layer.

5.3. Reduction of $Fe(CN)_6^{3-}$ in alkaline solutions

5.3.1. Introduction

In the previous section the electrochemistry at p-GaAs of the A-group
oxidizing agent $Fe(CN)_6^{3-}$ in a solution of $pH = 14$ was considered. Despite
the fact that the semiconductor band-edges are not fixed during the oxida-
tion of GaAs, no inhibition effects were noted and the hole injection rate
was found to be diffusion-controlled in the whole potential range (Fig. 5.2).
In this case, oxide formation does not occur during dissolution (eq. (4.13)).

In section 4.2 it has been shown that in alkaline solutions in the pH range
11-14, the maximum rate at which GaAs can be anodically dissolved de-
pends on the OH^- concentration in solution. When, in the initial stages of
the anodization process, the maximum dissolution rate is exceeded, oxide
formation occurs (eq. (4.14)). This limited dissolution rate should also influ-
ence the hole injection rate of $Fe(CN)_6^{3-}$ at positive potentials, certainly
when is taken into account that the shift of the semiconductor band-edges
can be very pronounced under oxide-forming conditions (section 4.4). In the
present section we will therefore compare two limiting cases, in which the
initial rate of hole injection is either higher or lower than the rate of hole
consumption for the dissolution reaction. These effects were studied at both
p- and n-type RRDEs using cyclic voltammetry and current transient mea-
surements. The influence of the photoanodic dissolution of n-GaAs on the
hole injection kinetics was also investigated.

It was shown in section 4.4 that positive charge, trapped at the semicon-
ductor/oxide interface during the oxidation of GaAs, results in a large
change in the position of the semiconductor band-edges. Therefore, impe-
dance measurements were essential to determine the position of the band-
edges and to obtain information about the charge distribution at the inter-

face for the two limiting cases. These measurements were made at n-type RDEs since with this semiconductor type the dissolution of GaAs takes place in the depletion potential range, thus allowing steady-state impedance measurements to be employed.

The importance of oxide formation in determining the morphology of the etched semiconductor surface was noted in the previous chapter. Smooth surfaces are obtained after (photo)anodic dissolution under oxide-forming conditions, while defects can be revealed under oxide-free conditions. Since these two limiting cases can also be distinguished during electroless etching of GaAs in the present $Fe(CN)_6^{3-}$ solutions, it is likely that the morphology of the etched surface can also be influenced by means of the solution composition. This has been investigated.

5.3.2. Results

p-GaAs

The reduction of $Fe(CN)_6^{3-}$ was studied at a Pt/p-GaAs RRDE. The $Fe(CN)_6^{4-}$ produced at the GaAs electrode was oxidized at the Pt-ring. The results are shown in Fig. 5.8 for the case in which the hole injection rate exceeds the maximum dissolution rate, i.e. $|i_{vb}^c| > i_{max}^a$. This is the case for a 0.5 M $Fe(CN)_6^{3-}$ solution of $pH = 13$. In the current-potential curve of the disk electrode (curve (a) of Fig. 5.8) three plateaus can be distinguished. At negative potentials corresponding to the first plateau, which will be denoted by I, the cathodic current is directly proportional to the $Fe(CN)_6^{3-}$ concentration and to the square root of the electrode rotation rate. This shows that $Fe(CN)_6^{3-}$ reduction is diffusion-controlled. From the anodic current at the Pt-ring in this potential range a collection factor of 0.23 is calculated, in agreement with the theoretical value (see chapter 3). Since the D_{ox} function of $Fe(CN)_6^{3-}$ overlaps very well with the valence band of GaAs in alkaline solutions (Table III), hole injection into the valence band occurs, as discussed in section 5.2. Moreover, recombination resistance measurements proved this to be the case (see Fig. 5.17) [2]. At a potential of about -0.65 V the cathodic current at the disk electrode decreases to give a second plateau (II) which extends over a small potential range. The anodic current at the Pt-ring, however, remains unchanged in this potential range. This must mean that the reduction of $Fe(CN)_6^{3-}$ at the GaAs electrode is unchanged and is still diffusion-controlled. After the second disk plateau at a potential of approximately -0.30 V the oxidation of $Fe(CN)_6^{3-}$ at the ring begins to decrease and becomes very low at more positive potentials, i.e.
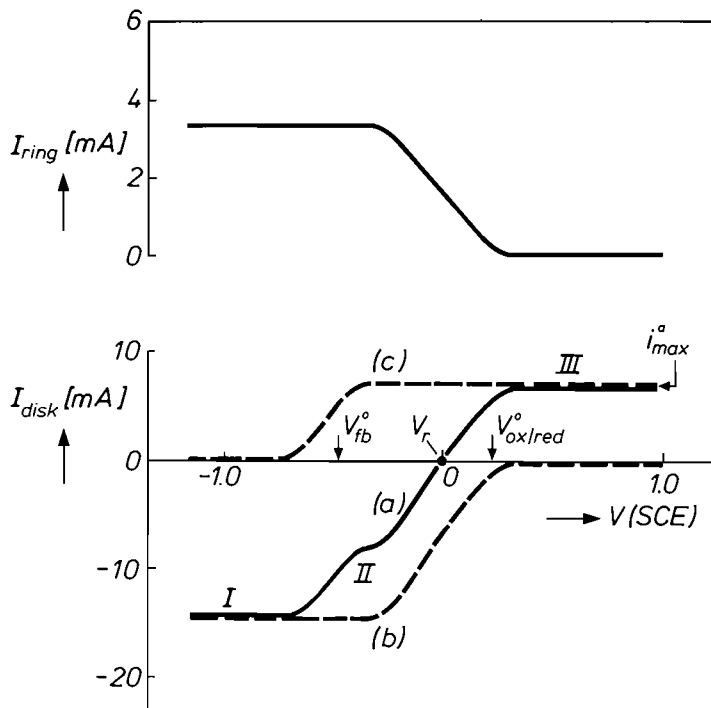
Fig. 5.8. Current-potential curves for a Pt/p-GaAs RRDE (500 rpm) in the dark in a 0.5 M $Fe(CN)_6^{3-}$ solution of $pH = 13$ at 20 mV·s^{-1}. The solid line of curve (a) shows the measured current density at the disk and the dashed lines of curves (b) and (c) the partial reduction current density of $Fe(CN)_6^{3-}$ and the partial oxidation current density of GaAs, respectively. The ring response was measured in the collection mode under potentiostatic control (+0.60 V). The three current plateaus in curve (a) at the GaAs disk are indicated by I, II and III.

the reduction of $Fe(CN)_6^{3-}$ at the GaAs electrode stops. At potentials positive with respect to V_{fb}^o, majority carriers accumulate at the electrode surface. This leads to a considerable increase in the space-charge capacitance (see Fig. 2.3). The semiconductor becomes degenerate and shows 'metallic' behaviour (see section 2.2) [1]. Consequently, the reduction of $Fe(CN)_6^{3-}$ is observed up to a potential corresponding to the redox potential of the $Fe(CN)_6^{3-/4-}$ couple as the ring current of Fig. 5.8 shows. The formation of an oxide film which starts at the second current plateau may contribute to some extent to the decrease of the disk current at −0.30 V. We will return

to this point later in the discussion. The partial reduction curve of $Fe(CN)_6^{3-}$ at the GaAs disk can be obtained by dividing the ring current by the collection factor. This partial reduction curve is shown as a dashed line in Fig. 5.8, curve (b). By taking into account the anodic curve for GaAs in solutions without $Fe(CN)_6^{3-}$ studied in Fig. 4.2, the shape of the measured current-potential curve (a) of Fig. 5.8 with its three plateaus can be explained. In addition, flow-cell measurements (chapter 3) in the same solution as that used for Fig. 5.8 are in full agreement with the partial anodic dissolution current of curve (c). Both the second (II) and third (III) plateaus in Fig. 5.8 are determined by the diffusion-controlled maximum dissolution rate of GaAs (i_{max}^a); the anodic current of plateau III must be equal to the difference in current of plateau I and plateau II. This is in good agreement with the result of Fig. 5.8. In this case the hole injection rate is larger than i_{max}^a and consequently a cathodic current is observed in plateau II. For the other case, when the hole injection rate is lower than i_{max}^a, plateau II is anodic (see Fig. 8.17). Such a current-potential curve would also be expected for GaAs in 0.1 M $Fe(CN)_6^{3-}$ solution of $pH = 14$ reported in the previous section. However, it was not practical to study this phenomenon because the limiting anodic current density in a $pH = 14$ solution is extremely large at an electrode rotation rate of 5000 rpm ($i_{max}^a > 500$ mA·cm^{-2}; see section 4.2).

The dependence of i_{max}^a on the pH of the solution containing $Fe(CN)_6^{3-}$ was the same as that observed in Fig. 4.3 for NaOH solutions. However, it should be noted that the magnitude of i_{max}^a in solutions containing $Fe(CN)_6^{3-}$ is lower than in NaOH solutions. The line has the same unit slope as that in Fig. 4.3, but is shifted to lower dissolution rates. This effect was observed under diverse experimental conditions and at both p-type and n-type electrodes. The difference in the limiting anodic currents for the two electrolytes, with and without $Fe(CN)_6^{3-}$, at a given pH changes somewhat as a function of the $Fe(CN)_6^{3-}$ concentration. Possibly, adsorption may play a role here [7].

Since i_{max}^a is exceeded at positive potentials (at the current plateau III of curve (c) of Fig. 5.8), it is very likely that in this case an oxide film is also formed at the electrode surface. In order to confirm this and to get an estimate of the oxide layer thickness, potential step measurements were performed. An example of the resulting current transient is shown in Fig. 5.9 for a rotating p-GaAs electrode (500 rpm) in a 0.5 M $Fe(CN)_6^{3-}$ solution of $pH = 11.5$. The reduction of $Fe(CN)_6^{3-}$ was used to indicate when the original steady-state at cathodic potentials was reached after anodic prepolarization. In the example of Fig. 5.9 the p-GaAs electrode was polarized for 100 s at a potential of +0.50 V. During this anodization time a steady-state
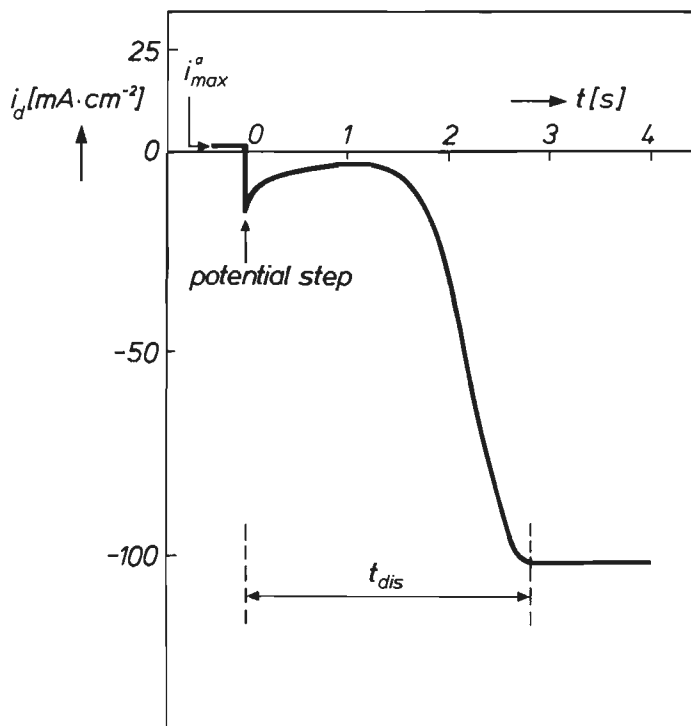
Fig. 5.9. Current transient for a p-GaAs RDE (500 rpm) in the dark in a 0.5 M $Fe(CN)_6^{3-}$ solution of $pH = 11.5$. After a prepolarization time of 100 s at $V_a = +0.50$ V ($t < 0$), the potential was stepped at $t = 0$ to $V_c = -1.20$ V. The time to dissolve the oxide layer is indicated (t_{dis}).

anodic current density of $+0.4$ mA·cm^{-2} was established after an initial period (see Fig. 5.9 at $t < 0$), which clearly depended on the electrode rotation rate. The anodic current density is only determined by the dissolution reaction of p-GaAs because reduction of $Fe(CN)_6^{3-}$ at p-GaAs does not occur at this potential, as the ring current of Fig. 5.8 reveals. At $t = 0$ the potential was stepped to a cathodic potential of -1.20 V at which the anodic dissolution of p-GaAs has stopped (curve (c) of Fig. 5.8) and the reduction of $Fe(CN)_6^{3-}$ should, in principle, be diffusion-controlled (curve (b) of Fig. 5.8). However, from the current transient of Fig. 5.9 it is obvious that the reduction of $Fe(CN)_6^{3-}$ is clearly inhibited. After approximately 1.5 s the reduction rate increases rapidly to reach a constant value at 2.8 s. The constant reduction current density at -1.20 V is then controlled by diffusion of

$Fe(CN)_6^{3-}$ in solution, in agreement with that found in Fig. 5.8 when the electrode area is taken into account. The induction time at cathodic potentials depends significantly on the electrode rotation rate. When the electrode rotation rate is increased the time needed to reach the cathodic diffusion plateau decreases. In the extreme case of a stationary electrode in a solution of $pH = 11.5$ an induction time of about 25 s was required before the diffusion-limited reduction current density was reached. It should be noted that the shape of current transients such as that shown in Fig. 5.9 is essentially different from that described in the previous section (compare with curve (a) in Fig. 5.4).

The current transient behaviour of p-GaAs at both anodic and cathodic potentials points to the formation of an oxide film during anodic polarization and the dissolution of this film at cathodic potentials. The oxide layer hinders hole injection by $Fe(CN)_6^{3-}$. Only when the oxide layer thickness is reduced, does the reduction rate of $Fe(CN)_6^{3-}$ increase. In a manner similar to that described in section 4.2, a steady-state film thickness can be obtained from i_{max}^a and the time (t_{dis}) needed to dissolve the oxide film (see Fig. 5.9). Oxide layer thicknesses in the range of 0.5 - 1.0 nm were found in all cases. Since it has been shown in section 4.2 that the rate of anodic dissolution of GaAs under oxide-forming conditions (i_{max}^a) is determined by diffusion of OH^- ions in solution, it is obvious that the electrode rotation rate influences the rate at which the oxide dissolves in the electrolyte. Consequently, it is understandable that the dissolution time of the oxide for a stationary electrode is large ($t_{dis} \approx 25$ s) because i_{max}^a is very low in a solution of $pH = 11.5$ ($i_{max}^a = 0.05$ mA·cm^{-2} at 0 rpm). As a result, the pH of the solution should also influence t_{dis}. Indeed, a much lower value of $t_{dis} \approx 0.5$ s was found with a stationary electrode in a 0.5 M $Fe(CN)_6^{3-}$ solution of $pH = 13$.

n-GaAs

In Fig. 5.10 the current-potential curves measured in the dark and under illumination are shown for an n-type RRDE in 0.1 M $Fe(CN)_6^{3-}$ solution of $pH = 13$. The rotation rate of the electrode was 500 rpm in all cases. At the cathodic current plateau the reduction of $Fe(CN)_6^{3-}$ at the GaAs electrode is diffusion-controlled; the Levich equation (2.42) is obeyed in this potential range and the measured collection factor is close to the theoretical value. In the dark (curve (a)), the cathodic disk current decreases to a very low value measured several hundred millivolts positive with respect to the flat-band potential, while hole injection by $Fe(CN)_6^{3-}$ is not changed in the entire potential range (see Pt-ring response, curve (a)). The holes are used in this positive potential range to dissolve the GaAs electrode, i.e. the hole
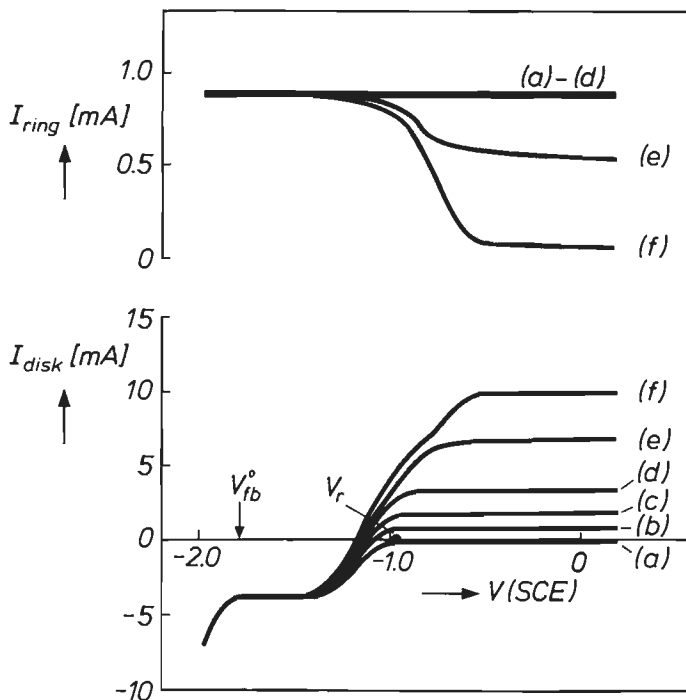
Fig. 5.10. Current-potential curves for an Pt/n-GaAs RRDE (500 rpm) in a 0.1 M $Fe(CN)_6^{3-}$ solution of $pH = 13$ at 20 $mV \cdot s^{-1}$. The (a) curves show the disk voltammogram and the ring response in the dark. Curves (b)-(f) show the voltammograms under illumination (Schott lamp) with increasing light intensity. The Pt-ring response was measured in the collection mode under potentiostatic control (+0.60 V). The open-circuit potential measured in the dark is indicated by V_r.

injection rate (i_{vb}^c) is equal to the dissolution rate in the dark (i_d^a). The dissolution rate of GaAs is controlled by $Fe(CN)_6^{3-}$ diffusion and is not limited by the OH^- concentration in the electrolyte; in other words, the hole injection rate is smaller than i_{max}^a ($|i_{vb}^c| < i_{max}^a$). It should be noted, as discussed in section 2.5, that due to a extremely small anodic current at positive potentials, resulting from electron injection into the CB, a stable open-circuit potential is established in the dark (see V_r in curve (a) of Fig. 5.10). At potentials corresponding to the cathodic plateau, the injected holes recombine with conduction band electrons in the space-charge layer. At potentials negative with respect to the flat-band potential hydrogen is, of course, evolved in addition to the $Fe(CN)_6^{3-}$ reduction.

When the electrode is illuminated, an anodic photocurrent is observed at the n-GaAs disk at positive potentials. The anodic current depends linearly on the light intensity; only at the highest light intensity (curve (f)) is a deviation from this linear behaviour observed. Similar results were already discussed for the photoanodic dissolution of n-GaAs in alkaline solutions without $Fe(CN)_6^{3-}$ shown in Fig. 4.5 of section 4.2. At low intensities the hole injection rate of $Fe(CN)_6^{3-}$ is not changed over the whole potential range (see Pt-ring, curves (b) - (d)); the reduction is diffusion-controlled. At positive potentials the GaAs electrode is dissolved both by photogenerated holes and by holes injected from $Fe(CN)_6^{3-}$. At negative potentials the photogenerated holes recombine with conduction band electrons. The Pt-ring response at higher light intensities shows that the hole injection rate at negative potentials is still diffusion-controlled. At positive potentials, however, this hole injection rate decreases to a potential-independent value, which depends clearly on the light intensity. It becomes almost zero at the highest photon density (see ring current in curve (f)). This means that the hole injection rate is no longer diffusion-controlled but has become 'kinetically'-controlled. The transition between diffusion-controlled and kinetically-controlled reduction occurs in the potential range in which recombination is replaced by the inhibited dissolution of GaAs. When the total dissolution rate resulting from photoanodic dissolution (i_{hv}^a) and the hole injection from solution (i_{vb}^c) is lower than the maximum dissolution rate, the hole injection reaction is diffusion-controlled (curves (a) - (d)). In this case no oxide film is formed at the electrode surface. When the light intensity is so high that $i_{hv}^a + |i_{vb}^c|$ exceeds i_{max}^a, then the dissolution rate is determined both by the pH of the solution and the electrode rotation rate (curve (e)). It is very likely that under this condition oxide formation occurs at positive potentials, as found at p-GaAs in $Fe(CN)_6^{3-}$-containing solutions (Fig. 5.9). Since the photoanodic current is still directly proportional to the light intensity, it is obvious that the photodissolution dominates over hole injection in this potential range. This must result in a lower hole injection rate. The $Fe(CN)_6^{3-}$ reduction can therefore no longer be diffusion-controlled. At the highest light intensity, i_{hv}^a alone exceeds i_{max}^a. The anodic current is no longer proportional to the light intensity. This implies that the excess holes generated by light must recombine and that the hole injection rate must become very small, as the ring current in curve (f) shows.

In Fig. 5.11 the corresponding curves are given for a 0.5 M $Fe(CN)_6^{3-}$ solution of pH = 13. Again, at negative potentials (plateau I) the Levich equation is obeyed and the $Fe(CN)_6^{3-}$ reduction is diffusion-controlled. However, in this case the hole injection rate changes even in the dark from diffusion-
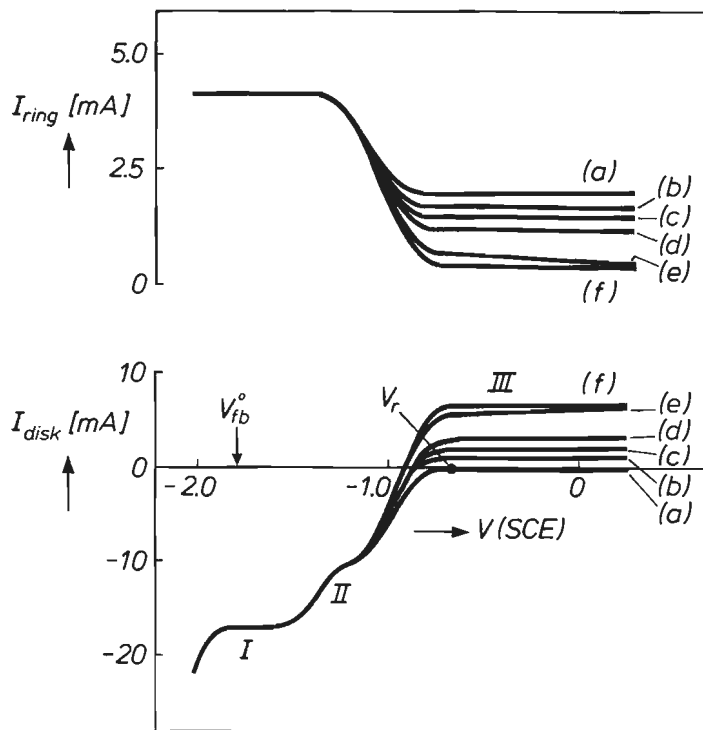
Fig. 5.11. The same experiment as in Fig. 5.10 in a 0.5 M $Fe(CN)_6^{3-}$ solution of $pH = 13$. The three current plateaus appearing at the GaAs disk in curve (f) are indicated by I, II and III.

control at cathodic potentials to kinetic-control in the anodic region as the ring response of curve (a) shows. From Fig. 5.8 it was clear that the reduction rate of p-GaAs in a 0.5 M $Fe(CN)_6^{3-}$ solution of $pH = 13$ exceeded i_{max}^a. It is therefore not surprising that reduction at n-GaAs at positive potentials in this solution becomes kinetically-controlled. In the potential range where the transition from diffusion-controlled to kinetic-controlled reduction takes place, the formation of an oxide layer starts which very likely inhibits the hole injection rate of $Fe(CN)_6^{3-}$. The injection rate in the anodic potential range decreases strongly as a function of the light intensity, even at low intensity. This effect is the same as that found for a 0.1 M $Fe(CN)_6^{3-}$ solution at higher light intensities. When the photoanodic dissolution rate exceeds i_{max}^a, the anodic dissolution at the disk reaches a limiting value (compare plateaus III of curves (e) and (f)). Consequently, the excess holes must

recombine and the hole injection rate becomes very small. Under this experimental condition it is striking that recombination occurs in the whole potential range even up to very positive potentials. A similar behaviour has been described during the photoanodic dissolution of n-GaAs under oxide-forming conditions in section 4.4.

Impedance measurements

Steady-state impedance measurements were made on n-GaAs in the dark in electrolytes with different $Fe(CN)_6^{3-}$ concentration and pH. Fig. 5.12 shows that the Mott-Schottky plot (curve (a)) is displaced when $Fe(CN)_6^{3-}$ is added to the solution (curves (b) and (c)). In 0.1 M NaOH solution the flat-band potential is -1.78 V (curve (a)) which is the value expected at this pH. In both $Fe(CN)_6^{3-}$ cases, for a 0.1 M solution which corresponds to $|i_{vb}^c| < i_{max}^a$ and for a 0.5 M solution where $|i_{vb}^c| > i_{max}^a$, a parallel displacement of the Mott-Schottky plot is found (curve (b) and (c), respectively). The parallel displacements are always found with the $Fe(CN)_6^{3-}$ system in the dark under a variety of experimental conditions.
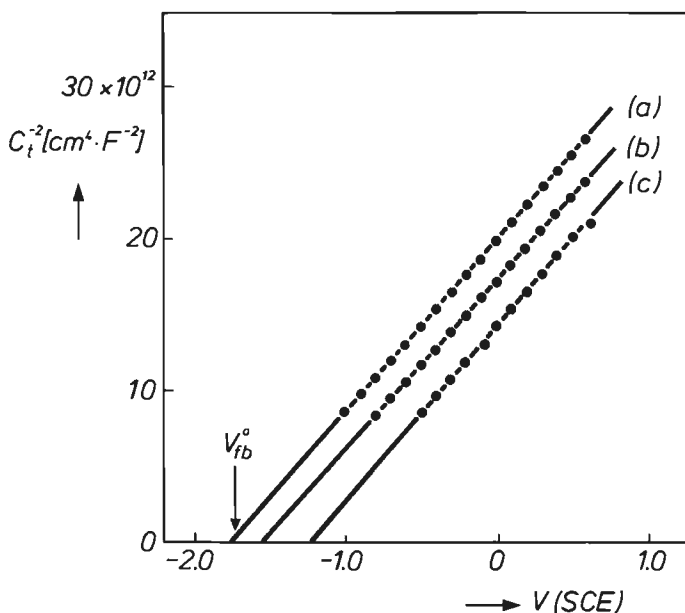
Fig. 5.12. Mott-Schottky plots for an n-type $(N_D = 1.0 \times 10^{18}$ cm$^{-3})$ GaAs RDE (500 rpm) in the dark in 0.1 M NaOH (curve (a)), 0.1 M $Fe(CN)_6^{3-}$ solution of $pH = 13$ (curve (b)) and 0.5 M $Fe(CN)_6^{3-}$ solution of $pH = 13$ (curve (c)).

The extrapolated flat-band potentials are shown in Fig. 5.13 as a function of the $Fe(CN)_6^{3-}$ concentration for solutions with three different pH values. In curve (a) at $pH = 14$, i_{max}^a is so high that it is not exceeded by the hole injection rate at any $Fe(CN)_6^{3-}$ concentration. The flat-band potential is shifted by about 200 mV at low injection rates and the shift levels off at 230 mV even though the injection current density, and thus the dissolution current density, increases to 100 mA·cm^{-2}. Again, it is striking that even at these high dissolution rates the Mott-Schottky plots only undergo a parallel displacement with respect to that found in 0.1 M NaOH. On the other hand, at $pH = 12$ (curve (c)), i_{max}^a is low (about 2.5 mA·cm^{-2} at 500 rpm) and is exceeded even at a concentration of 0.1 M $Fe(CN)_6^{3-}$. Curve (c) clearly shows that the shift of the flat-band potential is much larger than at $pH = 14$ and is almost independent of the $Fe(CN)_6^{3-}$ concentration. The intermediate case is shown in curve (b) for a solution of $pH = 13$. Here a discontinuity is clearly seen in the plot. At low $Fe(CN)_6^{3-}$ concentration the
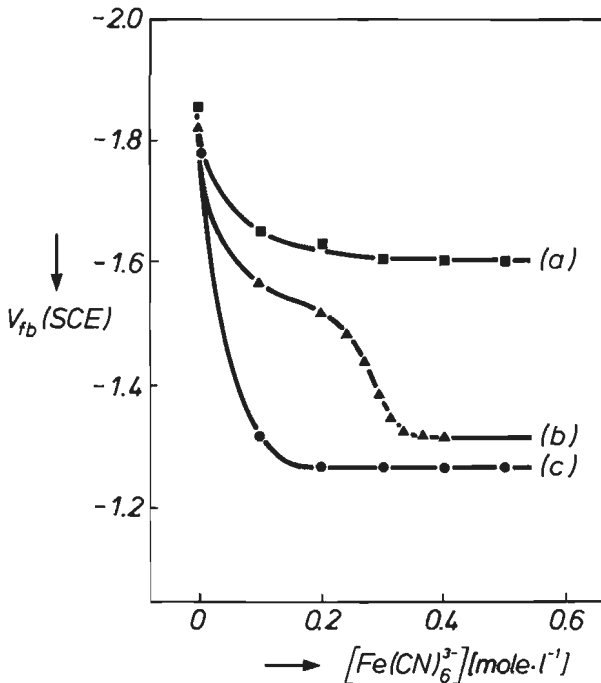
Fig. 5.13. The flat-band potential of an n-GaAs RDE (500 rpm) in the dark as a function of the $Fe(CN)_6^{3-}$ concentration in solutions of $pH = 14$ (curve (a)), $pH = 13$ (curve (b)) and $pH = 12$ (curve (c)).

flat-band potential is shifted to about -1.55 V. This value is close to that found for the $pH = 14$ electrolytes. At high $Fe(CN)_6^{3-}$ concentration V_{fb} suddenly becomes more positive. After this sharp transition, the flat-band potential levels off at a value close to that found for $pH = 12$ electrolytes. From the current-potential curve (f) in Fig. 5.10 it can be deduced that the hole injection rate is equal to i_{max}^a when the $Fe(CN)_6^{3-}$ concentration is about 0.27 mole·l^{-1}. This transition concentration agrees well with the discontinuity in Fig. 5.13, curve (b). Sodium hypochlorite was also used as an oxidizing agent in order to ensure that the results were not determined by specific $Fe(CN)_6^{3-}$ effects. The results obtained with alkaline hypochlorite solutions were essentially the same as shown in Fig. 5.13 for $Fe(CN)_6^{3-}$ solutions.

The hole injection rate can also be varied by changing the electrode rotation rate. Fig. 5.14 shows the flat-band potential as a function of the hole injection rate for three different solutions. The electrode rotation rates are 0 rpm (only used in curve (b)), 100, 500 and 5000 rpm. For both the 0.5 M $Fe(CN)_6^{3-}$ solution of $pH = 14$ (curve (a)) and the 0.1 M $Fe(CN)_6^{3-}$ solution of $pH = 13$ (curve (b)) the shift of the flat-band potential is moderate and V_{fb} becomes more positive at higher rotation rates, i.e. at higher
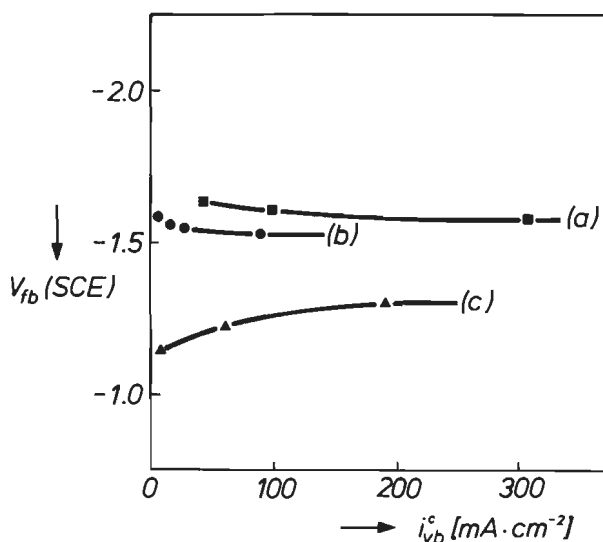
Fig. 5.14. The flat-band potential of an n-GaAs RDE in the dark as a function of the hole injection rate (i_{vb}^c) in solutions of 0.5 M $Fe(CN)_6^{3-}$, $pH = 14$ (curve (a)); 0.1 M $Fe(CN)_6^{3-}$, $pH = 13$ (curve (b)) and 0.5 M $Fe(CN)_6^{3-}$, $pH = 13$ (curve (c)). The hole injection rate is increased by increasing the electrode rotation rate.

hole injection rates. Since not only the injection rate but also the anodic dissolution rate of GaAs depends on the square root of the rotation rate (see section 4.2) the equation $|i_{vb}^c| < i_{max}^a$ is valid here at all rotation rates. For a 0.5 M $Fe(CN)_6^{3-}$ solution of $pH = 13$ (curve (c)) where $|i_{vb}^c| > i_{max}^a$, the shift of the flat-band potential is much larger but decreases with increasing rotation rate, this in contrast to curves (a) and (b).

Etching results

In Fig. 5.15 results are shown of the surface morphology of two n-GaAs crystals examined by an optical microscope after etching in the dark for
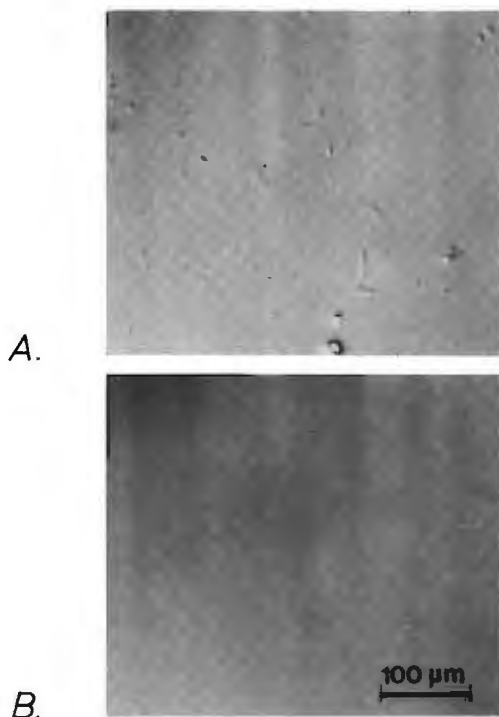
Fig. 5.15. Optical micrographs (Nomarski interference contrast) of n-type GaAs slices etched in the dark during 20 minutes in a non-stirred solution of 0.1 M $Fe(CN)_6^{3-}$, $pH = 13$ (A) and 0.5 M $Fe(CN)_6^{3-}$, $pH = 13$ (B). The same magnification is used in both photos.

20 minutes in two alkaline solutions with different $Fe(CN)_6^{3-}$ concentrations. In a 0.1 M $Fe(CN)_6^{3-}$ solution of $pH = 13$ which corresponds to the current-potential curve (a) of Fig. 5.10, defects are clearly revealed at the GaAs surface (Fig. 5.15.A). The result after etching in a 0.5 M $Fe(CN)_6^{3-}$ solution of $pH = 13$ which corresponds to the current-potential curve (a) of Fig. 5.11 is shown in Fig. 5.15.B. In contrast to Fig. 5.15.A, very smooth surfaces are always found.

5.3.3. Discussion

The most striking aspect of the results in this section is the strong interplay between processes in which holes are generated in n-type GaAs electrodes and the dissolution reaction in which holes are consumed. Before discussing these results, the charge transfer reaction between $Fe(CN)_6^{3-}$ and p-type GaAs electrodes will be considered first.

p-GaAs

As was shown in the previous section, $Fe(CN)_6^{3-}$ is a strong oxidizing agent (A-group agent in Table III) with a reorientation energy $\lambda = 0.7$ eV [13]; its D_{ox} function shows a good overlap with the valence band of GaAs in alkaline solutions (see solid lines of Fig. 5.16.B). Consequently, $Fe(CN)_6^{3-}$ can inject holes very efficiently into the VB of the solid according to

$$Fe(CN)_6^{3-} \rightarrow Fe(CN)_6^{4-} + h^+(VB). \tag{5.2}$$
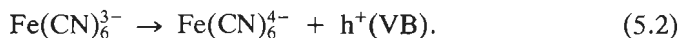
Recombination measurements confirmed this, as will be subsequently shown (Fig. 5.17).

From the mechanism of oxidative dissolution of p-GaAs in alkaline solutions, considered in section 4.2, it has become clear that two limiting cases can be distinguished. Firstly, when the supply of OH^- ions is sufficient the dissolution rate is determined by the rate at which holes are delivered to the electrode surface (eq. (4.8)). Under these conditions film formation at the electrode surface does not occur and charge exchange between the solid and solution is not inhibited, i.e. the reduction of $Fe(CN)_6^{3-}$ is diffusion-controlled in the entire potential range as was shown in the previous section (see Fig. 5.2). However, when i_{max}^a is exceeded at positive potentials, the dissolution rate depends on OH^- diffusion in the solution and according to eq. (4.9) an oxide consisting of gallium and arsenic oxides is formed. Indeed, we have shown that an oxide film with a thickness in the range of 0.5 to 1.0 nm (Fig. 5.9) is also formed at p-GaAs in alkaline $Fe(CN)_6^{3-}$ solutions.

It is obvious that such oxide films may hinder the hole injection kinetics from solution.

n-GaAs

The same two cases can also be distinguished for n-GaAs in the dark in alkaline $Fe(CN)_6^{3-}$ solutions. When, at a given pH, the rate of hole injection by $Fe(CN)_6^{3-}$ is lower than i_{max}^a,

$$|i_{vb}^c| < i_{max}^a, \tag{5.3}$$

the reduction of $Fe(CN)_6^{3-}$ at the oxide-free GaAs surface is diffusion-controlled not only at negative potentials but, also at positive potentials (see ring current of Fig. 5.10, curve (a)). When the recombination of injected holes in the potential range between -1.8 and -1.3 V stops, dissolution of GaAs takes over. During this dissolution process holes are trapped in surface states. These positively charged surface states were attributed in chapter 4 to intermediates in the dissolution reaction (eqs. (4.4)-(4.7)). As has been shown in section 4.3 these states (Q_{ss}) cause a change in the Helmholtz potential under oxide-free conditions and thus lead to a parallel shift of the Mott-Schottky plots. In curve (b) of Fig. 5.12, for example, the extrapolated flat-band potential is displaced by about 230 mV to more positive potentials. For $Fe(CN)_6^{3-}$ solutions of $pH = 14$, it is shown that the maximum shift of the flat-band potential is achieved even at low $Fe(CN)_6^{3-}$ concentrations and remains at this value at higher concentrations (see Fig. 5.13, curve (a)). Even at extremely high dissolution rates (> 300 mA·cm^{-2} at 500 rpm in curve (a) of Fig. 5.14) the shift of the flat-band potential is limited to this value of 0.20-0.25 V. The same results are observed in solutions of $pH = 13$ up to a $Fe(CN)_6^{3-}$ concentration of about 0.25 M (Fig. 5.13, curve (b)); below that concentration the hole injection rate is lower than i_{max}^a. The saturation in the shift of the flat-band potential was discussed by Memming [14]. According to eq. (4.22) a maximum surface state density of approximately 3×10^{13} cm^{-3} is calculated (with $C_H = 20 \times 10^{-6}$ F·cm^{-2}) from curve (a), Fig. 5.13.

These results strongly contrast with the results obtained during the photoanodic dissolution of n-GaAs also in alkaline solutions where much larger shifts in the flat-band potential are observed. Similar to the present $Fe(CN)_6^{3-}$ experiments, the anodic photodissolution rate of n-GaAs was, in that case, also lower than i_{max}^a so that oxide formation may be excluded. Parallel displacements of the Mott-Schottky plots were also observed in all cases (Fig. 4.12, curves (a)-(h)). However, no saturation in the shift of the flat-band potential occurred with increasing light intensity. Instead, a sharp

increase of V_{fb} at low intensity was followed by a continuous linear increase at higher light intensity (Fig. 4.13). At the highest photodissolution rate ($i_{hv}^a = 62$ mA·cm^{-2}), a δV_{fb} of about 800 mV was measured, which is much more than for the case of hole injection from Fe(CN)$_6^{3-}$; for the Fe(CN)$_6^{3-}$ case δV_{fb} is limited to 230 mV, even when much higher dissolution rates are used (up to 300 mA·cm^{-2} in Fig. 5.14, curve (a)). Obviously, it is important whether the holes needed for the dissolution of GaAs are created by light or are injected from the oxidizing agent into the VB. One significant difference is, of course, that in the former case light penetrates into the semiconductor thereby creating minority charge carriers within a certain penetration depth in the solid [15]. In section 4.3 the possibility was discussed that a certain steady-state concentration of these charge carriers is built-up in the space-charge layer. Gerischer [16] indeed suggested that accumulation of holes underneath the interface of n-type WSe$_2$ can occur upon illumination. A similar mechanism has been recently discussed by Memming et al. [11]. In the case of hole injection from solution the holes are delivered by the oxidizing agent directly to the electrode surface at which they are immediately used to oxidize the semiconductor. A build-up of extra charge in the space-charge layer does not occur as long as $|i_{vb}^c| < i_{max}^a$. In this way, processes which are connected with the space-charge region can apparently be excluded. These results support the suggestion made in the previous chapter that the sharp increase during the anodic dissolution of n-GaAs at low light intensity (see Fig. 4.13), which levels off after 200 - 250 mV, is related to intermediates of the dissolution reaction acting as surface states, and that the strikingly large shifts of the flat-band potential at much higher light intensities are related to charge in the space-charge layer of the semiconductor.

So far, we have discussed the case for n-GaAs in which the hole injection rate is smaller than the maximum dissolution rate. The second case can be distinguished in the dark when the initial hole injection rate exceeds i_{max}^a:

$$|i_{vb}^c| > i_{max}^a. \tag{5.4}$$

In this case the reduction of Fe(CN)$_6^{3-}$ is only diffusion-controlled at negative potentials, i.e. corresponding to the first (I) and second (II) cathodic plateaus in Fig. 5.11. At potentials corresponding to plateau (I), all injected holes recombine with electrons supplied from the bulk of the semiconductor (see also Fig. 2.10.B). In the potential range of plateau (II) only a fraction of the injected holes recombine with electrons giving the cathodic current; the remaining holes are used to dissolve the electrode at the reduced dis-

solution rate $i_{\text{max}}^{\text{a}}$. Since the dissolution rate is limited and the hole injection rate tends to exceed $i_{\text{max}}^{\text{a}}$, the formation of an oxide film starts in this potential range. It has been shown that oxide formation indeed occurs at p-GaAs at anodic potentials (Fig. 5.9). Similar results were found by Decker at n-GaAs also in alkaline $Fe(CN)_6^{3-}$ solutions [17]. It is very likely that film formation at more positive potentials influences the hole injection kinetics of $Fe(CN)_6^{3-}$. Consequently, the hole injection is no longer diffusion-controlled, but becomes kinetically controlled (see ring currents of Fig. 5.11 at positive potentials).

From the model of (photo)anodic dissolution of GaAs represented in Fig. 4.9, it was clear that in order to maintain a steady-state oxide layer at the semiconductor surface during the anodic dissolution, ionic conductivity in the oxide film is needed, whereas holes necessary to oxidize GaAs are supplied by an external power supply from the backside of the semiconductor to the semiconductor/oxide interface. This contrasts with the present case in which an oxidizing agent is used to oxidize GaAs. This means that holes which are delivered by the oxidizing agent must be transferred through the oxide layer to the semiconductor/oxide interface. Consequently, besides ionic conductivity, electron conductivity in the oxide film is also essential [18]. This is schematically represented in Fig. 5.16.A. A comparison of Fig. 4.9 and Fig. 5.16.A indeed reveals that the only difference between these two models is the way in which holes are supplied to the GaAs/oxide interface.

Oxides may be either insulating or semiconducting (sections 5.3 and 8.2 of [19], [20]). The band-gap of semiconducting oxides is, in general, large (page 187 of [19]). It is obvious that electron transport through an insulating oxide or through a wide band-gap semiconducting oxide becomes more difficult when the oxide layer thickness increases. Electron tunneling through the oxide can occur if the oxide is not too thick ($d_{\text{ox}} < 3.0$ nm; section 8.2 of [19]). Heusler and Yun have shown that the rate of electron transfer at metal electrodes (Nb, Ti) covered by an anodic oxide film decreases when d_{ox} increases, as the probability of electron tunneling (T_e) depends exponentially on d_{ox} [21]. They represented this dependence as

$$T_e = T_e^o \cdot \exp\{-\xi d_{\text{ox}}\}, \qquad (5.5)$$

where T_e^o and ξ are constants. T_e^o represents the probability of electron tunneling from the solid to the oxidizing agent when the electrode surface is free of oxide. In fact, T_e^o is generally included as a constant in the rate constant for the charge transfer reaction, in this case $\varkappa_{\text{vb}}^c$ of eq. (2.27) [1]. Re-
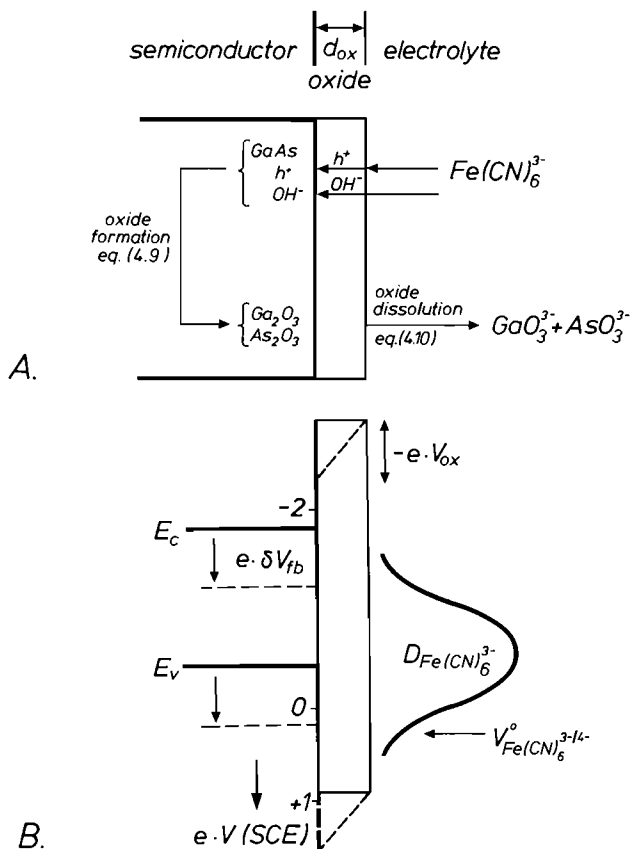
Fig. 5.16. Schematic representation of an oxide-covered GaAs electrode during electroless etching in the dark in an alkaline solution using $Fe(CN)_6^{3-}$ as oxidizing agent, when $|i_{vb}^c| > i_{max}^a$.

A) the various steps described in the text of the present section and those of section 4.2 are indicated, including both ionic and electronic transport through the oxide layer. Hole injection is provided by $Fe(CN)_6^{3-}$. For comparison, see also the corresponding scheme of Fig. 4.9.

B) energy band model of a Semiconductor/Oxide/Electrolyte surface structure. E_c and E_v (solid lines) refer to the conduction and valence bands in a solution of $pH = 13$ without an oxidizing agent in the dark. As a result of hole injection from $Fe(CN)_6^{3-}$, a positive charge density is built-up at the GaAs/oxide interface. Consequently, the band-edges shift to more positive potentials by an amount δV_{fb}, and a corresponding potential drop V_{ox} appears over the oxide layer (dashed lines). It is assumed in this figure that the potential drop across the Helmholtz layer at the oxide/electrolyte interface is not changed during dissolution of GaAs, so that $\delta V_{fb} = -V_{ox}$ ($\delta V_H = 0$).

cently, Ammar et al. [22] using the same eq. (5.5), explained the inhibited electron transfer between a redox system in solution and oxide-covered Sn electrodes. It is very likely that the same dependence holds for an oxide-covered GaAs electrode and that the rate at which $Fe(CN)_6^{3-}$ injects holes through the oxide film decreases significantly with increasing oxide film thickness, i.e. the reaction rate constant $\varkappa_{vb}^c$ depends on T_e and thus according to eq. (5.5) on d_{ox} [22].

In the steady-state the hole injection rate is equal to the rate of oxide dissolution at the oxide/electrolyte interface:

$$|i_{vb}^c| = i_{max}^a. \qquad (5.6)$$

Since i_{vb}^c is ultimately determined by i_{max}^a which has a constant potential-independent value for a given solution and electrode rotation rate (section 4.2), it follows that $\varkappa_{vb}^c$ (eq. (5.5)) is constant at positive potentials and must adapt to i_{max}^a. As $\varkappa_{vb}^c$ depends on T_e [1,21], it follows from eq. (5.5) that a steady-state oxide layer thickness should be established at anodic potentials independent of the electrode potential (see curve (a) of Fig. 5.11). This contrasts strongly with photoanodic dissolution of GaAs. In section 4.4 it was shown that in that case the oxide film thickness is clearly potential-dependent (Table II) as a result of Fermi level pinning at anodic potentials (curves (d) and (e) of Fig. 4.14). Indeed, the impedance behaviour during photoanodic dissolution of n-GaAs differs markedly from that of n-GaAs in $Fe(CN)_6^{3-}$ solutions. In the latter case perfect Mott-Schottky plots are obtained in all cases under oxide-forming conditions (see Fig. 5.12, curve (c) as an example), indicating that Fermi level pinning does not occur in this case. The parallel displacements of the Mott-Schottky plots point to a constant C_{ox} value and consequently according to eq. (4.26) to a constant potential-independent oxide layer thickness. This is in agreement with the mechanism of electron tunneling, as discussed above.

From curve (b) of Fig. 5.13 it is clear that under oxide-forming conditions the flat-band potential shifts to more positive potentials than in the case in which no oxide formation occurs. In a solution of $pH = 12$ (curve (c) of Fig. 5.13) i_{max}^a is so low that the transition between the two regions takes place at very low $Fe(CN)_6^{3-}$ concentration and is therefore not observed. During dissolution under oxide-forming conditions a build-up of interface charge at the semiconductor/oxide interface is expected. This charge was attributed in chapter 4 to intermediates in the dissolution reaction of GaAs (eqs. (4.4) - (4.7)). Although the steady-state oxide film which is established at positive potentials is very thin, it can be shown using eq. (4.26) that C_{ox}

is smaller than C_H. As a result, part of the potential drop occurs over the oxide layer as indicated in Fig. 5.16.B. Assuming that the interface charge density is of the same order of magnitude as the surface state density in the case of oxide-free dissolution (see section 4.4), it is clear with $C_{ox} < C_H$ and

$$Q_{if} = C_{ox} \cdot V_{ox}, \qquad (5.7)$$

that δV_{fb} $(= -V_{ox})$ is larger when the electrode is covered with an oxide film. This explains the shape of curves (a)-(c) in Fig. 5.13.

An additional effect which could influence the Helmholtz potential at the oxide/electrolyte interface is the depletion of OH^- at the electrode surface. The dissolution rate of GaAs is determined by OH^- diffusion in the solution. The OH^- concentration at the electrode surface is therefore very small. A decrease of the solution pH near the electrode surface may also cause a change in the Helmholtz potential. As a result of oxide formation and OH^- depletion at the electrode surface, the potential changes over both the oxide (V_{ox}) and Helmholtz (δV_H) layers. Consequently, the semiconductor band-edges move downwards by an amount $\delta V_{fb} = -(V_{ox} + \delta V_H)$. The shifted semiconductor bands are shown as dashed lines in Fig. 5.16.B. For simplicity, δV_H is assumed to be zero, which implies that $\delta V_{fb} = -V_{ox}$ as indicated.

In summary it can be concluded that oxide formation has two implications for the rate constant ($\varkappa^c_{vb}$) of the charge transfer reaction: (i) according to eq. (5.5) the tunnel probability decreases with increasing d_{ox} and (ii) the displacement of the semiconductor band-edges under oxide-forming conditions is more drastic than under oxide-free conditions, thereby reducing the overlap between the VB and the D_{ox} function of $Fe(CN)_6^{3-}$ significantly. A precondition for using equation (2.28) in section 2.3 for hole injection is that the valence band be fixed. If this is not the case, the following equation must be considered

$$i^c_{vb} = F\varkappa^c_{vb}[Fe(CN)_6^{3-}], \qquad (5.8)$$

where $\varkappa^c_{vb}$ depends on the number of states in both the VB and solution, and also on T_e, as discussed above. Inserting eqs. (2.27) and (2.18) into eq. (5.8) and taking T_e into account gives a modified expression for the hole injection rate which can account for situations in which the semiconductor band-edges are not fixed. The following expression is obtained [21]

$$i^c_{vb} \propto FN_vT_e[Fe(CN)_6^{3-}] \cdot \int_{-\infty}^{E_v} \exp\left\{\frac{-(E - E_{F,el} + \lambda)^2}{4kT\lambda}\right\} dE. \qquad (5.9)$$

In the present case, when the hole injection rate exceeds i_{max}^a the growth of the oxide film continues initially, thereby accommodating a more substantial potential drop over this film, until a new steady-state is established. The rate of hole injection must then be equal to the maximum dissolution rate of GaAs (eq. (5.6)). The new position of the semiconductor bands is indicated in Fig. 5.16.B.

From the Levich dependence of the maximum anodic dissolution it was clear that i_{max}^a depends not only on the pH of the solution but also on the electrode rotation rate. This dependence is expressed in eq. (4.12). Substituting eqs. (4.12) and eq. (5.9) into eq. (5.6) and taking eq. (5.5) into account gives an expression for the hole injection rate constant and the angular velocity of the rotated electrode:

$$\omega^{\frac{1}{2}} = C \cdot \exp\{-\xi d_{ox}\} \cdot \int_{-\infty}^{E_v} \exp\left\{\frac{-(E - E_{F,el} + \lambda)^2}{4kT\lambda}\right\} dE, \qquad (5.10)$$

where C is constant for a given $Fe(CN)_6^{3-}$ and OH^- concentration. From eq. (5.10) it is clear that d_{ox} is the only parameter as E_v depends on V_{ox} and thus, according to eq. (4.15), also on d_{ox}. It can be shown that when ω increases d_{ox} must decrease and consequently the integral decreases. This means that when the electrode rotation rate increases, the shift of the semiconductor bands becomes smaller under oxide forming conditions. This is exactly what we found for the case when $i_{vb}^c > i_{max}^a$ in curve (c) of Fig. 5.14.

So far, the discussion has been limited to electrodes in the dark. When an n-type electrode is illuminated in $Fe(CN)_6^{3-}$ solution, dissolution of GaAs takes place by photogenerated holes and by holes injected from $Fe(CN)_6^{3-}$. According to the current-potential curves of Figs. 5.10 and 5.11 it is obvious that as long as $(i_{hv}^a + |i_{vb}^c|) < i_{max}^a$, the hole injection rate can be diffusion-controlled (curves (a)-(d) of Fig. 5.10). When i_{max}^a is exceeded, oxide formation starts and the $Fe(CN)_6^{3-}$ reduction becomes kinetically-controlled. At these positive potentials recombination of injected holes with conduction band electrons becomes very difficult due to the low electron concentration in the space-charge layer. So it is inevitable that the photogenerated holes 'force' the rate of hole injection from solution to decrease. The reduction rate therefore decreases as a function of the light intensity, as the ring currents of Figs. 5.10 and 5.11 show.

Macroscopic etching

From the electrochemical results it is clear that etching of both p- and n-type GaAs at the open-circuit potential V_r in the dark in alkaline $Fe(CN)_6^{3-}$ solutions can be divided into two classes which, as in the case of anodic dissolution of GaAs (chapter 4), can be related to oxide-formation during etching. When the reduction rate of $Fe(CN)_6^{3-}$ is smaller than i_{max}^a, the macroscopic etch rate at V_r is determined by the reduction reaction, i.e. by mass-transport of $Fe(CN)_6^{3-}$ in solution. Dissolution proceeds under oxide-free conditions via an electroless mechanism and is cathodically controlled. The etch rate which can be calculated with eq. (2.39) from the partial reduction current density at V_r, depends on the electrode rotation rate and $Fe(CN)_6^{3-}$ concentration in solution (see eq. (2.42)). This situation has already been discussed for A-group oxidizing agents in the previous section (see Fig. 5.2). From the etching result of Fig. 5.15.A it is clear that under these conditions defects are revealed. A more detailed description of the mechanism of defect revealing during cathodically controlled electroless etching will be given in section 8.3.4. When, however, the hole injection rate exceeds i_{max}^a a thin oxide film is formed at the crystal surface and the macroscopic etch rate at V_r is determined by the rate at which the oxide dissolves chemically in the electrolyte. It has been shown that the dissolution rate of the oxide in alkaline solutions is controlled by diffusion of OH^- ions in solution. In the steady-state, the rate of oxide formation is equal to the rate of oxide dissolution. In this case, dissolution of GaAs is anodically controlled and depends on both the OH^- concentration and electrode rotation rate and is described by eq. (4.12). Etching under these conditions gives very smooth surfaces (Fig. 5.15.B), which is in accordance with the polishing behaviour under oxide-forming conditions, as discussed in chapter 4. Such solutions are very suitable for polishing applications. The results of Fig. 5.15 emphasize again the importance of oxide-formation during electroless etching and indicate that the conditions can be significantly changed, simply by changing the ratio of OH^- and $Fe(CN)_6^{3-}$ concentrations in solution. A similar dependence of surface morphology on the compositions of alkaline $Fe(CN)_6^{3-}$ solutions was found for germanium [23,24].

5.3.4. Conclusions

The anodic dissolution rate of GaAs in solutions with a *p*H in the range 11 - 14 is limited by OH^- diffusion in solution. When $Fe(CN)_6^{3-}$ is used as an oxidizing agent to dissolve GaAs, the injected holes give rise to surface

or interface charging and thus to a change in the potential distribution at the electrode/electrolyte interface. This influences the kinetics of the reduction reaction. Two cases were distinguished. In the first case, when the diffusion-controlled hole injection rate is lower than the maximum dissolution rate, the dissolution rate is determined by the $Fe(CN)_6^{3-}$ concentration and electroless etching occurs under oxide-free conditions. Impedance measurements show a limited shift of the flat-band potential of about 0.23 V to more positive potentials. This does not affect the kinetics of the reduction reaction. When the hole injection rate exceeds the maximum dissolution rate, however, oxide formation at the GaAs surface occurs. The holes necessary to oxidize GaAs are supplied by $Fe(CN)_6^{3-}$ through the oxide layer via a tunneling mechanism. As a result of GaAs oxidation a build-up of interface charge occurs. This charge in combination with the oxide layer results in a drastic shift of the semiconductor band-edges by 0.5-0.6 V to positive potentials. Consequently, the overlap between the D_{ox} function and the valence band decreases and the hole injection rate drops drastically. The $Fe(CN)_6^{3-}$ reduction becomes kinetically-controlled and its rate becomes equal to the rate of chemical dissolution of the oxide.

The difference between the two cases also has obvious consequences for the morphology of the GaAs surface etched at the open-circuit potential in the dark in these solutions. The particular etching mechanism determines whether defects are revealed or smooth crystal surfaces are obtained.

Illumination of an n-GaAs electrode also influences the kinetics of hole injection at positive potentials when the maximum dissolution rate is exceeded. Under these conditions GaAs is dissolved both by photogenerated holes and by injected holes. However, as recombination of the photogenerated charge at these positive potentials is very difficult, the rate of hole injection 'adapts' to the light intensity and can be dramatically reduced at higher photon densities. When the light intensity alone exceeds the maximum dissolution rate, the hole injection rate is decreased to zero and a similar situation to photoanodic dissolution of n-GaAs, described in chapter 4, arises.

5.4. Reduction of Br_2 and Cl_2 in acidic solutions

5.4.1. Introduction

Gerischer et al. found Br_2 reduction at n-GaAs in the dark and at p-GaAs under strong illumination to be diffusion-controlled, whereas the rate of Br_2

reduction in the dark at p-type GaAs electrodes is low [25,26]. As a result, it was concluded that for the reduction of bromine electrons are needed and thus the reaction proceeds via the conduction band. The standard redox potential of the bromine/bromide redox system ($V^o_{Br_2/Br^-}$ = +0.84 V [27]) is, however, rather positive with respect to the valence band-edge of GaAs in a solution of pH = 0 (V^o_{fb} = +0.30 V), and a valence band reaction should therefore be expected. In order to determine whether the CB or the VB is involved in the reduction of bromine, recombination resistance measurements can be applied, as will be discussed below.

It was shown in section 4.4 that the rate of recombination of minority and majority charge carriers during the photoanodic dissolution of an oxide-
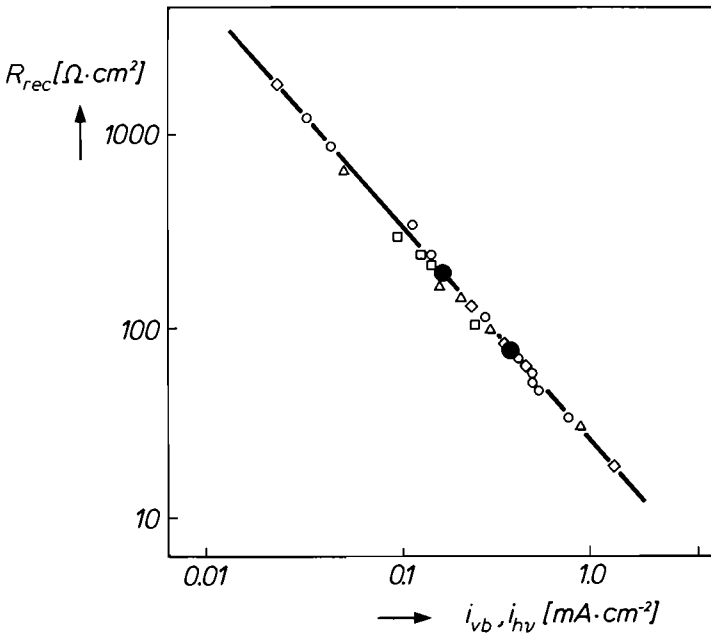
Fig. 5.17. Recombination resistance (R_{rec}) as a function of the hole injection rate (i_{vb}) and the hole generation rate by light (i_{hv}) at n-GaAs measured under oxide-free conditions in the potential range where recombination dominates. Open symbols refer to the impedance results from refs. [2,28] with various systems: Ce^{4+}, pH = 0 (o); $Fe(CN)_6^{3-}$, pH = 13 and 14 (□); I_2, pH = 0 (◇) and with light at pH = 0 and 5 (△). i_{vb} and i_{hv} were changed either by changing the concentration of the oxidizing agent, the electrode rotation rate or the light intensity. Filled circles refer to the present bromine results at an n-GaAs RDE (0 and 200 rpm) in the dark under potentiostatic control (−0.60 V) in a solution of 10^{-3} M Br_2, 0.5 M H_2SO_4.

covered n-GaAs electrode ($e \cdot \phi > i_{max}^a$), can be characterized by a recombination resistance R_{rec}. The importance of recombination at n-type electrodes under oxide-free conditions was also noted in sections 2.5 and 5.3. In a potential range, from V_{fb}^o up to approximately 600 mV positive with respect to V_{fb}^o, where n-GaAs might be expected to dissolve with holes injected by an oxidizing agent or generated by light, recombination dominates. This results in a cathodic current plateau in the case of oxidizing agents (Fig. 2.10.B) and negligibly low currents in the case of illumination (Fig. 2.9.B). Using impedance measurements it has been shown that the rate of recombination at n-GaAs under these conditions can also be characterized by a recombination resistance [2]. R_{rec} is found to be a function of the rate at which holes are injected from an oxidizing agent (i_{vb}) or photogenerated by light (i_{hv}). This dependence is shown in Fig. 5.17 (open symbols) for several oxidizing agents and for illumination under various conditions [2,28]. Since recombination at n-GaAs is typical of a minority carrier process, determination of the minority carrier recombination resistance is also an elegant way to determine which semiconductor band is involved in the charge transfer reaction with an oxidizing agent in solution. This method was therefore applied in the present study to decide whether the Br_2 reduction at n-GaAs occurs via hole injection into the valence band or by electron transfer via the conduction band.

In chapter 4 an equivalent circuit was presented which could account for the impedance behaviour of an n-GaAs electrode during photoanodic dissolution. In that case, oxide-formation clearly occurs and recombination takes place at the semiconductor/oxide interface. As a result, R_{rec}, C_{if} and an oxide capacitance C_{ox} were included in the circuit of Fig. 4.17.B. When recombination takes place under oxide-free conditions C_{ox} can, of course, be omitted from the circuit and the interface capacitance must be replaced by a surface state capacitance (C_{ss}). Since C_H may not be neglected in contrast to the oxide case, an analysis of the equivalent circuit under oxide-free conditions yields the following two equations

$$\frac{1}{Z_{re} - R_e} = (R_{rec}C_{sc}^2)\omega_f^2 + \frac{(C_{ss} + C_{sc})^2}{R_{rec}C_{ss}^2}, \qquad (5.11)$$

and

$$\frac{-\omega_f Z_{im}}{Z_{re} - R_e} = \left\{ \frac{R_{rec}C_{sc}(C_{ss} + C_H)}{C_H} \right\} \omega_f^2 + \left\{ \frac{(C_{ss} + C_{sc})(C_{ss} + C_{sc} + C_H)}{R_{rec}C_H C_{ss}^2} \right\}, \qquad (5.12)$$

which are similar to those deduced before (eqs. (4.23) and (4.24)). Thus, by measuring both the real and imaginary components of the impedance of an n-type electrode as a function of the frequency of the a.c. signal in the potential range where recombination occurs, information can be obtained about the rate of recombination and, consequently, about the mechanism of reduction [2,28].

The reduction of I_2 ($V^o_{I_2/I^-} = +0.38$ V) at GaAs was extensively studied by van den Meerakker [28]. He showed that when I_2 is not electrochemically reduced at the electrode, p-GaAs is etched by I_2 molecules in solution via a chemical mechanism. On the basis of an analogy with the I_2 case similar behaviour might be expected for p-GaAs with other halogens such as Br_2. Such a mechanism was proposed for n-GaAs in bromine solutions by Gerischer et al. [25] as discussed in section 2.6. To measure the Br_2 consumption at the p-GaAs electrode, ring/disk measurements were performed; Br^- ions produced at the disk electrode were detected at the Pt-ring.

Br_2 cannot be easily dissolved in aqueous solutions. The partial vapour pressure of bromine is large, which results in a rapid decrease of the bromine concentration in the solution as a function of time. According to Henri's law (page 288 of [29]) this is more serious when higher bromine concentrations are used, and also at higher electrode rotation rates. To overcome this problem Br_2 can be complexed in bromide solutions to Br_3^- and Br_5^- according to

$$Br_2 + Br^- \leftrightarrows Br_3^-, \qquad (5.13)$$

and

$$2Br_2 + Br^- \leftrightarrows Br_5^-. \qquad (5.14)$$
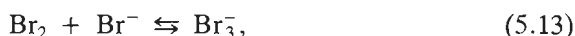
From the equilibrium constants $(0.051)^{-1}$ and $(0.0246)^{-1}$ for eq. (5.13) and (5.14), respectively [30.a,b], it can be shown that Br_2 is complexed almost completely to Br_3^- when a large excess of Br^- is available in solution. However, for the accuracy of the Br^- detection at the Pt-ring the background concentration of Br^- must not be too large. An optimum was found in a solution containing 0.01 M Br_2 and 0.03 M HBr at an electrode rotation rate of 1000 rpm. In this solution the current-potential curves were made at a Pt/p-GaAs RRDE in the dark and under illumination. For the impedance measurements both the Br_2 concentration and electrode rotation rates used were so low that complexing with Br^- was not essential and was therefore omitted.

The Cl_2 reduction was also studied at p-GaAs in acidic solution and compared with the results obtained in bromine solutions. Since the equilibrium constant for the Cl_2/Cl_3^- reaction is much smaller than that of the Br_2/Br_3^- system [30.b], complexing Cl_2, even with a large excess of Cl^-, is less effective than in the bromine case. Literature data [30.b] suggest that complexing Cl_2 with I^- might be more successful. In this work, however, this is omitted and pure Cl_2 solutions were investigated.

5.4.2. Results

Current-potential curves were measured at an n-GaAs RDE in the dark in bromine solutions of $pH = 0$. The results were very similar to that schematically represented in curve (c) of Fig. 2.10.B. The bromine reduction is diffusion-controlled at the cathodic reduction plateau [25]. Frequency dependent impedance measurements were made in the frequency range $5 \times 10^2 - 3 \times 10^4 \, s^{-1}$ at n-GaAs RDE under potentiostatic control at this cathodic reduction plateau (-0.60 V; compare with curve (c) of Fig. 2.10.B) in a 10^{-3} M Br_2 solution of 0.5 M H_2SO_4 in the dark. The hole injection rate was varied by changing the electrode rotation rate (0 and 200 rpm). The results plotted according to eqs. (5.11) and (5.12), as a function of ω_f^2, gave perfect straight lines in all cases. Assuming that $C_H \gg C_{sc}$, both C_{sc} and R_{rec} can be obtained from the slopes of the above equations. The measured values of R_{rec} are represented by filled circles in Fig. 5.17. The impedance results obtained with the Ce^{4+} system at n-GaAs, which was considered in section 5.2 as a reference redox system with regard to the hole injection reaction, are indicated by open circles in Fig. 5.17. From the good agreement of the present bromine results (filled circles) with the straight line it is clear that the Br_2 reduction in the dark proceeds entirely by hole injection into the valence band. From the calculated values of C_{sc} it was shown that the assumption $C_H \gg C_{sc}$ was justified. The straight line of Fig. 5.17 also indicates that the $Fe(CN)_6^{3-}$ reduction ($\square$ symbols), which was referred to in the previous section, is, indeed, a valence band process.

Fig. 5.18 shows the potentiodynamically measured current-potential curves of a p-GaAs RRDE and the Pt-ring response in a solution of 0.01 M Br_2 and 0.03 M HBr. The potential of the Pt-ring was fixed at $+1.20$ V. This value is considerably positive with respect to the $V_{ox/red}^o$ of the Br_2/Br^- redox system so that the oxidation of Br^- to Br_2 at the Pt-ring is diffusion-controlled. At negative potentials the cathodic current at p-GaAs, due to Br_2 reduction, is low in the dark (curve (a) of Fig. 5.18). The current increases at approximately -0.2 V as a result of anodic dissolution of GaAs. The oxi-

dation current observed at the Pt-ring in curve (c) is independent of the applied disk potential in the whole potential range. It should be noted that the onset of the anodic current is found at a relatively negative potential with respect to V_{fb}^o (compare with the anodic current onset in the Ce^{4+} case, also at $pH = 0$ in Fig. 5.2, curve (a)). For curve (b) illumination of the GaAs electrode resulted in an increase of the reduction current. The light intensity in this experiment was relatively high, i.e. the photon flux was higher than the rate of Br_2 reduction (e·ϕ > i_{vb}^c), which can also be deduced from the fact that hydrogen evolution occurs at potentials more nega-
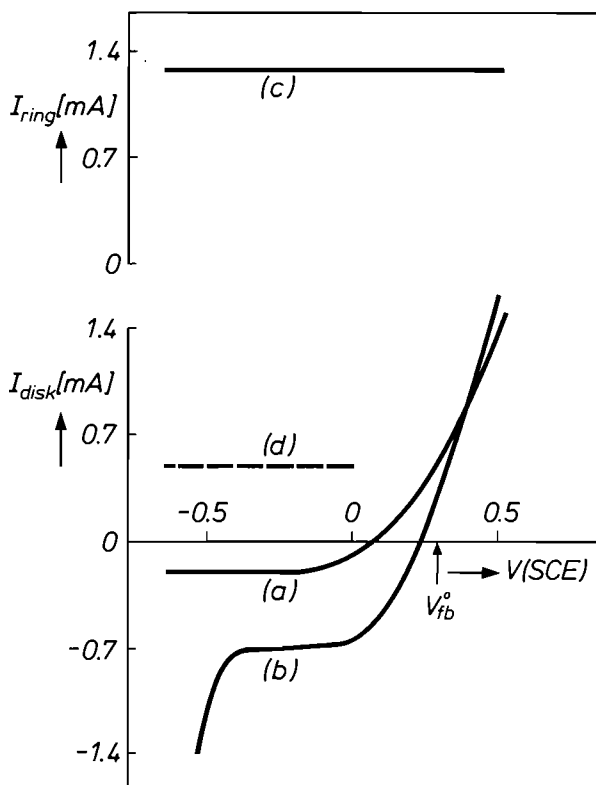
Fig. 5.18. Current-potential curves for a Pt/p-GaAs(001) RRDE (1000 rpm) in 0.01 M Br_2, 0.03 M HBr, 0.5 M H_2SO_4 solution at 50 mV·s^{-1}. Curve (a) shows the disk current in the dark and curve (b) under illumination (Schott lamp) with a high photon flux (e·ϕ > i_{vb}^c). Curve (c) refers to the corresponding Pt-ring current measured in the collection mode under potentiostatic control (+1.20 V), both in the dark and under illumination. From curves (a) and (c) a potential-independent chemical etch rate in the dark can be calculated (curve (d)).

tive than -0.4 V. The reduction current under potentiostatic control at -0.20 V was directly proportional to the square root of the electrode rotation rate (eq. (2.42)), indicating that Br_2 reduction at p-GaAs with a (001) crystal surface is diffusion-controlled under illumination. The Pt-ring response under illumination is exactly the same as in the dark case (curve (c)). We used a Pt/Pt RRDE in the same solution as used in Fig. 5.18 in order to check whether the Br^- background concentration was responsible for the unchanged ring current in curve (c) of Fig. 5.18. The Pt-ring was again fixed at $+1.20$ V while the potential of the Pt-disk was changed potentiodynamically. It was clear that in this case the oxidation current at the Pt-ring decreased sharply when the potential of the Pt-disk became more positive than $+0.8$ V. At this potential, close to the standard redox potential of the Br_2/Br^- system, the Br_2 reduction and thus the Br^- production at the Pt-disk stops. In spite of the Br^- background concentration the oxidation current at the Pt-ring was reduced by almost a factor of two. These results clearly indicate that the Br_2 consumption at the GaAs electrode is independent of the GaAs electrode potential and does not depend on illumination of the disk. It can be concluded that, under all conditions, the Br_2 consumption at GaAs is diffusion-controlled.

Since the rate of hole injection into the valence band by Br_2 in solution is low in the dark and the kinetics of these reactions is determined by the overlap of their D_{ox} functions and the VB (eq. (2.27)), it is essential to determine the position of the semiconductor band-edges. Therefore Mott-Schottky measurements were made at a p-GaAs RDE (1000 rpm) in the dark in a 0.005 M Br_2, 0.015 M HBr solution of 0.5 M H_2SO_4 and the results were compared with the plots obtained in 0.5 M H_2SO_4. In both solutions a linear dependence of C_t^{-2} on the electrode potential was found. However, the flat-band potential measured in the bromine solutions was 360 mV more positive than that found in a 0.5 M H_2SO_4 solution (V_{fb}^o). This indicates that the Helmholtz potential is changed as a result of positive charging of the electrode surface in the depletion potential range, i.e. for p-GaAs at negative potentials (see Fig. 5.18).

Current-potential measurements at p-GaAs were also made in freshly prepared Cl_2 solutions. As described in the experimental chapter 3, the solutions were made by mixing an OCl^- solution with HCl. According to eq. (3.3) chlorine is instantaneously formed. In this experiment a 0.10 M OCl^- solution was mixed with the same volume of a 1 M HCl solution which results in a 0.05 M Cl_2 solution. This solution was stable during the duration of the experiment because the Cl_2 concentration is well below that corresponding to the maximum solubility of Cl_2 in aqueous solutions [31]. The electrochemical results resemble closely the results obtained in Br_2

solutions. In the dark the reduction current is low, as found for Br_2 in curve (a) of Fig. 5.18. The rotation rate dependence under potentiostatic control (-0.20 V) is shown in Fig. 5.19.A. The reciprocal of the dark current density (i_d^{-1}) is found to be linearly dependent on $\omega^{-\frac{1}{2}}$ with a positive intercept on the Y-axis. According to eq. (2.43) this means that the Cl_2 re-
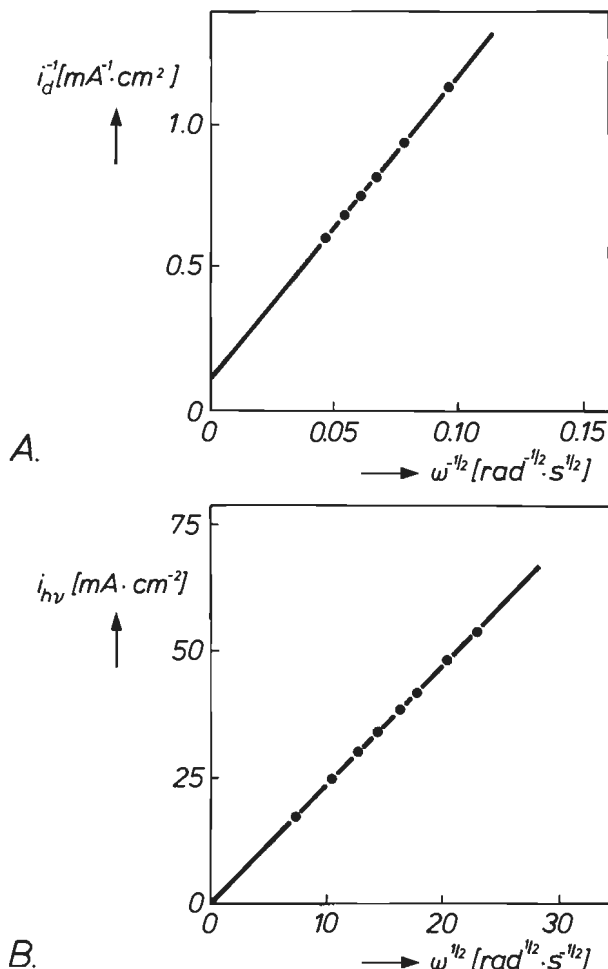
Fig. 5.19. Rotation rate dependence of the chlorine reduction current density at a p-GaAs RDE under potentiostatic control (-0.20 V) in a 0.05 M Cl_2, 1 M HCl solution. The working solution was prepared by mixing equal volumes of a 0.10 M OCl^-, $pH = 13$ solution with 1 M HCl.
A) in the dark; i_d^{-1} is plotted versus $\omega^{-\frac{1}{2}}$ according to eq. (2.43).
B) under illumination (Schott lamp) with a relatively high photon flux ($e \cdot \phi > i_{vb}^c$); i_{hv} is plotted versus $\omega^{\frac{1}{2}}$ according to eq. (2.42).

duction at p-GaAs in the dark is under mixed kinetic/diffusion control. From the intercept a rate constant for the hole injection reaction of 1.3×10^{-3} cm·s^{-1} is calculated (eq. (2.43)). When the p-GaAs electrode was illuminated with a relatively high light intensity ($e \cdot \phi > i^c_{vb}$) the rate of reduction increased and a cathodic current plateau was observed in the same potential range as found in Fig. 5.18, curve (b) for the Br$_2$ reduction. In this plateau range (-0.20 V) the Levich equation is obeyed as Fig. 5.19.B shows. From the slope a diffusion coefficient for Cl$_2$ in solution of $\mathcal{D}_{Cl_2} = 2.3 \times 10^{-6}$ cm^2·s^{-1} is calculated. It should be noted that due to the higher Cl$_2$ concentration the reduction current density under illumination is about a factor of 5 higher than that found for Br$_2$ reduction in Fig. 5.18, curve (b), as expected. These results show that, as in the case of Br$_2$, the rate of Cl$_2$ reduction at p-GaAs is low in the dark and is diffusion-controlled under illumination with a high photon flux.

5.4.3. Discussion

It is clear from the recombination resistance measurements that Br$_2$ is reduced at n-GaAs by hole injection into the VB (see Fig. 5.17). The reduction rate at this type of electrode in the dark is controlled by Br$_2$ diffusion in solution as one would expect as a result of the good overlap of the distribution function of Br$_2$ (D_{Br_2}) and the valence band of GaAs [25]. It is therefore rather unexpected that the rate of bromine reduction at p-GaAs in the dark is low (curve (a) of Fig. 5.18). Paradoxically, the Pt-ring response revealed that the Br$_2$ consumption at p-GaAs electrodes is diffusion-controlled both in the dark and under illumination (curve (c) of Fig. 5.18). From these observations it must be concluded that Br$_2$ is also consumed in another reaction. It therefore seems likely that p-GaAs in the dark is etched chemically by bromine molecules in the solution, as proposed by Gerischer for n-GaAs in bromine solutions [25] (see section 2.6). Characteristic of chemical etching is the potential-independent etch rate in a potential range where GaAs is not anodically oxidized (section 2.6). Since the low reduction rate at negative potentials is potential-independent (curve (a) of Fig. 5.18) and the total Br$_2$ consumption is diffusion-controlled (curve (c) of Fig. 5.18), it is obvious that the resulting high chemical etch rate is indeed potential-independent over a broad cathodic potential range as indicated by the dashed line of curve (d) in Fig. 5.18. The chemical etch rate is here expressed as a current density (see eq. (3.2) in section 3.2.3).

From the Mott-Schottky measurements it is clear that the semiconductor bands are shifted more than 300 mV downwards during chemical etching in

bromine solutions. The results obtained in Br_2 solutions resemble strongly the results van den Meerakker obtained at GaAs in I_2 solutions [28]. He also found the I_2 reduction at n-GaAs in the dark to be a diffusion-controlled hole injection process (see Fig. 5.17), whereas the I_2 reduction rate at p-GaAs in the dark is very low and, in addition, chemical etching by I_2 occurs. The total rate of I_2 consumption in this latter case was found to be kinetically controlled [28]. Impedance measurements at p-GaAs showed that during chemical etching in iodine solutions the semiconductor band-edges are shifted 350 mV downwards to more positive potentials, thereby reducing the overlap of the distribution function of I_2 and the VB of GaAs. As a consequence of this poorer overlap the rate of hole injection from I_2 in solution is dramatically reduced. The present results indicate that during chemical etching of GaAs in Br_2 solutions a similar mechanism operates.

In section 2.6 it was shown that chemical dissolution of GaAs in Br_2 solutions involves the rupture of $Ga - As$ and $Br - Br$ bonds as first proposed by Gerischer [25,26]. The first chemical step of this reaction was represented in eq. (2.40). A similar reaction sequence was proposed for the iodine case with the formation of $Ga - I$ and $As - I$ bonds [28]. Van den Meerakker attributed the shift of the semiconductor band-edges to the formation of these new bonds which have a dipole moment. Similarly, it is calculated that the $Ga - Br$ and $As - Br$ bonds also have a dipole character. We therefore propose that, as a result of chemical etching in bromine solutions, charge separation occurs at the semiconductor/electrolyte interface which influences the potential drop over the Helmholtz layer. The first chemical dissolution step in which the synchronous exchange of bonds is essential, can be respresented by

$$
\begin{array}{ccc}
\begin{array}{c} Br \rule{1em}{0.4pt} Br \\[2pt] \end{array} & & \begin{array}{c} Br^{\delta_1^-} \quad Br^{\delta_2^-} \\[2pt] | \qquad | \\ -Ga^{\delta_1^+}_{} As^{\delta_2^+} - \end{array} \\
-Ga \rule{1em}{0.4pt} As - & \longrightarrow &
\end{array}
\qquad (5.15)
$$

The potential across the Helmholtz layer changes due to these dipoles at the interface and as a consequence the semiconductor band-edges shift to positive potentials with respect to the solution. Obviously, this shift depends on the density of surface dipoles. As a result, the hole injection rate of Br_2 into the valence band is significantly reduced at p-type GaAs in the dark.

When sufficient electrons are available at the semiconductor surface the intermediates formed in eq. (5.15) can be reduced by electrons. Such a mechanism was found previously for the reduction of $Ge - OH$ bonds at the surface of germanium electrodes [32] and was also used to interpret some

results of the I_2 reduction at GaAs [28]. The reduction reaction in which the broken surface bond is restored by electrons at the surface can be represented by

$$
\begin{array}{cc}
Br^{\delta_1^-} & Br^{\delta_2^-} \\
| & | \\
-\underset{/}{Ga}^{\delta_1^+} & \underset{\backslash}{As}^{\delta_2^+}- \ + \ 2\,e^- \ \longrightarrow \ -\underset{/}{Ga}-As\underset{\backslash}{}- \ + \ 2\,Br^-.
\end{array} \qquad (5.16)
$$
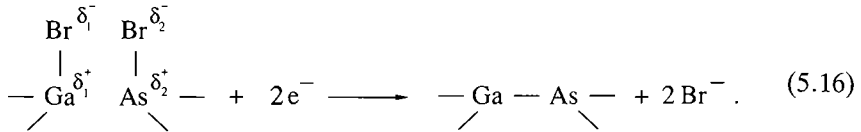
Due to this reaction the band-edges shift back to their original positions, the hole injection rate of Br_2 increases and the reduction rate at n-GaAs in the dark and at p-GaAs under illumination becomes diffusion-controlled at negative potentials.

Although recombination measurements were not performed at n-GaAs in chlorine solutions it seems likely, since the standard redox potential of the Cl_2/Cl^- system ($V_{Cl_2/Cl^-}^{o} = +1.11$ V) is even more positive than that of the Br_2/Br^- redox system, that Cl_2 is reduced by hole injection into the VB. Nevertheless, in spite of the very good overlap of the D_{Cl_2} and the VB, the rate of Cl_2 reduction is low (Fig. 5.19.A), similar to the bromine reduction at p-GaAs. It therefore seems reasonable to assume that p-GaAs in the dark is also etched chemically by Cl_2. Under illumination, the Cl_2 reduction at p-GaAs is diffusion-controlled (Fig. 5.19.B), as also found for Br_2 and I_2 systems.

Macroscopic etching

It is evident that the macroscopic etch rate of GaAs at the open-circuit potential in halogen-containing acidic solutions cannot be directly deduced from the electrochemical measurements. However, RRDE measurements yield useful information about the consumption of the oxidizing agent at the GaAs electrode. It was found that p-GaAs in bromine solutions is mainly etched by a chemical mechanism rather than an electroless mechanism. For n-GaAs the situation is somewhat more complex. It was shown that the reduction of halogens at cathodic potentials is diffusion-controlled as long as the surface electron concentration is sufficient to reduce the intermediate dipoles which are formed by chemical etching. For the iodine reduction at n-GaAs it was found [28] that, when the potential becomes more positive, i.e. when the electron concentration at the surface becomes very low, the I_2 reduction stops and chemical etching takes over. It was clearly shown that, in that case, n-GaAs is also etched at the rest potential in the dark by a chemical mechanism. It seems very likely that a similar mechanism is valid

for n-GaAs in other halogen-containing solutions. It can therefore be concluded that both p- and n-type GaAs are chemically etched at the open-circuit potential in acidic bromine and chlorine solutions.

5.4.4. Conclusions

The electrochemical and chemical etching properties of GaAs in acidic chlorine, bromine and iodine solutions bear a very strong resemblance to each other. Minority carrier recombination resistance measurements showed that the diffusion-controlled Br_2 reduction at n-GaAs at negative potentials is, similar to the I_2 reduction at n-GaAs, a valence band process. The rate of hole injection at p-GaAs in the dark is drastically reduced due to chemical etching in these solutions. The reduction rate at p-GaAs under illumination increases significantly and is, at negative potentials, determined by diffusion of halogen molecules in solution, in all cases.

It is concluded that chemical etching of both p- and n-type GaAs is important at the open-circuit potential in these solutions in the dark.

5.5. Hypochlorite reduction in alkaline solutions

5.5.1. Introduction

Sodium hypochlorite (NaOCl) is a strong oxidizing agent which is often used for etching applications. In the experimental chapter 3 it was shown that OCl^- is unstable in strongly acidic HCl solutions and that chlorine is instantaneously formed. The electrochemical and etching behaviour of GaAs in these chlorine solutions was described in the previous section. In this section the behaviour of OCl^- in alkaline solutions is described. These stable solutions are of considerable importance since they are often used as polishing agents to produce a smooth 'mirror-like' finish on semiconductor wafers [33,34] (see also chapter 3).

Since hypochlorite is a strong oxidizing agent, $V° = +0.70$ V at $pH = 13$ [27], it is expected to inject holes into the valence band of GaAs. Janietz et al. [35] found that the reduction rate of OCl^- at n-GaAs electrodes is controlled by diffusion of the oxidizing agent in the solution and proposed a VB process for the reduction. However, when studying the etching kinetics of p-type GaAs in alkaline OCl^- solutions we found results which could not be explained in terms of a single valence band reduction of the oxidizing agent [36]. Therefore, the kinetics of OCl^- reduction were investigated at

p-type GaAs RDEs. The influence of illumination on the OCl^- kinetics was studied with cyclic voltammetry and current transient techniques. These results are strongly dependent on surface charging effects which were investigated with impedance measurements. The reduction mechanism was investigated at cathodic potentials, so oxide formation at GaAs is avoided. Moreover, for the electrochemical experiments care was taken that the rate of OCl^- reduction was considerably lower than the maximum dissolution rate of GaAs. Since the electrochemical results strongly resemble the results found in halogen-containing solutions (section 5.4), it might be expected that chemical etching in these solutions also plays a significant role. To study the etching behaviour of GaAs, flow-cell experiments under potentiostatic control were carried out and the etch rate was correlated with the measured current density.

5.5.2. Results

Kinetics of OCl^- reduction

The reduction of OCl^- (0.005 M) at a p-GaAs electrode in a solution of $pH = 13$ is shown in Fig. 5.20, both in the dark (curve (a)) and under illumination (curve (b)). The reduction rate at negative potentials in the dark is lower than that expected for a diffusion-controlled reaction. At potentials near the flat-band value, GaAs begins to dissolve anodically. Under illumination the reduction rate increases markedly and a much higher cathodic current plateau is found (curve (b)). In addition, hydrogen is evolved at more negative potentials as $e \cdot \phi > i_{lim}^c$.

The influence of the electrode rotation rate on the limiting cathodic current was studied under potentiostatic control ($V = -1.0$ V(SCE)) in the same solution used for Fig. 5.20. The results were very similar to those found for the reduction of Cl_2 at p-GaAs in Fig. 5.19. In the dark the reciprocal of the dark current is found to be linearly dependent on $\omega^{-\frac{1}{2}}$ with a positive intercept on the Y-axis. This means that OCl^- reduction in the dark is under mixed kinetic/diffusion control. From the intercept a rate constant for the hole injection reaction of 2.5×10^{-3} cm·s^{-1} is calculated. Under strong illumination the limiting reduction current is directly proportional to $\omega^{\frac{1}{2}}$, indicating that reduction of OCl^- is diffusion-controlled. It should be emphasized that even at the highest rotation rates in these experiments the photon flux was much greater than the limiting reduction rate ($e \cdot \phi > i_{lim}^c$).

To measure the quantum efficiency of the reduction reaction it is, of course, necessary that the photon flux be considerably lower than the dif-
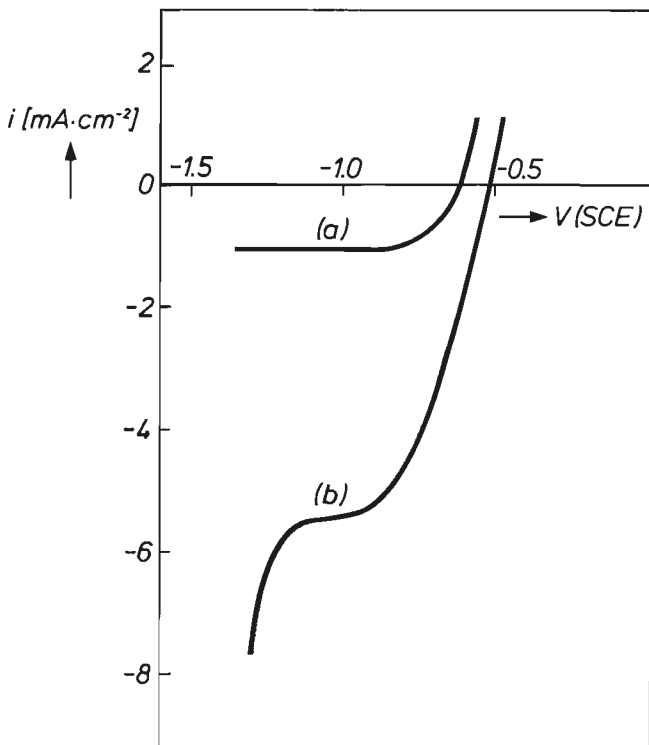
Fig. 5.20. Current-potential curves for a p-GaAs RDE (1000 rpm) in a 0.005 M OCl⁻ solution of $pH = 13$ in the dark (curve (a)) and when the electrode was illuminated with a He-Ne laser (curve (b)). The photon flux is higher than the diffusion-controlled reduction rate. Scan rate is 200 mV·s⁻¹.

fusion-controlled rate of OCl⁻ reduction. In curve (a) of Fig. 5.21 the photo-current-potential curve for a p-GaAs electrode in a 0.1 M NaOH is shown. The photocurrent is defined as the difference between the total current under illumination and the corresponding dark current ($i_{hv} - i_d$). Under illumination H_2 gas is evolved at negative potentials. The limiting cathodic current is determined by the light intensity. The quantum efficiency is in this case close to one [37], i.e. each photon is responsible for the transfer of one charge carrier to solution. At a potential of about −1.3 V the cathodic current decreases to a very low value as a result of recombination. Curve (b) of Fig. 5.21 was measured in a 0.05 M OCl⁻ solution of $pH = 13$ with the same rotation rate and the same light intensity as used for curve (a). Two important features are revealed in this curve: firstly, reduction of OCl⁻ oc-
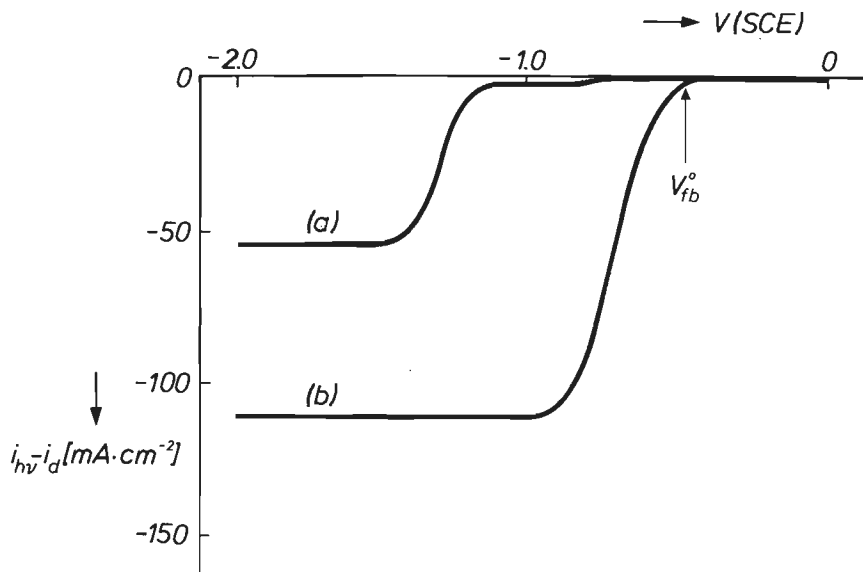
Fig. 5.21. Photocurrent $(i_{h\nu} - i_d)$-potential curves for a p-GaAs RDE (5000 rpm) under illumination (Schott lamp). Curve (a) represents the 0.1 M NaOH solution and curve (b) a 0.05 M OCl$^-$ solution of pH = 13. The photon flux is lower than the diffusion rate of OCl$^-$ ($e \cdot \phi < i^c_{lim}$). Scan rate is 50 mV·s^{-1}.

curs in the potential range in which in curve (a) recombination dominates; secondly, the limiting photocurrent is a factor of two higher than that measured in the NaOH solution. From this latter result it is clear that one photon results in the transfer of two charge carriers to the solution. The quantum efficiency is therefore two in this case.

The experiments of Figs. 5.20 and 5.21 refer to steady-state current measurements in the dark and under illumination. In section 5.2, it was shown that the kinetics of the hole injection can be influenced significantly by illumination. Current transients measured under potentiostatic control with chopped light can give information about the dark current immediately after illumination. In the present work this technique was also used. In Fig. 5.22 results are given for a p-GaAs electrode at a potential of -1.0 V in a 0.005 M OCl$^-$ solution of pH = 13. The frequency of the light chopper was 50 Hz, so one illumination period corresponds to 10 ms. Fig. 5.22.A shows the current-time dependence for the case in which the photon flux is larger than the diffusion-controlled reduction rate. The electrode rotation rate was 100 rpm. The steady-state dark current measured without illumination is in-
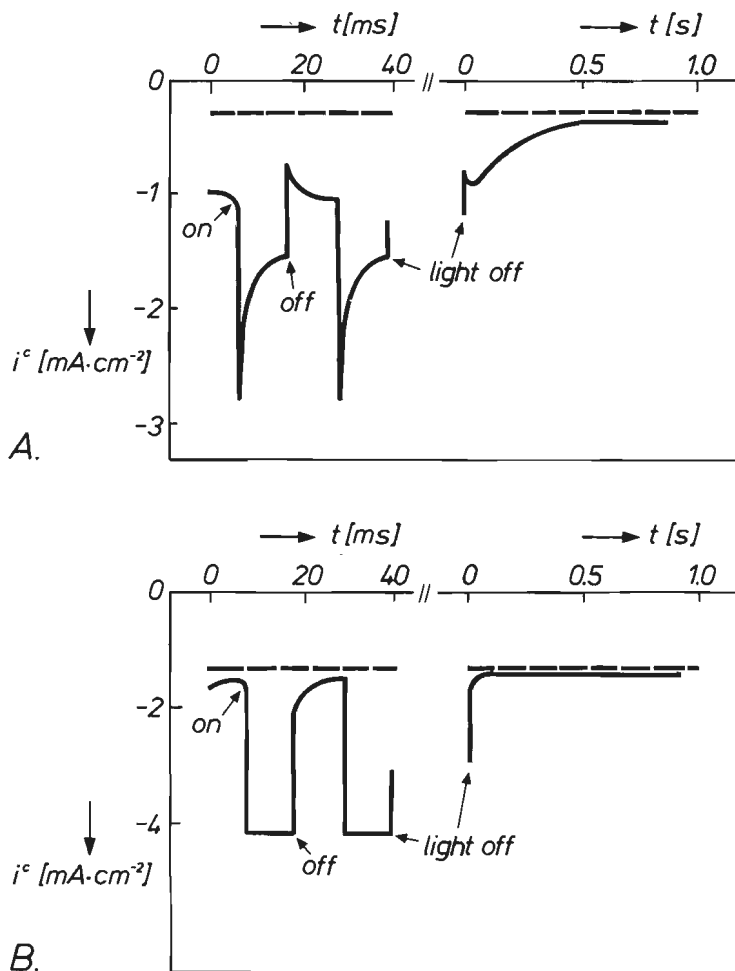
Fig. 5.22. Current transients for a p-GaAs RDE under potentiostatic control (−1.00 V) in a solution of 0.005 M OCl⁻, pH = 13. The dashed lines represent the steady-state dark current. The electrode was illuminated with chopped light from the He-Ne laser (solid lines).

A) the electrode rotation rate was 100 rpm, $e \cdot \phi > i_{lim}^c$.

B) the electrode rotation rate was 5000 rpm, $e \cdot \phi < i_{lim}^c$.

The frequency of the chopper was 50 Hz. The right parts of both figures show the relaxation of the dark current after illumination on a longer time scale.

dicated as a dashed line. The reduction current increases immediately after the illumination period has started. This is followed by a sharp decay of the current to an almost constant value after a few ms. After a period of 10 ms the light beam is interrupted by the chopper. The dark current decreases instantaneously but is restored very rapidly to some extent. The dark reduction current after 10 ms is at least a factor of three higher than the steady-state dark current (compare with the dashed line). After this dark period the electrode is again illuminated, which results in a repeat of the cycle described above. The relaxation of the enhanced dark current after the light is switched off is shown over a longer period in the right-hand side of Fig. 5.22.A. Again, we recognize the sharp peak at short times followed by a decay of the enhanced dark current to the steady-state value. This relaxation process is almost complete in 0.5 s. Fig. 5.22.B corresponds to the case in which the photon flux is lower than the diffusion-controlled reduction rate ($e \cdot \phi < i_{lim}^c$). This is achieved under exactly the same experimental conditions as in Fig. 5.22.A, simply by increasing the electrode rotation rate to 5000 rpm. The supply of OCl^- to the electrode surface is dramatically improved and is no longer a limiting factor with respect to the photon flux. The steady-state dark current is also indicated by a dashed line. When the electrode is illuminated the photocathodic reduction starts immediately. In this case the photo-current is determined solely by the light intensity. A cathodic peak is not observed. The cathodic current under illumination is constant. The decay of the dark current after the illumination period is fast and the steady-state dark current is rapidly attained in contrast to the case in Fig. 5.22.A. The difference with the diffusion-controlled case is also clearly shown in the 1 second transient in the right-hand side of Fig. 5.22.B.

Impedance measurements

Impedance measurements were made under the same experimental conditions as used for the current transient experiments except that, during illumination, the chopper was not used. Fig. 5.23, curve (a) shows the Mott-Schottky plot in a 0.005 M OCl^- solution of $pH = 13$ in the dark at an electrode rotation rate of 100 rpm. The flat-band potential of -0.40 V is close to the value expected at this pH. When the electrode was illuminated with an excess of light at the rotation rate of 100 rpm a parallel displacement of the Mott-Schottky plot was found (curve (b)). The flat-band potential ($V_{fb} = -0.96$ V) was shifted more than 500 mV in the negative direction. This V_{fb} value was also found in 0.1 M NaOH solution, using the same light intensity and electrode rotation rate. When the rotation rate was increased to 5000 rpm in the 0.005 M OCl^- solution (curve (c)) and the light intensity
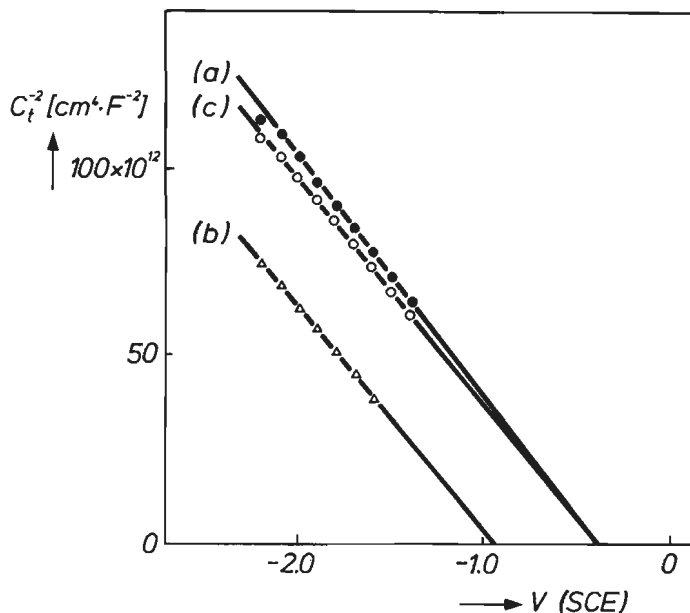
Fig. 5.23. Mott-Schottky plots for a p-type ($N_A = 1.0 \times 10^{17}$ cm^{-3}) GaAs RDE in a 0.005 M OCl$^-$ solution of $pH = 13$. Curve (a) represents the dark case at an electrode rotation rate of 100 rpm. In curve (b), the electrode (100 rpm) is illuminated with a Schott lamp; the photon flux here is larger than the reduction rate ($e \cdot \phi > i^c_{lim}$). In curve (c), the light intensity was the same as for curve (b) but the rotation rate was increased to 5000 rpm. The photon flux is now lower than the diffusion-controlled reduction rate ($e \cdot \phi < i^c_{lim}$).

remained unchanged, the Mott-Schottky plot shifted back to its original dark position of curve (a). The experimental conditions here are the same as in Fig. 5.22.B in which the light intensity limits the OCl$^-$ reduction rate.

Flow-cell experiments

Fig. 5.24 shows the potentiostatically measured current densities ($\bullet$) and etch rates ($\circ$) of a p-GaAs electrode in a 0.1 M OCl$^-$ solution of $pH = 13$, both in the dark and under illumination. For convenience, the etch rate is expressed as a current density assuming that etching is an electrochemical process and six holes are needed to dissolve one GaAs entity. At positive potentials, the anodic current density is independent of the electrode potential (curves (a) of Figs. 5.24.A and B). Dissolution of GaAs is here controlled by diffusion of OH$^-$ ions in the solution (see sections 4.2 and 5.3). In

this range the etch rate agrees exactly with the anodic current density (curves (b) of Figs. 5.24.A and B). In the intermediate potential range a transition is observed between the cathodic and anodic plateau currents similar to that observed for the $Fe(CN)_6^{3-}$ system in section 5.3, and an enhanced etch rate is found. At negative potentials the reduction current density is low in the dark (curve (a) of Fig. 5.24.A). Surprisingly it was found that, in this potential range more than 1.0 V negative with respect to the
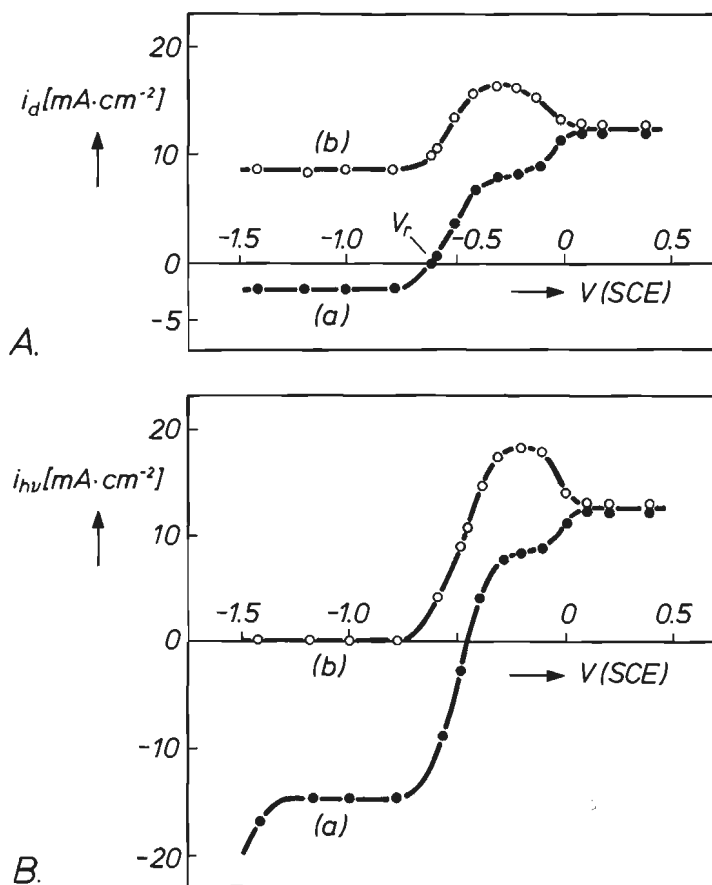
Fig. 5.24. Flow-cell measurements at a stationary p-GaAs electrode in a 0.1 M OCl⁻ solution of $pH = 13$.
A) in the dark.
B) under illumination (Schott lamp) with $e \cdot \phi > i_{lim}^c$.
Curves (a) represent the potentiostatically measured current density and curves (b) the corresponding etch rates. The open-circuit potential in the dark is given by V_r.

flat-band value, GaAs is etched at a significant rate. This unusual behaviour is typical of a 'chemical' etchant, as has also been found for other etching systems (see section 2.6) [38,39]. When the electrode is illuminated with a high light intensity the reduction rate increases and becomes diffusion-controlled (curve (a) of Fig. 5.24.B). The etch rate is negligible as long as the OCl^- reduction is diffusion-controlled (curve (b) of Fig. 5.24.B). The same behaviour has been described for the reduction of halogens at GaAs in the previous section.

5.5.3. Discussion

On the basis of the standard redox potential of OCl^-/Cl^- ($V^o = +0.70$ V) [27] and the position of the GaAs band-edges ($E_v = -0.45$ V) one would expect a good overlap of the OCl^- distribution function (D_{OCl^-}) and the valence band, and consequently a diffusion-controlled hole injection rate by OCl^-. However, from the current-potential curve in Fig. 5.20, curve (a) and the dependence of the current on the electrode rotation rate, it is clear that the reduction rate in the dark is controlled both by the kinetics and OCl^- diffusion. When the p-GaAs electrode is illuminated, the OCl^- reduction indeed becomes diffusion-controlled at negative potentials (see Fig. 5.20, curve (b)). We confirmed the result of Janietz et al. [35] that at n-GaAs the reduction reaction is diffusion-controlled even in the dark. From these results it can be concluded that reduction occurs not only via hole injection into the valence band but that electrons from the conduction band can also reduce OCl^-. When the light intensity determines the reduction rate of OCl^- at negative potentials, as in Fig. 5.21, it was shown that the photocurrent is exactly twice that measured in a NaOH solution. We must therefore conclude that OCl^- is a 'current doubling' agent. Two charge carriers are required to reduce OCl^- to Cl^-. Under illumination both a hole and an electron are involved in the reduction reaction. In a manner similar to that proposed by Memming for the 'current doubling' effect of H_2O_2 [1], the reduction of OCl^- under illumination can be represented by two steps in which an electron is first transferred via the conduction band (CB) or via surface states (SS), very likely forming a $Cl^\bullet$ radical:

$$OCl^- + H_2O + e^- \overset{CB}{\underset{SS}{\rightarrow}} Cl^\bullet + 2OH^-, \qquad (5.17)$$
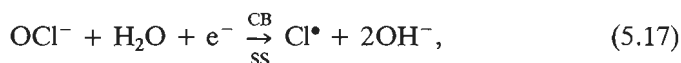
followed by the hole injection reaction via the valence band

$$Cl^{\bullet} \overset{VB}{\to} Cl^- + h^+. \tag{5.18}$$

A reaction sequence which considers the formation of $Cl^{\bullet}$ radicals is also proposed for the reduction of OCl^- at Pt electrodes [40]. These two reactions are indicated in the energy scheme of Fig. 5.25 by arrows (a) and (b), respectively. The solid lines represent the GaAs bands under normal conditions in a solution of $pH = 13$ and D_{ox} functions are located around the overall standard redox potential. For simplicity, only the distribution functions of OCl^- and $Cl^{\bullet}$ are considered in Fig. 5.25. For the reorientation
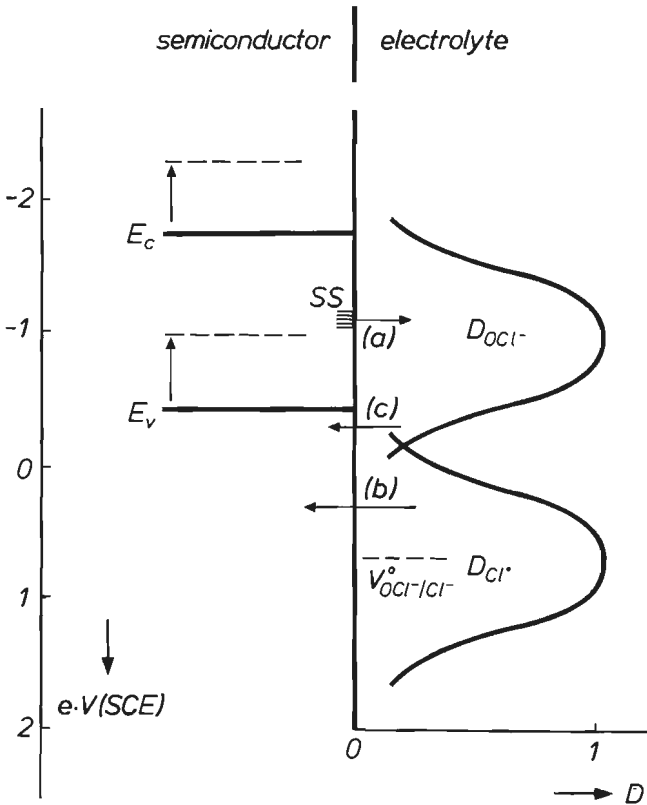
Fig. 5.25. Distribution functions of the $OCl^-/Cl^{\bullet}$ system with respect to the band-edges (E_c and E_v) of GaAs in a solution of $pH = 13$ in the dark (solid lines) and under illumination (dashed lines). The charge transfer reactions, as described in the text, are indicated by arrows: arrow (a) corresponds to eq. (5.17), arrow (b) to eq. (5.18) and arrow (c) to eq. (5.19). The overall standard redox potential of the OCl^-/Cl^- system is given by $V^o_{OCl^-/Cl^-}$.

energy (λ) a value of 0.9 eV is assumed, which is within the range found for many other redox couples [41]. Charge transfer between a semiconductor and an oxidizing agent requires an overlap of the D_{ox} function of the oxidizing agent with the valence band in the case of hole exchange and with the conduction band and/or surface states in the case of electron exchange (section 2.3). When the overlap is very favourable, the rate of charge transfer is determined by diffusion of the oxidizing agent in solution. The rate is kinetically controlled when the overlap is poor. Since reduction of OCl⁻ in the dark is controlled both by kinetics and diffusion, a relatively poor overlap of D_{OCl^-} and the valence band must be assumed. The potential difference between the overall $V^o_{OCl^-/Cl^-}$ and the valence band is about 1.1 V so that a λ of 0.9 eV is reasonable in order to fulfil this condition (see Fig. 5.25). The first reduction step of OCl⁻ via the valence band in the dark can be represented by

$$OCl^- + H_2O \overset{VB}{\to} Cl^\bullet + 2OH^- + h^+, \qquad (5.19)$$

followed by the second hole injection step already given in eq. (5.18). The first reduction reaction (eq. (5.19)) is also indicated in Fig. 5.25 by arrow (c). With a λ of 0.9 eV the overlap of the D_{OCl^-} function and the conduction band is poor, so it is unlikely that the electron transfer under illumination occurs via the conduction band. It was, however, shown by Kelly and Memming [10] that electron transfer can also occur via surface states which have energy levels in the band-gap. They proposed a model in which the various charge transfer reactions are considered. This model is shown in Fig. 5.26. The rate constants of both possible electron transfer reactions are denoted by k_{cb} and k_{ss}, respectively. Recombination of electrons and holes must, of course, also be considered. The rate constants for electron and hole capture are denoted by k_n and k_p, respectively. The magnitude of the various rate constants and the electron and hole concentrations at the semiconductor surface determine which reactions are dominant. When in the case of a 0.1 M NaOH solution a p-type GaAs electrode is illuminated electrons are created in the conduction band. At moderate potentials negative with respect to the flat-band potential the hole concentration in the space-charge layer of the semiconductor is relatively large (eq. (2.6)). Here recombination via surface states is preferred to the electron transfer reactions. The surface becomes negatively charged and the surface charge depends on the ratio of the rate constants k_n and k_p. This results in a displacement of the flat-band potential to negative values. A shift of 0.2 V was reported in acid solutions
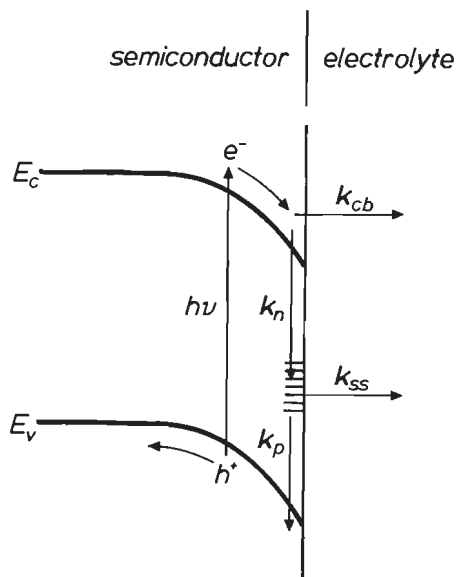
Fig. 5.26. Model for charge-transfer reactions involving surface recombination (from ref. [10]).

[10]. A shift of about 0.5 V was found in the present alkaline solutions of $pH = 13$. The very low current in the potential range of -1.1 V to -0.5 V in Fig. 5.21, curve (a) is also a consequence of the recombination reaction. Since at negative potentials the hole concentration at the electrode surface becomes very low, the recombination reaction stops and hydrogen gas is evolved. This results in the limiting cathodic current in curve (a). In the case of an OCl^- solution almost no recombination is found at potentials negative with respect to V_{fb}^o (Fig. 5.21, curve (b)). This means that the rate constant k_{ss} for the first reduction step of OCl^- via surface states must be much higher than the corresponding rate constant for the H_2 reaction. Reduction of OCl^- can effectively compete with the recombination. In general an order of magnitude difference in rate constant should correspond to a potential difference in the photocurrent onset of 60 mV. From a comparison of curves (a) and (b) of Fig. 5.21, it must be concluded that k_{ss} for the OCl^- reduction is several orders of magnitude higher than that for the H^+ reduction. Due to this higher k_{ss} most of the photo-generated electrons are used for the OCl^- reduction and charging of surface states should be drastically reduced. Indeed, according to the impedance measurements of Fig. 5.23, curve (c), it is clear that the semiconductor bands are not shifted with re-

spect to the dark case. The electrode rotation rate is here so high that the OCl⁻ supply to the electrode surface is not a limiting factor. This result shows that electron trapping in surface states can be effectively prevented using a suitable oxidizing agent as discussed before in section 5.2.3. However, when the photon flux is higher than the OCl⁻ reduction rate at a low rotation rate, surface state charging again occurs, which results in the shift of the Mott-Schottky plot as found in curve (b).

The same two cases which depend on the electrode rotation rate can be distinguished in the transient measurements at negative potentials in Fig. 5.22. At a low rotation rate when $e \cdot \phi > i_{lim}^c$, reduction of OCl⁻ is diffusion-controlled. This can be seen from the cathodic peak in Fig. 5.22.A which appears immediately after a dark period. The current decrease results from depletion of OCl⁻ at the electrode surface. After this initial effect, the photocurrent approaches the steady-state diffusion current towards the end of the illumination period. The reverse effect is seen in the dark immediately after the illumination period. At that moment the OCl⁻ concentration at the electrode surface is almost zero and the kinetically controlled reduction current is therefore low. Since in the dark not all OCl⁻ ions are reduced, a build-up of OCl⁻ at the electrode surface occurs. This results in an increase of the dark current during the initial period, which lasts about 10 ms. Apart from this initial effect the dark current after illumination is markedly higher than the steady-state dark current (compare with the dashed line of Fig. 5.22.A). It was concluded from the impedance measurements that under these experimental conditions the flat-band potential is shifted to negative potentials with respect to the dark case (compare curves (a) and (b) of Fig. 5.23). A consequence is that the overlap between the shifted valence band-edge, indicated in Fig. 5.25 as a dashed line, and the D_{OCl^-} function improves, which results in the enhanced 'dark current' under illumination. Immediately after illumination the semiconductor bands remain shifted to negative potentials. The surface states begin to discharge and the bands shift back to their original dark position. From the current transient in the right-hand side of Fig. 5.22.A this relaxation process can be followed. It is evident that the discharging of surface states in the dark after illumination lasts about half a second. The second case is shown in Fig. 5.22.B at a high electrode rotation rate. The photocurrent is here constant in time. All photo-generated electrons are now transferred to OCl⁻ at a high transfer rate (k_{ss} is large). The semiconductor bands are not shifted with respect to the dark case. Consequently, the hole injection rate is not changed during illumination and after illumination the dark current returns immediately to the steady-state value as Fig. 5.22.B reveals.

Macroscopic etching

From Fig. 5.20 it was clear that anodic dissolution of GaAs only starts in the vicinity of the flat-band potential. The flow-cell experiments of Fig. 5.24.A demonstrate, however, that GaAs also dissolves in the dark chemically in OCl^- solution at a potential-independent rate (see curve (b) of Fig. 5.24.A). The chemical dissolution of GaAs discussed so far in sections 2.6 and 5.4 involved symmetrical bifunctional etching agents such as H_2O_2 and halogens. In this section OCl^- is found to be the first asymmetric chemical etching agent.

The enhanced dissolution rate in the intermediate potential range can be attributed to a combination of chemical and anodic etching processes (curve (b) of Fig. 5.24.A). At more positive potentials, anodic etching occurs via an oxide film (compare with Fig. 5.8) and chemical dissolution is obviously prevented by this oxide. Such an effect has been observed with other systems. This will be further discussed in the following chapter.

The constant cathodic current observed at negative potentials begins to decrease at approximately -0.75 V (curve (a) of Fig. 5.24.A) as a result of anodic dissolution of p-GaAs. The further change in the current-potential curve at -0.1 V is due to the fact that OCl^- reduction stops. This is evident from ring-disk experiments. At potentials positive with respect to the flat-band value, the semiconductor electrode becomes degenerate and behaves like a metal electrode (see section 2.2). This effect is further accentuated by oxide formation which very likely hinders charge transfer reactions.

No chemical etching is found under strong illumination at negative potentials because OCl^- is reduced at a diffusion-controlled rate; the oxidizing agent is not available for chemical etching (see curve (a) of Fig. 5.24.B). This supports the conclusion that k_{ss} for the OCl^- reduction is very large and that the competition with the chemical dissolution reaction is very effective.

For polishing applications concentrated OCl^- solutions of $pH = 13$ are often used [33]. In these concentrated solutions, the rate of OCl^- reduction in the dark exceeds the maximum dissolution rate of GaAs at $pH = 13$. Consequently, a more positive value of V_r is found, at which oxide formation occurs. In relation to Fig. 5.24.A at positive potentials, it was argued that direct chemical attack of GaAs by OCl^- is then prevented. It therefore seems likely that GaAs is etched under these polishing conditions by an anodically controlled electroless mechanism; oxidation of the semiconductor occurs by hole injection from OCl^- through the oxide film, while the oxide is dissolved by OH^- ions at the oxide/electrolyte interface. An identical

anodically controlled dissolution mechanism was shown to take place in concentrated $Fe(CN)_6^{3-}$ solutions in the previous section (see also Fig. 5.16.A). This also explains the good polishing properties of these solutions [33].

5.5.4. Conclusions

Despite the fact that hypochlorite is a strong oxidizing agent in alkaline solution, hole injection from OCl^- ions into the valence band of p-GaAs in the dark is not efficient. Illumination increases the rate of reduction: at high light intensity the rate is controlled by mass-transport of OCl^- ions in solution; at low intensity photocurrent doubling is observed. These results show that reduction is a two-step process, the first step of which can occur either via the valence band or via the conduction band. In the latter case, electrons may be transferred directly from the conduction band or indirectly via surface states. The product of the first step, very likely a $Cl^•$ radical, can subsequently inject a hole into the valence band. When the flux of OCl^- ions to the electrode surface is lower than the photon flux, a considerable upward displacement (500 mV) of the band-edges is observed due to negative charging of the surface. This results in a better overlap of the distribution function D_{OCl^-} and the valence band and, consequently, in an enhanced hole injection rate during and after illumination. The negative charging of the surface does not occur when the photon flux is decreased or when the transport of electroactive species to the electrode is improved. These results indicate that electron transfer, in fact, occurs via surface states.

It is shown that OCl^- chemically dissolves GaAs in the dark. Under illumination however OCl^- is reduced at a diffusion-controlled rate and no chemical etching is found at negative potentials.

References

[1] R. Memming, *'Electroanalytical Chemistry. A Series of Advances'*, Ed. A.J. Bard, Vol. 11, pp. 1-84. Marcel Dekker, New York, (1979).

[2] J.E.A.M. van den Meerakker, J.J. Kelly and P.H.L. Notten, *J. Electrochem. Soc.*, **132**, 638, (1985).

[3] S. Menezes and B. Miller, *J. Electrochem. Soc.*, **130**, 517, (1983).

[4] E. Haroutiounian, J. Sandino, P. Clechet, D. Lamouch and J. Martin, *J. Electrochem. Soc.*, **131**, 27, (1984).

[5] F. Decker, B. Pettinger and H. Gerischer, *J. Electrochem. Soc.*, **130**, 1335, (1983).

[6]   W.J. Albery and M.L. Hitchman, *'Ring-Disc Electrodes'*, Clarendon Press, Oxford, (1971).

[7]   S. Pons, M. Datta, J. Mc.Aleer and A. Schott Hinmann, *J. Electroanal. Chem.*, **160**, 369, (1984).

[8]   Y. Nakato, A. Tsumura and H. Tsubomura, *'Photoeffects at Semiconductor-Electrolyte Interfaces'*, Ed. A.J. Nozik, p. 145, A.C.S. Symposium, Houston, March, (1980).

[9]   R. Memming and J.J. Kelly, *'Photochemical Conversion and Storage of Solar Energy'*, Ed. J.S. Connolly, Chapter 9, Academic Press, New York, (1981).

[10] J.J. Kelly and R. Memming, *J. Electrochem. Soc.*, **129**, 730, (1982).

[11] K. Schröder and R. Memming, *Ber. Bunsenges., Phys. Chem.*, **89**, 385, (1985).

[12] *'International Critical Tables of Numerical Data, Physics, Chemistry and Technology'*, Vol. 5, first edition, Ed. E.W. Wasburn, Mc.Graw-Hill Book Comp. Inc., New York, (1929).

[13] R.A.L. van den Berghe, F. Cardon and W.P. Gomes, *Surf. Sci.*, **39**, 368, (1973).

[14] R. Memming, *'Photoelectrochemistry, Photocatalysis and Photoreactors'*, Ed. M. Schiavello, Nato Sec. C, Vol. 146, p. 107, D. Reidel, Dordrecht, (1984).

[15] W.W. Gärtner, *Phys. Rev.*, **116**, 84, (1959).

[16] H.J. Lewerenz, H. Gerischer and M. Lübke, *J. Electrochem. Soc.*, **131**, 100, (1984).

[17] F. Decker, *Electrochim. Acta*, **30**, 301, (1985).

[18] K.J. Vetter, *'Electrochemical Kinetics'*, Academic Press, London, (1967).

[19] S.R. Morrison, *'Electrochemistry at Semiconductor and Oxidized Metal Electrodes'*, Plenum Press, New York, (1980).

[20] C.W. Wilmsen, *'Physics and Chemistry of III-V Compound Semiconductor Interfaces'*, chapter 7, p. 403, Ed. C.W. Wilmsen, Plenum Press, New York, (1985).

[21] K.E. Heusler and K.S. Yun, *Electrochim. Acta*, **22**, 977, (1977).

[22] I.A. Ammar, S.A. Darwish, M.W. Khalil and S. El-Tahler, *Electrochim. Acta*, **33**, 231, (1988).

[23] H. Löwe and I. Barry, *Z. Phys. Chemie, Leipzig*, **249**, 73, (1972).

[24] H. Löwe, *Z. Phys. Chemie, Leipzig*, **249**, 30, (1972).

[25] H. Gerischer and W. Mindt, *Electrochim. Acta*, **13**, 1329, (1968).

[26] H. Gerischer and I. Wallem-Mattes, *Z. Phys. Chem. N.F.*, **64**, 187, (1969).

[27] M. Pourbaix, *'Atlas d'Equilibres Électrochimiques'*, Gauthier-Villars, Paris, (1963).

[28] J.E.A.M. van den Meerakker, *Electrochim. Acta*, **30**, 435, (1985).

[29] G.M. Barrow, *'Physical Chemistry'*, Mc.Graw-Hill Int. Book Comp., London, (1983).

[30] (a) *'Gmelins Handbuch der Anorganischen Chemie'*, Brom (7), p. 115, Verlag Chemie, Berlin, (1931).
(b) N.V. Sidgwick, *'The Chemical Elements and their Compounds'*, vol. II, page 1193, Oxford University Press, Oxford, (1951).

[31] *'Handbook of Chemistry and Physics'*, 37th edition, Ed. C. Hodgman. The Chemical Rubber Co., (1955).

[32] H. Gerischer and W. Mindt, *Surf. Sci.*, **4**, 440, (1966).

[33] J.S. Basi, *U.S. Patent* 3,738,882.

[34] A. Reisman and R. Rohr, *J. Electrochem. Soc.*, **111**, 1425, (1964).

[35] P. Janietz, R. Weiche, J. Westfahl and R. Landsberg, *Electroanal. Chem.*, **112**, 63, (1980).

[36] P.H.L. Notten, J.J. Kelly and H.K. Kuiken, *J. Electrochem. Soc.*, **133**, 1226, (1986).

[37] J. van de Ven, J.E.A.M. van den Meerakker and J.J. Kelly, *J. Electrochem. Soc.*, **132**, 3020, (1985).

[38] H. Gerischer and I. Wallem-Mattes, *Z. Phys. Chem. N.F.*, **64**, 187, (1969).

[39] P.H.L. Notten, *J. Electrochem. Soc.*, **131**, 2641, (1984).

[40] J.A. Harrison and Z.A. Khan, *J. Electroanal. Chem.*, **30**, 87, (1971).

[41] K.W. Frese, Jr., *J. Phys. Chem.*, **85**, 3911, (1981).

Chapter 6

Reactions at InP electrodes

6.1. Introduction

In contrast to GaAs relatively little is reported in the literature concerning the behaviour of InP in solutions containing conventional oxidizing agents such as Ce^{4+}. This is surprising since aqueous etching of InP is very important in the production of opto-electronic devices. Most of the commonly used etchants are based on concentrated solutions of HCl or HBr or a combination of one of these with other acids [1-4]. Bromine solutions are also used [5,6]. The Br_2 solutions were shown to be chemical etchants for GaAs (section 5.4) and not electroless etchants as one might expect. It might be expected that InP is also etched chemically by bromine. These observations suggest that InP does not readily dissolve in etchants involving simple oxidizing agents. In order to determine the reason for this behaviour, charge transfer reactions between InP and various redox systems were investigated. This is described in section 6.2. The implications of these results with regard to macroscopic etching of InP are considered.

To get more insight into the dissolution mechanism and dissolution kinetics, macroscopic etching of InP in solutions of HCl, HBr or bromine was reexamined (section 6.3 and 6.4). These results are discussed in relation to the electrochemical results obtained at p-type electrodes in the same solutions.

The results obtained at InP in this chapter will be separately summarized together with those obtained at GaAs in chapter 7.

6.2. VB and CB charge transfer reactions

6.2.1. Introduction

In this section charge transfer reactions at InP electrodes will be examined. For electroless systems which etch in the dark, only valence band reactions need be considered (section 2.5). To examine the limitations of such reactions, electron transfer via the conduction band of the solid will also be taken into account. For this purpose two redox systems ($pH = 0$)
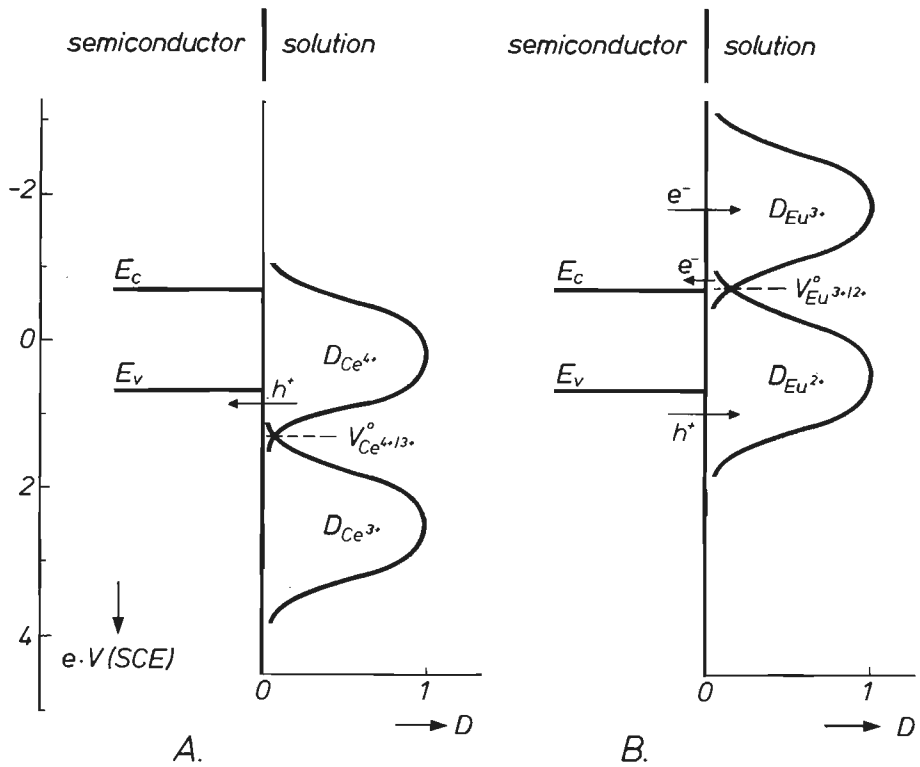
Fig. 6.1. Energy band model for InP, given on a voltage scale (versus SCE) in contact with solutions of $pH = 0$. E_c and E_v refer to the conduction and valence band-edges. The solutions contain:
A) $Ce^{4+/3+}$ system having a positive V^o value of $+1.20$ V.
B) $Eu^{3+/2+}$ system having a negative V^o value of -0.68 V.
$\lambda = 1.0$ eV for all distribution functions. The various charge transfer reactions between the VB or the CB of InP and the redox systems in solution, described in the text, are indicated.

were selected from Fig. 2.8 with a large difference in standard redox potential, viz. $Ce^{4+/3+}$ with a $V^o_{Ce^{4+/3+}} = +1.20$ V and $Eu^{3+/2+}$ with a $V^o_{Eu^{3+/2+}} = -0.68$ V [7]. The position of the band-edges in acid solution as obtained from Mott-Schottky measurements at both p- and n-type InP [8,9] is indicated in Fig. 6.1. The distribution functions of both the $Ce^{4+/3+}$ and $Eu^{3+/2+}$ redox systems are also represented schematically in Fig. 6.1.A and B, respectively. For both systems a reorientation energy of $\lambda = 1.0$ eV is assumed, similar to that reported for $Fe^{3+/2+}$ [10], and which is within the range of many other uncomplexed redox couples [11].

From Fig. 6.1.A it is clear that as a result of the positive value of $V^o_{Ce^{4+/3+}}$ with respect to the VB ($V^o_{Ce^{4+/3+}} - V^o_{fb} \approx +0.5$ V) the rate of Ce^{4+} reduction by hole injection should be very high and should be determined by diffusion of Ce^{4+} in solution. On the other hand, since there is a good overlap between the D_{ox} function of Eu^{3+} and the CB, it should be possible to reduce Eu^{3+} at a high rate when sufficient electrons are available at the semiconductor surface (Fig. 6.1.B). These reduction reactions were studied at p-InP electrodes in the dark and under illumination.

As far as the oxidation of Eu^{2+} at InP is concerned, it is clear from Fig. 6.1.B that, as the overlap between the D_{ox} function of Eu^{2+} is much better with the VB than with the CB, oxidation of Eu^{2+} should be dominated by the hole transfer reaction. However, this does not prove to be the case [12]. By studying this system at both p- and n-type InP electrodes, useful additional information has been obtained about the charge transfer reactions at both semiconductor bands. These results will also be presented and will be discussed in relation to the results obtained in V^{2+} solutions, another strong reducing agent.

Finally, the results obtained at InP will, in some cases, be compared with results obtained at GaAs. The implications with regard to electroless etching of InP in simple oxidizing agents both in the dark and under illumination, are also discussed.

6.2.2. Results

When a stationary p-InP electrode is held at a potential of 0.00 V in a 0.1 M Ce^{4+} solution of $pH = 0$ a reduction current density of about -0.075 mA·cm^{-2} is found in the dark. This value varies from one electrode to another but is always very low compared to the 3 mA·cm^{-2} expected for a diffusion-controlled hole injection rate found at Pt and GaAs under the same conditions (compare with the A-group oxidizing agents in section 5.2.3). After introducing the electrode into the solution at 0.00 V, the

potential was scanned potentiodynamically $(20 \text{ mV} \cdot \text{s}^{-1})$ to positive potentials. The current-potential curve is shown as curve (a) of Fig. 6.2. The cathodic current is essentially constant at negative potentials and decreases at 0.40 V as a result of anodic dissolution of p-InP. At about 0.75 V a shoulder in the anodic curve is found, followed by a clear hysteresis in the reverse scan as curve (b) of Fig. 6.2 shows. After anodic oxidation, the reduction of Ce^{4+} at negative potentials is decreased to a negligibly low rate (curve (b)). It is further noted that the Ce^{4+} reduction is not restored in the following scans and that the onset potential for the anodic oxidation of InP becomes more positive in the subsequent scans. Moreover, when an InP crystal was immersed in the dark for longer times at the open-circuit potential in the same solution as used in Fig. 6.2, no etching was found. This result in combination with the electrochemical results clearly indicates that holes are not injected from Ce^{4+} into the VB of InP.

In contrast to the blocked VB reaction in the case of Ce^{4+} reduction, it was found [9,12] that the photoreduction of Eu^{3+} via the CB of p-InP (Fig. 6.1.B) is very efficient. The onset of the cathodic photocurrent due to
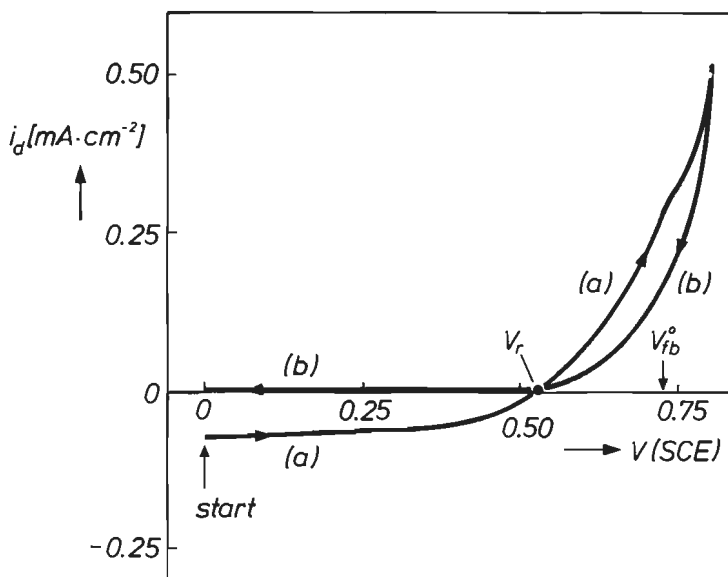
Fig. 6.2. Potentiodynamic $(20 \text{ mV} \cdot \text{s}^{-1})$ current-potential curves for a stationary p-InP electrode in the dark in a 0.1 M Ce^{4+}, 0.5 M H_2SO_4 solution. The electrode was immersed in the electrolyte at 0.00 V and the potential was then scanned in the positive direction (curve (a)). Curve (b) gives the reverse scan. The open-circuit potential (V_r) and the flat-band potential (V_{fb}^o) are indicated.

Eu^{3+} reduction starts at a potential approximately 400 mV more positive than that for the photoreduction of water to hydrogen (for comparison see Fig. 2.10.B). At more negative potentials the Eu^{3+} reduction is determined by the light intensity. This result shows that the reduction of Eu^{3+} by photo-electrons can effectively compete with the recombination reaction and this further indicates that charge transfer via the CB occurs readily.

Since the D_{ox} function of Eu^{2+} ($D_{Eu^{2+}}$) overlaps with both semiconductor bands (Fig. 6.1.B), oxidation of Eu^{2+} can occur either by hole capture from the valence band, i.e.

$$Eu^{2+} + h^+(VB) \rightarrow Eu^{3+}, \qquad (6.1)$$
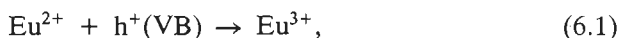
or by electron injection into the conduction band, i.e.

$$Eu^{2+} \rightarrow Eu^{3+} + e^-(CB). \qquad (6.2)$$
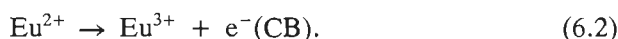
As the overlap of $D_{Eu^{2+}}$ with the VB is very favourable it should be possible to oxidize Eu^{2+} easily at p-InP in the dark (eq. (6.1)). However, no additional anodic current was found besides that resulting from anodic dissolution of p-InP at positive potentials [12]. This is strange since we have shown that this oxidation reaction (eq. (6.1)) takes place at p-GaAs in the dark several hundred millivolts before the anodic dissolution starts, indicating that charge transfer via the VB of GaAs is indeed very efficient [12]. This difference with InP does not result from the slightly more negative position of the VB-edge of GaAs ($E_v = +0.30$ e·V(SCE) at $pH = 0$), as no additional oxidation current was found at p-InP in electrolytes of higher pH [12]. When the pH of the solution is raised the position of the semiconductor bands is shifted to more negative potentials (see section 2.2) but this has thus no influence on the oxidation of Eu^{2+}. Similar behaviour was also found at InP with V^{2+} as reducing agent [12], despite the fact that the standard redox potential of the $V^{3+/2+}$ system is even 200 mV more positive than that of the $Eu^{3+/2+}$ system ($V^0_{V^{3+/2+}} = -0.50$ V [7]). Since the reorientation energies of both redox systems are similar ($\lambda = 1.2$ eV for V^{2+} [11]) this also results in a better overlap between the VB of InP and the $D_{V^{2+}}$ function compared to the $D_{Eu^{2+}}$ function. No additional oxidation of V^{2+} was found at p-InP, while the rate of oxidation at p-GaAs is again very fast [12].

On the other hand, although the overlap of $D_{Eu^{2+}}$ and the CB is poor at InP (Fig. 6.1.B) it was found that electron injection into the CB (eq. (6.2)) is still possible [12]. This is shown in the voltammogram of Fig. 6.3, curve (a) for a stationary n-InP electrode in the dark in a 0.01 M Eu^{2+} so-
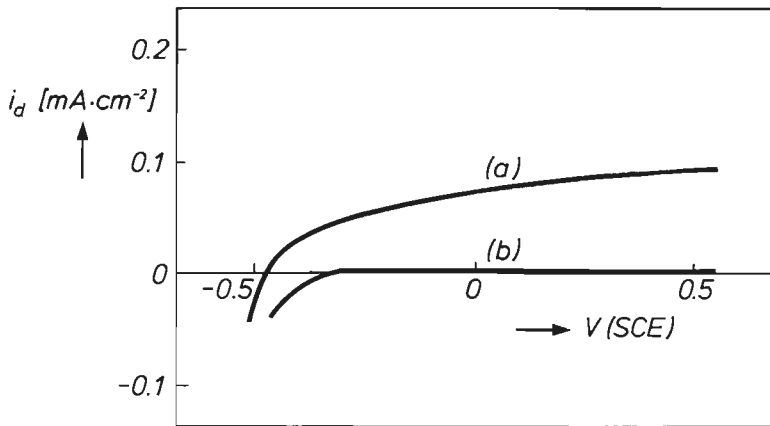
Fig. 6.3. Current-potential curves for a stationary n-type InP electrode in the dark in a solution of 1 M HCl containing 0.01 M Eu^{2+} (curve (a)) and in a solution of 1 M HCl without redox system (curve (b)).

lution of $pH = 0$. The anodic dark current at positive potentials, which must be attributed to electron injection at this type of electrode, is only slightly potential-dependent over a wide potential range (compare curves (a) and (b) of Fig. 6.3). This is in agreement with an electron transfer reaction from the solution into the CB (see eq. (2.30)). The rate of electron injection is reasonably high for the Eu^{2+} concentration used, certainly when the poor overlap between $D_{Eu^{2+}}$ and the conduction band is taken into account. Similar results are also reported for the V^{2+} oxidation at InP [12].

In conclusion, these results show that oxidation of Eu^{2+} and also of V^{2+} can proceed via the CB of InP (eq. (6.2)) but that these reactions via the VB (eq. (6.1)) are hindered despite the fact that the density of occupied states in solution corresponding to the VB is much higher than that corresponding to the CB.

6.2.3. Discussion

Both the anodic oxidation of InP at positive potentials (curves (a) and (b) of Fig. 6.2) and the blocked cathodic reduction of Ce^{4+} at negative potentials (curve (b) of Fig. 6.2) point to the formation of an anodic oxide layer. Menezes et al. [13] discussed the anodic dissolution of several III-V semiconductors and showed that a surface film is formed at InP electrodes not only in alkaline and neutral solutions but even in acidic solutions of

pH = 0 and at very low anodic current densities ($i^a < 10 \ \mu A \cdot cm^{-2}$ [13]). The composition of oxide films grown on InP with different techniques and under various conditions has been widely studied and is reviewed by Wilmsen [14]. It was found that anodically grown films consist mainly of In_2O_3 [14]. It is obvious that when such oxide layers reach a certain thickness the rate of electron transport through this layer will be negligibly low (see eq. (5.5) in the previous chapter). As has been shown, this affects not only hole injection from an oxidizing agent (Ce^{4+} reduction) but also hole capture by a reducing agent in solution (Eu^{2+} and V^{2+} oxidation).

On the other hand, it is found that charge transfer via the CB, viz. the photoreduction of Eu^{3+} at p-InP and the oxidation of Eu^{2+} at n-InP in the dark (Fig. 6.3, curve (a)), is not hindered. We must therefore assume that the oxide film has energy levels which correspond to the CB of InP. It is known that In_2O_3 is a semiconductor with a large band-gap [14]. The E_g^{ox} is reported to be 3.55 eV [15,16]. We have suggested [12] that the CB of the thin anodically formed oxide film (E_c^{ox}) is located close to that of InP, so that electrons can be transferred between InP and redox species in solution via the CB of the oxide. This is schematically represented in Fig. 6.4. As a consequence of the large band-gap of In_2O_3, the position of the valence band-edge of the oxide (E_v^{ox}) is located at extremely positive potentials, far more positive than that of InP (E_v). As a result, charge transfer between the VB of InP and Ox_2^{n+} or Red_2 in solution is blocked (Fig. 6.4). This energy band model can account for the observed features only when the thickness of the anodic oxide film is considerable, say more than 3 - 4 nm ([12] and section 8.2 of [17]; see also section 5.3), so that the rate of electron tunneling via the VB is decreased to very low values. Charge transfer via the CB is not affected by these oxide films.

This does not explain the low reduction rate of Ce^{4+} at cathodic potentials ($i_d^c \approx 0.075 \ mA \cdot cm^{-2}$) when an anodic oxide is not present (curve (a) of Fig. 6.2). It is, however, well-known that InP readily forms a native oxide when exposed to oxygen and/or water [14]. The initial growth rate of these oxides is very rapid and it has been shown that the growth continues, though at a lower rate, even when the storage period under ambient conditions is more than a year. Therefore, the thickness of the native oxide is strongly dependent on the exposure time of InP crystals but is, in general, more than 2.5 nm [14]. This must be the reason for the inhibited Ce^{4+} reduction at cathodic potentials (curve (a) of Fig. 6.2) and this also explains why the reduction current density varies somewhat from one electrode to another.

That the hole injection by Ce^{4+} (at pH = 0) can indeed occur at almost
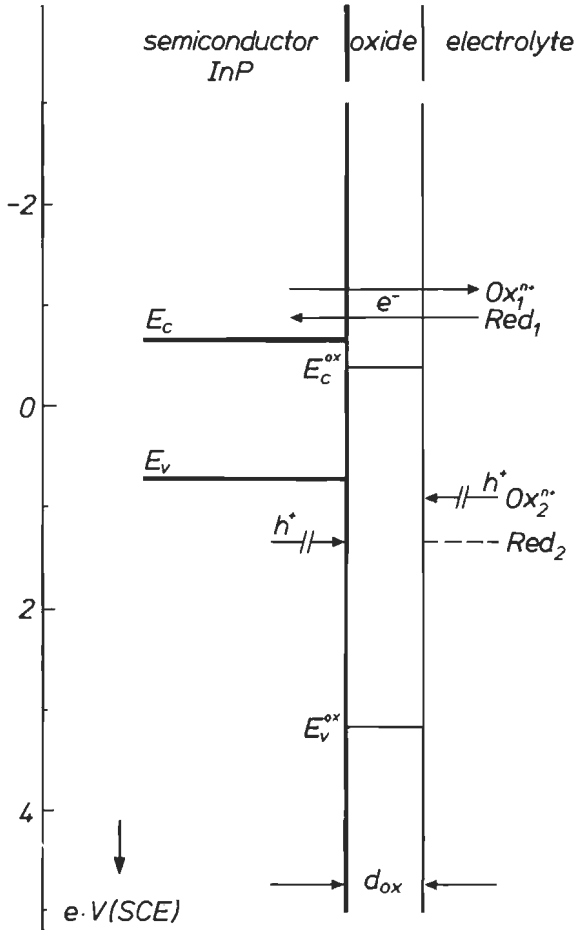
Fig. 6.4. Energy band model of an oxide (In_2O_3) covered InP electrode in a solution of $pH = 0$. The thickness of the oxide layer is indicated by d_{ox}. E_c and E_v refer to the conduction and valence band-edges of InP at this pH. The semiconducting properties of the oxide layer ($E_g^{ox} = 3.55$ eV for In_2O_3) are of essential importance in this model. E_c^{ox} and E_v^{ox} refer to the conduction and valence band-edges of the oxide. It is postulated that E_c^{ox} is positioned close to the CB of InP. As a consequence electron transfer between InP and redox systems in solution via the CB of the oxide is possible whereas hole transfer via the VB of the oxide is blocked. The various charge transfer reactions, described in the text, are indicated.

a diffusion-controlled rate, as expected from the good overlap of the distribution function of Ce^{4+} and the VB (Fig. 6.1.A), has recently been shown at a depassivated InP electrode [18]. The depassivation and consequently the increase of the hole injection rate as a function of time resembles very closely the passivation results obtained at p-GaAs in alkaline $Fe(CN)_6^{3-}$ solutions as shown in Fig. 5.9. However, in the InP case depassivation times of up to one hour are found, indicating that the resistant oxide does not readily dissolve in these electrolytes.

These results have obvious consequences for dark electroless etching systems. It is clear that, even when a depassivated InP crystal is taken as starting material, these etchants cannot be very successful, since electroless dissolution involves the anodic oxidation of InP which is always accompanied by oxide formation [13]. Oxide formation cannot therefore be prevented and pretreatment to remove the native oxides [5] does not work in the InP case.

On the basis of the above results, it should be possible to photo-etch InP under electroless conditions. In section 2.5 it has been shown that photo-etching systems require oxidizing agents whose energy levels correspond to those of the CB. Since charge transfer via the CB of InP is not hindered, these photo-electroless systems may be more successful than dark electroless systems. It is indeed reported [19] that InP can be etched under illumination in Fe^{3+}-containing acid solutions whereas etching is not found in the dark. Since the $Fe^{3+/2+}$ system has a $V_{ox/red}^{o}$ of $+0.53$ V which lies within the bandgap of InP, and Fe^{3+} has a λ of 1.0 eV [10], the overlap between $D_{Fe^{3+}}$ and the CB is very favourable (compare with Fig. 6.1). This complies with the condition described above for photo-etching. It seems likely that other oxidizing agents having a negative $V_{ox/red}^{o}$ can also be used as electroless photo-etchants. It should, however, be noted that minority charge carriers are always involved in photo-systems (see section 2.5) and consequently, a very fast electron transfer from the CB to the oxidizing agent in solution is essential in order for charge transfer to compete effectively with the recombination of majority and minority charge carriers. Electrochemical measurements have shown that this is the case for the reduction of Fe^{3+} by photo-electrons at p-InP. As this thesis is restricted to dark etching systems (section 5.2) we have not investigated these possibilities.

Since simple VB redox systems cannot be applied to dissolve InP crystals we must resort to chemical etching methods. Evidently, a precondition is that chemical etchants dissolve both the native oxide and the underlying semiconductor. This will be considered in the following two sections.

6.2.4. Conclusions

Electrochemical measurements on InP in acidic solutions containing various oxidizing and reducing agents have shown a significant difference between charge transfer reactions via the valence band and via the conduction band. Charge transfer via the VB is found to be strongly inhibited by a native oxide layer. Both reduction and oxidation reactions are completely blocked when InP is covered with an anodic oxide film. In contrast to the VB reactions it has been shown that redox reactions via the CB can occur efficiently at these oxide-covered electrodes. An energy band model is presented to account for these results. The wide band-gap semiconducting properties of the oxides are of essential importance in this model.

As a consequence of these electrochemical observations in acidic media it is concluded that due to oxide formation, dark electroless etchants, which involve charge transfer via the VB, fail at InP whereas photo-electroless systems in which the CB is involved can be more successful. Examples of both systems were given. Since an anodic oxide film is also readily formed in solutions of high pH [13], this very likely also holds for alkaline solutions.

6.3. Electrochemistry and etching in HCl and HBr solutions

6.3.1. Introduction

As already noted in section 6.1, etchants based on HCl and HBr are widely used for the production of InP semiconductor devices [1-3]. The presence of other acids, for example concentrated acetic acid, in these solutions has a significant influence on the etch rate [1,2]. In the previous section it was concluded that simple oxidizing agents cannot be applied for InP. Furthermore, it is obvious that HCl and HBr cannot be considered as simple conventional oxidizing agents. For these reasons it was interesting to investigate the dissolution mechanism of InP in these solutions. For this purpose flow-cell measurements were performed at p-type InP electrodes under potentiostatic control in the dark and the etch rate was correlated with the measured current density. This was investigated as a function of the HCl and HBr concentration in two different etching systems; viz. aqueous solutions and solutions of concentrated acetic acid [1,2].

The macroscopic etching kinetics of InP(001) in both systems was investigated by measuring the rotation rate dependence of the etch rate at p-InP RDEs in the dark.

During the etching experiments gas is evolved at the crystal surface. This

result can give useful information with regard to the dissolution mechanism of InP. Therefore, this gas was analyzed both qualitatively and quantitatively.

Finally, to study the effect of the dissolution of InP in these solutions on the position of the semiconductor band-edges and on the electrochemical behaviour of these electrodes, both impedance and current-potential measurements were made at p-InP electrodes in the dark.

6.3.2. Results

Flow-cell experiments

In Fig. 6.5, results are given for the potentiostatic etching of p-InP in the dark in HCl solutions. Curves (a) and (b) of this figure show the current-potential curves of this electrode in 3 M and 6 M HCl, respectively (filled and open circles). At negative potentials the current is very low in both cases. In the vicinity of the flat-band potential the anodic current increases, as expected. It should be noted that the anodic curve for the 6 M HCl solution is shifted slightly in the cathodic direction with respect to that for the 3 M solution.

The total dissolution rate, according to the ICP analysis, is shown for both solutions in curves (c) and (d), respectively, as a function of the potential. For the 3 M solution (curve (c)), the dissolution rate follows the current closely. At negative potentials the etch rate (v_t) is very low and increases considerably near the flat-band potential. If we assume that in this case etching is due solely to anodic dissolution, then it can be easily shown, using eq. (2.39), that six holes are required to dissolve one InP entity. The total etch rate-potential curve for the 6 M HCl case (curve (d)) differs markedly from that of the corresponding current-potential curve (b). This difference is most obvious at negative potentials, at which the InP dissolves at a rate essentially independent of the applied potential. Since InP does not dissolve anodically in this range, it can be concluded that the semiconductor is chemically dissolved by HCl (see section 2.6). If we assume that anodic dissolution in 6 M HCl here also requires six holes per InP, then the chemical etch rate can be calculated from the total etch rate and the measured anodic current. Curve (f) shows that the chemical etch rate (v_{ch}) remains constant, even at potentials at which the electrode dissolves anodically. In 3 M HCl no chemical etching is found (curve (e)).

A further example is shown in Fig. 6.6 for 1.5 M HCl in concentrated acetic acid solution. Etchants based on HCl and acetic acid are often used in
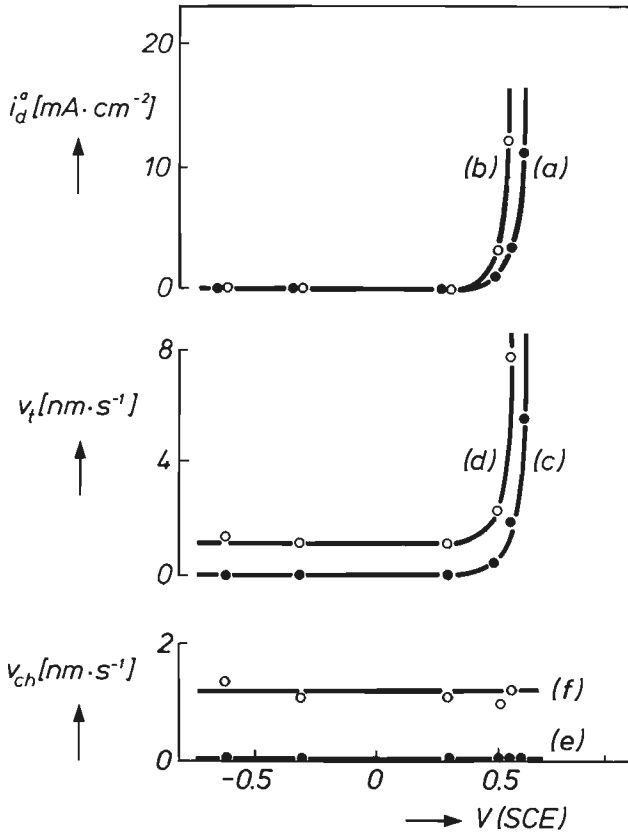
Fig. 6.5. Potentiostatic current-potential curves (a) and (b), total etch rate (v_t) as a function of the electrode potential (curves (c) and (d)), and chemical etch rate (v_{ch}) as a function of the electrode potential (curves (e) and (f)) for a p-InP electrode in the dark in 3 M HCl (●) and 6 M HCl (○) aqueous solutions. The measurements were performed with the flow-cell.

InP technology [1]. Curve (a) of Fig. 6.6 shows the current-potential curve, and curve (b) the measured chemical etch rate as a function of the electrode potential. The results in the cathodic region are similar to those found with 6 M HCl solution; the current is low and a remarkably high chemical etch rate is found (compare with curves (e) and (f) of Fig. 6.5). The slow increase of the chemical etch rate with potential is probably due to a roughening of the electrode surface during the experiment. The increase in the anodic current at potentials near V_{fb}^o is considerably lower than that found
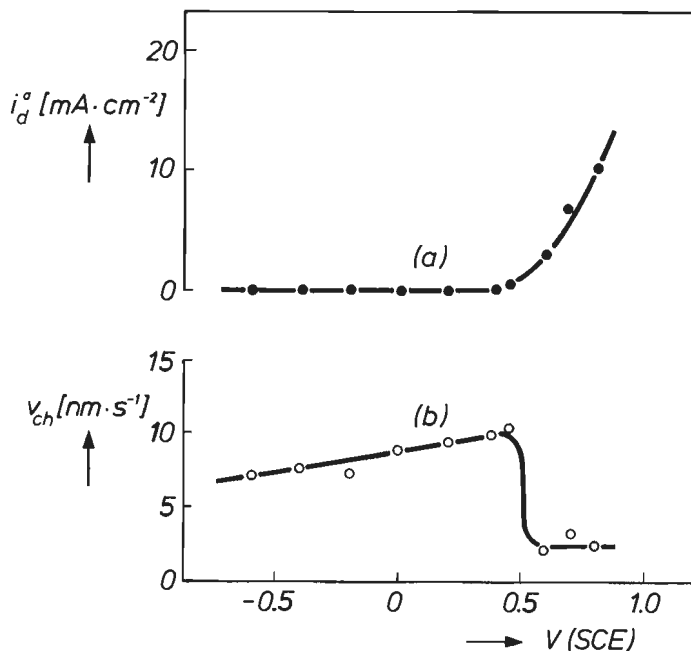
Fig. 6.6. Potentiostatic current-potential curve (a) and chemical etch rate (v_{ch}) as a function of the electrode potential (curve (b)) in the dark for a p-InP electrode in a solution of 1.5 M HCl in concentrated acetic acid. The measurements were performed with the flow-cell.

in a HCl solution of the same concentration but without acetic acid. A dramatic decrease of the chemical dissolution rate is observed when the anodic dissolution starts. The formation of an orange-coloured film at the electrode was observed in this potential range. Only phosphorus was found in this film by EDAX analysis. Obviously, a passivating film is formed during anodic dissolution. This film inhibits both the anodic and the chemical dissolution reactions. That the chemical etch rate can be influenced by the presence of an anodic oxide film was noted before in section 5.5, where chemical attack of OCl^- at GaAs in alkaline solutions was also found to be reduced to a negligibly low rate in the anodic potential region (see Fig. 5.24).

It should be noted that the chemical dissolution rate depends markedly on the surface condition of the InP electrode. Since induction effects are observed, care must be taken to ensure a constant dissolution rate before measurements are made. This is done by pre-etching the electrode in the
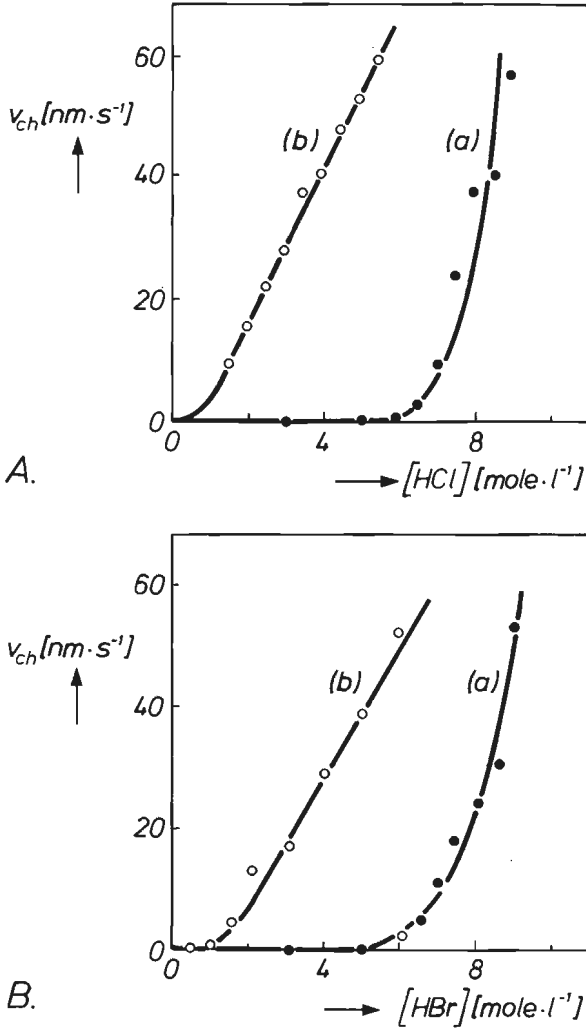
Fig. 6.7. Chemical etch rate (v_{ch}) for a p-InP crystal in the dark was measured at the open-circuit potential as a function of the HCl concentration (A) and as a function of the HBr concentration (B). The HCl and HBr concentration was varied by diluting with water (curves (a)) or concentrated acetic acid (curves (b)). The experiments were made in the flow-cell.

same etching solution. The induction effects are related to the presence of a native oxide film at the crystal surface, as discussed in section 6.2.3. Once the oxide layer is chemically dissolved, direct chemical attack of InP by HCl can proceed and a constant dissolution rate is established.

The results shown so far suggest that the chemical etch rate of InP is strongly dependent on the HCl concentration. Results very similar to those found for the HCl solutions in Figs. 6.5 and 6.6 were also found for HBr solutions. To study the chemical etch rate dependence on both the HCl and HBr concentration, the concentration of both acids was varied over a wide range. Two different systems were investigated: aqueous and acetic acid solutions. An InP crystal was chemically etched in these solutions in the flow-cell (at the open-circuit potential), and the chemical dissolution rate was again analytically determined by ICP emission spectrometry. The results are shown in Fig. 6.7.A for the HCl solutions and in Fig. 6.7.B for the HBr solutions. For curves (a), the concentration was varied by diluting concentrated HCl and HBr with water. The resemblance between the two curves is striking. At a concentration of 9 M, the chemical dissolution rate is high and decreases rapidly as the HCl or HBr concentration is lowered. For a concentration of 5 M, the etch rate is less than 0.07 nm·s^{-1} and even lower for more dilute solutions in both cases. For curves (b), the concentration was varied by diluting with concentrated acetic acid. It is striking that here a linear relationship between the etch rate and HCl and HBr concentration is observed and that the etch rate is significantly higher than in the corresponding HCl/H$_2$O and HBr/H$_2$O solutions (curves (a) of Fig. 6.7.A and B, respectively).

Rotation rate dependence

To investigate whether the dissolution is a diffusion-controlled or a kinetically controlled process, the etch rate was measured as a function of the electrode rotation rate using a p-InP RDE at the open-circuit potential. In this experiment the flow-cell was not used; instead the RDE was etched for 10 minutes at a constant electrode rotation rate. For each rotation rate a freshly prepared solution (15 ml) was used. Afterwards, the indium concentration was again determined with ICP. Two etchants based on HCl and HBr, in which InP is dissolved at a considerable rate, were selected from Fig. 6.7 to investigate the dissolution kinetics, viz. a 3 M HCl in concentrated acetic acid solution and an aqueous 8 M HBr solution. For the HCl solution the chemical etch rate is essentially independent of the electrode rotation rate. This means that the rate of the dissolution reaction is kinetically controlled (see eq. (2.45)). For the HBr solution the chemical etch

rate is found to be clearly dependent on the electrode rotation rate. A plot of the results according to eq. (2.45) reveals that the dissolution of InP in this HBr solution is under mixed kinetic and diffusion control.

Gas analysis

When an InP crystal was dissolved at the open-circuit potential in concentrated solutions of either HCl or HBr, gas evolution was observed at the solid surface. Using the colour-detector method (see experimental chapter 3), this gas was shown to be phosphine. The amount of phosphine was also determined with a gas burette and it was found that the phosphorus is converted quantitatively (100% $\pm$ 1%) to PH_3 gas.

Electrochemical measurements

Potentiodynamic (10 mV·s^{-1}) current-potential curves were measured at a stationary p-InP electrode in the dark in 0.5 M H_2SO_4 and in different aqueous solutions of either HCl or HBr. The results obtained in the former two solutions are shown in Fig. 6.8. In all cases, the blocking current in the
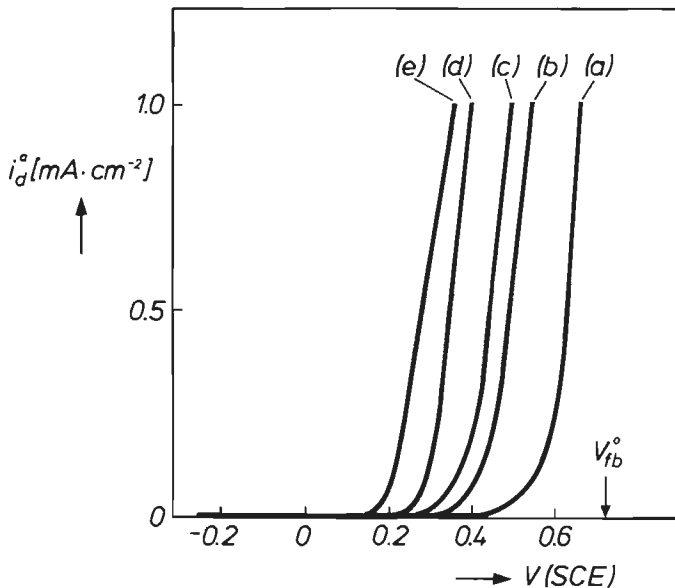
Fig. 6.8. Potentiodynamic (10 mV·s^{-1}) current-potential curves for a stationary p-InP electrode in the dark in 0.5 M H_2SO_4 (curve (a)), 1 M HCl (curve (b)), 5 M HCl (curve (c)), 7 M HCl (curve (d)), and 9 M HCl (curve (e)) in water. The results obtained with p-InP in various HBr solutions resemble very closely the above HCl results in curves (b)-(e).

cathodic region was very low (< 0.02 mA·cm^{-2}). The onset of the anodic current in the case of 0.5 M H$_2$SO$_4$ (curve (a)) occurs near the flat-band potential, as expected. The anodic current for 1 M HCl (curve (b)) is shifted some 150 mV in the negative potential direction with respect to the H$_2$SO$_4$ case. With an increase in the HCl concentration, this effect becomes more pronounced (curves (c)-(e)). For the 9 M HCl solution (curve (e)), the shift amounts to 350 mV. When the curve was measured again in 0.5 M H$_2$SO$_4$ after the HCl experiments, exactly the same result was obtained as in the first measurement with the anodic current onset at approximately +0.45 V. It should be noted that the increase of the anodic current is often accompanied by a shoulder as observed before in Fig. 6.2, and sometimes by a peak. The current density at which this appears is, however, rather irreproducible and seems to depend on the previous history of the electrode. Shifts of the current-potential curves similar to those obtained in HCl solutions in Fig. 6.8 were also obtained at p-InP in solutions of HBr. In that case the magnitude of the shift is also found to be clearly dependent on the HBr concentration.

Impedance measurements

Mott-Schottky plots were also measured at p-type InP for each of the solutions used in Fig. 6.8. In all cases a perfect linear dependence of C_t^{-2} on the electrode potential was found. The flat-band potential, as obtained after extrapolating to $C_t^{-2} = 0$, did not depend on the HCl concentration. In both H$_2$SO$_4$ and HCl solutions a V_{fb} of 0.725 ± 0.050 V was measured. The slope of the Mott-Schottky plots decreased somewhat as the HCl concentration was increased. This is probably due to an increase in the surface area of the electrode due to roughening as a result of chemical etching. A similar effect can also be seen in Fig. 6.6.

6.3.3. Discussion

From Fig. 6.5 and 6.7.A, it is obvious that chemical dissolution occurs in aqueous solution when the HCl concentration exceeds a certain critical value. The rate is strongly dependent on the HCl concentration and becomes very low at values lower than 5 M (see Fig. 6.7.A, curve (a)). A similar result is found for chemical dissolution in HBr solutions (curve (a) of Fig. 6.7.B). These results suggest that the etch rate depends on the degree of dissociation of HCl and HBr molecules. Although it is clear that at low concentration the dissociation of HCl and HBr is complete, there is a considerable discrepancy in the literature with respect to the higher concentra-

tions [20]. Calculations based on vapour pressure measurements and on Hammett functions show that the concentration of undissociated HCl begins to increase significantly above 5 mole·l^{-1} [21,22]. In order to avoid the uncertainty involved when HCl is diluted with water, the dissolution rate was studied in HCl/acetic acid solutions. The dissociation constant of HCl in acetic acid ($K_a = 10^{-8.55}$) is much lower than in water ($K_a \approx 10^{+3}$) [23]. Consequently, the degree of dissociation of HCl in acetic acid is negligible, even at low HCl concentrations. The chemical etch rate could therefore be studied as a function of the molecular HCl concentration. The linear dependence of the chemical dissolution rate on the HCl concentration in concentrated acetic acid (Fig. 6.7.A, curve 8b)) indeed confirms that chemical dissolution is determined by the molecular HCl concentration. A similar reasoning can be applied to HBr. Since HBr is an even stronger acid than HCl in aqueous solutions ($K_a \approx 10^{+6}$ [23]) dissociation is complete at HBr concentrations lower than 5 molar, and no etching occurs. Only at high concentrations is the degree of dissociation lower as a result of water deficiency and InP is etched by HBr molecules (curve (a) of Fig. 6.7.B). This is confirmed in curve (b) of Fig. 6.7.B where HBr is diluted with acetic acid. In this environment HBr also becomes a weak acid ($K_a = 10^{-7}$ [24.a,b]) and a linear relationship with high etch rates is therefore expected (curve (b) of Fig. 6.7.B) in contrast to aqueous solutions. A high etch rate in HCl and HBr solutions diluted with concentrated acetic acid, also found by Adachi and Kawaguchi [1], can be understood in this way. From the rotation rate dependence of the chemical etch rate it is clear that in the case of HCl the rate is kinetically determined by molecular HCl and that the chemical etch rate is under mixed kinetic/diffusion control in the case of HBr solutions.

The mechanism presented by Gerischer et al, for the chemical dissolution of semiconductors involves symmetrical bifunctional etching agents such as H_2O_2 and bromine molecules [25,26] (see also sections 2.6 and 5.4). However, in the previous chapter OCl$^-$ was reported to be the first asymmetrical chemical etching agent for GaAs (section 5.5). In the present section asymmetrical molecules are again involved in chemical etching reactions, now at InP. Although we are dealing with asymmetrical HCl and HBr molecules, a reaction scheme similar to that for symmetrical agents is proposed. The first step involves a synchronous exchange of bonds: for the InP/HCl system this means that In $-$ Cl and P $-$ H bonds replace the original H $-$ Cl and In $-$ P bonds. This is very likely the rate-determining step. This step can be represented as

$$\text{(6.3)}$$

To complete the dissolution of one InP entity two more HCl molecules are necessary:

$$\text{(6.4)}$$

Indium is therefore dissolved as hydrolyzed $InCl_3$ and PH_3 is evolved as a gas. Such a mechanism can account for the etching results observed in HCl solutions. A similar reaction sequence can be given for the chemical dissolution of InP in HBr solutions in which hydrolyzed $InBr_3$ and phosphine are formed.

The chemical etch rate is independent of the electrode potential. At potentials near the flat-band value the p-InP electrode dissolves anodically (Figs. 6.5 and 6.6). The rate of the anodic etching increases as the surface hole concentration is increased, i.e. as the potential is made more positive (eq. (2.6)). In aqueous HCl solutions, it is shown that six holes are required to dissolve one InP entity. This means that both In and P are oxidized to the trivalent state, as is common for III-V materials (see section 2.4) [25-28]. With a considerable concentration of acetic acid in the HCl solution, however, a film is formed on the electrode which inhibits both the chemical and anodic dissolution (Fig. 6.6). EDAX measurements have shown that this layer contains phosphorus but no indium or chlorine. We suspect that, in this case, phosphorus is not oxidized directly during anodic dissolution:

$$InP + 3h^+(VB) \rightarrow In^{III} + P. \qquad \text{(6.5)}$$
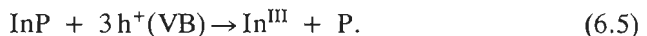
A similar three-hole mechanism has been shown for Gap [29].

Two different effects which are related to chemical etching and which were noted before in chapter 5 during chemical etching of GaAs, should be discussed:

– in the first place, it was postulated in section 5.4 that as a result of chemical dissolution of GaAs in bromine solutions, dipoles are formed at the semiconductor/solution interface which affect the potential drop over the Helmholtz layer (eq. (5.15)). Consequently, the flat-band potential shifted a few hundred mV toward positive potentials. During chemical etching of

InP in the present concentrated HCl and HBr solutions, a change of the Helmholtz potential might also be expected. However, Mott-Schottky measurements clearly showed that this is not the case ($V_{fb} = +0.725 \pm 0.050$ V in all solutions). Apparently, the density of surface dipoles is negligible in these solutions. It was already noted that the first chemical dissolution step of eq. (6.3) is very likely the rate determining step. If the second and third chemical steps are much faster than the rate-determining step, the density of surface dipoles should be low and the flat-band potential should not change significantly during chemical etching in HCl and HBr solutions. A similar explanation can be given for GaAs in alkaline solutions of OCl^-. Here too, only a slight positive shift of the flat-band potential is observed during chemical etching in the dark (curve (a) of Fig. 5.23).

- in the second place, it is obvious from Fig. 6.8 that the chemical dissolution rate strongly influences the electrochemical behaviour of InP. Anodic dissolution starts at a more negative potential as the HCl or the HBr concentration is increased, although the flat-band potential does not change. This must mean that the reaction rate constant for electrochemical dissolution is improved by chemical etching. A similar effect has been demonstrated by Gerischer and Wallem Mattes [26] and was observed in Fig. 5.18, curve (a) for the dissolution of GaAs in bromine solution. This result can be explained if the rupture of the first In $-$ P bond is assumed to be rate determining for the anodic dissolution reaction. This is generally assumed to be the case for the anodic dissolution of GaAs electrodes (see section 4.2.3). This assumption also seems reasonable for InP electrodes. As in the GaAs case, this first electrochemical step can be represented as

$$-\!\!\!\!\diagdown\!\!\text{In} \cdot\cdot \text{P} \!\diagdown\!\!\!\!- \quad + \quad h^+(VB) \quad \xrightarrow{\;k_1^a\;} \quad -\!\!\!\!\diagdown\!\!\text{In}^\oplus \cdot \text{P} \!\diagdown\!\!\!\!- \;, \qquad (6.6)$$
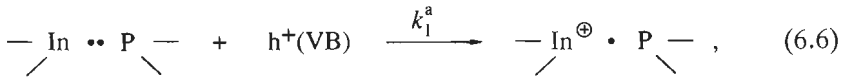
(compare with eq. (4.4)). If this In $-$ P bond is broken during a chemical attack by either HCl or HBr molecules, then the remaining bonds are more easily attacked anodically and the onset potential for anodic dissolution is consequently shifted to negative values [26].

6.3.4. Conclusions

The dissolution of InP in HCl and HBr solutions follows a chemical mechanism in which undissociated HCl and HBr molecules play a decisive

role. Since the dissociation of these strong acids in aqueous solutions is complete up to a concentration of approximately 5 molar, no chemical etching was found in 'dilute' solutions. However, at higher concentrations the etch rate increases rapidly since as a result of water deficiency total dissociation can no longer occur. On the other hand, in concentrated acetic acid solutions, both HCl and HBr are weak acids and chemical etching of InP can take place even at relatively low concentrations; a linear dependence of the etch rate on both the HCl and HBr concentration were found in these acetic acid solutions. The chemical etching kinetics were found to be under kinetic control in HCl solutions and under mixed kinetic/diffusion control in HBr solutions.

Before chemical etching of InP can occur, the native oxide layer has to be dissolved. It was found that this oxide layer is also dissolved in the present HCl and HBr solutions, although variable induction times for the various oxide films have to be taken into account.

The electrochemical behaviour of InP is found to be strongly influenced by the chemical dissolution reaction. The overpotential for anodic dissolution is significantly reduced when the rate of chemical etching increases. Negative shifts of about 350 mV were found for the anodic current onset. Chemical and electrochemical dissolution mechanisms can account for these results.

6.4. Electrochemistry and etching in Br$_2$ solutions

6.4.1. Introduction

Various etchants used in InP technology are based on bromine [1,5,30]. Bromine can be dissolved either in an organic solvent, for instance methanol [30,31], or in aqueous solution [1]. In the present section only aqueous bromine solutions will be considered.

It was already noted in the introduction to section 5.4, that the partial vapour pressure of Br$_2$ in aqueous solutions is high; as a result the Br$_2$ concentration in solution usually decreases as a function of time. Working solutions are obtained when Br$_2$ is complexed by bromide (eqs. (5.13) and (5.14)). It is evident that when a large excess of Br$^-$ is available in these solutions, complexing is more effective. It was, however, shown in section 6.3 that undissociated HBr molecules also etches InP chemically. Etching in aqueous HBr solutions only becomes important at higher HBr concentrations (with HBr > 5 molar; curve (a) of Fig. 6.7.B). Therefore, in the

present work 4.5 M HBr solutions were used. It can be shown from the equilibrium constants given in section 5.4.1, that Br_2 is complexed almost completely at this HBr concentration (mainly to Br_3^- via eq. (5.13)).

It was concluded in section 5.4.4 that the dissolution of GaAs in the dark in bromine solutions proceeds via a chemical mechanism. Taking into account the fact that dark electroless etching systems in which the valence band of InP is involved are not successful (section 6.2), it is likely that InP is also etched by Br_2 via a chemical mechanism. To investigate this, flow-cell measurements were made at p-InP electrodes under potentiostatic control in the dark and the etching results are considered in relation to the electrochemical results. The influence of light on the chemical etch rate of GaAs in bromine solutions was found to be significant. Therefore flow-cell measurements under illumination are also considered at p-InP in this section.

To investigate the macroscopic dissolution kinetics of InP, two different measurements were made: first, to determine the order of the dissolution reaction, the Br_2 concentration in 4.5 M HBr was varied over a wide range and the etch rate was measured, again with the flow-cell; secondly, to determine whether the reactions are kinetically or diffusion-controlled, the rotation rate dependence of both the etch rate and electrochemical Br_3^- reduction was measured at a p-InP RDE. The results are compared. There are indications in the literature that the etch rate of InP may depend on the surface orientation of the InP crystals [1,32,33]. The above measurements were therefore made not only on the (001) surface orientation but also on the (111)In orientation. The latter crystal plane is generally found to have the lowest etching rate [1,33].

6.4.2. Results

Flow-cell experiments

The flow-cell experiments of Fig. 6.9 show the potentiostatically measured current density (curve (a)) and etch rate (curve (b)) of a p-InP electrode in the dark in a 0.1 M Br_2, 4.5 M HBr solution. The etch rate is expressed as a current density assuming that six charge carriers are needed to dissolve one InP entity (see section 3.2.3). At negative potentials the current density is low (curve (a)). The anodic dissolution starts at 0.2 V, a rather negative potential with respect to flat-band potential ($V_{fb}^o = 0.72$ V at $pH = 0$) and the rate increases at more positive potentials. In the potential range where no current is observed, InP is etched chemically (curve (b)). The etch rate is independent of the applied potential. This behaviour is typical of a chem-
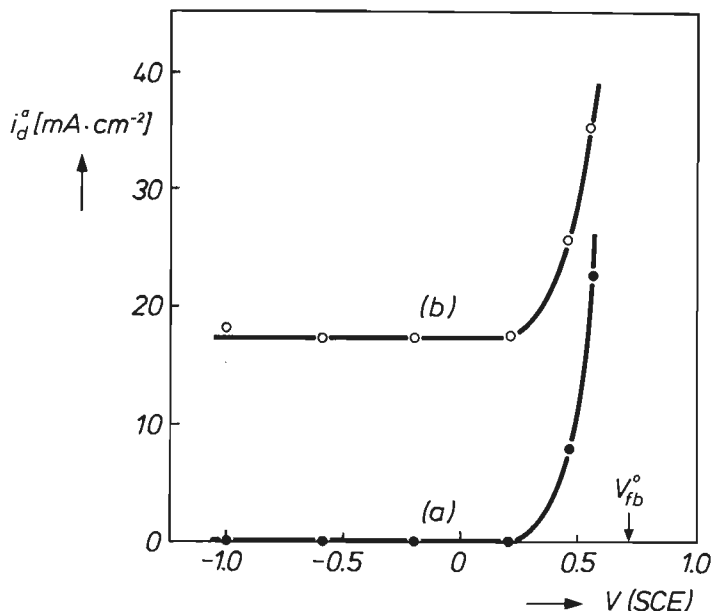
Fig. 6.9. Flow-cell measurements at a stationary p-InP electrode in the dark in a solution of 0.1 M Br$_2$ and 4.5 M HBr. The current-potential curve (a) and the chemical etch rate (curve (b)) were measured under potentiostatic control. The etch rate is expressed as a current density.

ical etchant and is similar to that found before for GaAs in bromine solutions (section 5.4). In the potential range where an anodic current is observed the etch rate increases; in addition to chemical etching, anodic dissolution of InP occurs. Chemical etching also explains why the onset of the anodic current (curve (a) of Fig. 6.9) occurs at a rather negative potential; the rate constant for the electrochemical dissolution of InP is significantly enhanced. A similar effect was described before for p-GaAs in bromine solutions in section 5.4, and for p-InP in HCl and HBr solutions (compare with Fig. 6.8). It should be noted that in the present Br$_2$/HBr solutions both Br$_2$ and HBr contribute to the total shift of approximately 300 mV to negative potentials.

The chemical etch rate at the open-circuit potential was measured as a function of the Br$_2$ concentration in a 4.5 M HBr solution for p-InP crystals with two different surface orientations. The results are presented in Fig. 6.10 on a double logarithmic scale. The bromine concentration was varied over almost two orders of magnitude. Curve (a) shows that the slope of the line
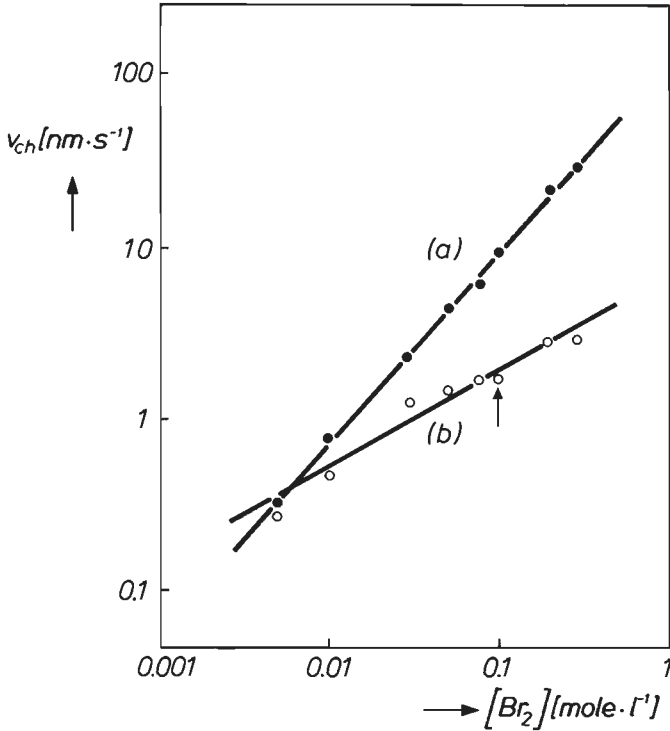
Fig. 6.10. Chemical etch rate (v_{ch}) for a p-InP crystal was measured at the open-circuit potential as a function of the Br_2 concentration in a solution of 4.5 M HBr with the flow-cell; curve (a): (001) surface orientation, curve (b): (111)In orientation. Measurements were made in the dark.

for the (001) orientation is close to one. This means that the etch rate is first order in bromine concentration. This in turn means that the etch rate can either be kinetically or diffusion-controlled. Curve (b) shows the dependence found for InP with the (111)In orientation. The slope is in this case close to 0.5, which means that the chemical etch rate must be kinetically controlled and depends on the square root of the Br_2 concentration.

So far, only results obtained in the dark have been presented. In Fig. 6.11 flow-cell experiments under illumination are shown. The experimental conditions are the same as those described for the dark experiment in Fig. 6.9. In Fig. 6.11 two different light intensities were used. For case A of this figure a moderate light intensity was used. It reveals a large potential-independent reduction current over a broad potential range (curve (a)). In this
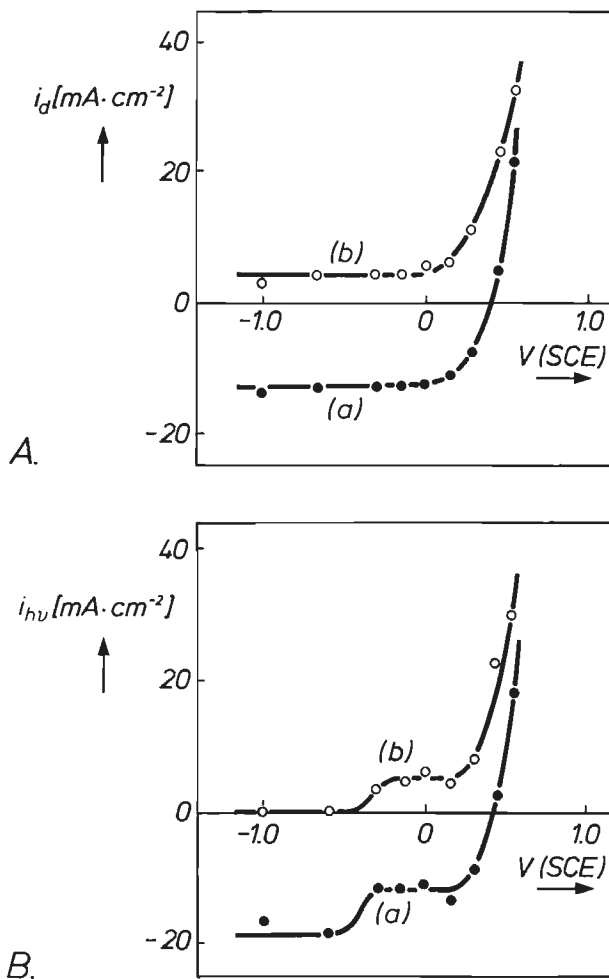
Fig. 6.11. Flow-cell experiments at a stationary p-InP electrode under illumination (Schott lamp) in the same solution as used for Fig. 6.9 (0.1 M Br_2, 4.5 M HBr). Two different light intensities were used:
A) a moderate light intensity ($e \cdot \phi \approx i_{lim}^c$).
B) a high light intensity ($e \cdot \phi > i_{lim}^c$).
The current-potential curves (a) and the chemical rates (curves (b)) were measured under potentiostatic control.

potential range no hydrogen evolution is observed and the chemical etch rate is reduced to a potential-independent value of 4 mA·cm^{-2} (curve (b)) compared to 17.5 mA·cm^{-2} in the dark (see curve (b) of Fig. 6.9). As in the dark case, the current density increases at about 0.2 V as a result of anodic dissolution of InP. Consequently, the total etch rate increases at positive potentials (curve (b)). In Fig. 6.11.B the electrode was illuminated with a higher light intensity. Curves (a) and (b) correspond again to the potentiostatically measured current density and chemical etch rate, respectively. The results at potentials more positive than −0.3 V are essentially the same as those found at the lower light intensity (Fig. 6.11.A). However, at potentials more negative than −0.3 V the reduction current in curve (a) of Fig. 6.11.B increases to a higher value and hydrogen evolution occurs. Due to this gas evolution the reduction current fluctuates to some extent. It is clear from curve (b) of Fig. 6.11.B that in this potential range the chemical etch rate is reduced to zero.

Rotation rate dependence

From the results of the flow-cell experiments in the dark it is concluded that the dissolution rate of InP with a (001) surface orientation was first order in bromine concentration. In order to decide whether the etch rate is under kinetic or diffusion control, v_{ch} was measured at the open-circuit potential as a function of the electrode rotation rate using a p-InP RDE. The etch rate was again determined analytically by measuring the indium concentration in the etching solution with ICP. Fig. 6.12 shows the chemical etch rate as a function of the square root of the angular velocity for a p-InP (001) RDE in the dark. A perfect straight line passing through the origin is found. This means that the Levich equation is obeyed and that the chemical etch rate for this crystal orientation is diffusion-controlled (see eq. (2.45) with k_{ch} very large).

In Fig. 6.13 the dependence of the cathodic current density on the electrode rotation rate is shown for a p-InP(001) RDE. The working electrode was illuminated with a high light intensity at a potential of +0.15 V. Thus the experimental conditions are the same as at the cathodic plateau in the flow-cell experiment of Fig. 6.11.B. The straight line through the origin indicates that the reduction is also diffusion-controlled under these conditions (eq. (2.42)).
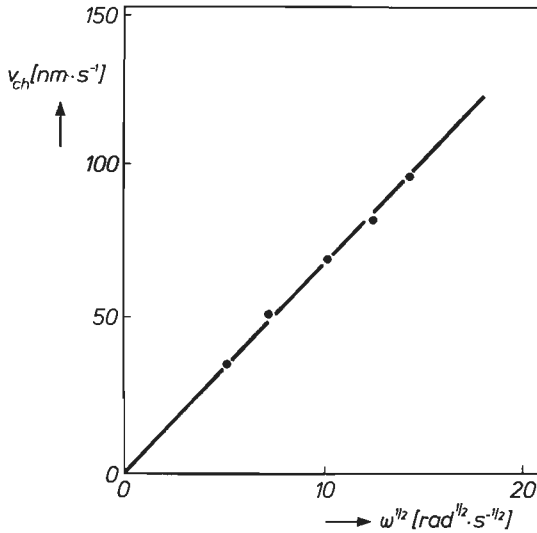
Fig. 6.12. Chemical etch rate (v_{ch}) in the dark as a function of the square root of the angular velocity ($\omega^{\frac{1}{2}}$) of a p-InP RDE at the open-circuit potential in a solution of 0.1 M Br_2 and 4.5 M HBr (the same solution as used in Fig. 6.9).
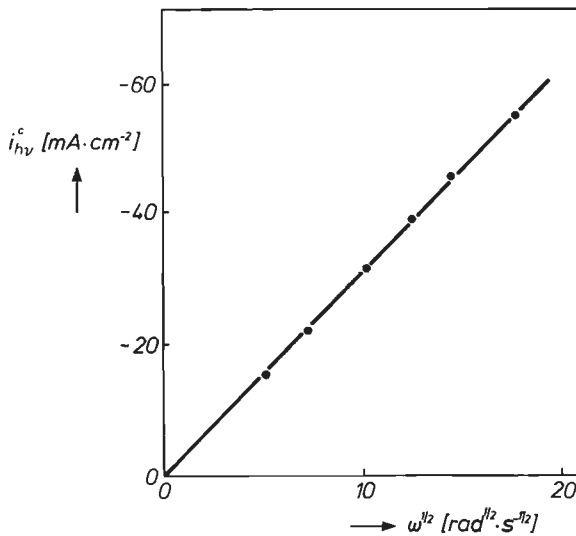
Fig. 6.13. Plateau current density (i_{hv}^c) at a potential of +0.15 V as a function of the square root of the angular velocity ($\omega^{\frac{1}{2}}$) for a p-type InP(001) RDE under illumination (Schott lamp) with a high light intensity ($e \cdot \phi > i_{lim}^c$) in a solution of 0.1 M Br_2, 4.5 M HBr.

6.4.3. Discussion

From the potential-independent etch rate in the flow-cell experiment of Fig. 6.9, curve (b) it is concluded that InP is etched chemically in a solution of 0.1 M Br_2, 4.5 M HBr. Etching must be attributed to complexed Br_2. That InP is etched chemically by Br_2 can also be seen in curve (a) of Fig. 6.9. Here the shift of the anodic dissolution curve is even more pronounced than that found in a 4.5 M HBr solution. The explanation of this shift is the same as that given in the previous section (see Fig. 6.8). The mechanism of the chemical dissolution of InP by symmetric Br_2 'molecules' can also be represented by a synchronous exchange of bonds according to

$$
\begin{array}{ccc}
\text{Br} \text{—} \text{Br} & & \text{Br} \quad \text{Br} \\
\qquad \text{—In—P—} & \xrightarrow{\;k_{ch}\;} & \text{—In} \quad \text{P—} \;,
\end{array}
\tag{6.7}
$$

where k_{ch} is the rate constant of the first rate-determining step in the dissolution process. Evidently, two more Br_2 molecules are needed to remove one InP entity from the crystal lattice. From the electrode rotation rate dependence in Fig. 6.12 and the etch rate dependence on the Br_2 concentration (curve (a) of Fig. 6.10), it must be concluded that the chemical dissolution rate is controlled by Br_2 diffusion in the solution and thus that k_{ch} is large. This holds for InP with a (001) orientation. For InP with a (111)In surface the etch rate is significantly lower (curve (b) of Fig. 6.10). The etch rate is here kinetically controlled. From the slope of this figure a reaction order of 0.5 is observed, which implies that one bromine atom may be involved in the rate-determining dissolution step. This would suggest that a simultaneous exchange of bonds does not occur. A possible explanation could be that due to steric hindrance a bromine molecule cannot attack In and P atoms simultaneously. From a crystallographic point of view the phosphorus atoms are 'buried' beneath the relatively large indium atoms of the (111)In surface and are therefore not accessible to a large species such as Br_3^-.

The electrochemical results of Fig. 6.11 under illumination indicate that Br_2 is reduced at negative potentials (curves (a) of Fig. 6.11.A and B) according to

$$
Br_2 + 2e^- \xrightarrow{k_e} 2Br^-. \tag{6.8}
$$

From these results it is not clear whether the reduction takes place via a simple conduction band process or a mixed conduction band/valence band

process. It should be noted that it is not easy to distinguish the two cases as has been shown for the bromine reduction at GaAs (section 5.4). In the present case, however, it is not important to discriminate between the two reactions. When the photon flux is high the Br_2 reduction is diffusion-controlled as the Levich dependence of Fig. 6.13 shows. This means that k_e is large. Due to the high photon flux an excess of photoelectrons is created. The electrons recombine with holes at potentials more positive than -0.6 V in curve (a) of Fig. 6.11.B. Recombination stops at potentials negative with respect to -0.6 V and hydrogen is evolved in addition to Br_2 reduction. This also indicates that the light intensity used in Fig. 6.11.A is critical since the rate of Br_2 reduction in curve (a) of this figure is the same as in curve (a) of Fig. 6.11.B and the current does not increase at cathodic potentials; here no hydrogen is evolved. Due to the electrochemical reduction of Br_2 the chemical etch rate of InP is reduced dramatically (compare curve (b) of Fig. 6.9 with curves (b) of Fig. 6.11). Similar results have been found for the reduction of bromine at p-GaAs (section 5.4) and for the reduction of hypochlorite at p-GaAs (section 5.5). However, since the Br_2 reduction is diffusion-controlled it is strange that the etch rate is not zero. This behaviour can only be explained as follows: both k_{ch} and k_e are large, so the reaction rate of each reaction is determined by Br_2 diffusion in the solution. The ratio of the k's can be deduced from the ratio of the chemical etch rate (curve (a) and the reduction rate (curve (b) in Fig. 6.11.B). It follows that

$$\frac{k_e}{k_{ch}} \approx 3. \tag{6.9}$$

The two values must be similar in magnitude. The rate constants and thus the k_e/k_{ch} ratio are independent of the electrode rotation rate. It is then possible that the Levich equation is obeyed for both processes at the same time, while the total Br_2 consumption is, of course, diffusion-controlled. Note that the sum of the chemical etch rate and the Br_2 reduction rate under illumination in Fig. 6.11 is exactly the same for the chemical etch rate in the dark (see Fig. 6.9, curve (b)).

In curve (b) of Fig. 6.11.B it is found that the chemical etch rate is decreased to zero in the potential range where hydrogen is evolved. Gagnaire et al. [35] described the cathodic decomposition of InP in alkaline solutions as a result of hydrogen evolution. An indium-rich surface is formed. Recently, Gorochov et al. [36], using various surface analysis techniques, showed that a white-coloured indium-rich surface is also formed in acidic

solutions during hydrogen evolution at cathodic potentials. We suggest that such a cathodically decomposed surface layer prevents Br_2 from etching the InP surface at a significant rate. The importance of hydrogen for the decomposition of InP is clearly shown in curve (b) of Fig. 6.11.A where the chemical etch rate does not decrease when hydrogen evolution is absent.

In the literature, a 'new' class of etching systems was presented for both InP [37,38] and GaAs [39] based on three components, viz. concentrated HBr, concentrated acetic acid and $K_2Cr_2O_7$. Adachi and co-workers [37-39] concluded that the etching mechanism of InP in the solutions is very complex. The results can, however, be simply understood as follows: $Cr_2O_7^{2-}$ is a strong oxidizing agent ($V^o_{Cr_2O_7^{2-}/Cr^{3+}} = +1.08$ V(SCE) [7]) whose D_{ox} function shows a very good overlap with the VB of InP at $pH = 0$ (compare with Fig. 6.1). It is argued in section 6.2, however, that the VB is blocked due to oxide formation and consequently that electroless dissolution of InP cannot occur in the dark. We confirmed the etching results of Weyher and Giling [40] and found, in accordance with section 6.2, that InP does not dissolve in the dark in acid solutions containing $Cr_2O_7^{2-}$; etching of InP in the above etchants [37-39] cannot therefore be attributed to $Cr_2O_7^{2-}$. Since the standard redox potential of the $Cr_2O_7^{2-}/Cr^{3+}$ redox system is much more positive than that of the Br_2/Br^- system ($V^o_{Br_2/Br^-} = +0.84$ V(SCE), $Cr_2O_7^{2-}$ can oxidize Br^- in the HBr solutions, used by Adachi et al. [37-39]. The overall electrochemical reaction in these acid solutions can be represented by

$$Cr_2O_7^{2-} + 14H^+ + 6Br^- \rightarrow 2Cr^{3+} + 3Br_2 + 7H_2O. \qquad (6.10)$$

When the orange-coloured $Cr_2O_7^{2-}$ solution is mixed with a colourless HBr solution, Br_2 is formed instantaneously as can be recognized by the immediate formation of a dark brown solution. Etching of InP in these solutions must therefore be attributed to complexed Br_2 and proceeds, as concluded in the present section, by a chemical mechanism. In addition, besides chemical dissolution by bromine, chemical attack by HBr molecules may contribute to some extent to the overall etch rate of InP. This is even likely since dissociation of HBr is strongly inhibited in solutions containing acetic acid (see Fig. 6.7.B). It is obvious, that the Br_2 formed in the $Cr_2O_7^{2-}$/HBr solution is also responsible for the chemical dissolution of GaAs [39] (see section 5.4). In contrast to InP, GaAs does not dissolve in concentrated HBr solutions.

Finally, we conclude this section by stressing the importance of the various etchants in InP technology. In contrast to organic Br_2 solutions, aque-

ous Br_2 solutions do not attack photoresist layers, usually used to fabricate devices (see chapters 3 and 8). An additional advantage of the present Br_2/ HBr solutions is that they are far more 'stable' than organic bromine solutions as a result of the strong complexing by Br^- ions. It is therefore possible to perform etching experiments safely in an open vessel without this resulting in a significant decline of the bromine concentration in time.

6.4.4. Conclusions

InP, like GaAs, is dissolved in acidic bromine solutions by a chemical mechanism. Stable solutions are obtained when Br_2 is complexed, mainly to Br_3^-, by an excess of Br^- in solution. To reduce the contribution of chemical etching by HBr, however, its concentration should not exceed 5 molar. As a result of electrochemical bromine reduction, the chemical dissolution of InP by Br_2 under illumination is significantly reduced at negative potentials.

The kinetics of chemical dissolution are found to be dependent on the crystal orientation of the semiconductor: the etch rate of InP with a (001) surface orientation is controlled by transport of Br_3^- in solution and is thus first order in bromine concentration, whereas the etch rate of a crystal with a (111)In surface orientation is controlled by the kinetics of the dissolution reaction. In the latter case a reaction order of 0.5 was found, indicating that one bromine atom is involved in the rate determining chemical dissolution step.

As found with other chemical etchants, the onset potential of anodic dissolution of p-InP in the present bromine solutions is significantly shifted in the negative direction by more than 300 mV.

References

[1] S. Adachi and H. Kawaguchi, *J. Electrochem. Soc.*, **128**, 1342, (1981).
[2] S. Adachi, Y. Noguchi and H. Kawaguchi, *J. Electrochem. Soc.*, **129**, 1053, (1982).
[3] A. Huber and N.T. Link, *J. Cryst. Growth*, **29**, 80, (1975).
[4] C.J. Keavney and H.I. Smith, *J. Electrochem. Soc.*, **131**, 452, (1984).
[5] A. Guivarc'h, H.L.'Haridon, G. Pelous, G. Hollinger and P. Pertosa, *J. Appl. Phys.*, **55**, 1139, (1984).
[6] L.A. Coldren, K. Furuya and B.I. Miller, *J. Electrochem. Soc.*, **130**, 1918, (1983).

[7]   M. Pourbaix, *'Atlas d'Equilibres Électrochimiques'*, Gauthier-Villars, Paris, (1963).

[8]   P.H.L. Notten, *J. Electrochem. Soc.*, **131**, 2641, (1984).

[9]   K. Tubbesing, D. Meissner, R. Memming and B. Kastening, *J. Electroanal. Chem.*, **214**, 685, (1986).

[10] R. Memming and F. Möllers, *Ber. Bunsenges. Phys. Chem.*, **76**, 475, (1972).

[11] K.W. Frese Jr., *J. Phys. Chem.*, **85**, 3911, (1981).

[12] D. Meissner, Ch. Sinn, R. Memming, P.H.L. Notten and J.J. Kelly, *'Homogeneous and Heterogeneous Photocatalysis'*, Eds. E. Pelizzetti and N. Serpone, p. 317, D. Reidel Publ. Comp., Dordrecht, (1986).

[13] S. Menezes, B. Miller and K.J. Bachmann, *J. Vac. Sci. Technol. B*, **1**, 48, (1983).

[14] C.W. Wilmsen, *'Physics and Chemistry of III-V Compound Semiconductor Interfaces'*, chapter 7, page 403, Ed. C.W. Wilmsen, Plenum Press, New York, (1985).

[15] P.J. Harrop and D.S. Campbell, *Thin Solid Films*, **2**, 273, (1968).

[16] R.L. Weiher, *J. Appl. Phys.*, **33**, 2834, (1962).

[17] S.R. Morrison, *'Electrochemistry at Semiconductor and Oxidized Metal Electrodes'*, Plenum Press, New York, (1980).

[18] J. van de Ven and H.J.P. Nabben, to be published.

[19] D. Lubzens, *Electron. Lett.*, **13**, 171, (1977).

[20] *'Gmelins Handbuch der Anorganischen Chemie'*, Chlor (6), Ergänzungsband, Teil B – Lieferung 1, p. 223, Verlag Chemie GmbH, Weinheim, Germany, (1968).

[21] A. Eucken, *Z. Electrochem.*, **52**, 255, (1948).

[22] W. Kangro, *Z. Phys. Chem.*, **32**, 273, (1962).

[23] W. Huber, *'Titrations in Nonaqueous Solvents'*, pp. 215 and 216, Academic Press, New York, (1967).

[24] (a) I. Gyenes, *'Titrations in Non-aqueous Media'*, p. 39, Iliffe Books, London, (1967).
      (b) see Ref. [23], p. 226.

[25] H. Gerischer and W. Mindt, *Electrochim. Acta*, **13**, 1329, (1968).

[26] H. Gerischer and I. Wallem-Mattes, *Z. Phys. Chem. N.F.*, **64**, 187, (1969).

[27] M.M. Faktor, T. Ambridge, C.R. Elliott and J.C. Regnault, *Curr. Top. Mat. Sci.*, **6**, 1, (1980).

[28] H. Gerischer and I. Mattes, *Z. Phys. Chem. N.F.*, **49**, 112, (1966).

[29] R. Memming and G. Schwandt, *Electrochim. Acta*, **13**, 1299, (1968).

[30] S. Adachi, H. Kawaguchi and G. Iwane, *J. Electrochem. Soc.*, **129**, 883, (1982).

[31] Y. Tarni, Y. Komiya and Y. Harada, *J. Electrochem. Soc.*, **118**, 118, (1971).

[32] H.C. Gatos and M.C. Levine, *J. Electrochem. Soc.*, **107**, 427, (1960).

[33] H.C. Gatos, *Science*, **137**, 311, (1962).

[34] J.E.A.M. van den Meerakker, *Electrochim. Acta*, **30**, 435, (1985).

[35] A. Gagnaire, J. Joseph, A. Etcheberry and J. Gautron, *J. Electrochem. Soc.*, **132**, 1655, (1985).

[36] O. Gorochov and L. Stoicoviciu, *J. Electrochem. Soc.*, **135**, 1159, (1988).

[37] S. Adachi, *J. Electrochem. Soc.*, **129**, 609, (1982).

[38] S. Adachi, Y. Noguchi and H. Kawaguchi, *J. Electrochem. Soc.*, **129**, 1524, (1982).

[39] S. Adachi and K. Oe, *J. Electrochem. Soc.*, **130**, 2427, (1983).

[40] J.L. Weyher and L.J. Giling, *J. Appl. Phys.*, **58**, 219, (1985).

Chapter 7

Overview of etching mechanisms and kinetics of various etchants

7.1. Introduction

This chapter is intended as a link between the electrochemical chapters, in which conclusions were drawn concerning macroscopic etching of III-V semiconductors, and the last chapter in which microscopic etching at resist edges is considered. New results will not be presented here. Instead, a summary will be given of electrochemical and macroscopic etching results obtained with GaAs and InP in various etching systems. Conclusions will be presented at two levels: a general consideration of the dissolution of III-V semiconductors and a more detailed description of the individual etchants for GaAs and InP.

The general considerations, resulting from the electrochemical studies at GaAs and InP, described in chapters 4, 5 and 6, will be presented in section 7.2. Features which are important in classifying the various etching systems are reviewed. Conclusions with regard to the etching mechanisms and macroscopic etching kinetics will be emphasized. It seems likely that a similar classification can also be applied to the dissolution of other III-V semiconductors.

The special etching conditions for each individual etchant studied in chapters 5 and 6 at GaAs and InP will be summarized in section 7.3. The conclusions are condensed in the form of an Etching Table (Table IV) which is presented at the beginning of that section. The review will be given on the basis of this Table. The Etching Table mainly comprises results from the previous chapters. In some cases, however, results from the literature will be discussed and will be included in this Table.

7.2. General considerations

On the basis of electrochemical and flow-cell measurements (section 3.2.3) it is clear that two etching mechanisms can be distinguished for the dissolution of III-V compounds:

Electroless dissolution

This dissolution mechanism is based on two separate electrochemical reactions which take place simultaneously on the same surface, viz. the anodic oxidation of the semiconductor in which holes are consumed and the reduction of an oxidizing agent which supplies these holes. Electroless etching can be described by the Mixed Potential Theory (section 2.5) and proceeds at the open-circuit potential (V_r) at which the partial anodic current (i^+) must be equal to the partial cathodic current (i^-). Since anodic oxidation depends on the surface hole concentration, the etch rate in these solutions can be changed by applying an external potential.

Obviously, during etching under electroless conditions at the rest potential, no external current flows (see Fig. 2.10). A precondition for electroless etching is that charge transfer can take place between an oxidizing agent in solution and the solid. Since only dark etching systems are considered, hole injection by an oxidizing agent into the valence band of the semiconductor is essential. This condition is fulfilled when the distribution function of the oxidizing agent (D_{ox}) overlaps with the VB. The degree of overlap determines the rate of hole injection: when this is poor the hole injection rate is kinetically-controlled; when, on the other hand, the overlap is favourable, the rate is limited by transport of the oxidizing agent in solution and the kinetics of the electroless dissolution reaction become diffusion-controlled. As a consequence, the position of the valence band-edge with respect to the standard redox potential of the oxidizing agent considered $(V_{ox/red}^{o})$ is of essential importance. From the discussion above, it is obvious that both the anodic oxidation of the semiconductor and the cathodic reduction of the oxidizing agent are important in determining the specific characteristics of each electroless etchant.

The anodic oxidation of GaAs was extensively studied in chapter 4. There it was argued that only acidic and alkaline solutions can be used to dissolve the solid since oxide passivates the semiconductor surface in the intermediate pH range. In general, etching systems are employed only at low and high pH. It was, however, found that the anodic oxidation of GaAs in alkaline solutions can also be accompanied by oxide formation when in the

initial stages of the oxidation process the maximum dissolution rate (i_{max}^a) is exceeded. Whether oxide formation occurs depends on the pH of the solution and the initial oxidation rate; the maximum dissolution rate was found to be controlled by OH^- diffusion in solution (section 4.2). It is clear that this oxide formation must be taken into account when alkaline electroless etchants are used. The anodic oxidation of GaAs in acidic solutions is, in general, not accompanied by film formation, unless oxide-promoting agents are added to the electrolyte (see section 4.2). In the case of InP it was shown (section 6.2) that, even in acidic solution, passive oxide films are easily formed, which prevent hole injection from solution.

Surface or interface charging during dissolution must also be taken into account. With impedance measurements it was shown at GaAs that positively charged intermediates of the oxidation reaction can act as surface states and cause a change in the Helmholtz potential (δV_H) under oxide-free conditions. As a result, the semiconductor band-edges are shifted downwards towards positive potentials during dissolution (section 4.3). When an oxide layer is formed during this reaction, these intermediates, now acting as interface states, induce a much larger potential drop over the oxide layer (V_{ox}), as the capacitance of this layer is significantly smaller than that of the Helmholtz layer. Consequently, the shift of the semiconductor band-edges is much larger under oxide-forming conditions (section 4.4). Since the hole injection rate depends on the degree of overlap between the D_{ox} function and the VB, it is obvious that these shifts can dramatically influence the kinetics of electroless dissolution of GaAs.

From the studies of the anodic oxidation it is clear that both oxide formation and surface/interface charging effects may influence the cathodic reduction of the oxidizing agent and consequently, electroless etching at the open-circuit potential (V_r). On the basis of these results two electroless systems can be distinguished:

(i) Oxide-free dissolution

When the maximum dissolution rate is not exceeded and the value of $V_{ox/red}^o$ is considerably positive with respect to the position of the VB, a high hole injection rate is obtained. The hole injection reaction is, in this case, cathodically controlled by diffusion of the oxidizing agent in solution and proceeds under oxide-free conditions.

When, however, the value of $V_{ox/red}^o$ is close to the position of the VB-edge, the hole injection rate is kinetically-controlled. During electroless etching of the semiconductor, the VB is shifted downwards, which further reduces the injection kinetics.

The macroscopic etching kinetics at the open-circuit potential can, under these oxide-free conditions, be obtained from the rotation rate dependence of the partial anodic (i^+) or partial cathodic current density (i^-) at V_r, when eq. (2.39) is used in combination with eq. (2.43). i^+ and i^- can be obtained from ring/disk measurements.

(ii) Oxide-forming conditions

When the initial hole injection rate exceeds the maximum dissolution rate, oxide formation limits the etch rate at V_r. As a result, holes supplied by the oxidizing agent must tunnel through the oxide layer in order to oxidize the solid at the semiconductor/oxide interface. It is obvious that this oxide layer hinders the charge transfer between the solution and semiconductor. Due to charging of the interface during etching, a large potential drop over the oxide film is established, which reduces the overlap between D_{ox} and the VB dramatically; a kinetically-controlled hole injection rate is, consequently, obtained. As the anodic oxidation rate is anodically limited, electroless etching of GaAs in alkaline solutions under these oxide-forming conditions is therefore anodically controlled by diffusion of OH^- in solution. The dissolution rate is ultimately determined by the rate at which the oxide dissolves chemically by OH^- into solution.

The macroscopic etching kinetics can, under these conditions, be determined by measuring the rotation rate dependence of i_{max}^a which is given by eq. (4.11). Combining eq. (4.11) with eq. (2.39) leads, of course, to eq. (2.45); the rotation rate dependence of the chemical dissolution rate of the oxide film.

In the case of InP a relatively thick oxide film influences the charge transfer between the VB and solution dramatically whereas charge transfer via the CB can proceed without difficulty. A model involving a wide band-gap semiconducting oxide was presented (Fig. 6.4 in section 6.2), to account for these results. Tunneling of holes from solution to the semiconductor/oxide interface cannot occur through these thick oxide layers. Since the VB is involved in dark electroless systems, this has serious consequences for the dissolution of InP in such etchants. In general, it can be concluded that electroless etchants cannot be employed to dissolve InP in the dark (see Table IV).

Chemical dissolution

In contrast to electroless dissolution, the chemical etch rate is not influenced by the surface hole concentration in the valence band of the semicon-

ductor. The rate is potential-independent over a wide potential range. This feature is actually used to distinguish between chemical and electroless dissolution mechanisms. From the results obtained with various chemical etchants, it was concluded that bifunctional etching-species are involved. These species were found to be either symmetrical, e.g. H_2O_2, Br_2 and Cl_2, or asymmetrical, such as OCl^-, HCl and HBr. A dissolution reaction scheme was proposed in which direct chemical attack of these bifunctional etching species at the semiconductor surface is essential; dissolution is initiated by a synchronous exchange of bonds between the solid and the etchant. This description can account for the fact that free charge carriers are not involved in the dissolution reaction (see e.g. section 6.3).

Since direct chemical attack of the semiconductor is necessary, chemical etching stops when an oxide is formed on the surface. As electron tunneling can still occur when the oxide layer is not too thick, it is, in principle, possible that an electroless mechanism takes over. Electroless etching at the open-circuit potential is anodically controlled under these conditions. An example in which the chemical dissolution rate is inhibited (InP in HCl/acetic acid) and an example in which an anodically controlled electroless mechanism takes over (GaAs in alkaline OCl^- solutions), were discussed in sections 6.3 and 5.5, respectively.

A plot of the rotation rate dependence of the chemical etch rate, according to eq. (2.45), reveals the macroscopic etching kinetics of III-V semiconductor in chemical etchants.

7.3. Etching Table

The most important features of the various etching systems for GaAs (001) and InP(001) are presented in the Etching Table IV. Some additional remarks have to be made before using this Table:

- Since the position of the valence band-edge with respect to $V^o_{ox/red}$ is only relevant for electroless etchants, these values are not presented for chemical etching systems.
- All potentials are given with respect to a Saturated Calomel Electrode (SCE).
- The electroless mechanism is cathodically controlled, unless otherwise stated.
- (i) and (ii) refer to electroless dissolution under oxide-free and oxide-forming conditions, respectively.
- In most cases the etching kinetics were determined by measuring the ro-

Table IV

Etching Table summarizing the macroscopic etching properties of both GaAs(001) and InP(001) in various etching systems considered in chapters 5 and 6. The most relevant features are given for each etchant: the standard redox potential of the active redox system ($V^o_{ox/red}$); the pH of the etching solution; the position of the valence band-edge (E_v) under standard conditions at that pH (only given for electroless systems); the etching kinetics and references (Ref).

Etching system	$V^o_{ox/red}$ (SCE)	pH	GaAs(001)				InP(001)		
			VB-edge V(SCE)	Etching mechanism	Etching kinetics	Ref	Etching mechanism	Etching kinetics	Ref
Ce^{4+}	+1.20	0	+0.30	electroless (i)	diffusion Ce^{4+}	(5.2)	–	–	(6.2)
$Fe(CN)_6^{3-}$	+0.22	11-14	−0.36/−0.54	electroless (i)	diffusion $Fe(CN)_6^{3-}$	(5.3)	electroless**	kinetic**	(6.2), [2,3]
				electroless (ii)	diffusion OH^- anodic control	(4.2, 5.3)			
$Fe(CN)_6^{3-}$	+0.22	4-5	+0.06/0.00	electroless (i)	kinetic ($\nu_e \approx 0$)	(5.2)	–	–	(6.2)
$Fe^{III}(EDTA)$	−0.12	5	0.00	electroless (i)	kinetic ($\nu_e \approx 0$)	(5.2)	–	–	(6.2)
$Fe^{III}(Oxa)$	−0.24	5	0.00	electroless (i)	kinetic ($\nu_e \approx 0$)	(5.2)	–	–	(6.2)
Fe^{3+}	+0.53	0-1.5	+0.30/+0.21	electroless (i)	kinetic ($\nu_e \approx 0$)	(5.2)	–	–	(6.2)
Cl_2	+1.11	0		chemical	diffusion* Cl_2	(5.4, 8.3)	chemical	diffusion* Cl_2	(8.3)
Br_2	+0.84	0		chemical	diffusion Br_2	(5.4)	chemical	diffusion Br_2	(6.4)
I_2	+0.38	0		chemical	kinetic	[4]	chemical	kinetic*	(8.2)
H_2O_2	+1.53	0		chemical	diff/kin H_2O_2	[6-9,14,15]	chemical	kinetic	[10,11]
		10-12		chemical	kinetic	[12,13]			
OCl^-	+0.70	11-14		chemical	diffusion* OCl^-	(5.5, 8.4)			
			−0.36/−0.54	electroless (ii)	diffusion OH^- anodic control	(4.2, 5.3, 5.5)			
HCl	–	0		–	–	–	chemical	kinetic	(6.3)
HBr	–	0		–	–	–	chemical	mixed control	(6.3)

* concluded from profile etching experiments near resist edges
** pH > 13.6, kinetically controlled electroless dissolution (see text)

tation rate dependence of the etch rate. In a few cases this was not done. However, on the basis of microscopic etching experiments, to be described in chapter 8, the macroscopic dissolution kinetics can also be deduced from the shape of etched profiles near resist edges. In these cases which are indicated with *, the reader is referred to the relevant section of chapter 8.

– References to sections of this thesis and to the literature are represented by ( ) and [ ], respectively.

On the basis of the Etching Table, the results obtained with each system will now successively be summarized.

$Ce^{4+}/pH = 0$; section 5.2.

Due to the very good overlap of $D_{Ce^{4+}}$ with the VB of GaAs at $pH = 0$ ($V_{Ce^{4+}/3+}^o - V_{fb}^o = +0.90$) hole injection is diffusion-controlled at negative potentials. The hole injection rate is not influenced by the downward shift of the semiconductor bands (by 50-150 mV) when GaAs is oxidized at more positive potentials (Fig. 5.1.A). Electroless etching at the open-circuit potential is therefore cathodically controlled by diffusion of Ce^{4+} in the solution (Fig. 2.10) and proceeds under oxide-free conditions. It should be noted that an electrochemically inert acid, such as H_2SO_4, should be used to obtain a strong acidic solution. HCl solutions are not suitable since Ce^{4+} oxidizes Cl^- to chlorine.

$Fe(CN)_6^{3-}/pH = 11$ - 14; section 5.3.

The overlap of $D_{Fe(CN)_6^{3-}}$ with the VB of GaAs in alkaline solutions is excellent (Table IV) and similar to the $Ce^{4+}/pH = 0$ case. However, the rate of anodic oxidation of GaAs in the pH range 11-14 is limited by the diffusion of OH^- (section 4.2). Oxide formation can influence the kinetics of the hole transfer reaction and must be taken into account. Therefore, two cases can be distinguished:

(i) Oxide-free dissolution; section 5.3.

When the hole injection rate is lower than the maximum dissolution rate in alkaline solutions, the dissolution of GaAs at the open-circuit potential is not accompanied by oxide formation. Electroless etching is cathodically controlled by $Fe(CN)_6^{3-}$ diffusion in solution (Fig. 2.10). Due to the positively charged intermediates of the dissolution reaction, a limited downward displacement of the semiconductor band-edges is found of the same order of magnitude as found for the Ce^{4+} case. This

does not affect the kinetics of hole injection (Fig. 5.1.A). In this case crystallographic defects are clearly revealed during etching (Fig. 5.15.A).

(ii) Oxide-forming conditions; sections 4.2 and 5.3.

When the initial hole injection rate is higher than the maximum dissolution rate, etching of GaAs by $Fe(CN)_6^{3-}$ at the open-circuit potential is accompanied by oxide formation. A model which describes the complex dissolution mechanism was presented in section 5.3 (Fig. 5.16): the thin oxide films, which were found to be of the order of 0.5-1.0 nm, inhibit the transport of holes from $Fe(CN)_6^{3-}$ in solution to the semiconductor/oxide interface where they serve to oxidize the solid. As a result $Fe(CN)_6^{3-}$ reduction becomes kinetically controlled. The actual dissolution rate is determined by the rate at which the oxide is dissolved at the oxide/solution interface. Electroless etching is therefore anodically controlled by OH^- diffusion (see Fig. 5.8) and proceeds in the presence of an oxide at an open-circuit potential about 200 mV more positive than that for oxide-free dissolution. The positively charged intermediates of the GaAs dissolution reaction which are now separated from the solution by an oxide layer, have a more drastic effect on the potential distribution at the semiconductor/oxide/electrolyte interface. Displacement of the semiconductor band-edges by 0.5-0.6 V to positive potentials were found (Fig. 5.16). This significantly reduces the overlap of $D_{Fe(CN)_6^{3-}}$ and the VB of GaAs. The hole injection rate becomes kinetically controlled. Very smooth surfaces are obtained in this case (Fig. 5.15.B).

In section 6.2 it was argued that electroless etching of InP cannot take place as a result of the formation of an oxide film, which does not readily dissolve into both acidic and alkaline [1] solutions. Therefore, InP is not expected to dissolve in alkaline $Fe(CN)_6^{3-}$-containing solutions either. Etching experiments in solutions of moderate pH confirmed this. However, preliminary results [2,3] indicate that etching, though kinetically inhibited, does take place in very strong alkaline $Fe(CN)_6^{3-}$ solutions ($pH > 13.6$ [3]). These results suggest that the oxide layer can dissolve in strong alkaline solutions making electroless etching by an oxidizing agent possible.

$Fe(CN)_6^{3-}/pH = 4\text{-}5$; section 5.2.

The dissolution of GaAs in acid solutions is, in general, not accompanied by oxide formation (section 4.2) and etching occurs under oxide-free conditions. However, since the position of the semiconductor band-edges depends significantly on the pH of the solution (section 2.2), the overlap of

$D_{Fe(CN)_6^{3-}}$ and the VB of GaAs in acid solutions is much more critical than in alkaline solutions. This has hardly any effect on the kinetics of the hole injection reaction at negative potentials. But, as a result of surface charging during electroless dissolution, the overlap is further reduced by 50-150 mV at the open-circuit potential (Fig. 5.1.B). This has dramatic consequences for the rate of the hole injection reaction at V_r. Dissolution proceeds under these oxide-free conditions via a cathodically controlled electroless process. The etch rate is, however, much too low ($v_e \approx 0$) to be of practical importance. Changing the pH of the solution is not effective in solving this problem; lowering the pH further reduces the overlap and thus the hole injection rate, as V_{fb}^o is pH-dependent and shifts to positive potentials (section 2.2); increasing the pH induces oxide formation, which completely passivates the semiconductor surface in the intermediate pH range (pH $\geqslant$ 6; section 4.1) and hinders the hole injection reaction.

$Fe^{III}(EDTA)/p$H = 5; section 5.2.
$Fe^{III}(Oxa)/p$H = 5; section 5.2.
Fe^{3+}/pH = 0-1.5; section 5.2.

Similar etching results as described above for the $Fe(CN)_6^{3-}$ system at pH = 5 were found for the electroless dissolution of GaAs in either $Fe^{III}(EDTA)$, $Fe^{III}(Oxa)$ or Fe^{3+}-containing acidic solutions (Tables III and IV). In all cases, the correspondence of energy levels between the D_{ox} functions and the VB of GaAs is very critical. Despite the fact that the rate of hole injection is high at negative potentials (even diffusion-controlled in the Fe^{3+} case), the rate of charge transfer is dramatically reduced at the open-circuit potential due to surface charging (Fig. 5.1.B). The negligibly low cathodically controlled electroless etch rate at V_r makes these systems unsuitable for practical use. Changing the pH of these solutions to increase the etch rate is not effective for the same reasons as discussed above in the $Fe(CN)_6^{3-}/p$H = 4-5 system at GaAs.

Cl_2/pH = 0; section 5.4.
Br_2/pH = 0; sections 5.4 and 6.4.
I_2/pH = 0; ref. [4].

It was concluded that both p- and n-type GaAs are etched in the dark at the open-circuit potential by Cl_2, Br_2 and I_2 via a chemical mechanism. From electrochemical measurements and profile etching experiments it was concluded that the kinetics of chemical etching of GaAs(001) are controlled

by diffusion of the halogen molecules in solution in the case of chlorine (section 8.3) and bromine (sections 5.4 and 8.4). The chemical etch rate in iodine solutions was reported to be kinetically controlled [4].

InP was also found (Fig. 6.9) to be dissolved in bromine solutions by a chemical mechanism (section 6.4). The kinetics of this reaction are controlled by Br_2 diffusion in solution at InP(001) and kinetically controlled at InP with the (111)In surface orientation. This result confirms the observation that the etch rate of III-V semiconductors can be strongly dependent on the crystal orientation.

It seems likely that InP is also etched by Cl_2 and I_2 via a chemical rather than an electroless mechanism, certainly when it is taken into account that acidic electroless etchants cannot, in general, be applied to InP, as concluded from section 6.2. Profile etching experiments (chapter 8) show that the chemical etch rate of InP(001) is diffusion-controlled in Cl_2 solutions and kinetically controlled in I_2 solutions.

H_2O_2; refs. [5-15].

Etchants based on H_2O_2 were briefly discussed in section 2.6, with regard to the chemical dissolution of Ge [5]. These etchants are also employed for III-V semiconductors [6,7]. H_2O_2 is either used in acidic [8-11] or alkaline solution [12,13]. The same distinction is made in Table IV. Since most comprehensive studies of the etching mechanism were made with GaAs [8,9,12-15], these conclusions will be summarized first. The few results reported on InP [10,11] are then discussed.

Acidic H_2O_2 solutions

The etching mechanism of GaAs in the dark in strongly acidic ($pH = 0$) H_2O_2 solutions containing either HCl or H_2SO_4 is reported in references [14] and [15], respectively. In both cases, the results found at a p-GaAs electrode resembled very closely the results obtained at the same type of electrode in an acidic bromine solution (section 5.4), i.e. H_2O_2 is not cathodically reduced in the dark at a significant rate (see curve (a) of Fig. 5.18). As the cathodic current required to account for an electroless mechanism was absent (sections 5.4 and 5.5), it was concluded that GaAs is also dissolved in acidic H_2O_2 solutions by a chemical mechanism.

The kinetics of the chemical dissolution reaction were found to be strongly dependent on the ratio of the acid and H_2O_2 concentrations, for HCl [6], H_2SO_4 [8] and H_3PO_4 solutions [9]. The etch rate of the (001) crystal surface of GaAs is reported to be controlled by H_2O_2 diffusion in so-

lution at very high acid to H_2O_2 concentration ratios. When this ratio is low, the etch rate becomes kinetically controlled. It is suggested [9] that for the removal of oxidized GaAs products into solution, adsorption of the acid at the surface is essential. When the acid content is relatively low, desorption of the oxidized products into solution becomes rate determining and the overall etch rate becomes kinetically controlled. Obviously, at high acid content, desorption is not a limiting factor and the dissolution rate is controlled by the supply of H_2O_2 from solution.

In contrast to GaAs, no detailed etching studies were made with InP in acidic H_2O_2 solutions. Since dark electroless systems cannot be employed at low pH (section 6.2), it is very likely that InP is also etched in H_2O_2 by a chemical mechanism. Etch rates of the (001) crystal orientation are reported to be very low in H_2O_2/concentrated H_2SO_4 etchants [10,11] indicating a kinetically controlled chemical dissolution of InP.

As discussed in chapter 3, H_2O_2 etchants based on HCl solution are, in principle, unstable as $V^o_{H_2O_2/H_2O} > V^o_{Cl_2/Cl^-}$ (Table IV). However, the chlorine formation is kinetically inhibited and begins rather slowly, so that freshly prepared H_2O_2/concentrated HCl solutions can be applied.

Alkaline H_2O_2 solutions

Since H_2O_2 solutions of high pH have, as far as we know, not been used as etchants for InP, only results obtained at GaAs can be summarized [7,12,13]. A phenomenological review of these etchants is given by Adachi and Oe [7]. In a more detailed study of the dissolution mechanism, Kelly and Reijnders [13] concluded from electrochemical measurements that GaAs is etched via a chemical mechanism. Their result was already discussed in section 2.6 (see Fig. 2.11). The macroscopic etch rate was found to be strongly dependent on the pH of the solution and on complexing agents added to the solution. Below $pH = 10$ effective etching was prevented by oxide formation. Although GaAs dissolution in the pH range 10-12 was also accompanied by oxide formation, a significant kinetically controlled etch rate was found. Complexing agents such as NH_3 and EDTA influence this oxide formation in a negative sense and consequently, increase the dissolution rate. The etch rate in solutions above $pH = 12$ drops markedly as H_2O_2 is strongly dissociated [13]. These strongly alkaline H_2O_2 solutions are therefore unsuitable as etchants.

$OCl^-/pH = 11$-14; section 5.5.

Although the $V^o_{OCl^-/Cl^-}$ is very positive (Table IV), the overlap between D_{OCl^-} and the VB of GaAs is not very favourable. This is caused by the

fact that the reaction of OCl^- to Cl^- is a two-step reduction process. As a result the D_{OCl^-} is positioned at much more negative potentials with respect to the overall standard redox potential (Fig. 5.25). Consequently, the rate of hole injection is kinetically controlled in the dark, and a low electroless etch rate at the open-circuit potential would be expected. However, two effects drastically influence the dissolution mechanism, viz. chemical etching by OCl^- ions and oxide formation in alkaline solutions. Therefore, two cases can be distinguished which are similar to those found with the alkaline $Fe(CN)_6^{3-}$ etching system at GaAs. The formation of an oxide layer depends on the relative OCl^- and OH^- concentrations in solution.

(i) Oxide-free dissolution; section 5.5.

In section 5.5, OCl^- was found to be the first chemical etchant for GaAs (Fig. 5.24) in which asymmetrical etching species are involved. Direct chemical attack of the semiconductor can take place when the transport of dissolution products to solution is not limited and is not hindered by oxide formation. This is the case as long as the chemical etch rate is lower than the maximum dissolution rate of GaAs in alkaline solutions. The maximum dissolution rate was shown to be determined by the OH^- concentration in these solutions (section 4.2). Together with results of profile etching experiments (chapter 8) it can be concluded that the chemical etch rate of GaAs(001) under these oxide-free conditions is controlled by OCl^- diffusion in solution.

(ii) Oxide-forming conditions; sections 4.2, 5.3 and 5.5.

When the maximum dissolution rate of GaAs is exceeded, an oxide is formed at the semiconductor surface. This oxide prevents direct chemical attack of GaAs by OCl^-. GaAs etching can, however, still occur in these relatively concentrated OCl^- solutions, though via another dissolution mechanism. As is shown in section 5.3, hole exchange between an oxidizing agent in solution can still take place through a thin oxide layer to the semiconductor: OCl^- inject holes into the VB of GaAs under these conditions and oxidation proceeds at the GaAs/oxide interface while dissolution of the oxide takes place at the oxide/solution interface. The dissolution rate of the oxide, which depends on OH^- transport in solution (section 4.2), ultimately determines the overall etch rate. We may conclude that GaAs is dissolved in solutions with a high OCl^-/ OH^- concentration ratio under oxide-forming conditions via an electroless mechanism. The etch rate is anodically controlled by OH^- diffusion. This anodically controlled dissolution mechanism explains the good

polishing properties which are reported for these solutions [16]. The role of CO_3^{2-} anions, which are often added to these polishing solutions as Na_2CO_3 [16] to increase the etch rate, can very likely be attributed to an increased dissolution rate of the oxide; both the OH^- and CO_3^{2-} nucleophilic species contribute to the dissolution of the oxide layer (section 4.2).

HCl and HBr; section 6.3.

In contrast to GaAs, which is immune in the complete concentration range, InP dissolves in HCl and HBr solutions. It was found that the etch rate in aqueous solutions only becomes appreciable above a concentration of 5 molar. The dissolution rate increases rapidly at higher concentrations (curves (a) of Fig. 6.7). It was suggested that etching takes place by undissociated HCl and HBr molecules. This was confirmed by using concentrated acetic acid as solvent instead of water; since both HCl and HBr are weak acids in this environment, high etch rates were obtained even at low HCl and HBr concentrations (curves (b) of Fig. 6.7). On the basis of these and electrochemical results (Fig. 6.5), it was concluded that InP is dissolved via a chemical mechanism by undissociated bifunctional HCl and HBr molecules. Evidently, direct chemical attack of InP can only take place once the native oxide film is dissolved. A reaction scheme was proposed for the chemical dissolution reaction which can account for the phosphine (PH_3) evolution observed during the dissolution of InP in these acids. The chemical etching kinetics were found to be under kinetic control in HCl solutions and under mixed kinetic/diffusion control in HBr solutions.

References

[1] S. Menezes and B. Miller, *J. Vac. Sci. Technol. B*, **1**, 48, (1983).
[2] K.L. Conway, A.G. Dentai and J.C. Campbell, *J. Appl. Phys.*, **53**, 1836, (1982).
[3] J.J. Kelly and A.C. Reijnders, unpublished results.
[4] J.E.A.M. van den Meerakker, *Electrochim. Acta*, **30**, 435, (1985).
[5] H. Gerischer and W. Mindt, *Surf. Sci.*, **4**, 440, (1966).
[6] D.W. Shaw, *J. Electrochem. Soc.*, **128**, 874, (1981).
[7] S. Adachi and K. Oe, *J. Electrochem. Soc.*, **130**, 2427, (1983).
[8] S. Lida and K. Ito, *J. Electrochem. Soc.*, **118**, 768, (1971).
[9] Y. Mori and N. Watanabe, *J. Electrochem. Soc.*, **125**, 1510, (1978).

[10] Y. Nishitani and T. Kotani, *J. Electrochem. Soc.*, **126**, 2269, (1979).

[11] S. Adachi and H. Kawaguchi, *J. Electrochem. Soc.*, **128**, 1342, (1981).

[12] J.C. Dyment and G.A. Rozgonyi, *J. Electrochem. Soc.*, **118**, 1346, (1971).

[13] J.J. Kelly and A.C. Reijnders, *Appl. Surf. Sci.*, **29**, 149, (1987).

[14] P.H.L. Notten, J.J. Kelly and H.K. Kuiken, *J. Electrochem. Soc.*, **133**, 1226, (1986).

[15] J.J. Kelly, J.E.A.M. van den Meerakker and P.H.L. Notten, *'Grundlagen von Elektrodenreaktionen'*, Dechema Monographien Band 102, page 453, Dechema, Frankfurt, (1986).

[16] J.S. Basi, *U.S. Patent* 3,738,882.

Chapter 8

Etching profiles at resist edges

8.1. Introduction

The one-dimensional, macroscopic, etching behaviour of III-V semiconductors was described in the first part of this thesis (chapters 2-7). Both etching mechanisms and etching kinetics were investigated for a number of systems, almost exclusively at the (001) surface (Table IV). When, however, a part of the solid surface is protected by a thin impermeable resist layer, local etching near the resist edges has to be considered and a two- or three-dimensional approach is necessary. When the resist is oriented in the manner defined in section 3.3.1 (see Fig. 3.5) a two-dimensional description is adequate. As profiles etched near resist edges are, in general, only considered on a micron scale, this type of etching is denoted as 'microscopic' in contrast to macroscopic etching [1,2]. Since the semiconductor materials studied in this work are all monocrystalline, the microscopic etching kinetics of all crystallographic planes has to be considered near the resist edge.

It has been shown by several authors that the macroscopic etch rate of different crystallographic faces of III-V compounds in the same etchant can differ significantly [3,4]. In general, the etch rate of the (111)A face is much lower than that of the (111)B face, where A and B represent the group III and group V atoms, respectively [3,4]. It is, of course, impractical to determine the macroscopic dissolution rate of all crystal planes. The question arises as to whether, in the cases in which the macroscopic etch rates of certain individual planes have been determined, these rates can be used to predict the shape of microscopic profiles at the resist edge. The experimentally obtained profiles etched under kinetic control are described in section 8.2. The results will be compared with the corresponding macroscopic etching results.

When the dissolution rate of each crystal plane is very large, mass-transport of active etching components in solution becomes rate-determining.

Only one-dimensional diffusion is important at unmasked surfaces (chapters 2-7). However, when the solid surface is partly protected by a mask, supply of etching species can occur from the masked area and, consequently, two-dimensional diffusion has to be taken into account. Recently, a number of authors [5-8] have considered models to predict the profile shapes for two-dimensional diffusion. The results of these calculations are compared in section 8.3 with the experimentally obtained profiles etched under diffusion-controlled conditions.

In section 8.4 intermediate etching profiles are described; these are obtained when parts of the profile are under kinetic control while other parts are controlled by mass-transport in solution. The parameters determining the transition from the intermediate case to either a kinetically or diffusion-controlled shape are also discussed.

From the profile etching experiments described in sections 8.2-8.4, it was concluded that, with certain systems, anomalous results were found which could not be explained with the macroscopic etching theory. A model is proposed in section 8.5 to account for these results. The influence of native oxide layers is considered essential in this model.

The macroscopic results can provide a guide-line for making a suitable choice of etching system for a given application. Table IV, which summarizes these results, will therefore serve as a starting point for this chapter. Besides the influence of the dissolution kinetics, the effect of the etching mechanism on the shape of the profiles was investigated. The etching experiments were performed with both GaAs and InP crystals. As described in the experimental chapter, two different resist patterns were used, viz. a semi-infinite pattern and a pattern of variable stripe width. The influence of the slit width on the shape of the microscopic structures has also been taken into account in the experiments.

Finally, the profile etching results are summarized in section 8.5. The different profiles obtained with various etching systems are reviewed in Table VIII.

8.2. Kinetically controlled etching profiles

Introduction

As stated in the introductory section 8.1, the macroscopic etching kinetics of various crystal planes have to be considered in predicting the shape of profiles near resist edges. Faceted structures are expected when the dissolution rate constants of these crystal planes are low [1]. This holds, of

course, for both the hole injection rate constant ($k_{vb}^c \equiv k_e$) in the case of electroless etching (see eq. (2.44)) and for the chemical rate constant (k_{ch}) in the case of chemical etching (see eq. (A.5)). It is evident that under these conditions mass-transport of etching species in solution does not influence the shape of the etched profiles. On the basis of the macroscopic etching kinetics of each individual crystal plane, the profile geometry can be accurately described by so-called Wulff plots [1]. Obviously, the etching kinetics of the slowest facets mainly determine the shape of these profiles.

In this section some examples of kinetically controlled profiles are described. Ways of regulating the etching kinetics and thus influencing the profile shape are also discussed.

Results and discussion

In Fig. 8.1.A and C profiles are shown for InP in two etchants selected from Table IV, viz. an 0.1 M Br$_2$, 4.5 M HBr solution (Fig. 8.1.A) and an aqueous solution of 7 M HBr (Fig. 8.1.C). In A an SiO$_2$ mask was used with a slit width (a) of 3 μm, whereas the solid was covered with a semi-infinite photoresist layer in Fig. 8.1.C. In both cases clearly-defined facets are revealed, indicating that etching of InP is indeed kinetically controlled along the entire profile.

The two crystallographic facets in Fig. 8.1.A form a characteristic angle of approximately 54° with the overhanging SiO$_2$ layers, as is schematically indicated in Fig. 8.1.B. Since the SiO$_2$ mask covering the (001)InP surface was aligned in the [$\bar{1}$10] orientation, these facets must be attributed to the (111)In plane [9], the same plane whose macroscopic etch rate was found to be kinetically controlled in section 6.4. The local, microscopic, etch rate of the (111)In facet ($v_{(111)In}$) is defined as the quotient of the displacement of this facet with respect to the resist edge and the etching time (t), where the displacement is defined as the normal to these planes ($= v_{(111)In} \times t$), as indicated in Fig. 8.1.B [1]. The microscopic etch rates obtained from the profile of Fig. 8.1.A are in good agreement with the corresponding macroscopic etch rate shown in curve (b) of Fig. 6.10 ($v_{ch} \simeq 1.7$ nm·s^{-1}).

In the 'semi-infinite' case of Fig. 8.1.C two different crystallographic planes are revealed. Since the (001) surface orientation of the InP crystal was also used in this experiment, the facet at the bottom of the profile must also be attributed to the (001) crystal plane. It is surprising that the etch rate of this face is kinetically controlled despite the fact that the macroscopic dissolution kinetics of this face in the HBr etchant are under mixed kinetic/ diffusion control (see Table IV). However, due to an improved supply of etching species (HBr) near the resist edge, microscopic etching of the (001)

facet very likely becomes kinetically controlled. This phenomenon will be discussed in more detail in the following section. This also explains why the microscopic etch rate of this facet (17 nm·s^{-1}), which can be calculated from the etch depth in the profile of Fig. 8.1.C, is slightly larger than the macroscopic etch rate of the same face (11 nm·s^{-1}) in the same etchant, studied in section 6.3 (compare with curve (a) of Fig. 6.7). Since only the (001) face of InP was studied macroscopically in the HBr etchant, the microscopic etch rate of the facet appearing near the resist edge cannot be compared with macroscopic results.

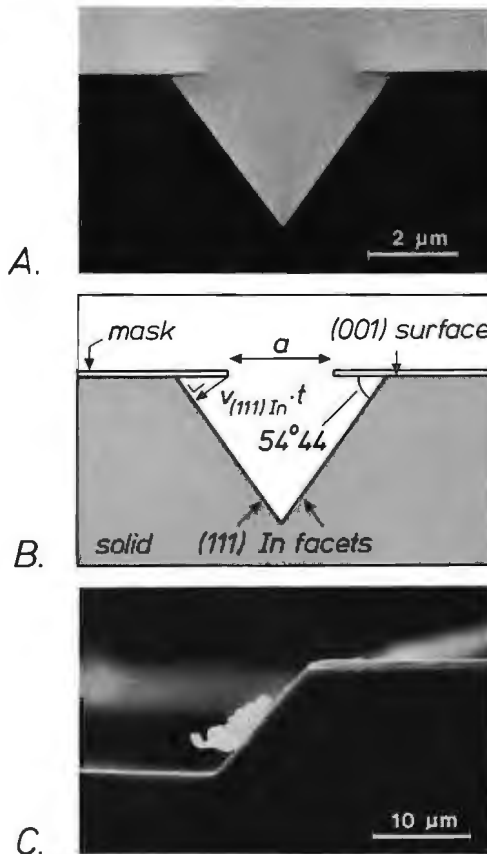**Fig. 8.1.** SEM photographs of kinetically controlled profiles in InP.
A) after 7.5 min. etching in a solution of 0.1 M Br$_2$, 4.5 M HBr; $a = 3$ μm with the SiO$_2$ resist aligned in the [$\bar{1}$10] direction. The etch rate of the (111)In facets is defined in B. C) profile obtained with a semi-infinite mask after 10 min. etching in a 7 M HBr solution; the photoresist was oriented in the [$\bar{1}$10] direction.
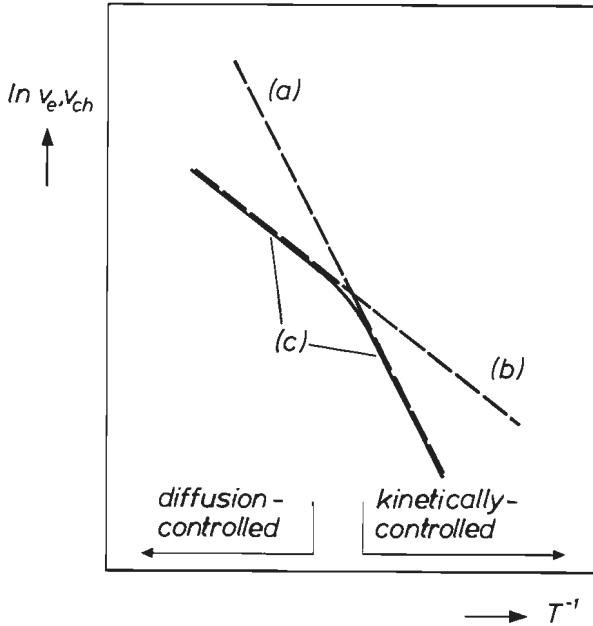
Fig. 8.2. Schematic Arrhenius plots, showing the logarithm of either the electroless or chemical etch rate as a function of the reciprocal temperature (see eq. (8.1)). The temperature dependence of a kinetically controlled dissolution reaction (curve (a)) is much stronger than that of a diffusion-controlled reaction (curve (b)). A transition from a kinetically controlled to a diffusion-controlled etching process can occur with increasing temperature when the rates are of the same order of magnitude (solid line of curve (c)).

In conclusion we may say that anisotropic faceted profiles are etched in monocrystalline materials, such as III-V semiconductors, when dissolution of the various crystallographic planes is under kinetic control and the rates differ from one crystal plane to the other. The microscopic etch rates of the revealed faces are in good agreement with the macroscopic etch rates of the corresponding faces studied in previous chapters. This shows that etched profiles can, in principle, be predicted from macroscopic etching results.

As for every chemical reaction, the rate of an etching reaction depends on the temperature. This, of course, holds for each individual crystal plane. Consequently, the shape of an etched profile can be influenced by the temperature. The temperature dependence of both a chemical rate constant and an electroless rate constant is given by

$$k_{\text{ch}}, k_{\text{e}} = k^{\circ} \cdot \exp\left\{-\frac{E_{\text{a}}}{RT}\right\}, \qquad (8.1)$$

where E_{a} is the activation energy of the reaction, R is the gas constant and k°, the preexponential factor, is a constant. As schematically represented in Fig. 8.2, an 'Arrhenius' plot of the logarithm of the etch rate (v_{ch} or v_{e}), as a function of T^{-1} yields a straight line with a slope of $-E_{\text{a}} \cdot R^{-1}$. The activation energy can be determined from the slope. For kinetically controlled reactions E_{a} is of the order of 40×10^3 J·mole^{-1} [10]. This strongly contrasts with diffusion-controlled reactions to be described in the following section. Since the diffusion coefficient of the rate-determining species is proportional to the reciprocal of the viscosity of the solution (page 773 of [11]) it can be shown that for a diffusion-controlled reaction the activation energy in aqueous solutions is about 18×10^3 J·mole^{-1}, considerably lower than that found for kinetically controlled reactions (compare curves (a) and (b) of Fig. 8.2) [10]. Thus measurements of the activation energy of the dissolution reaction yield information on the rate-determining step of the etching process.

If the rate of the surface reaction is of the same order of magnitude as the diffusion rate, then the difference in temperature dependence of the two processes can be used to alter the rate-determining step. This transition is indicated in curve (c) of Fig. 8.2; at low temperatures the reaction is kinetically controlled whereas at high temperatures the reaction becomes diffusion-controlled. This transition, which also has a considerable influence on the shape of the profiles, will be discussed in section 8.4.

8.3. Diffusion-controlled etching processes

8.3.1. Introduction

For kinetically controlled processes the shape of an etched profile can, in principle, be deduced directly from macroscopic kinetic considerations. When etching becomes limited by mass-transport in solution a concentration gradient of active etching species is built up at the solid/solution interface.

In the appendix of chapter 2 it was shown in eq. (A.6) that the flux $\dfrac{\delta Ch}{\delta t}$ of chemical etching species (Ch) can be described by Fick's First Law of Diffusion:

$$\frac{\delta Ch}{\delta t} = 10^{-3}A\mathcal{D}_{ch} \cdot \frac{\delta[Ch]}{\delta y}, \qquad (8.2)$$

where $\dfrac{\delta[Ch]}{\delta y}$ is the concentration gradient in solution. From eqs. (A.2) and (A.3) it is clear that the flux of the chemical etchant is related to that of the dissolution products of a solid S as

$$\frac{\delta S}{\delta t} = \frac{1}{p} \cdot \frac{\delta Ch}{\delta t}. \tag{8.3}$$

Inserting eq. (8.2) into eq. (8.3) and eliminating $\dfrac{\delta S}{\delta t}$ from eq. (8.3), using eq. (A.4), yields an expression for the chemical etch rate as a function of the concentration gradient:

$$v_{ch} = \frac{10^4 M_s \mathcal{D}_{ch}}{p \varrho_s} \cdot \frac{\delta[Ch]}{\delta y}. \tag{8.4}$$

A similar equation can, of course, be derived for an electroless dissolution reaction. Replacing $\mathcal{D}_{ch}$ and $[Ch]$ in eq. (8.4) by $\mathcal{D}_{ox}$ and $[Ox^{n+}]$, respectively, and p by m, the number of oxidizing species needed to dissolve one 'solid molecule' yields an expression for the electroless etch rate as a function of the concentration gradient:

$$v_e = \frac{10^4 M_s \mathcal{D}_{ox}}{m \varrho_s} \cdot \frac{\delta[Ox^{n+}]}{\delta y}. \tag{8.5}$$

It is obvious from eqs. (8.4) and (8.5) that the etch rate of a semiconductor can be calculated on the basis of a description of the concentration field in the etching solution.

In the previous chapters only one-dimensional diffusion was considered at a macroscopic surface; this implies that the concentration gradient and consequently the etch rate (see eqs. (8.4) and (8.5)) are independent of the position at the semiconductor surface. However, when the solid is partly protected by a resist layer, and a parallel stripe of the solid is left uncovered (see Fig. 3.5), two-dimensional diffusion of the active components in solution has to be considered in the vicinity of the mask edges. As a result, the concentration gradient is dependent not only on the etching time but also on the position at the surface. Therefore, to predict the development of etching profiles near resist edges, the concentration field should be calculated as a function of both the etching time and the position with respect to the resist edges.

In the past, several authors [5-8] have developed theoretical models which take these considerations into account. It is obvious that the mathematical analyses are rather complex. In addition, the concentration field along the interface may also be influenced by convection and by the moving boundary presented by the etching surface. As the complex mathematical derivations are beyond the scope of this thesis, only the results will be presented in section 8.3.2. In particular, the special features characteristic of diffusion-controlled etching profiles are emphasized. The theoretically predicted profiles are then compared with experimental structures. This is described in section 8.3.3. It was found that the experiments do not always agree with the theoretical prediction. This apparent anomaly, which can be interpreted on the basis of electrochemical interaction of crystallographic facets, is finally described in section 8.3.4.

8.3.2. Results of mathematical modelling

The mathematical models presented in the literature [5-8] can be divided into two groups. The first group considers the development of etching profiles near resist edges of solids which are protected by a thin semi-infinite mask [5,6]. The second group describes the development of profiles when only a parallel stripe of the surface is left uncovered. In these latter cases etching proceeds through a slit whose width may vary over a wide range [7,8]. Obviously, the slit width is an additional parameter which may affect the profile shape. In the following paragraphs the most relevant results of each model are described.

Semi-infinite mask pattern

It is clear that the concentration gradient in eqs. (8.4) and (8.5) is also influenced by the rate of the dissolution reaction. To reduce the complexity, Kuiken [5,6] derived a mathematical model in which the etching reaction was assumed to proceed infinitely fast, irrespective of the crystallographic orientation. In our terminology this would mean that k_{ch}, $k_e \rightarrow \infty$, at all crystal planes and thus that the rate-determining step in the dissolution reaction is only determined by transport of active etching components from the bulk of the etchant to the solid/solution interface. A further simplification was made by assuming that transport in solution is provided by diffusion and that convection is not important. As a result, a continuous extension of the diffusion layer occurs. An exact solution of the mathematical problem can be obtained when the displacement of the solid/solution interface is relatively slow compared to the rate of extension of the diffusion layer [5,6].

Under this condition a singular perturbation technique can be applied to solve the problem; the concentration field is calculated by assuming the interface to remain fixed at its original position. In order to determine when this condition is fulfilled, a dimensionless physical parameter β was introduced, representing the molar density of the solid relative to that of the solution. β can be defined for both a chemical and an electroless etching reaction as

$$\beta = \frac{10^3 p \varrho_s}{[Ch]_b M_s}, \tag{8.6}$$

and

$$\beta = \frac{10^3 m \varrho_s}{[Ox^{n+}]_b M_s}, \tag{8.7}$$

respectively. Kuiken pointed out [5,6] that the perturbation technique can, in general, be employed when β is large, e.g. $\beta > 100$. In that case the surface concentration gradient is not affected by the relatively slow displacement of the moving interface. Once the etch rate of the solid is determined
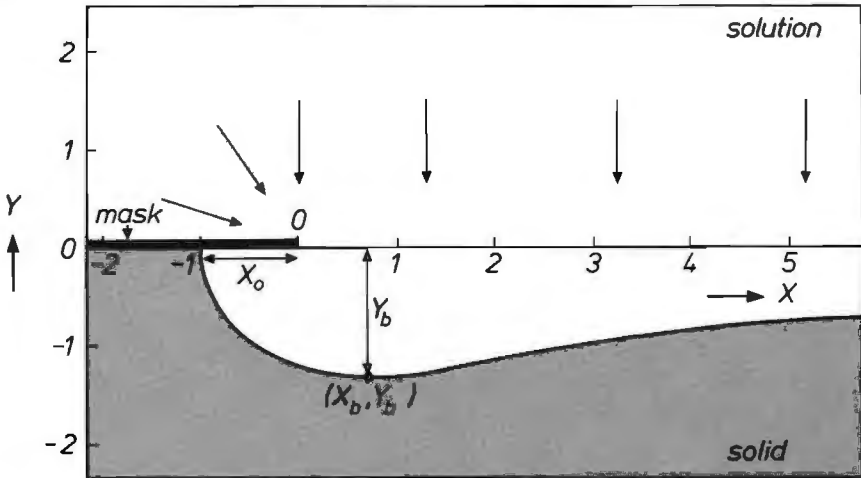

Fig. 8.3. Theoretically predicted profile etched at a semi-infinite masked edge under mass-transport control. The position of the interface is represented by two dimensionless coordinates X and Y, which are defined in the text (eqs. (8.8) and (8.9)). The underetching is indicated by X_o and the position of the deepest point in the bulged profile is given by (X_b, Y_b).

as a function of time and of the position with respect to the resist edge, the shape of diffusion-controlled etching profiles can be calculated.

It was concluded that the shape of the profiles is independent of the etching time. The results of these calculations are represented graphically in Fig. 8.3. The two-dimensional shape can be fully characterized by the coordinates x and y when the resist edge, which serves as a reference point, is positioned at the origin of the graph. As the shape was found to be independent of time, it is convenient to represent both the x and y coordinates on the same dimensionless scale. The dimensionless coordinates X and Y are defined by

$$X = \frac{x}{x_o},$$ (8.8)

and

$$Y = \frac{y}{x_o},$$ (8.9)

with respect to the absolute underetching which is denoted by x_o. The position at which the etching profile meets the underside of the resist edge is then defined by the coordinates $(-1.00, 0.00)$, i.e. the relative underetching X_0 is defined by the coordinates

$$(X_o, Y) = (-1.00, 0.00);$$ (8.10)

see Fig. 8.3.

Some characteristic features of diffusion-controlled etching profiles are worth noting:
– Due to two-dimensional diffusion in the vicinity of the resist edge the dissolution rate of the solid is significantly enhanced. This results in a bulged shape of the profile near the resist edge. The enhanced supply of etching species in solution is schematically illustrated by the arrows in the upper part of Fig. 8.3.
– The deepest point in the profile is denoted by (X_b, Y_b), (see Fig. 8.3), and is characterized by the coordinates

$$(X_b, Y_b) = (0.68, -1.33).$$ (8.11)

– The etch factor can be obtained from eqs. (8.10) and (8.11):

$$\text{etch factor} = \frac{|Y_b|}{X_o} = \frac{|y_b|}{x_o} = 1.33. \tag{8.12}$$

From eqs. (8.8) and (8.9) it is obvious that this factor is also equal to the quotient of y_b and x_o. The etch factor is an important parameter in characterizing etching structures [12].
– The angle which the etched edge makes with the underside of the resist layer is calculated to be exactly 90°.
– The shape of the profiles is independent of the etching time. However, it is evident that the absolute position of the interface changes as a function of time. It was shown that the rate of displacement of the interface is proportional to the square root of the etching time [5,6]. Consequently, this means that

$$y_b \propto t^{\frac{1}{2}}. \tag{8.13}$$

To compare the calculated and experimental profiles (section 8.3.3), it is convenient to have available numerical data from the theoretical calculations. These results are therefore presented in tabular form (see Table V).

In this mathematical model, transport of etching components in solution is only provided by diffusion. However, it is generally known that convection can seldom be ruled out [13,14]. Concentration differences caused by the etching process lead to density gradients in the etchant and give rise to solutal convection near the interface. Consequently, in practical etching systems supply of etching species is also provided by convective diffusion. Electrochemical measurements have shown that solutal convection at a macroscopic surface becomes dominant after a few seconds (page 126 et seq. of [14]).

A theoretical model which also takes convection into account was presented by Kuiken et al. [6]. To reduce the complexity of the mathematical description, the velocity field extending from the solid/solution interface into the solution was assumed to be linear, independent of the position along the interface, and constant in time. When it is further assumed that β is again very large, so that the singular perturbation technique can be applied, a mathematical solution can be obtained [6]. It was concluded that at moderate etch depths the shape of the profiles in the corner region around the mask edge is exactly the same as that derived for the case of

Table V

Numerical data describing the theoretical position of the
interface of semi-infinite, diffusion-controlled, etching
profiles. The position is given by two dimensionless co-
ordinates X and Y (see eqs. (8.8) and (8.9)).

$X = \dfrac{x}{x_0}$	$Y = \dfrac{y}{x_0}$
$-$ 1.000	0.000
$-$ 0.985	-0.192
$-$ 0.936	-0.379
$-$ 0.858	-0.558
$-$ 0.750	-0.727
$-$ 0.613	-0.882
$-$ 0.446	-1.015
$-$ 0.256	-1.129
$-$ 0.041	-1.219
0.195	-1.282
0.449	-1.317
0.720	-1.324
1.002	-1.311
1.295	-1.276
1.597	-1.225
1.908	-1.169
2.227	-1.109
2.558	-1.046
2.902	-0.987
3.258	-0.934
3.630	-0.884
4.420	-0.794
5.291	-0.720
6.206	-0.661
7.201	-0.608
8.287	-0.564
11.27	-0.477
14.73	-0.413
18.64	-0.365
23.02	-0.322
27.85	-0.295
33.15	-0.265

a stagnant etchant, as presented in Fig. 8.3 and Table V. This includes the etch factor of 1.33 and the 90° angle at the upper edge of the profile. Clearly, the time dependence is different. It was shown that when the velocity field does not change in time the rate of displacement of the etched interface is proportional to $t^{\frac{1}{3}}$. On the basis of analogy with eq. (8.13) we conclude that when transport in solution is provided by such convective diffusion, eq. (8.14) holds [6]:

$$y_b \propto t^{\frac{1}{3}}. \tag{8.14}$$

Variable mask width pattern

When only a small parallel stripe of solid is not covered by a resist layer (see Fig. 3.5), the transport of etching species to the interface can be significantly enhanced. As long as the diffusion layer thickness is small in comparison to the width of the slit, the diffusion fields developing near each resist edge do not interfere with each other and the mathematical problem is exactly the same as that described in the previous section. However, as etching proceeds and the diffusion fields propagate, and overlap, the mathematical problem becomes more complicated. It is obvious that besides the parameters already discussed, the slit width (a) may play an important role.

Mathematical models which describe the development of the profiles when dissolution occurs through a slit have been treated by several authors [7,8]. These models are again based on the calculation of the concentration gradients as a function of both time and position at the interface. Only stagnant solutions were considered. Despite this simplification a full solution can only be obtained by numerical methods [7,8].

It has been shown by Kuiken [7] that certain aspects can be dealt with analytically when the surface reaction is assumed to be infinitely fast (k_{ch}, $k_e \to \infty$) and β is assumed to be large. A more general solution of the mathematical problem was described by Vuik and Cuvelier [8]. Using a finite element method to calculate the concentration gradient at the interface at discrete time intervals, the problem could be tackled numerically for all values of β and the reaction rate constant. Since low values of β were also allowed, changes in the position of the interface had to be taken into account in their model [8]. Besides the dimensionless parameter β (eqs. (8.6) and (8.7)) Vuik et al. pointed out that two more dimensionless parameters are important in describing the development of the etching profile. The Sherwood number (Sh) represents the relative magnitude of the surface reaction rate and the rate of diffusion. Sh is defined as
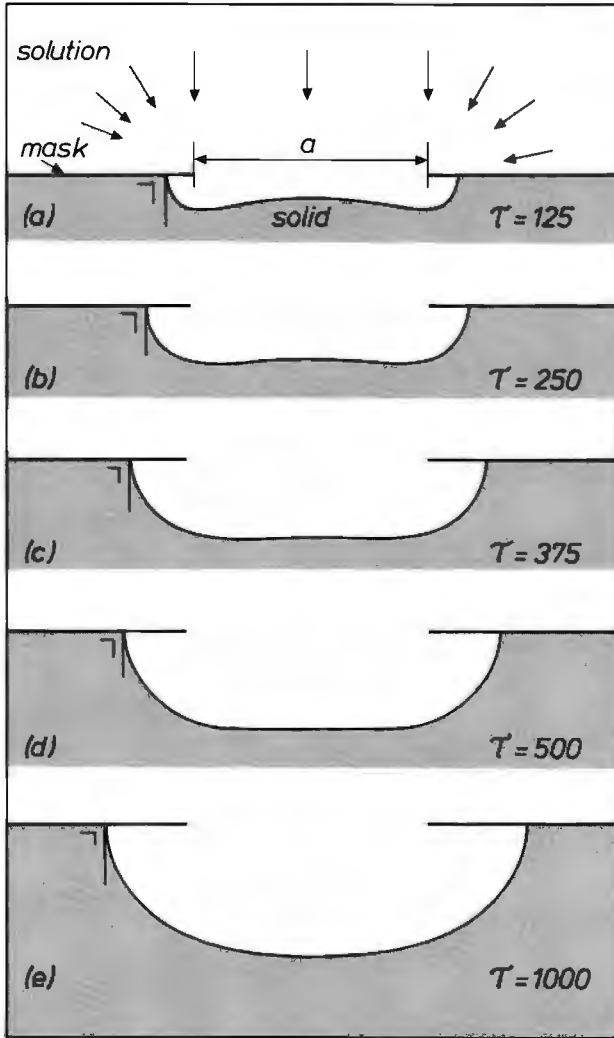
Fig. 8.4. Development of etching profiles as a function of dimensionless etching time (τ) (eq. (8.16)), as predicted by theory. Parameters of the etching system are $\beta = 1000$ and $Sh = 1000$. Etching proceeds through a slit of width a. $\tau = 125$ (curve (a)); 250 (curve (b)); 375 (curve (c)); 500 (curve (d)); 1000 (curve (e)).

$$Sh = \frac{ak_{ch}10^{-4}}{\mathcal{D}_{ch}} - \; ; \quad Sh = \frac{ak_e10^{-4}}{\mathcal{D}_{ox}}. \tag{8.15}$$

Etching is diffusion-controlled when the Sherwood number is large. On the other hand dissolution becomes kinetically controlled when Sh approaches or becomes smaller than unity. The influence of the slit width on the dissolution kinetics can also be recognized in eq. (8.15). Furthermore, it is important to note that only isotropic etching was considered by Vuik et al. [8], i.e. the dissolution rate of the solid is the same in all crystallographic directions. The third parameter influencing the profile shape is a dimensionless etching time, τ, defined as [8]

$$\tau = \frac{10^8 \mathcal{D}_i}{a^2} \cdot t. \tag{8.16}$$

A computer programme in which the various parameters can be introduced was developed by Vuik. We also used this programme to calculate the development of the shape for one limiting case. A very large value for β was introduced ($\beta = 1000$). This corresponds to the actual situation for most etching solutions, as will be shown in the following section (see Table VI). In Fig. 8.4 calculated profiles are plotted for several intervals of τ with an etching system having a large Sherwood number ($Sh = 1000$). Such a large value of Sh corresponds to a diffusion-controlled dissolution reaction (see eq. (8.15)). It is obvious that, in contrast to the semi-infinite profiles, the shape is now clearly dependent on the etching time. That the profiles at short times (curves (a) and (b)) are deeper at the resist edges must again be attributed to an enhanced supply of active etching-species in both regions. This is schematically indicated by the arrows above profile (a). At longer times the bulges become less pronounced (curves (c) and (d)) and finally disappear (curve (e)). At large values of τ the shape tends to that of an ellipse. Characteristic of all diffusion-controlled etching profiles (curves (a)-(e)) is the 90° angle which the etched surface makes with the resist layer.

8.3.3. Experimental confirmation

Semi-infinite mask pattern

In section 8.3.2 results were presented of mathematical models for diffusion-controlled etching at resist edges of a solid which was covered with a

semi-infinite resist layer. In this section attempts are made to verify these models experimentally. Etching systems are therefore needed which meet two main requirements.

In the first place, since various crystallographic facets can be exposed to the solution near the resist edge, the etch rate of all crystal planes of the solid must be determined by mass-transport, i.e. the rate constant for the rate-determining step of the dissolution process must be sufficiently large to ensure a very low surface concentration of the rate-determining species, even at the slowest etching crystal plane. From Table IV both diffusion-controlled electroless and chemical etchants can be selected.

The second requirement involves a large dimensionless etching parameter β, defined in eqs. (8.6) and (8.7) ($\beta > 100$). Once the nature of the rate-determining species in the etchant and the number of these species (m or p) needed to dissolve one III-V entity have been identified, β can be calculated for a given semiconductor with density ϱ_s and molecular weight M_s. Using the relevant constants for GaAs and InP given in chapter 3, β has been calculated for the diffusion-controlled etching systems listed in Table IV. The results are presented in Table VI together with relevant information about the etchants with regard to their practical application. From the values collected in this table, it follows that β is, in general, very large. Moreover, the concentration of the rate-determining species can be used to adjust β (see eqs. (8.6) and (8.7)). It is obvious that the etchants listed in Table VI all comply with the requirement of a large value of β.

In Fig. 8.5 the result is shown of a profile etching experiment obtained with GaAs in a diffusion-controlled etchant (H_2O_2/conc. HCl (1/40)) selected from Table VI. In this example an SiO_2 layer, aligned in the [110] direction, was used to mask half the GaAs slice. During etching the sample was placed vertically in the etching solution with the resist edge parallel to the solution surface and the free GaAs surface below the masked area. It is clear from Fig. 8.5.A that due to two-dimensional supply of H_2O_2 to the solid/solution interface the etch rate is significantly enhanced near the resist edge, in accordance with the mathematical model. A further magnification of the corner region (Fig. 8.5.B) shows that a smooth curved surface is obtained, not revealing any facet. This indicates that etching of not only the (001) surface (Table IV) but of all crystal planes is diffusion-controlled. It should be noted that, when very thin resist layers were used as in Fig. 8.5, a slight curling of the resist at the etched edge was sometimes observed in the SEM. This occurred after the sample was removed from the etchant. Somewhat thicker resist layers did not show this effect. The shape of the etched profiles was the same in all cases. In Fig. 8.5.C, the measured profile

Table VI

β values for the diffusion-controlled etching systems considered in Table IV.

Solid	Etchant	Etching mode	Rate-determining		m or p	β
			species	concen-tration		
GaAs	0.1 M $Ce(SO_4)_2$	electroless (i)	Ce^{4+}	0.1	6	2200
	0.1 M $K_3Fe(CN)_6$, $pH = 13$	electroless (i)	$Fe(CN)_6^{3-}$	0.1	6	2200
	0.5 M $K_3Fe(CN)_6$, $pH = 13$	electroless (ii)	OH^-	0.1	12	4400
	0.5 M $K_3Fe(CN)_6$, $pH = 14$	electroless (i)	$Fe(CN)_6^{3-}$	0.5	6	440
	0.5 M NaOCl/conc. HCl (5/1)	chemical	Cl_2	$\simeq 0.1$*	3	$\simeq 1100$
	0.1 M Br_2 in 4.5 M HBr	chemical	Br_2	0.1	3	1100
	H_2O_2/conc. HCl (1/20)	chemical	H_2O_2	≤ 0.46	3	≥ 240
	H_2O_2/conc. HCl (1/40)	chemical	H_2O_2	≤ 0.24	3	≥ 460
	0.1 M NaOCl, $pH = 13$	chemical	OCl^-	0.1	3	1100
	0.5 M NaOCl, 0.1 M Na_2CO_3, $pH = 13$	electroless (ii)	OH^-/CO_3^{2-}	$\simeq 0.1$	12	$\simeq 4400$
InP	0.5 M NaOCl/conc. HCl (5/1)	chemical	Cl_2	$\simeq 0.1$*	3	$\simeq 1000$
	0.1 M Br_2 in 4.5 M HBr	chemical	Br_2	0.1	3	1000

(i) and (ii) refer to cathodically and anodically controlled electroless etchants, respectively

*) determined by the solubility of Cl_2 in aqueous solution (see chapter 3)

is compared with that calculated from the theoretical model, using Table V.
The calculated curve was fitted at one point, viz. that at which the under-
etched GaAs surface meets the resist edge (see Fig. 8.3.). The excellent
agreement between the measured and calculated curves demonstrates clearly
the validity of the mathematical treatment. It should be emphasized that the
measured etch factor, defined by eq. (8.12), agrees very well with the value
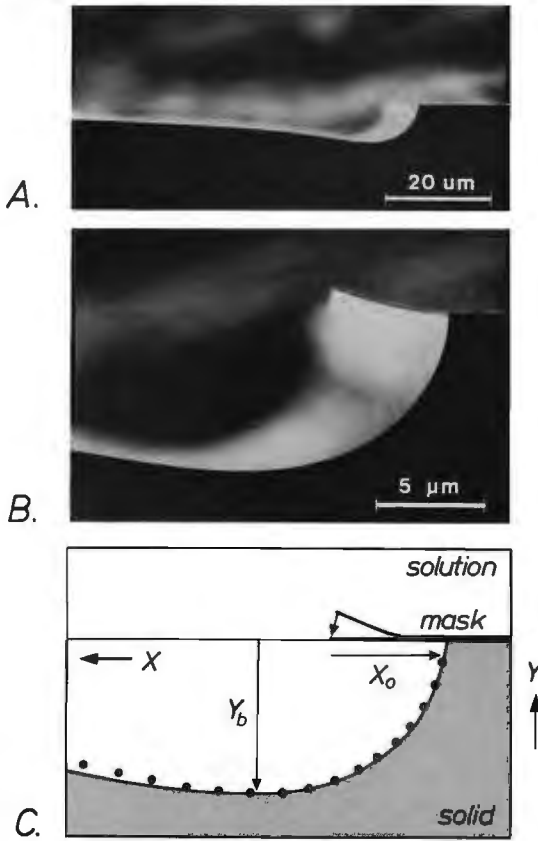of 1.33 predicted by theory. The 90° angle at which the profile meets the

Fig. 8.5.A) SEM photograph of a profile etched in GaAs with a semi-infinite SiO_2
mask aligned in the [110] direction. Etching was carried out for 5 min. in a $H_2O_2/$
HCl (1/40) solution with the wafer placed in a vertical position. A higher magnifi-
cation of the same profile in the mask-edge region is shown in B. C) shows the
agreement between the profile measured in B (continuous line) and that calculated
from theory, using Table V (filled circles). The underetching and the maximum
etched depth are indicated by X_o and Y_b, respectively.

underside of the mask is also in full agreement with theory. Further away from the mask edge a slight difference between theory and experiment is observed which must be attributed to convection. This could be due to either 'solutal' convection or 'forced' convection, as will be discussed below [32].

To study the influence of solutal convection on the etched profiles, a different etching experiment was performed. Instead of masking half the GaAs surface, a parallel stripe, 4 mm wide, was left uncovered between resist areas at the top and bottom of the crystal as shown schematically in Fig. 8.6.A. As in the previous case, the substrate was kept in a vertical position with the resist edges parallel to the solution surface. Etching was now performed in an anodically controlled electroless etchant (0.5 M $K_3Fe(CN)_6$ solution of $pH = 13$; Table VI). In contrast to the previously described H_2O_2 etching solution, gas evolution is absent in this etchant. As a result, 'forced' convection, initiated by the movement of gas bubbles in solution, is not expected here. Fig. 8.6.B shows the profile near the upper mask edge
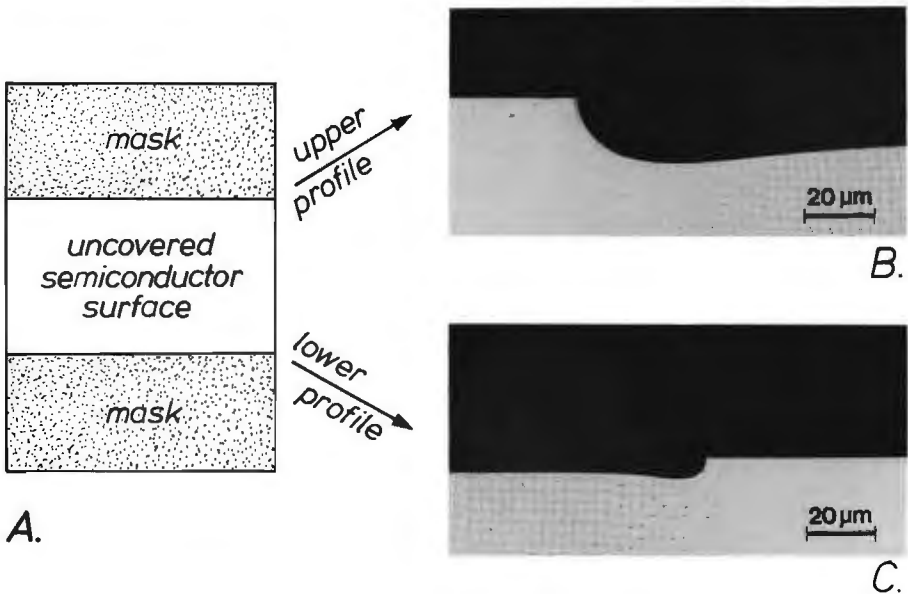

Fig. 8.6. The influence of solutal convection on GaAs etching in a 0.5 M $K_3Fe(CN)_6$ solution of $pH = 13$. The crystal was etched for 10 min. in a vertical position. The sample geometry shown in A is described in the text. B) shows the profile obtained at the top edge of the resist/unmasked GaAs strip. That observed at the lower resist edge is shown in C.

and Fig. 8.6.C that near the lower mask edge, etched at the same time. Clearly these etched depths are different.

This effect can be attributed to convection caused by density gradients in the solution. It seems likely that dissolving products give rise to regions of higher density in the etching solution near the solid/solution interface. As a result, a downward-directed solutal flow along the surface is expected. This flow induces two different effects: an enhanced supply of fresh etching solution increases the etch rate of the solid near the upper mask edge; as the concentration of the active etching species is gradually depleted in the downward direction, significantly lower etch rates are expected in the lower regions. This is in agreement with the result of Fig. 8.6 and shows the importance of solutal convection.

From the result discussed above it follows that solutal convection should be more uniform along the interface when the substrate is placed horizontally in the etching solution with the masked surface facing upwards. In this case the denser etching solution containing the dissolution products would be expected to be more stagnant. A gradual depletion of the etching components along the interface is not expected and, as a result, the differences in etch depth at the resist edges should disappear. This was indeed found experimentally.

The development of the profiles was also studied as a function of time and compared with the theoretically calculated profiles. GaAs substrates with a semi-infinite mask were placed for various times in the same etchant as used in Fig. 8.5. In this experiment, however, the samples were etched in a horizontal position. The etching results are shown in the left-hand side of Fig. 8.7. The etching times were 1,2,5 and 10 minutes in A-D, respectively. The bulged shape is observed in all cases, independent of the etching time. It should be noted that two different magnifications are used in Fig. 8.7. In the right-hand side of this figure the corresponding theoretical profiles (solid circles) are compared with the measured profiles (continuous lines). Again these curve fits were only carried out on the shape and not on absolute position (compare with Fig. 8.3). It is clear that the agreement between theoretical and experimental profiles is excellent in the cases B-D (compare with Fig. 8.7.F-H, respectively), even further away from the resist edges. Comparing these results with that of Fig. 8.5.C reveals that in the latter case a difference between theoretical and experimental profiles is observed closer to the resist edge. From the discussion above it is obvious that this must be attributed to solutal convection, which is not so dominant in Fig. 8.7.B-D. This is further illustrated in the time-dependent profile etching experiments discussed in [15]. There too, a considerable deviation was
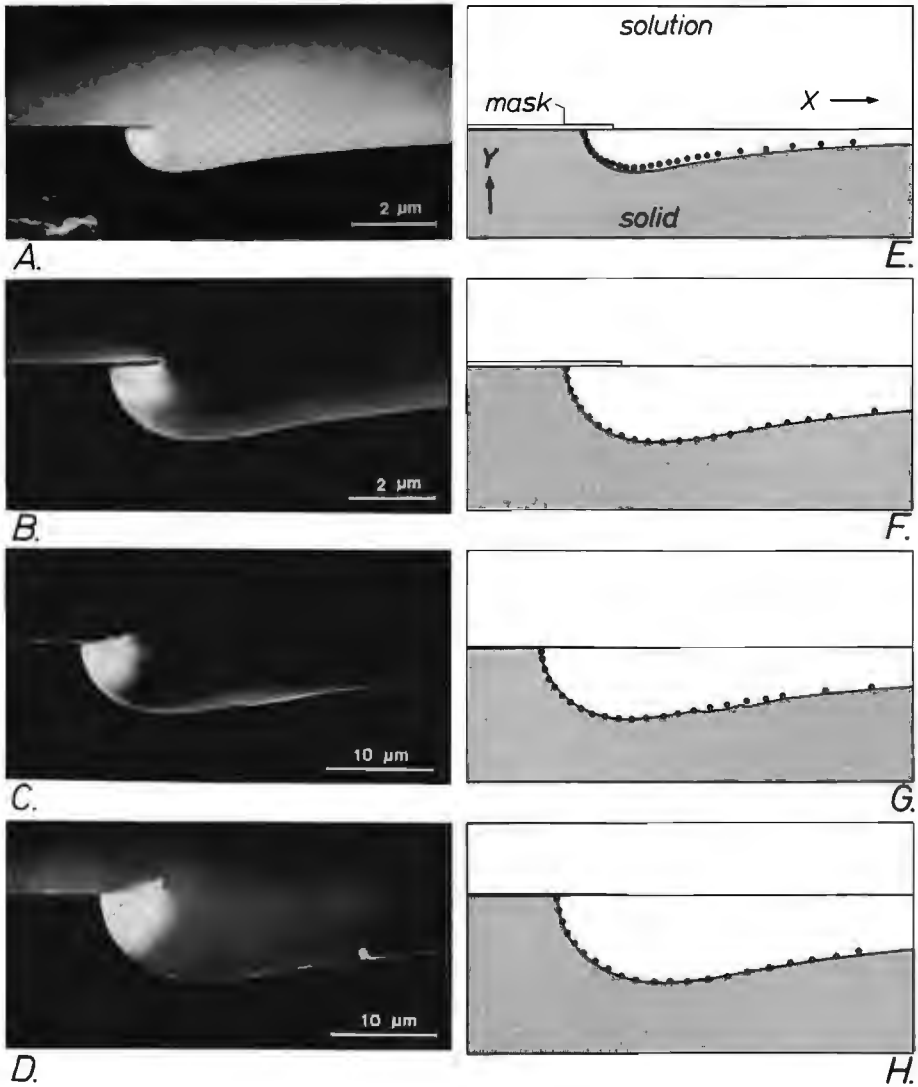
Fig. 8.7. The development of the etched profile with etching time for GaAs in a H_2O_2/HCl (1/40) solution. A semi-infinite SiO_2 mask was used. GaAs wafers were etched in a horizontal position for 1, 2, 5 and 10 min. (SEM photograph A-D, respectively). A comparison of the measured profiles (continuous lines) and those calculated using Table V (filled circles) is shown in E-H.

observed away from the corner region in all experiments, due to vertical positioning of the substrate in the etchant.

The result obtained at the shortest etching time in the present experiment (Fig. 8.7.A) is in less good agreement with the theoretical profile. A strong deviation from the theoretical profile is observed even in the corner region and this is very likely due to convection; it is obvious that immersion of a semiconductor crystal mounted on a relatively large glass plate causes agitation of the etching solution. This effect will be most pronounced in the initial stages of the etching process and will be extinguish after longer times (compare the fit of Fig. 8.7.E with those of Fig. 8.7.F - H). It is evident that due to this deviation a relatively large etch factor of 1.47 is calculated for the one minute experiment, whereas at longer times the theoretical value of 1.33 is found (see eq. (8.12)). In all cases a right angle is found between the etched profile and the resist layer, in accordance with theory. It can be concluded that the shape of the diffusion-controlled profiles does not change as a function of etching time. The etch depth can, of course, be regulated by the etching time.

According to the theory [6], the time dependence of the etch depth depends markedly on the hydrodynamics of the etching process. For a purely diffusion-controlled reaction without convection, the depth at the deepest point (y_b; see also Fig. 8.3) should depend on the square root of the etching time (eq. (8.13)). Since convection always plays a role in mass-transport, this case is rarely encountered in real systems. This observation has already been corroborated by experimental evidence, as discussed above. If convective diffusion is considered with a linearized and stationary velocity assumption, then a $t^{\frac{3}{4}}$ dependence is expected for etching in the mask edge region (see eq. (8.14)) [6].

Fig. 8.8 shows a plot of y_b as a function of the etching time on a double logarithmic scale for three different diffusion-controlled systems of Table VI. For curve (a) measured with the NaOCl etchant of $pH = 13$, which operates without gas evolution, the slope of 0.6 suggests a case intermediate between the two cases discussed above. The NaOCl/conc. HCl etchant (curve (b)) gives a slope of 0.78, which is reasonably close to that expected for the convective diffusion model. This etchant produces very little gas during the experiment and the rate of gas evolution does not change significantly. The third solution, H_2O_2/conc. HCl (1/20), shows a much stronger time dependence, as a slope of 1.27 is observed in curve (c). This is clearly due to 'forced' convection, which results from gas evolution during etching. In this etchant the rate of gas evolution increased significantly with time, as described in the experimental chapter 3.
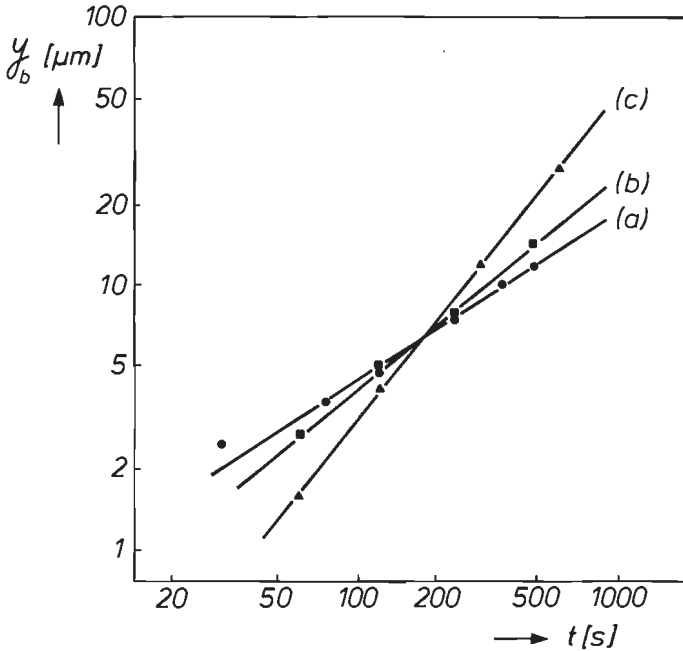
Fig. 8.8. The etched depth y_b at the deepest point of the diffusion-controlled profile as a function of etching time. Etching was performed with a semi-infinite mask. GaAs crystals were dissolved in three different etchants (see Table VI): a 0.5 M NaOCl, 0.1 M Na_2CO_3 solution of $pH = 13$ (curve (a)); a 0.5 M NaOCl/ conc. HCl (5/1) solution (curve (b)) and a H_2O_2/conc. HCl (1/20) solution (curve (c)).

Profiles similar to those shown here were also obtained with InP in the NaOCl/conc. HCl etchant and, under certain conditions, in the bromine-containing HBr solution (see Table VI).

Although the macroscopic etch rates in solutions listed in Table VI were all diffusion-controlled, rounded profiles were not always observed. In a number of cases, crystallographic facets were clearly revealed near the resist edges. These exceptions can be divided into two categories:

(i) A requirement for diffusion-controlled profiles is that the rate constant for all crystal planes should be large. Since the etching results listed in Table VI only refer to the (001) orientation, this requirement is not necessarily fulfilled for other planes. For example, in section 6.4 it was shown that the macroscopic etching kinetics of InP with the (001) and the (111)In surface orientation differ considerably (see Fig. 6.10). These

cases in which the macroscopic etch rate of certain crystal planes is kinetically controlled, while that of others is mass-transport controlled, are denoted by intermediate cases. The intermediate profiles will be described in section 8.4.

(ii) Etching profiles obtained with electroless etching systems form the second category. Seemingly anomalous behaviour was observed in the results with some of these systems; for those electroless etchants in which the dissolution rate was diffusion-controlled via the anodic partial reaction (see Table VI; electroless (ii) cases), the etched profiles had indeed a curved shape, as expected (see Fig. 8.9.A). However, for electroless etchants that were cathodically controlled (electroless (i) cases in Table VI), faceted profiles were found, in spite of the fact that the macroscopic etch rate of the revealed crystal planes was found to be diffusion-controlled. An example of such an anomalous result obtained at GaAs in a 0.05 M $K_3Fe(CN)_6$ solution of $pH = 13$ is illustrated in Fig. 8.9.B. This phenomenon, which results from a characteristic electrochemical interaction between different crystal faces during etching, will be described in more detail in section 8.3.4.
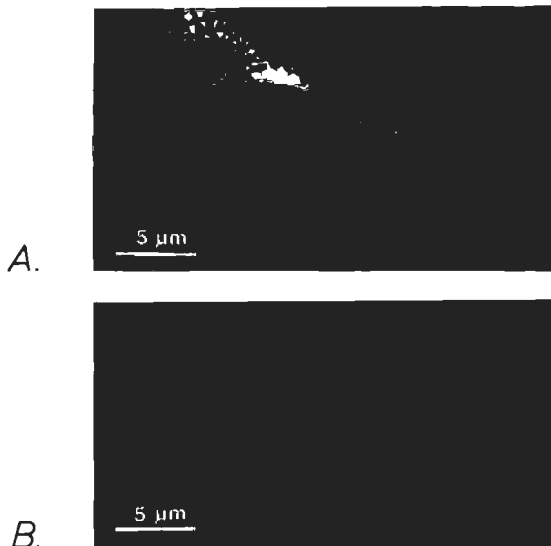

Fig. 8.9. Profiles obtained with a semi-infinite mask on GaAs in two electroless etchants; an anodically controlled 0.5 M NaOCl, 0.1 M Na_2CO_3 etching solution of $pH = 13$ (A) and a cathodically controlled 0.05 M $K_3Fe(CN)_6$, $pH = 13$ etchant (B). The photoresist was aligned in the [$\bar{1}10$] direction.

Variable mask width pattern

The mathematical model presented in section 8.3.2 for a variable mask width pattern, was developed for stationary etching solutions without convection. For practical etching this is not realistic. However, a qualitative comparison between experimental and calculated profiles should be possible.

In section 8.3.2 it was shown that three dimensionless parameters are important in describing the shape of symmetrical etching profiles:
- The parameter β has a pronounced influence on the time-dependence of the profile shape, e.g. via the concentration of the etching-species (see eqs. (8.6) and (8.7)). For practical etching systems it was shown in Table VI that β, which is a constant for a given etchant, is generally very large.
- The influence of the slit width on the kinetics of the etching reaction was expressed in the Sherwood number, Sh, as defined in eq. (8.15). It is obvious from this equation that etching is mass-transport-controlled when Sh is large. When Sh is smaller than one, kinetically controlled profiles should be obtained. When monocrystalline materials are etched under these conditions, differences in the rate constants of individual crystal planes give rise to facets. In this section only diffusion-controlled etchants are considered, i.e. with Sh large.
- The third dimensionless parameter, τ, was defined as

$$\tau = \frac{10^8 \mathcal{D}_i}{a^2} \cdot t. \tag{8.16}$$

The influence of τ on the theoretical diffusion-controlled profiles was stressed in Fig. 8.4.

The validity of eq. (8.16) was investigated for systems with large values of Sh and β. Both the slit width and the etching time were varied in two different experiments. The H_2O_2/conc. HCl (1/40) solution was again used as etchant.

In Fig. 8.10 profiles obtained with GaAs after various etching times are shown. The samples were placed horizontally in the solution. The slit width had a constant value ($a = 10$ μm) in all cases. Three typical examples obtained after 1, 2 and 5 minutes are shown in A, B and C of this figure, respectively. It is obvious that both the shape of the profile and the etch depth depend on the etching time. The bulge at resist edges at the shortest etching time (Fig. 8.10.A) clearly indicates that two-dimensional diffusion is important. As etching proceeds, the etch depth increases significantly and the bulged shape becomes less pronounced (Fig. 8.10.B) and eventually disap-

pears to give a relatively deep ellipse-shaped profile (Fig. 8.10.C). It should be noted that the magnification used in this latter photograph is a factor of two lower than that used in A and B. When the etch time was further increased, almost circular, deep profiles were found (not shown). Since a has a constant value in this experiment, it follows from eq. (8.16) that an increasing etching time results in an increase in the dimensionless parameter τ. The theoretical profiles, as represented in Fig. 8.4, agree well with those found experimentally in Fig. 8.10.

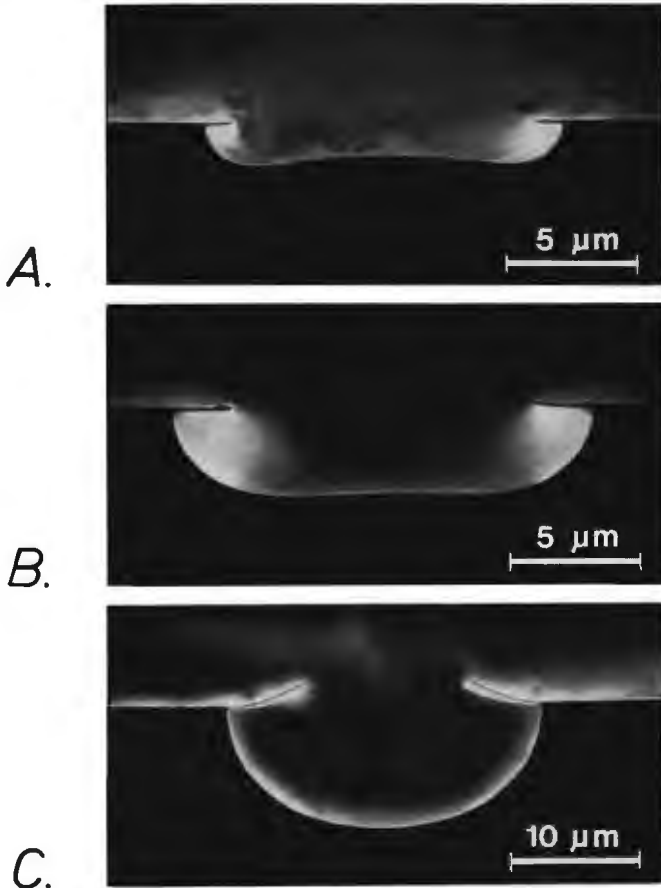**Fig. 8.10.** SEM photographs showing the profile development under diffusion-controlled conditions as a function of etching time. The GaAs was masked with an SiO_2 layer and etched in a horizontal position through a constant slit width of 10 μm in a solution of H_2O_2/conc. HCl (1/40). The etching time was 1, 2 and 5 min. in A-C, respectively. Note the difference in magnification between A, B and C.

Another way to investigate the influence of τ on the development of the etching profile is to keep the etching time constant and to change the slit width (eq. (8.16)). The results of such an experiment are shown in Fig. 8.11. A GaAs crystal was etched for two minutes in a horizontal position in the same etchant as used in Fig. 8.10. The slit width of the SiO_2 resist layer was varied from 1 - 1000 μm in seven successive steps (see experimental section 3.3). Four representative results obtained with $a = 3$, 10, 30 and 1000 μm are shown in A - D of Fig. 8.11. It is clear that in this case the shape of the etched profiles and the etch depth strongly depend on the value of a. As a result of the pronounced influence of two-dimensional diffusion at the smallest resist opening, a relatively deep ellipse-shaped profile is obtained (Fig. 8.11.A). This effect becomes less pronounced at larger values of a, and results in a considerable decrease of the etch depth in Fig. 8.11.B - D. The bulges at the resist edges indicate, however, that two-dimensional diffusion is still important (see Fig. 8.11.B and at a lower magnification the insert of Fig. 8.11.C). Despite the fact that a is increased from 30 to 1000 μm in C and D, the shape of the etched profile is scarcely changed.

As an increase in the value of a (Fig. 8.11.A - D) results in a decrease of τ (eq. (8.16)), the development of the profiles in the present experiment is also in agreement with the theoretical profiles of Fig. 8.4. A right angle between the experimental profile and the resist layer is found in all cases (see Figs. 8.10 and 8.11), as expected for diffusion-controlled etching. In conclusion we may say that, despite the fact that the theoretical model is only valid for stationary etchants without convection, the theory turns out to be very useful in predicting the shape of the experimental profiles in a qualitative way. Results similar to those shown in Figs. 8.10 and 8.11 were also found with InP in bromine-containing HBr solutions under certain conditions (Table VI).

On the basis of an anology with the results obtained for semi-infinite resist layers (previous section), facets can be expected in profiles etched in some of the etchants of Table VI. This is due to either an electrochemical interaction of crystallographic facets or to a low rate constant at certain crystal planes ($Sh <$). With regard to the latter, intermediate cases, it should be emphasized that due to the considerable increase in the supply of etching-species at small slit widths, it is possible that the etch rate of a crystallographic facet becomes kinetically controlled while the etch rate of the same facet in a semi-infinite profile is controlled by mass-transport in solution. This can also be recognized in eq. (8.15) from the influence of the slit width on the Sherwood number. The effect of electrochemical interaction on the etched profiles will be the subject of the following section.

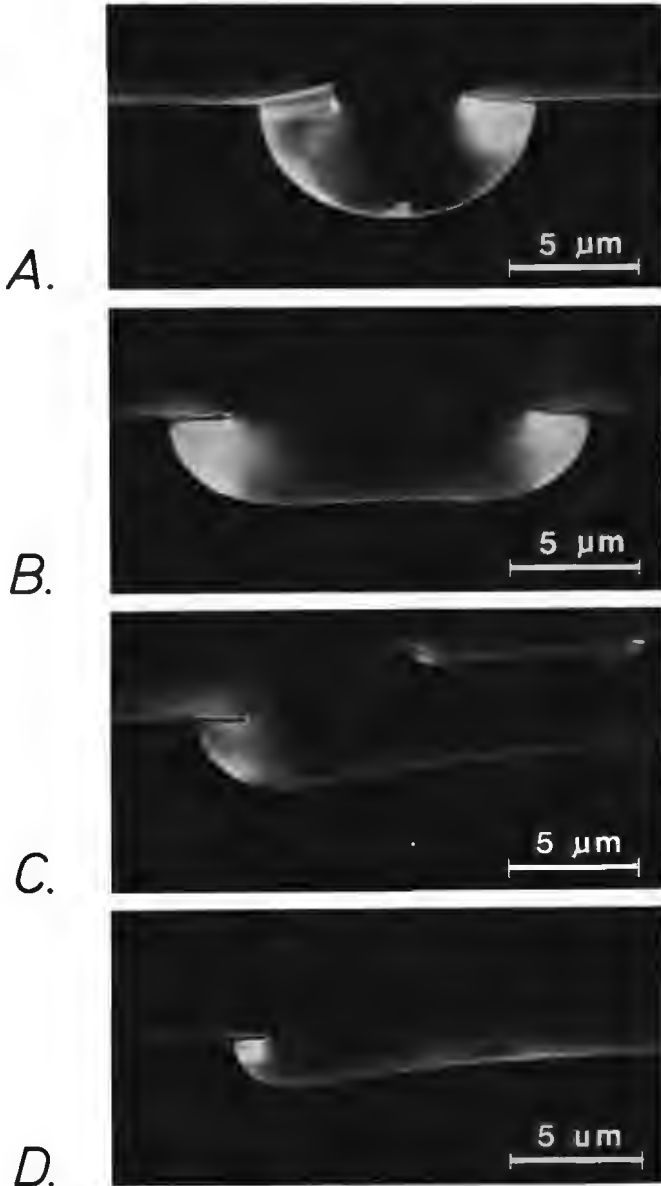**Fig. 8.11.** SEM photographs revealing the dependence of the profile shape on the slit width. The SiO$_2$-masked GaAs crystals were etched for two minutes in a horizontal position in the same etchant as used in Fig. 8.10. The slit width was 3, 10, 30 and 1000 μm in A - D, respectively. The insert of Fig. 8.11.C shows the complete profile at a lower magnification; the resist opening was $a = 30$ μm.

8.3.4. Cathodic protection of crystallographic facets

In section 8.3.2 mathematical models were presented which describe diffusion-controlled etching at resist edges. When the rate constants for dissolution of a monocrystalline solid are very high for all crystallographic planes, then mass-transport in the solution is generally rate-determining, and etching is expected to be isotropic. At resist edges, therefore, rounded profiles are predicted (Figs. 8.3 and 8.4). These models were verified in section 8.3.3 for both GaAs and InP using various chemical etchants. With electroless systems, however, anomalous results were sometimes found. In several cases in which the macroscopic etch rate of the various crystal planes of GaAs was clearly diffusion-controlled, etching at resist edges was nevertheless anisotropic. To predict the etched shape with electroless etchants, it was found that a distinction between the two electroless mechanisms has to be made. When electroless etching is anodically controlled by OH^- diffusion in solution, diffusion profiles, similar to those found with chemical etchants, were obtained. These rounded profiles were found not only with the anodically controlled $OCl^-/pH = 11$-14 system but also with the $Fe(CN)_6^{3-}/pH = 11$-14 system (see Table IV; electroless (ii) systems). When, on the other hand, electroless etching was cathodically controlled, rounded profiles were not observed. Instead, clearly defined crystallographic facets were exposed during dissolution. With the $Fe(CN)_6^{3-}$ system the (111)Ga face was exposed (Fig. 8.9). Similar results were also found with other cathodically controlled electroless etchants, such as Ce^{4+} solutions at low pH (Table IV).

In the present section this apparent anomaly is described in more detail. Results of current-potential and impedance measurements are used to assist in understanding the unusual etching results. The conclusions have, however, a wider relevance since they show the importance of electrochemical interaction between different crystallographic facets in single-crystal electrodes. This is obvious at a microscopic level, not only in the shape of the etched profiles but also in the morphology of a macroscopically etched surface.

Since the electrochemistry of both p- and n-type GaAs electrodes in alkaline $Fe(CN)_6^{3-}$ solutions was described extensively in section 5.3, this system is appropriate for comparing the results of profile etching and electrochemical experiments. Etching of n-GaAs in an 0.1 M $Fe(CN)_6^{3-}$ solution of $pH = 13$ corresponds to cathodically controlled electroless dissolution in which the transport of $Fe(CN)_6^{3-}$ in solution is the rate-determining step, as was concluded from Fig. 5.10, curve (a). The (111)Ga facet is clearly revealed near the resist edge, as is shown in Fig. 8.12.A. A rounded profile
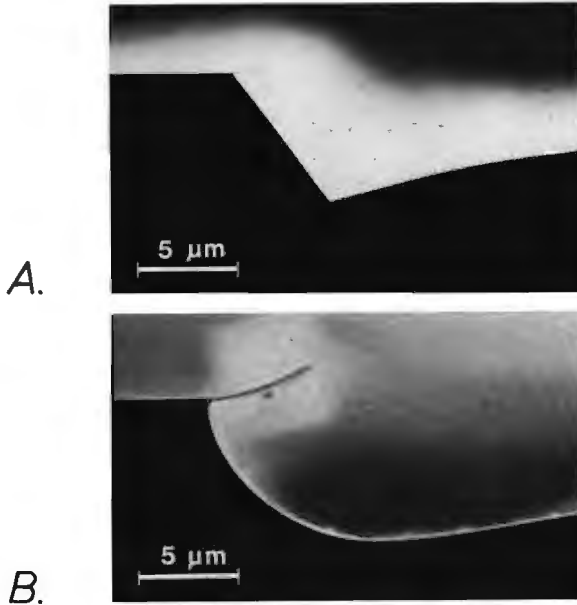
Fig. 8.12. SEM photographs of profiles etched for 10 min. in n-type GaAs in two solutions of $pH = 13$ containing different concentrations of $K_3Fe(CN)_6$; 0.1 M $K_3Fe(CN)_6$ (A) and 0.5 M $K_3Fe(CN)_6$ (B). The semi-infinite SiO_2 mask was aligned in the $[\bar{1}10]$ direction in both cases.

is obtained when n-GaAs is dissolved in a 0.5 M $Fe(CN)_6^{3-}$ solution of $pH = 13$ (Fig. 8.12.B). This case, in which electroless etching is anodically controlled by OH^- diffusion in solution, corresponds to the current-potential curve (a) of Fig. 5.11. That etching is anodically controlled can be recognized from the second cathodic plateau appearing at approximately -1.1 V and from the relatively positive open-circuit potential compared to that found in the cathodically controlled case (compare V_r in curves (a) of Figs. 5.10 and 5.11). Similar profile etching results as shown in Fig. 8.12 were also found with p-type, (001), GaAs crystals. The etching results are in agreement with the two cases which were distinguished electrochemically at p-type electrodes in section 5.3.2 (see Fig. 5.8).

It is well established that different crystallographic orientations of III-V materials can differ considerably in electrochemical properties. In Table VII values of the flat-band potential obtained from Mott-Schottky measurements for both p- and n-type GaAs electrodes are presented. Three different crystal orientations were considered. The results, measured in 0.1 M NaOH solution, are self-consistent; the difference between V_{fb}^o values of p- and n-type

Table VII

The influence of crystallographic orientation on the flat-band potential of GaAs electrodes in 0.1 M NaOH solution. V_{fb}^o is given in volts versus SCE.

Surface orientation	$V_{fb}^o(p)$	$V_{fb}^o(n)$
(001)	−0.50	−1.80
(111)As	−0.45	−1.75
(111)Ga	−0.25	−1.55

samples of the same crystallographic orientation is close to the band-gap of GaAs, as expected. While the (001) and (111)As electrodes have quite similar flat-band potentials, the value for the (111)Ga face was generally more positive. Such effects can be understood in terms of differences in the Helmholtz layer (see eq. (2.14)) [16].

The difference in V_{fb}^o values shown in Table VII are also reflected in the anodic current-potential curves. In Fig. 8.13 results are shown for the
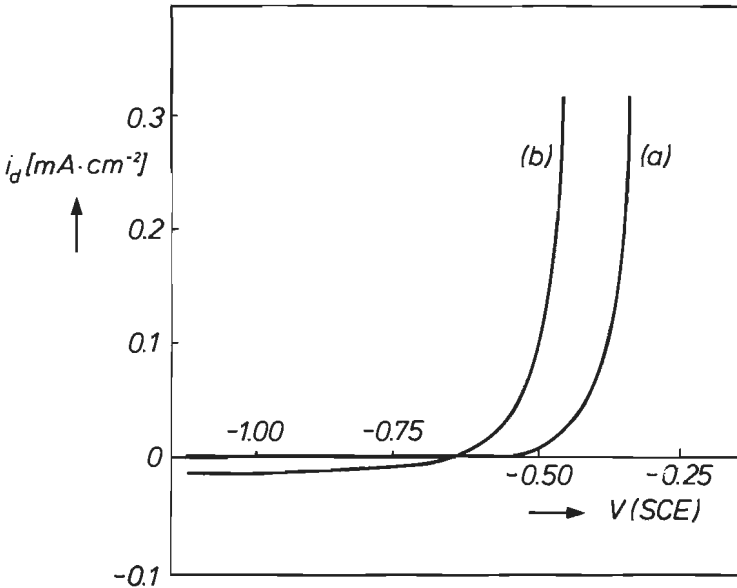

Fig. 8.13. Current-potential curves for p-type (111)GaAs electrodes in the dark in an 0.1 M NaOH solution. Curve (a) refers to the (111)Ga surface and curve (b) to the (111)As face.

(111)Ga and (111)As surfaces of p-type materials in the dark in curves (a) and (b), respectively. Anodic dissolution of the Ga face starts at a potential more than 100 mV positive with respect to that of the As face. Differences in current-potential curves of n-type electrodes were also observed for different orientations. The faceted profiles can be explained on the basis of these electrochemical differences.

When a single crystal is etched at a resist edge, various crystal planes are exposed to the solution. It is clear from the results described above that such faces differ in electrochemical activity. The importance of crystallographic orientation for etching kinetics has long been recognized. As noted before, the (111)A face of III - V crystals generally etches more slowly than the other faces, when dissolution is not diffusion-controlled [3,4]. Gatos and Levine report that the rest potential of A surfaces in oxidizing etchants is more positive than that of the other surfaces [3,4]. The result of Fig. 8.13 is in agreement with this observation. In electrochemical terms all these results mean that the A face is more 'noble'. Such a difference in nobility suggests the possibility of local element formation [17,18] between crystallographic facets. It has been shown in section 5.3 that the open-circuit potential of the electrode depends markedly on the electrolyte composition (compare V_r in curves (a) of Figs. 5.10 and 5.11). Differences in the open-circuit potential can have an important influence on the etching results in the case of local element formation in metals [18].

The effects are illustrated schematically in Figs. 8.14 and 8.16 for a p-type material. For Fig. 8.14 it is assumed that the reduction of the oxidizing agent is diffusion-limited. Here, two arbitrary crystal planes denoted by K and L are considered. The difference in nobility between these planes is indicated by the difference in potential for anodic current onset. For simplicity, diffusion limitation on the anodic side is disregarded, i.e. electroless etching is cathodically controlled. A further simplification is the assumption that the area of each plane in contact with the etchant is the same. It is clear that at the separate rest potentials $V_{r(K)}$ and $V_{r(L)}$, the etch rates of the two planes, given by the partial anodic currents I_K^+ and I_L^+, are the same, being determined by diffusion of the oxidizing agent (see also Fig. 2.10 in section 2.6). When, however, the two planes are brought into electrical contact, it is necessary to consider the total anodic and total cathodic current-potential curves as indicated by the dashed lines (KL) in Fig. 8.14. The new rest potential, $V_{r(KL)}$, lies between the values for the individual surfaces. It is assumed that the electrical resistance within the solid is negligible. Since $V_{r(KL)}$ is negative with respect to $V_{r(K)}$ and positive with respect to $V_{r(L)}$, the etch rate of the more noble surface is diminished from I_K^+ to $I_{K(KL)}^+$, while
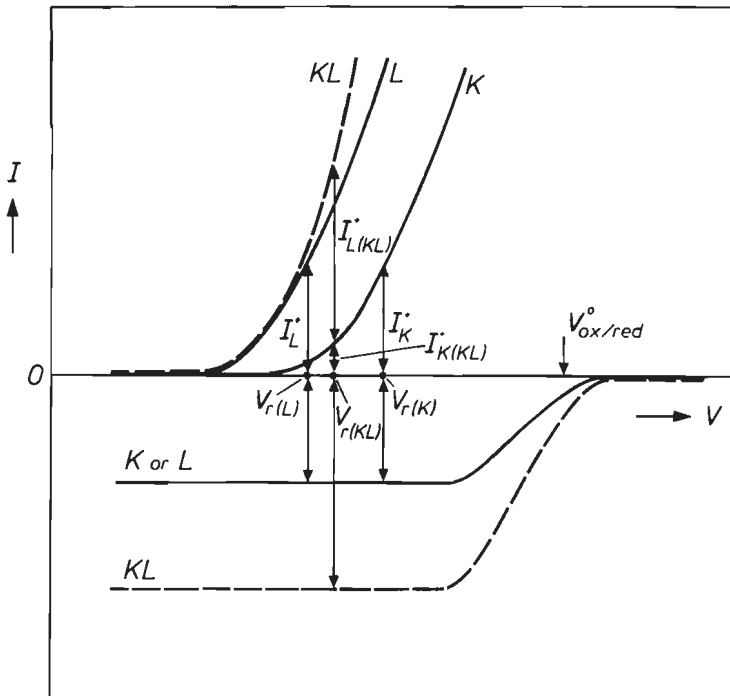
Fig. 8.14. Schematic representation of galvanic element formation between two crystal planes, K and L. The solid lines give the partial current-potential curves for the individual planes. The mixed potentials of these planes in the solution containing an oxidizing agent are indicated by $V_{r(K)}$ and $V_{r(L)}$. At V_r the partial anodic current (I_K^+ and I_L^+) is equal to the partial cathodic current (I_K^- and I_L^-). The dashed lines refer to the total anodic and cathodic curves for the two planes in electrical contact (KL). At the value of the mixed potential of the combined system ($V_{r(KL)}$) the partial anodic current (I_{KL}^+) is equal to the partial cathodic current (I_{KL}^-), with $I_{KL}^+ = I_{K(KL)}^+ + I_{L(KL)}^+$, where $I_{K(KL)}^+$ and $I_{L(KL)}^+$ represent the etch rate of the individual facets in contact with each other. In this example, reduction of the oxidizing agent is diffusion-controlled.

that of the less noble surface is enhanced from I_L^+ to $I_{L(KL)}^+$ (see Fig. 8.14); $I_{K(KL)}^+$ and $I_{L(KL)}^+$ are the partial anodic currents of the K and L surfaces, respectively, when the surfaces are in contact with each other. Holes supplied to the K face are used to etch preferentially the L face.

The consequences of this process for profile etching (see Fig. 8.12.A) are schematically represented in Fig. 8.15. The K face of Fig. 8.14 corresponds to the more noble (111)Ga facet (see also Table VII). Supply of $Fe(CN)_6^{3-}$
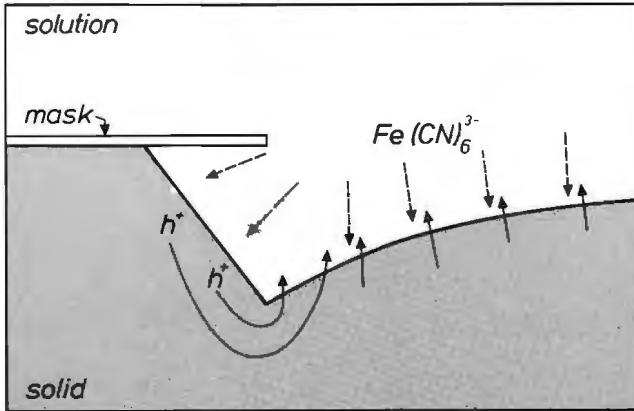
Fig. 8.15. Schematic representation of the processes occurring in the mask-edge region of a semiconductor during etching in a cathodically diffusion-controlled electroless etchant. The diffusion-controlled hole injection rate by $Fe(CN)_6^{3-}$ in solution is indicated by the dashed arrows. The 'noble' facet near the resist edge is cathodically protected and the excess holes are transported to the less noble parts of the interface, where they enhance the dissolution rate of the semiconductor (solid arrows).

species in the solution to the solid/solution interface occurs by two-dimensional diffusion and hole injection takes place at a diffusion-controlled rate over the entire semiconductor surface, as is schematically indicated by the dashed arrows in solution (Fig. 8.15). However, as the (111)Ga facet is more noble than other crystal planes, the holes injected at the faceted interface are, at least partly, transported through the semiconductor to the neighbouring less noble interface where they are used for the dissolution reaction. This is illustrated in Fig. 8.15. 'Cathodic protection' of the (111)Ga plane results in a relatively low kinetically controlled etch rate of this facet at the expense of the rest of the solid surface. The bulged shape at some distance from the resist edge indicates that the etch rates of all other crystal planes are diffusion-controlled (see also Fig. 8.12.A).

Although the case shown in Fig. 8.14 may be oversimplified, it nevertheless illustrates how, in the case of cathodically controlled electroless etching, certain facets can be cathodically protected by the neighbouring surface. This model can therefore explain a faceted profile even though the individual macroscopic faces are etched at a diffusion-controlled rate.

In Fig. 8.16 the alternative case is considered in which a limiting anodic reaction determines the etching kinetics. The cathodic diffusion current is now assumed to be sufficiently large, so that it need not be included in the
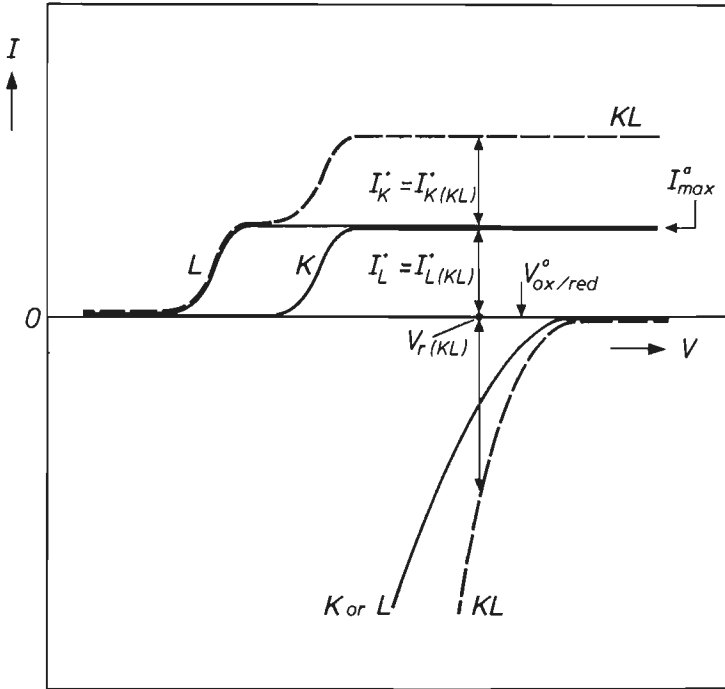
Fig. 8.16. Schematic representation of the interaction between two crystal planes, K and L, for the case in which anodic oxidation of the solid is diffusion-controlled. The notation is the same as for Fig. 8.14. At the mixed potential of the combined system $(V_{r(KL)})$, the etch rate of each crystal plane is controlled by $i^a_{max}(= I^+_{K(KL)} = I^+_{L(KL)})$.

figure (compare with Fig. 5.8). The difference in nobility between the K and L planes is again clear from the anodic current onset. On the basis of this figure it can be concluded that, because the anodic current is potential-independent, the etch rates of the K and L planes are not affected when they are connected electrically, i.e. $I^+_K = I^+_{K(KL)}$ and $I^+_L = I^+_{L(KL)}$ (see Fig. 8.16). It is clear that in this anodically controlled case the open-circuit potential is not changed and that the more noble surface is not cathodically protected. In fact, all surfaces are dissolved at the same rate, determined by OH^- diffusion. Etching at resist edges is expected to be isotropic and takes place at a relatively positive rest potential. From electrochemical measurements in sections 4.2 and 5.3 it was concluded that under these anodically controlled conditions the surface is uniformly covered with a thin oxide layer and that

hole injection through the oxide film takes place via a tunnelling mechanism.

The description of cathodic protection given above refers to p-type electrodes. However, a similar reasoning can be applied to n-type electrodes. It was already noted that, at this type of electrode, a considerable difference in the rest potential is also observed between cathodically and anodically controlled electroless etchants (see Figs. 5.10 and 5.11). Furthermore, Table VII shows that the crystallographic orientation has an important effect on the flat-band potential and a significant difference in open-circuit potential between different crystal planes would therefore also be expected. Electrochemical measurements at n-GaAs electrodes in alkaline $Fe(CN)_6^{3-}$ solutions showed this to be the case. At n-type electrodes minority charge car-
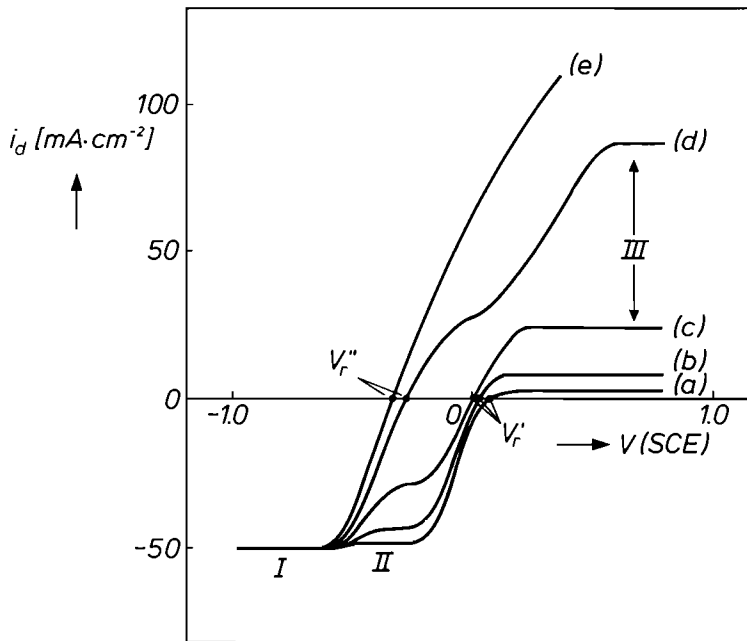
Fig. 8.17. Potentiodynamically (20 mV·s^{-1}) measured current-potential curves for a p-type GaAs(001) RDE (100 rpm) in the dark in 0.5 M $K_3Fe(CN)_6$ solution, as a function of the pH: $pH = 12.0$ (curve (a)); $pH = 12.5$ (curve (b)); $pH = 13.0$ (curve (c)); $pH = 13.5$ (curve (d)); $pH = 14.0$ (curve (e)). The collection of rest potentials measured with cathodically controlled electroless etchants is indicated by V_r'', while that obtained with anodically controlled etchants is represented by V_r'. The three current plateaus which can be distinguished in the curves are denoted by I, II and III (see also Fig. 5.8).

riers are injected by the oxidizing agent into the valence band of the solid and recombination must be taken into account. However, it seems reasonable to expect that local galvanic elements can also be formed in a monocrystalline n-type system, and that certain facets can be cathodically protected. This has, indeed, been found experimentally (Fig. 8.12.A) with cathodically controlled electroless etchants.

We may conclude that the form of the GaAs profiles etched in alkaline $Fe(CN)_6^{3-}$ solutions is determined by the ratio of OH^- and $Fe(CN)_6^{3-}$ concentrations. The change in profile in Fig. 8.12 was brought about at a fixed pH by increasing the concentration of the oxidizing agent. The importance of the solution pH is shown in Fig. 8.17. Measured current-potential curves at a p-GaAs RDE are given at a constant $Fe(CN)_6^{3-}$ concentration. These curves fall into two groups. At relatively low pH, the limiting anodic current is smaller than the cathodic current. Etching is determined by OH^- diffusion and, as in the case of n-type electrodes (Fig. 5.11), a second cathodic plateau (II) is found in combination with a relatively positive rest potential ($V_r' \geq 0.0$ V). In these cases no preferential etching of facets is expected. At higher pH, the situation is reversed and reduction of the oxidizing agent is the determining reaction at V_r''. The rest potential is 200-300 mV more negative than in the previous case and the second plateau is anodic (see curve (d) of Fig. 8.17). Cathodic protection is therefore expected in these cases. This is confirmed experimentally in Fig. 8.18. The rounded profile shown in Fig. 8.18.B was obtained with an 0.5 M $Fe(CN)_6^{3-}$ solution of $pH = 13$ (see also Fig. 8.12.B). The profile can be made anisotropic not only by lowering the $Fe(CN)_6^{3-}$ concentration at constant pH (see Figs. 8.18.A and 8.12.A) but also simply by raising the pH from 13 to 14 at constant $Fe(CN)_6^{3-}$ concentration as is shown in Fig. 8.18.C (compare curves (c) and (e) of Fig. 8.17). It should be noted that, as etching in both Fig. 8.18.A and C is cathodically controlled by the $Fe(CN)_6^{3-}$ concentration, the etch rate in an 0.5 molar solution is 5 times higher than in an 0.1 molar solution. Lowering the etching time in the concentrated $Fe(CN)_6^{3-}$ solution by a factor of 5 should yield the same etch depth of the faceted profile. This is in fair agreement with the result of Fig. 8.18.A and C. Results similar to those in Fig. 5.18 were also found with n-type crystals in these etchants.

Formation of galvanic elements can, in a similar way, also influence the corrosion properties of semiconductor materials on a macroscopic scale. Since crystallographic defects correspond to disturbed regions of the solid, they are less noble than the surrounding material [19]. As a result of local element formation a distinction between the etch rate of such defects and that of the surrounding surface would therefore be expected. In section 5.3
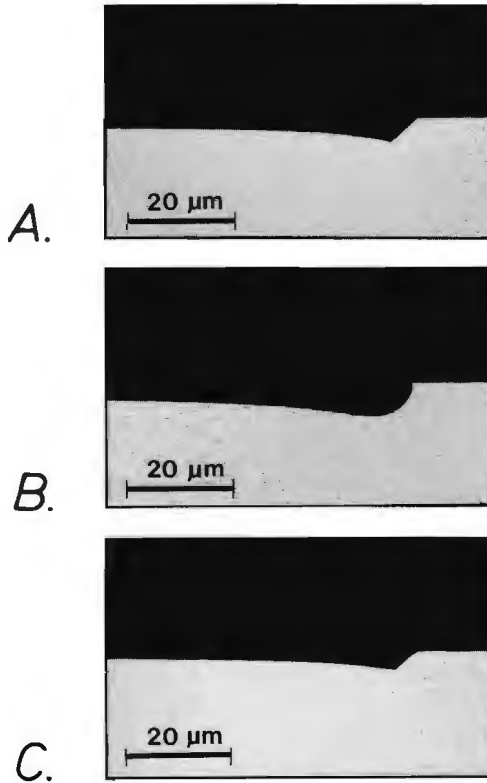
Fig. 8.18. Optical micrographs of profiles etched in p-type GaAs(001) in alkaline Fe(CN)$_6^{3-}$ solutions of various composition during various etching times: 10 min. in a solution of 0.1 M K$_3$Fe(CN)$_6$, pH = 13 (A); 10 min. in 0.5 M K$_3$Fe(CN)$_6$, pH = 13 (B); 2 min. in 0.5 M K$_3$Fe(CN)$_6$, pH = 14 (C). A and C refer to cathodically controlled, and B to anodically controlled electroless etching.

it was shown that during cathodically controlled electroless etching of GaAs defects are clearly revealed (Fig. 5.15.A). It is therefore concluded that the ability of these electroless etchants to reveal defects must be attributed to cathodic protection of the surface in the vicinity of these defects. When, on the other hand, electroless etching is anodically controlled, cathodic protection cannot take place and preferential etching of defects does not occur. This is also in agreement with the good polishing properties of these solutions (see Fig. 5.15.B).

Essential for cathodic protection is that free charge carriers (holes) injected by an oxidizing agent can be transported from 'noble' parts to 'less

noble' parts of the solid/solution interface. Galvanic element formation is therefore observed with electroless systems but not with chemical etchants. Consequently, purely diffusion-controlled rounded profiles are always found with the latter systems. That cathodic protection is restricted to cathodically controlled electroless etchants and is not found with anodically controlled systems can also be understood in this way: anodically controlled electroless etching is, in fact, also determined by the kinetics of the chemical dissolution of the oxide film at the oxide/solution interface. This also explains why under these conditions smooth polished surfaces are always obtained.

8.4. Intermediate etching profiles

Introduction

In the previous sections, two limiting cases were considered. Firstly, kinetically controlled processes were described in section 8.2. This resulted in profiles in which only crystallographic facets were revealed. The kinetics of the surface reaction of certain facets ultimately determine the shape of the profiles. Secondly, diffusion-controlled profiles were considered in section 8.3. The dissolution rate was controlled by mass-transport of etching species in solution at the entire semiconductor/solution interface. This resulted in most cases in rounded profiles. Facets were revealed only when electroless etching was cathodically controlled by diffusion.

In this section the intermediate case will be considered: the dissolution rate constant of many crystal planes is large and the etch rate of these facets is thus controlled by diffusion, whereas etching of other crystal planes is kinetically controlled. On the basis of the previous two sections, combined faceted/curved profiles are expected. That such an intermediate case is realistic can be deduced from the macroscopic etching experiments made with InP in bromine-containing solutions, which were described in section 6.4. From flow-cell measurements it was concluded that the macroscopic chemical etch rate of InP with the (001) surface orientation is controlled by Br_2 diffusion (see curve (a) of Fig. 6.10) while that of the (111)In orientation is kinetically controlled (curve (b) of Fig. 6.10). This etching system would therefore seem to be appropriate for investigating the intermediate case. Furthermore it is possible to check if the macroscopic etching results can be used to predict the microscopic profiles at resist edges.

In section 8.2 it was suggested that the kinetics of a dissolution reaction can be influenced by changing the temperature of the etching solution. It should therefore be possible to observe a transition from a kinetically-con-

trolled to a diffusion-controlled etch rate (see curve (c) of Fig. 8.2). This would also have consequences for the shape of the etched profiles. The temperature dependence of the etched profiles was investigated for two different etching systems using both InP and GaAs. It will also be shown that a similar transition can be achieved by varying the slit width in the resist layer.

Results and discussion

Profile etching experiments were performed with InP(001) in a solution of 0.1 M Br_2 and 4.5 M HBr at various temperatures. The surface was
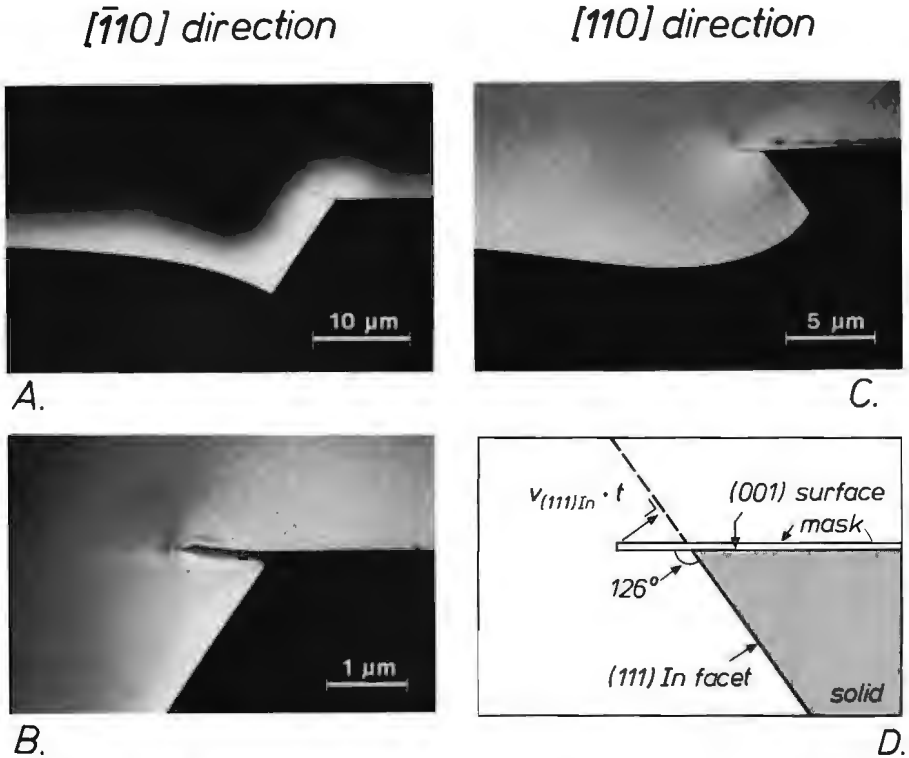
Fig. 8.19. SEM photographs of intermediate profiles in InP after 7.5 min. etching in a solution of 0.1 M Br_2, 4.5 M HBr. The crystals were covered with a semi-infinite SiO_2 mask. The profile shown in A was obtained with the resist aligned in the [$\bar{1}$10] direction at an etching temperature of 20 °C. A higher magnification of the same profile in the resist-edge region is shown in B. Profile C was etched with the resist oriented in the [110] direction at a temperature of 0 °C. The etch rate of the (111)In facet in the [110] orientation is defined in D (see also Fig. 8.1.B).

masked with an approximately 0.1 μm thick semi-infinite SiO_2 resist layer aligned in either the [$\bar{1}$10] direction or the [110] direction. The semiconductor was etched for 7.5 minutes in a horizontal position at a temperature between −8 °C and +40 °C.

Two typical examples of etching profiles obtained with each resist orientation are shown in Fig. 8.19. The profile obtained in the [$\bar{1}$10] direction at a temperature of 20 °C is shown in A of this figure. A facet is clearly revealed near the resist edge. As this is a chemical etchant (Table IV) cathodic protection of crystallographic facets cannot occur. This indicates that the etch rate of the facet is kinetically controlled. The faceted edge makes an angle of 54° with the (001) surface and is thus attributed to the (111)In plane [9], the same face whose macroscopic etch rate was also found to be kinetically controlled (section 6.4). The etch rate of this facet ($v_{(111)In}$) can be obtained from its displacement with respect to the resist edge and the etching time, as defined before in Fig. 8.1.B. To obtain an accurate estimate of the etch rate a higher magnification of the corner region of the same profile was used (Fig. 8.19.B).

Curve (a) of Fig. 8.20 shows the dependence of the etch rate of the (111)In facet on the temperature in an Arrhenius plot for [$\bar{1}$10] alignment of the resist layer. In accordance with eq. (8.1), the logarithm of $v_{(111)In}$ is linearly dependent on the reciprocal of the temperature. From the slope of this line an activation energy of 41×10^3 J·mole^{-1} is calculated. This value is typical of kinetically controlled processes (see section 8.2) [10]. The agreement of the etch rate of this plane in the etched profiles and the macroscopic etch rate of the plane at the same temperature is striking (compare the values indicated by the arrows in curve (a) of Fig. 8.20 and curve (b) of Fig. 6.10). The curved surface further removed from the mask (Fig. 8.19.A) shows that the etch rate of other facets, including that of the (001) surface, is diffusion-controlled. These results show that macroscopic etching results can be used to predict the shape of the etching profiles.

A typical example of a profile obtained in the [110] direction at a temperature of 0 °C is shown in Fig. 8.19.C. In this case the facet makes an angle of approximately 126° with the overhanging resist layer. Since the resist edge is aligned in the [110] direction, crystallographic considerations lead us to conclude that a (111)In facet has again been exposed [1,9]. The etch rate of the (111)In facet can again be obtained from its displacement with respect to the resist edge and the etching time, as shown schematically in Fig. 8.19.D. Curve (b) of Fig. 8.20 reveals a linear dependence of the logarithm of this etch rate on T^{-1} in the temperature range −8 °C to +20 °C. This line has the same slope as curve (a) of this figure. It is, how-
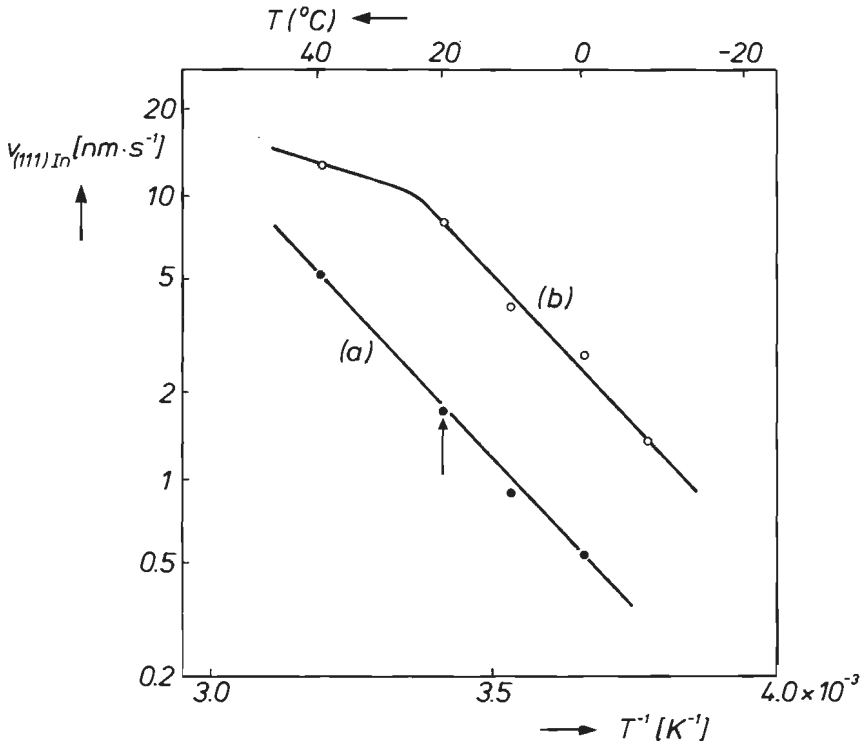
Fig. 8.20. The microscopic etch rate of the (111)In plane of InP, as obtained from profile etching experiments performed with a semi-infinite SiO$_2$ mask as a function of the reciprocal temperature. The same etchant was used as in Fig. 8.19. The etching time was 7.5 min. Curve (a): the SiO$_2$ mask aligned in the [$\bar{1}$10] direction; curve (b): alignment in the [110] direction. The arrow in curve (a) shows the good agreement between the microscopic and macroscopic etch rates of this plane found under the same experimental conditions (see also the corresponding arrow in Fig. 6.10, curve (b)).

ever, strange that the etch rate of the (111)In plane in the [110] direction is about five times higher than that in the [$\bar{1}$10] direction in the corresponding temperature range (compare curves (a) and (b) of Fig. 8.20). This is even more surprising since the microscopic etch rates in curve (a) agree with the macroscopic etch rate. This result shows that the kinetics of the dissolution reaction of the (111)In facet strongly depends on the orientation of the masking pattern. Rounded profiles were etched at InP(001) covered with a photoresist layer at 20 °C in the same etchant as used with the present InP/SiO$_2$ system; this indicates that the etch rate of the (111)In plane can

be further increased to become even diffusion-controlled (see also section 8.3.3). All these results suggest that the microscopic etching kinetics depend, not only on the orientation of the resist layer, but also on the nature of these layers. This unexpected feature will be discussed in detail in the following section.

Returning to the results of Fig. 8.20, curve (b), we note a deviation from the straight line at 40 °C. This must be attributed to the fact that etching of the (111)In facet is no longer kinetically controlled but has become diffusion-controlled. Indeed, at this temperature a rounded profile is obtained in the [110] direction, without any facet. The temperature dependence of the etch rate is significantly lower under these diffusion-controlled conditions, which is indicated by a decreased slope in the Arrhenius plot (curve (b) of Fig. 8.20). This is in agreement with the considerations presented in section 8.2 (see curve (b) of Fig. 8.2) [10]. That a gradual transition from kinetically controlled to diffusion-controlled etching process occurred in this temperature range could also be deduced qualitatively from the fact that, on going from lower to higher temperature, the length of the (111)In facet in the profiles strongly decreased, to disappear ultimately at the highest temperature. This is not observed with the profiles in the [$\bar{1}$10] direction.

Another example in which the shape of the etching profile is dramatically influenced by the temperature is shown in Fig. 8.21. In this case profiles were etched in a bromine solution through a slit of an SiO_2 resist layer on GaAs. Etching was performed in the temperature range 0-40 °C for 5 minutes in all cases. In Fig. 8.21.A, a kinetic profile is obtained at 0 °C with 54° facets at each side of the resist opening. Since the resist layer was aligned in the [$\bar{1}$10] direction it is obvious that these facets must be attributed to (111)Ga planes. The etch rate of these facets is increased at higher temperatures (see eq. (8.1)) and diffusion becomes important at 20 °C. This resulted in Fig. 8.21.B in a slightly rounded shape at both the lower and upper parts of the profile. This result corresponds to the intermediate case. When the temperature is further increased to 40 °C, the etching kinetics of the (111)Ga facet are no longer rate-determining and an almost rounded, diffusion-controlled, profile is obtained in Fig. 8.21.C. Surprisingly, the profiles obtained with the SiO_2 resist aligned in the [110] direction all have a rounded shape in the corresponding temperature range. We will discuss this effect in section 8.5.

These results, found at both InP and GaAs, show that temperature is an important parameter in determining the shape of the etching profiles. A precondition for achieving such a transition in shape is, of course, that the dis-
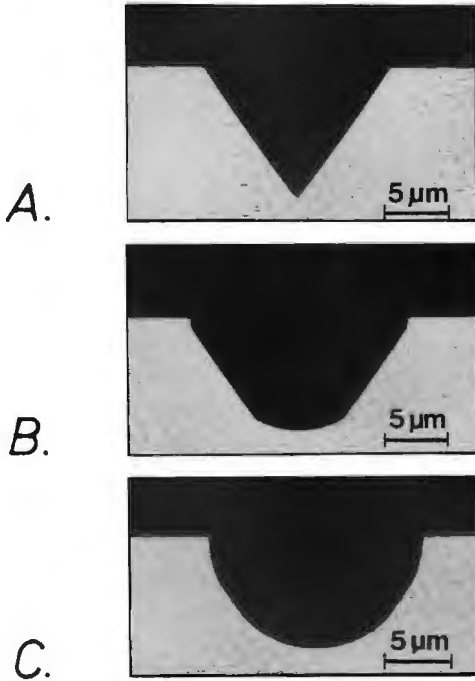
Fig. 8.21. Optical micrographs revealing the dependence of profile shape on the temperature. GaAs(001) was etched for 5 min. in a 0.1 M Br$_2$/HBr solution. The photoresist was oriented in the [$\bar{1}$10] direction with $a = 3$ μm. A transition from a kinetically controlled profile obtained at 0 °C (A), via an intermediate profile at 20 °C (B), to a diffusion-controlled profile at 40 °C (C), was observed.

solution rate of the crystallographic planes must be of the same order of magnitude as the diffusion rate.

In section 8.3.3 it was shown that the shape of the rounded profiles which were etched under diffusion-controlled conditions could be considerably changed by varying the dimensionless etching time (see Figs. 8.10 and 8.11). τ could be varied by changing the absolute etching time or the slit width in the resist layer (eq. (8.16)). In the present intermediate case τ might be expected to have a similar effect on the shape of profiles. To investigate the dependence of the shape on τ, etching experiments were made at InP covered with an SiO$_2$ layer in which the slit width was varied while the absolute etching time was held constant (7.5 minutes). Some profiles obtained in the same solution as used in Fig. 8.19 at a temperature of −8 °C are presented in Fig. 8.22. The profiles were again studied in both the [$\bar{1}$10] and
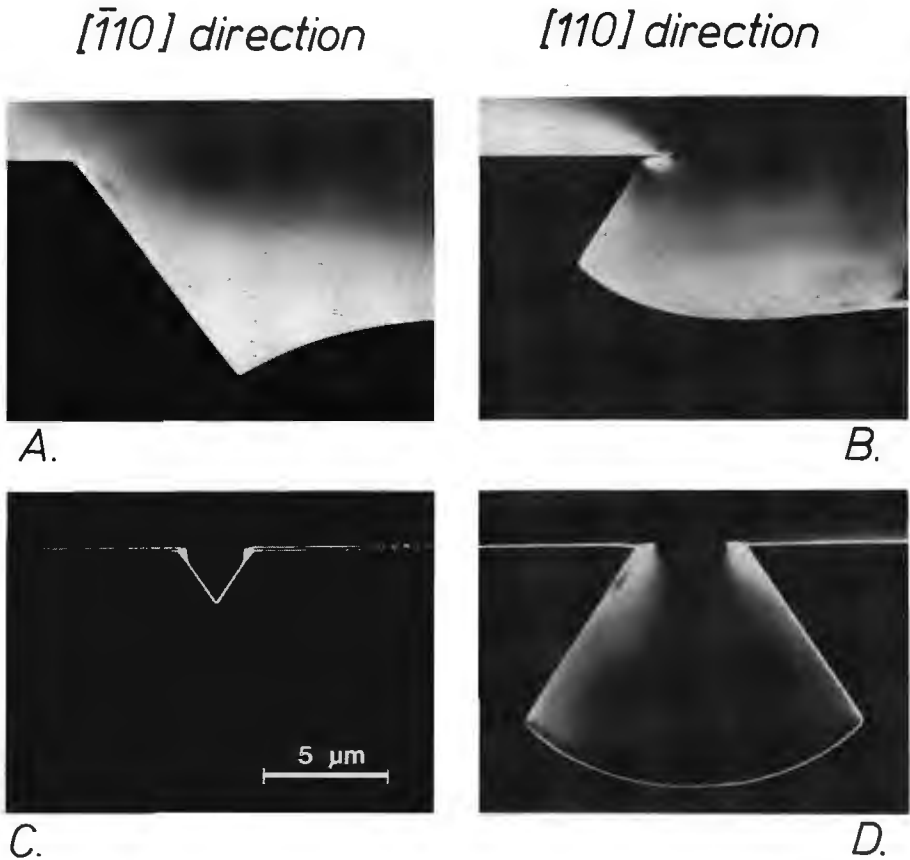
Fig. 8.22. Dependence of the profile on both the slit width and resist orientation: n-type InP was etched for 7.5 min. in a solution of 0.1 M Br$_2$, 4.5 M HBr at a temperature of −8 °C. The SiO$_2$ resist was aligned in the [$\bar{1}$10] direction (SEM photographs A and C) and in the [110] direction (B and D). The slit width was either 30 μm (A and B) or 3 μm (C and D). The same magnification is used in all photographs.

the [110] resist orientation. At a slit width of 30 μm the results are very similar to those found with the semi-infinite resist layer (compare Fig. 8.22.A and B with Fig. 8.19.A and C). In both directions the (111)In facet appears near the resist edges. The curved shape at the bottom of the profiles indicates the diffusion-controlled etch rate of other crystal planes. Decreasing the slit width to $a = 3$ μm causes a significant increase in the value of τ (eq. 8.16)). In accordance with the theoretical (Fig. 8.4) and ex-

perimental results (Fig. 8.11) obtained under diffusion-controlled conditions, this results in a much deeper rounded profile in the [110] direction; the double-bulge has disappeared (Fig. 8.22.D). The etch rate of the (111)In facet is not found to be dependent on the slit width, as expected for a kinetically controlled surface reaction. Only the length of this facet is obviously larger. This strongly contrasts with the result obtained in the [$\bar{1}$10] direction (Fig. 8.22.C). Comparing A and C of this figure reveals that, as a result of a decreasing slit width, a transition has been taken place from an intermediate etching profile to a kinetically controlled profile. It is obvious that this transition takes place at the moment that the two (111)In planes meet at the middle of the profile. Evidently, due to the low etch rate of the (111)In facets and due to the fact that diffusion is no longer important, the cavity is much less deep than in the corresponding profile in the [110] direction (compare C and D). In this respect, it is important to note that all profiles in Fig. 8.22 are presented at the same magnification. The discrepancy between the shapes in the two directions becomes even more pronounced when τ is further increased. Obviously, this can be achieved either by decreasing the slit width in the resist layer or by increasing the absolute etching time (see eq. (8.16)).

Finally, it should be emphasized that, although the shape of the intermediate profiles were in many cases similar to those found with cathodically diffusion-controlled electroless etchants (compare for example with Fig. 8.12.A), the etching mechanism in the present cases is fundamentally different (see section 8.3.3). It should further be noted that it is possible to deduce from profile etching experiments whether macroscopic etching of certain crystallographic facets is controlled by mass-transport in solution. This has been done for a number of etching systems. These systems were indicated in Table IV by an asterisk (see chapter 7).

8.5. Influence of native oxide layers on the etched profiles

Introduction

From the foregoing it is clear that the microscopic and macroscopic etching kinetics may be quite different. Experiments on InP in the Br_2/HBr etchant of Table VI revealed that profiles are strongly dependent on the orientation of the resist layers (Fig. 8.20) and also on the nature of these layers. This shows that factors other than those determining the macroscopic etching kinetics may contribute to the dissolution kinetics near resist edges. The aim of the present section is to determine these factors. The InP system described above was therefore investigated in more detail.

In section 6.2 it was argued that native oxide layers, present at the surface of III - V semiconductors [20], may have a considerable thickness in the case of InP. The fact that the etching profiles obtained with InP are strongly dependent on whether an SiO_2 layer or a photoresist layer is used suggests that the resist induces changes in the morphology of the oxide. Recently, several authors [21-23] attributed changes in the shape of profiles at InP to changes in both the thickness and the nature of the thermally grown oxide layers. The shape of the profiles was found to be dependent on the temperature and on the conditions under which the various oxide layers were formed.

It is well-known that thin surface layers can influence the shape of profiles etched near resist edges [24-27]. Materials are often intentionally covered with a thin surface film of different composition to obtain special effects. This so-called bevel or taper etching is based on the fact that the etch rate of the thin top layer covering a substrate material under the resist layer is higher than the etch rate of the substrate material in the same etchant. By regulating the etch rate of the top layer, either by changing the nature of this layer [26,27] or the composition of the etchant [24,25], the beveling angle could be adjusted between 3° and 40°. To regulate the beveling angle
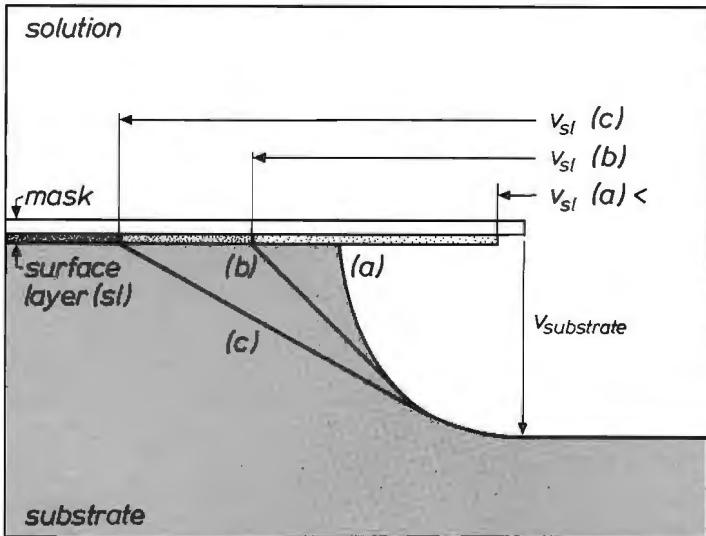
Fig. 8.23. Schematic representation of the bevel etching mechanism. The angle which the beveled 'face' makes with the surface is dependent on the lateral etch rate of the surface layer (v_{sl}). The substrate is assumed to be etched isotropically at a kinetically controlled rate ($v_{substrate}$). Curve (a) shows the etch profile expected when $v_{sl}(a) < v_{substrate}$. When $v_{sl}(b)$, $v_{sl}(c) > v_{substrate}$, the profile is changed significantly as curves (b) and (c) show.

over such a wide range etching of the substrate must be isotropic [26]. For this reason only polycrystalline [24] and amorphous materials [25-27], very often metals [24,25] or oxides [26,27], can be successfully submitted to this procedure. The principle of the bevel etching mechanism is illustrated schematically in Fig. 8.23 [24]. Three different situations are shown. Etching of the substrate material is assumed to be kinetically controlled and iso-tropic, in all cases, i.e. the dissolution rate is the same in all directions. When the etch rate of the surface layer (sl) is lower than that of the sub-strate ($v_{sl}(a) < v_{substrate}$), isotropic etching of the substrate is found (curve (a) of Fig. 8.23), as predicted by theory [8]. Evidently, in contrast to diffusion-controlled profiles, no enhanced etching near the resist edge is found in this case. When, however, the lateral etch rate of the surface layer exceeds that of the substrate ($v_{sl}(b) > v_{substrate}$), the underlying substrate is exposed and brought into contact with the etchant; dissolution of the newly formed sur-face results in a beveled face in the profile of curve (b). The angle this face makes with the surface is clearly dependent on the lateral etch rate of the surface layer (compare curves (b) and (c) of Fig. 8.23). In this way, the bevel angle can be adjusted by regulating the etch rate of the surface layer.

From these results [24-27] it is clear that thin surface layers covering amorphous or polycrystalline substrates have a strong influence on the shape of profiles near resist edges. Although bevel etching is restricted to these isotropic materials, it might be expected that thin surface films could also have important implications for the etching of microscopic structures in monocrystalline materials. It is clear from the above discussion that the na-tive oxide layers on the surface of III - V compounds can also function as a thin etchable top layer.

In order to investigate the effect of a native oxide film at InP on the micro-scopic etching kinetics, etchants were required which could dissolve the oxide below resist layers selectively with respect to the InP substrate. HBr solutions were found to be appropriate for this purpose. In section 6.3, it was shown that InP is not dissolved in 'dilute' aqueous HBr solutions. On the other hand it is known that oxides generally dissolve in strong acidic so-lutions. A 4.5 M HBr solution was therefore used at various temperatures to investigate this selectivity. Two aspects were studied: the anisotropy in the etch rate of the (111)In facet in [$\bar{1}$10] and the [110] orientations (see e.g. curves (a) and (b) of Fig. 8.20) and the pronounced differences obtained with different resist layers. On the basis of these results a model will be pre-sented to explain the various etching profiles obtained with InP. It seems likely, however, that this model has a wider relevance for etching of mono-crystalline materials. An example found with GaAs will also be discussed.

Finally, the different etching profiles obtained with monocrystalline materials and amorphous or polycrystalline materials will be discussed.

Results and discussion

Profile etching experiments were performed with InP masked with either an SiO_2 or a photoresist layer in a 0.1 M Br_2 solution of 4.5 M HBr at various temperatures. The slit width was varied between 1 and 1000 µm. The resist layers were aligned in both the [$\bar{1}10$] and [110] directions. Typical examples of profiles etched for 7.5 minutes through a 10 µm slit at a temperature of 20 °C are shown in Fig. 8.24. The results obtained with the SiO_2 resist in both orientations (Fig. 8.24.A and B) are similar to those described
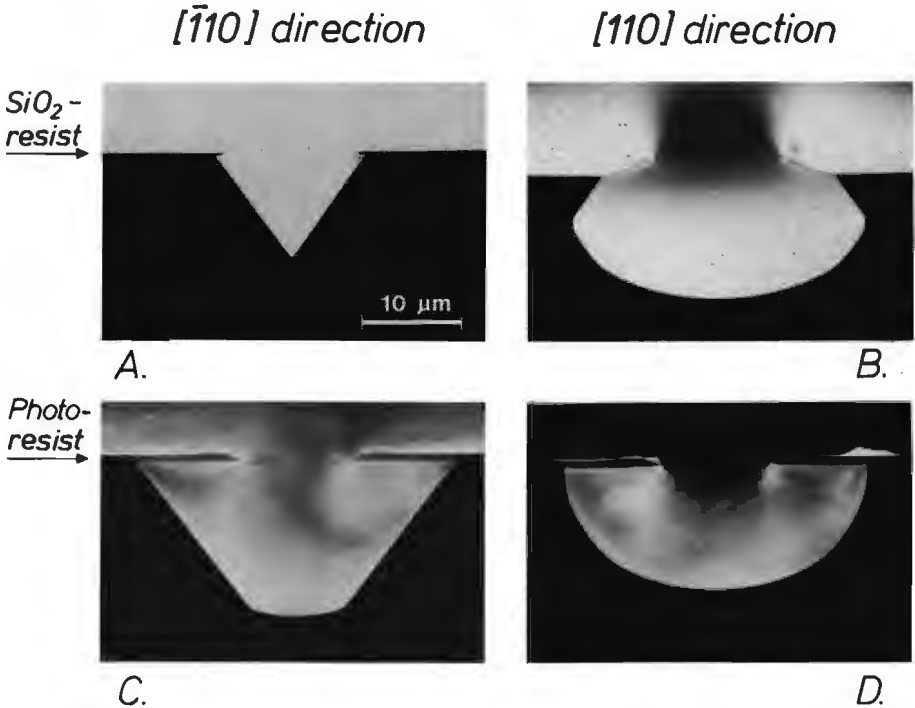
Fig. 8.24. Dependence of the profile on both the nature and the orientation of the resist for the InP/0.1 M Br_2, 4.5 M HBr etching system. Etching time was 7.5 min. and $a = 10$ µm in all cases. The results found with SiO_2 resist is shown in the SEM photographs A and B. Those obtained with photoresist are shown in C and D. The resist was aligned in either the [$\bar{1}10$] direction (A and C) or the [110] direction (B and D). The same magnification is used in all photographs.

in a previous section where a semi-infinite resist pattern was used. The etch rate of the (111)In facet in the $[\bar{1}10]$ orientation (Fig. 8.24.A) agrees with the macroscopic etch rate. In the [110] orientation (Fig. 8.24.B) the etch rate is significantly enhanced (compare also curves (a) and (b) of Fig. 8.20).

Results obtained with photoresist layers in the $[\bar{1}10]$ direction show a V-groove shape (Fig. 8.24.C), similar to that found with the SiO_2-resist in the corresponding orientation (compare with Fig. 8.24.A). Here too, a linear dependence of $\log v_{(111)In}$ on T^{-1} was observed. The line has the same slope as found before in curve (a) of Fig. 8.20, thus indicating that the dissolution rate of the (111)In facet is kinetically controlled. Strikingly, the profiles found in the [110] orientation did not reveal any crystallographic facet (Fig. 8.24.D). In contrast to the result found with SiO_2 in the corresponding resist orientation, rounded profiles are observed (compare B and D). These profiles were observed not only at 20 °C but even at very low temperatures (-10 °C $< T < 20$ °C). A plot of the logarithm of the underetch rate as a function of the reciprocal temperature also yields a straight line. However, the slope of this line is much lower than that found for kinetically controlled reactions. This is expected for a diffusion-controlled process (compare curves (a) and (b) of Fig. 8.2) [10]. From the slope, an activation energy of 15×10^3 J·mole^{-1} is calculated.

It has been suggested by several authors that a reduced adhesion between the resist layer and the substrate may be the cause of the various etching profiles [23]. In this respect it should be emphasized that the profiles are completely reproducible under a variety of etching conditions. This is also evident from the reproducible linear dependence found in the Arrhenius plots. Moreover, the lack of adhesion cannot explain the anisotropy found with each resist layer in the two orientations. Furthermore, it has been shown that surface modifiers or primers, which function in often attributed to improve the adhesion between a substrate and a resist layer, accomplish just the opposite effect, i.e. an enhancement of etch rates of crystallographic facets near the primer layer, while reduced etch rates would be expected as a result of a better adhesion [22,23]. For these reasons, it seems very likely that the different etching profiles are not due to adhesion problems.

To investigate the anisotropy, etching experiments were made at InP in a solution of 4.5 M HBr at various temperatures. Both SiO_2 and photoresist were used as a semi-infinite mask. The results found with an SiO_2 resist at 40 °C are shown in Fig. 8.25. The cross-section near the SiO_2 edge in the [110] direction is shown in A of this figure. It is obvious that the under-etching is relatively large. It is further noted that etching mainly occurred in the region where the resist layer was originally positioned at the InP sur-

face. Outside this region the InP has hardly been etched, as expected from the low macroscopic etch rate measured in HBr solutions of this composition (see curve (a) of Fig. 6.7.B). In contrast to the result of Fig. 8.25.A no underetching is found in the [$\bar{1}$10] direction. This can also be seen in the top-view shown in Fig. 8.25.B. Underetching is not found along the entire resist edge in the [$\bar{1}$10] direction. An almost constant value of 5.6 μm is found in the [110] orientation, which shows that etching proceeds uniformly along the entire resist edge.

Similar results, revealing the importance of the crystal orientation, were also found at InP covered with photoresist. The effects at the resist/substrate interface are even more pronounced than in the SiO$_2$ case. This is il-
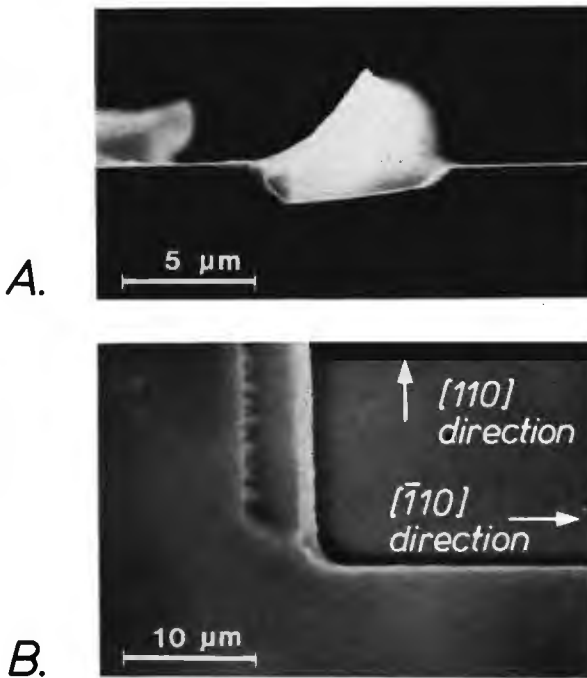
Fig. 8.25. Anisotropic results obtained with InP after 10 min. etching in a 4.5 M HBr solution at 40 °C. SEM photograph A shows a cross-section of the profile with the SiO$_2$ mask aligned in the [110] direction. Lateral etching only occurred in the mask-edge region; the white area below the curled resist is due to charging in the SEM. The top-view (B) confirms uniform underetching in the [110] direction; no underetching is found in the [$\bar{1}$10] direction.

lustrated in Fig. 8.26. A comparison between the results obtained in the [110] direction under identical etching conditions with a photoresist (Fig. 8.26.A) and an SiO_2 resist (Fig. 8.26.B) reveals that the lateral etch rate in the former case is approximately three times higher. As in the SiO_2 case, etching proceeds uniformly along the entire resist edge and is limited to the region below the mask. The etch rate of the uncovered InP outside this region is again negligibly low. It was found that the lateral etch rate in the present HBr solution depends strongly on the temperature of the etchant. However, etching stops completely below a critical value, around 20-25 °C.

The importance of the oxide film for microscopic etching of profiles at InP has been clearly shown by Dautremont et al. [21]. Two important conclusions can be drawn on the basis of their work and the present etching results in HBr solutions at elevated temperatures.
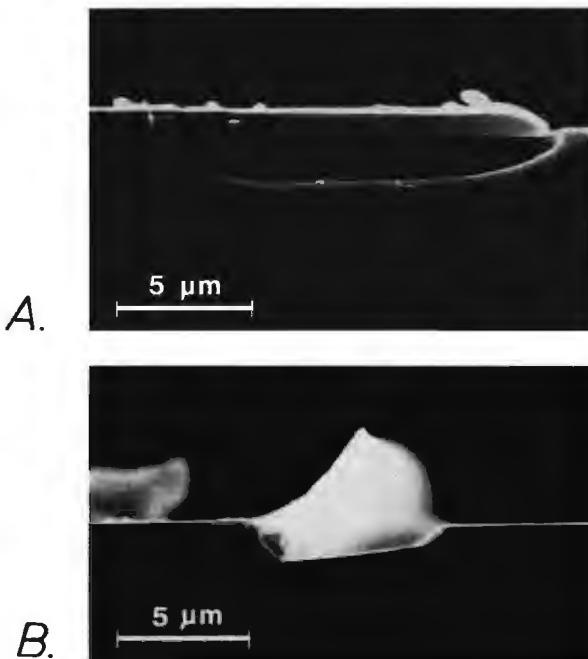

Fig. 8.26. The influence of the type of resist on the lateral etch rate in the mask-edge region. InP with a semi-infinite mask was etched for 10 min. in a 4.5 M HBr solution at 40 °C. Both the photoresist (A) and the SiO_2 resist (B) were aligned in the [110] direction.

– In the first place, it is obvious that resist layers induce changes in the native oxide as a result of which etching is initiated only in the vicinity of the resist (see Fig. 8.26). Since oxides have, in general, an amorphous structure [26-28], it is rather surprising that the etch rate is orientation-dependent (see Fig. 8.25.B). It should, however, be kept in mind that the underlying InP is monocrystalline and that initially the oxide may grow epitaxially. That such a mechanism is realistic was recently shown by Ourmazd et al. [29] for Si, covered with an amorphous SiO_2 film. Using high resolution Transmission Electron Microscopy, they showed that the transformation from crystalline Si to amorphous SiO_2 proceeds via a thin crystalline transition layer. The crystalline SiO_2 layer was found to have a completely different atomic structure in the $[\bar{1}10]$ and $[110]$ directions. We suggest that the thin native oxide film on InP has an ordered crystal structure. Whether the complete oxide layer or only a thin transition region is crystalline is not important for the present discussion. The anisotropic etching behaviour of the oxide layer found in the $[\bar{1}10]$ and $[110]$ orientations (Fig. 8.25.B) can be explained by assuming that the chemical resistivity is dependent on the atomic structure of the oxide.

– In the second place it is clear that the type of resist influences considerably the etch rate of the oxide layer (Fig. 8.26). This may be attributed to differences in oxide structure. In this respect it is important to note that the procedure for applying the mask to the substrate is different for the two resists used. In particular, the considerable difference in temperature is probably important; photoresist is applied at room temperature whereas the SiO_2 is sputtered at 400 °C (see chapter 3). The pretreatment temperature was reported to have a significant influence on etching profiles [21-23].

It can be concluded that the dissolution rate of a crystalline top layer strongly depends on its orientation and also on the nature of the mask. It is not clear whether the top layer consists only of a crystalline oxide film or whether that part of the substrate, which might be deformed by the pretreatment procedure, must also be considered. This is, however, not important for the model described below.

It has been shown that the native oxide layer is dissolved at elevated temperatures in a solution of HBr, a chemical etchant. When we assume that Br_2, also a chemical etchant (Table IV), is able to etch the oxide layer even at moderate temperatures, and we further assume anisotropy similar to that found with HBr, then the apparent anomaly of Fig. 8.24 can be explained as follows. The actual situation near the monocrystalline semiconductor surface is schematically represented in Fig. 8.27.A-D. Cases A-D of this figure
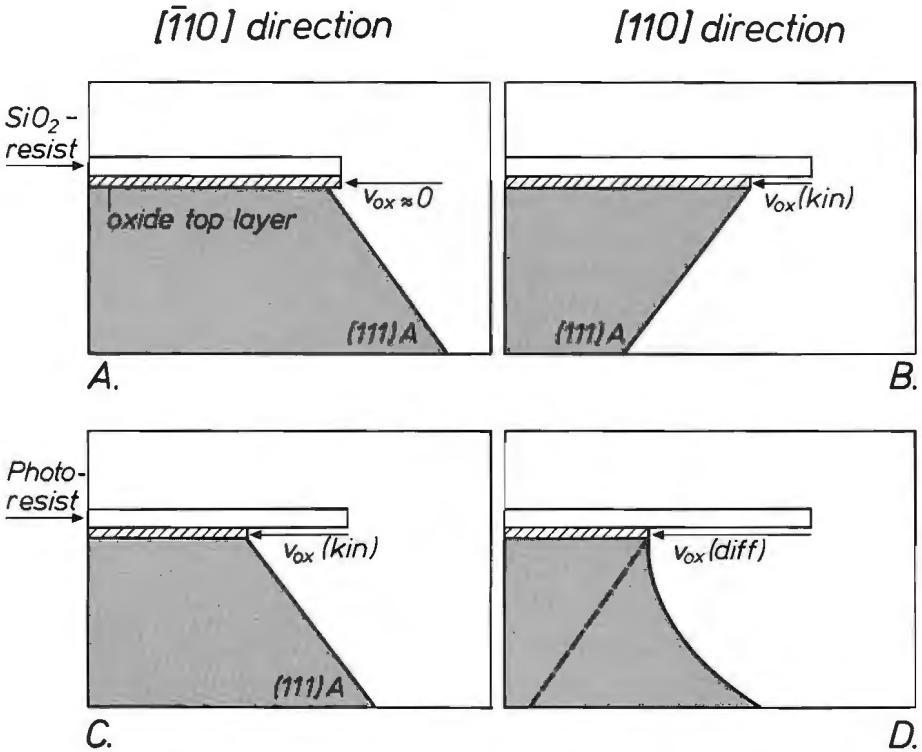
Fig. 8.27. Schematic model which shows the influence of an oxide top layer on the shape of the profiles etched in monocrystalline materials (compare with the model for isotropic materials shown in Fig. 8.23). As described in the text, the lateral etch rate of the oxide layer (v_{ox}) is considered to be dependent on whether an SiO_2-resist (A and B) or a photoresist (C and D) is used, and on whether the resist is oriented in the [$\bar{1}$10] direction (A and C) or the [110] direction (B and D). This model explains the microscopic etching results obtained with InP and GaAs (compare with Fig. 8.24).

refer to the corresponding cases of Fig. 8.24. The thin native oxide, between the resist layer and the lightly shaded InP substrate is represented in Fig. 8.27 by the dark shaded area. When the lateral etch rate of the oxide (v_{ox}) is negligibly low in the [$\bar{1}$10] direction (see Fig. 8.25.B), it is evident that the oxide layer does not influence the microscopic etching kinetics (see Fig. 8.27.A). Consequently, the low etch rate of the (111)In facet in the etching profile of Fig. 8.24.A corresponds exactly to the measured macroscopic etch rate of this facet. This good agreement has already been discussed. From Fig. 8.25.B it is clear that when SiO_2 is aligned in the [110] di-

rection, v_{ox} is considerable (see Fig. 8.27.B). Owing to the relatively high etch rate of the native oxide, the (001) surface orientation of the underlying InP substrate is immediately brought into contact with the bromine etchant. Since the etch rate of InP with this crystallographic orientation is controlled by diffusion of Br_2 (Table IV), this newly formed surface is instantly dissolved at a high rate until the slowest etching plane, the (111)In facet, is again encountered. In fact, the displacement of this facet is, under these conditions, regulated by the lateral etch rate of the native oxide, as is indicated in Fig. 8.27.B. This explains why the microscopic etch rate of this facet near an SiO_2 resist layer can be enhanced significantly as the results of Fig. 8.24.B and Fig. 8.20 showed.

A similar reasoning can, in principle, be applied to explain the etching profiles when a photoresist layer is used as a mask. The faceted profile of Fig. 8.24.C, revealing a high etch rate of the (111)In facet, can be understood if the product of v_{ox} and the etching time corresponds with the underetching x_0 (see Fig. 8.27.C). The diffusion-controlled profile of Fig. 8.24.D found in the [110] direction is more difficult to understand. Using HBr as 'indicator etchant' at 40 °C it was concluded from Fig. 8.26 that v_{ox} is dramatically increased when a photoresist layer is used as mask instead of an SiO_2 layer (compare A and B of Fig. 8.26). Again assuming that bromine accomplishes a similar effect at room temperature, the lateral etch rate of the native oxide might become so high that v_{ox} is no longer kinetically controlled as in Fig. 8.27.A-C, but that the supply of Br_2 becomes rate-determining (see Fig. 8.27.D). Continuing this reasoning the (111)In facet would be expected to extend from the oxide edge into the substrate (see the dashed line in Fig. 8.27.D). However, the flux of Br_2-species in solution is not sufficient to allow this facet to be encountered, as both the dissolution rates of the oxide layer and the InP substrate are now controlled by Br_2 diffusion. Consequently, a rounded profile is etched (see Figs. 8.24.D and 8.27.D). The shape of these profiles follows closely the mathematical models described in section 8.3.2.

In the model just presented it was assumed that at 20 °C only the bromine component in solution dissolves the oxide layer. This was in agreement with the observations that at this temperature etching did not occur in solutions only containing 4.5 M HBr. However, etching does take place in a 4.5 M HBr solution at 40 °C, as was shown in Figs. 8.25 and 8.26. It would therefore be expected that when profile etching experiments are performed in a solution of 0.1 M Br_2, 4.5 M HBr at higher temperatures, both Br_2 and HBr contribute to etching the oxide layer, whereas the InP substrate is still only etched by the bromine species. This is indeed what we found experi-

mentally at 40 °C, viz. rounded profiles similar to that shown in Fig. 8.24.D and, in addition, in the region close to the resist layer, lateral etching of the oxide layer. These results are thus in good agreement with the model.

In conclusion, we believe that the microscopic etch rate of crystallographic facets can be significantly enhanced by a surface oxide layer when the lateral etch rate of the oxide is substantially higher than the macroscopic etch rate of the facets. As a result, the shape of etching profiles in monocrystalline materials can be influenced dramatically. A change-over from kinetic to diffusion control may even be observed.

As described in the introduction to this section, thin surface layers are often used to influence the shape of etching profiles in polycrystalline [24] and amorphous [25-27] materials. Since preferential etching cannot occur in these materials, the surface films have a different impact on the profile shape. A comparison of the results of Fig. 8.27 with the corresponding profiles depicted in Fig. 8.23, clearly shows the importance of the substrate. Beveled faces are revealed with isotropic materials. The angle these faces make with the substrate surface can be adjusted over a wide range by changing the lateral etch rate of the surface layer (see curves (b) and (c) of Fig. 8.23). It should, however, be emphasized that these beveled faces are not crystallographic facets. The lateral etch rate of the surface layer can, in these cases, also be varied either via the composition of this layer [26,27], or via the composition of the etchant [24,25].

The model proposed to explain the anomalous profile etching results obtained with InP is not restricted to this material. For example, it was shown in section 8.4 that the kinetically controlled and intermediate profiles etched at low temperatures in GaAs were only found when the resist was aligned in the [$\bar{1}$10] orientation (see Fig. 8.21.A and B). Surprisingly, diffusion-controlled profiles were always found in the same etchant and in the corresponding temperature range (0 °C < T < 40 °C) when the resist was aligned in the [110] direction. This can now be understood by assuming that the microscopic etch rate of the (111)Ga faces is significantly enhanced by an anisotropic native oxide of GaAs.

Clearly, the influence of thin surface layers on the etching properties of monocrystalline materials is more important than has been realized. This opens new interesting ways of investigating more systematically and regulating more accurately etching profiles. For instance, intentional application to the substrate of a thin surface layer with a different chemical composition could create new possibilities. Since monolayers were found to be sufficiently thick to induce large changes in the etching kinetics [25], chemical surface modification in combination with variations in etchant composition might be successfully applied to regulate etching profiles [30,31].

8.6. Summary

It has been shown that the shape of profiles etched near resist edges depends not only on the dissolution kinetics but also on the dissolution mechanism. The results obtained from the profile etching experiments with GaAs and InP, described in this chapter, are summarized schematically in the Etching Table VIII. This table comprises results obtained with a semi-infinite masking pattern. Similar results were also obtained when a variable masking pattern was used.

As monocrystalline semiconductors are used in this work, the etching kinetics of all crystallographic faces must be considered near resist edges.

Table VIII

Etching table summarizing schematically the dependence of the microscopic shape of profiles near resist edges, on the etching mechanism and etching kinetics, obtained with monocrystalline III - V semiconductors.

The macroscopic etching kinetics, have been shown in many cases to be a good guide-line in predicting the microscopic profile shape. On the basis of the etching kinetics three profile types were distinguished with chemical etchants (see Table VIII):

(i)   anisotropic faceted structures are etched when the profile is controlled entirely by the dissolution kinetics of individual facets;

(ii) in accordance with theoretical models, rounded profiles are found when the etching rate constants of all crystal planes are very large, so that mass-transport in solution determines the profile shape;

(iii) when the profiles are partly under kinetic-control and partly under diffusion-control, intermediate structures are obtained.

A similar classification can also be made for electroless etchants. The distinction made in previous chapters between cathodically and anodically controlled etchants is important in determining the profile shape under diffusion-controlled conditions. A model based on galvanic element formation was presented to account for the intermediate profiles obtained with cathodically controlled electroless etchants (Table VIII). If, on the other hand, electroless etching is anodically controlled, dissolution proceeds under oxide-forming conditions and the kinetics are determined by the diffusion-controlled chemical dissolution rate of the oxide. Consequently, rounded profiles are again found with these systems. Although detailed profile etching experiments were not made with kinetically- and intermediate-controlled electroless systems, it seems very likely that the results will be very similar to those found with chemical etching systems, as is indicated by the arrows in Table VIII.

With regard to the diffusion-controlled rounded profiles it should be emphasized that, for the cases in which a semi-infinite mask is used, the shape is independent of the etching time. This strongly contrasts with the situation when symmetrical profiles are etched through a slit of a resist layer; it was found that the shape can be influenced by means of the dimensionless etching time τ. The experimental profiles changed from a 'double-bulge' shape to an ellipse shape when either the etching time was increased or the slit width was decreased. This is in agreement with the theory.

Despite the fact that the macroscopic etch rate can often be used to predict accurately the profile shape, the microscopic etching kinetics of particular crystallographic facets were found to be significantly enhanced near resist edges in a number of cases, depending on the type and orientation of the resist. A model was proposed to account for the sometimes dramatic changes in profile shape. Thin surface layers, very likely native oxide layers, play a decisive role in this model. Using an 'indicator etchant', the lateral

etch rate of this oxide was found to be strongly dependent on the crystallographic orientation of the underlying semiconductor substrate. Besides an orientation dependence, the lateral etch rate was also dependent on the nature of the resist; this was attributed to changes induced in the oxide layer during the different pretreatment procedures. It was concluded that the microscopic etching kinetics of crystallographic facets is determined by the lateral etch rate of the oxide layer. This model shows that thin surface layers can have a considerable impact on the profile shape near resist edges.

References

[1]   D.W. Shaw, *J. Cryst. Growth*, **47**, 509, (1979).

[2]   S. Adachi, Y. Noguchi and H. Kawaguchi, *J. Electrochem. Soc.*, **129**, 1053, (1982).

[3]   H.C. Gatos and M.C. Levine, *J. Electrochem. Soc.*, **107**, 427, (1960).

[4]   H.C. Gatos, *Science*, **137**, 311, (1962).

[5]   H.K. Kuiken, *Proc. R. Soc., London, Ser. A*, **392**, 199, (1984).

[6]   H.K. Kuiken, J.J. Kelly and P.H.L. Notten, *J. Electrochem. Soc.*, **133**, 1217, (1986).

[7]   H.K. Kuiken, *Proc. R. Soc., London, Ser. A*, **396**, 95, (1984).

[8]   C. Vuik and C. Cuvelier, *J. Comput. Phys.*, **59**, 247, (1985).

[9]   S. Adachi and H. Kawaguchi, *J. Electrochem. Soc.*, **128**, 1342, (1981).

[10] Y. Mori and N. Watanabe, *J. Electrochem. Soc.*, **125**, 1510, (1978).

[11] G.M. Barrow, *'Physical Chemistry'*, Mc Graw-Hill International Book Company, London, (1979).

[12] M.M. Abu-Zeid, *J. Electrochem. Soc.*, **131**, 2138, (1984).

[13] J. Albery, *'Electrode Kinetics'*, Oxford University Series, Clarendon Press, Oxford, (1975).

[14] J.O.M. Bockris and D. Drazic, *'Electrochemical Science'*, Taylor and Francis Ltd., London, (1972).

[15] P.H.L. Notten, J.J. Kelly and H.K. Kuiken, *J. Electrochem. Soc.*, **133**, 1226, (1986).

[16] K. Rajeshwar and T. Mraz, *J. Phys. Chem.*, **87**, 742, (1983)

[17] K.J. Vetter, *'Electrochemical Kinetics'*, chapter 5, Academic Press, New York, (1967).

[18] J.J. Kelly and C.H. de Minjer, *J. Electrochem. Soc.*, **122**, 931, (1975).

[19] K.W. Frese, M.J. Madou and S.R. Morrison, *J. Phys. Chem.*, **84**, 3172, (1980).

[20] C.W. Wilmsen, *'Physics and Chemistry of III-V Compound Semiconductor Interfaces'*, chapter 7, page 403, Ed. C.W. Wilmsen, Plenum Press, New York, (1985).

[21] W.C. Dautremont-Smith and D.P. Wilt, Patent Cooperation Treaty (PCT), Int. Publ. Number WO 86/01367, Int. Publ. Date 13.03, (1986).

[22] D.T.C. Huo, J.D. Wynn, S.G. Napholtz, F.R. Lenzo and D.P. Wilt, *J. Electrochem. Soc.*, **134**, 2850, (1987).

[23] D.T.C. Huo, J.D. Wynn, S.G. Napholtz and D.P. Wilt, *J. Electrochem. Soc.*, **135**, 2334, (1988).

[24] J.J. Kelly and G.J. Koel, *J. Electrochem. Soc.*, **125**, 860, (1978).

[25] O.J. Wimmers, F.J. Touwslager and J.J. Ponjeé, *J. Electrochem. Soc.*, accepted for publication.

[26] Y.I. Choi, C.K. Kim and Y.S. Kwon, *IEE Proc. Pt. I*, **133**, 13, (1986).

[27] L.K. White, *J. Electrochem. Soc.*, **127**, 2687, (1980).

[28] S.R. Morrison, *'Electrochemistry at Semiconductor and Oxidized Metal Electrodes'*, chapter 8, Plenum Press, New York, (1980).

[29] A. Ourmazd, D.W. Taylor, J.A. Rentschler and J. Bevk, *Phys. Rev. Lett.*, **59**, 213, (1987).

[30] J.J. Ponjeé and P.N.T. van Velzen, *Philips Techn. Rev.*, **44**, 81, (1988).

[31] J.J. Ponjeé, V.B. Marriott and H. van der Wel, to be published.

[32] W. van Erk and H.K. Kuiken, *J. Cryst. Growth*, **51**, 397, (1981).

Chapter 9

Summary and general conclusions

The application of III-V semiconductors has become very important in opto-electronic and integrated-circuit device technology. The need for dependable processes for fabrication and quality control of such devices continues to increase. In particular, wet etching of III-V compounds plays an essential role in these processes. The large variety of etchants available for the different semiconductors suggested the need for a fundamental and systematic investigation of etching systems, which would ultimately lead to a more appropriate choice of etching solution and conditions for a given application. For that purpose an experimental study of the etching properties of GaAs and InP in the dark in a large number of aqueous etching solutions was undertaken. A distinction was made between the characterization of the various etching solutions and the application of the insight obtained to practical etching systems.

Electrochemistry plays an essential role in the first and more extensive part of this thesis, which is formed by the chapters 2 to 7. From electrochemical and macroscopic etching experiments it is clear that III-V semiconductors can be dissolved via two different mechanisms: an electroless mechanism and a chemical etching mechanism. In electroless dissolution the etching process can be separated into two partial reactions, occurring simultaneously at the same surface: the anodic oxidation of the semiconductor and the cathodic reduction of the oxidizing agent. Transfer of free charge carriers takes place between the solid and the oxidizing agent in solution. A study of the partial processes has yielded insight into the factors influencing each reaction. In particular, the dependence of the anodic oxidation, and thus of the dissolution rate of the semiconductor, on the applied potential is a characteristic feature of this mechanism. On the other hand, the chemical dissolution rate is not influenced by an externally applied potential. Chemical etchants are found to consist of bifunctional molecules and ions. A general reaction model is presented in which a simultaneous rupture

of bonds in the solid and in the bifunctional etching agent is followed by the instantaneous formation of new surface bonds. Free charge carriers are therefore not involved in these reactions. This explains the potential independence of the chemical dissolution rate of III-V compounds.

Besides the etching mechanism, the etch rate is also important in practical applications. The etching kinetics for the various systems are therefore studied by means of electrochemical methods. The investigation of the dissolution mechanism and kinetics has led to a classification of the etching systems. On the basis of this classification, the influence of both the mechanism and kinetics on the shape of etched structures in these semiconductors is described in the second part of the thesis (chapter 8).

Certain theoretical aspects, which are essential in understanding the electrochemical and etching properties of semiconducting materals, are considered in chapter 2. In particular, the potential distribution at the semiconductor/electrolyte interface is shown to be completely different from that at a metal/electrolyte interface. This has a significant influence on charge transfer reactions between the semiconductor and redox systems in solution. The factors which are important for these reactions are discussed. Besides a consideration of the fundamental differences between electroless and chemical mechanisms, attention is also paid to the determination of the kinetics of etching reactions by means of ring/disk measurements.

The experimental conditions for the various electrochemical and etching experiments are described in chapter 3. Special attention is devoted to flow-cell measurements with which the potential dependence of both the anodic oxidation and macroscopic dissolution rates of the semiconductor can be measured simultaneously. On the basis of these experiments the dissolution mechanism of the various etching systems has been determined.

In chapter 4 it is concluded that oxide formation plays a very important role in the anodic dissolution of GaAs in both acidic and alkaline electrolytes. When the rate of oxidation is lower than the maximum dissolution rate of the oxide, dissolution takes place under oxide-free conditions. When, however, the maximum dissolution rate of the oxide is exceeded, it is found that a thin oxide layer is formed at the surface. Impedance measurements have shown that the formation of charged intermediates during the anodic dissolution reaction changes the potential distribution at the interface. This effect is much stronger when the surface is covered with an oxide film.

The effect of such potential changes on the electroless etching of GaAs in solutions containing an oxidizing agent is described in chapter 5. From the study of the electrochemistry of these etching systems, both in the dark and under illumination, it is clear that the redistribution of the potential

under oxide-free conditions leads to the suppression of the etch rate of GaAs in a large number of electroless etchants. The influence of anodic oxide formation on the reduction kinetics of the oxidizing agent was investigated extensively in alkaline solutions. The pH is found to be an important parameter in regulating the oxide formation. The ratio of the OH^- concentration and the concentration of the oxidizing agent determines whether electroless etching is cathodically controlled under oxide-free conditions or anodically controlled under oxide-forming conditions. It is also shown that GaAs can be dissolved via a chemical mechanism in certain other etching solutions.

In chapter 6 results are described of an electrochemical study of InP in a number of simple redox systems. From these results it is concluded that charge exchange between the solid and the solution in the pH range investigated is only possible via the conduction band of the semiconductor. As a result of a relatively thick oxide layer formed during anodic oxidation, charge exchange via the valence band is blocked. Consequently, electroless systems cannot be used for the dissolution of InP and chemical etchants must be employed. This is confirmed experimentally for a number of chemical etching solutions.

In chapter 7 conclusions are drawn with regard to the etching mechanism and macroscopic etching kinetics of the various systems. The results are summarized in Table IV.

This table is used as an introduction to the investigation of the etching of special forms at resist edges in both GaAs and InP, described in chapter 8. It is established that the etching kinetics play an important role in the determination of the profile shape. When the dissolution rate is controlled by the surface reaction, certain crystallographic facets are revealed in these monocrystalline materials. When, however, the rate of the surface reaction is very high, as found for a large number of etching systems, then the shape is determined by the rate at which the active etching components are supplied from the bulk of the solution to the semiconductor surface. This generally results in rounded profiles. The etch depth near resist edges is strongly enhanced due to two-dimensional diffusion. Intermediate profiles, whose shape is partly determined by the kinetics of the surface reaction and partly by mass-transport in solution, were also found experimentally. Apart from the dissolution kinetics, the dissolution mechanism can also influence the profile shape, in particular under mass-transport controlled conditions. Rounded profiles are only obtained with chemical and anodically controlled electroless etchants. With cathodically controlled electroless systems, intermediate profiles are always found. A model is presented which shows that,

as a result of the mobility of free charge carriers in the semiconductor, certain 'noble' facets are cathodically protected in these electroless systems by the neighbouring 'less noble' surface in the profile. Anodically controlled electroless systems do not show this effect, as oxide formation prevents preferential etching of the less noble surface. Since free charge carriers are not involved in chemical etching, rounded profiles are always found with this class of etchants under diffusion-controlled conditions. Finally, in the last part of chapter 8, it is shown that the microscopic etch rate of certain crystallographic planes does not always agree with the macroscopically measured etch rate. It is suggested that native oxide on the semiconductor surface significantly enhances the microscopic dissolution rate of these planes and consequently, influences the profile shape. The results described in chapter 8 with regard to the dependence of the profile shape on both the etching mechanism and etching kinetics are summarized in Table VIII.

It can be concluded that electrochemical measurements are very suitable for investigating the etching of semiconductor compounds. The dissolution properties of both GaAs and InP have been characterized in a large number of etching solutions. A correlation is shown between the dissolution mechanism and the macroscopic etching kinetics on the one hand, and the microscopic profiles etched in these materials on the other hand. The main conclusions with regard to macroscopic etching and its relation to microscopic etching can be found in Tables IV and VIII, respectively. It seems likely that the etching properties of other semiconducting materials can be characterized in a similar way. The insight obtained from this investigation makes possible a more effective choice of etching solutions and etching conditions for the various applications of modern device technology.

Samenvatting

De toepassing van III-V halfgeleidermaterialen in opto-elektronische devices, welke een belangrijke rol spelen in de digitale informatieverwerking, maakt momenteel een zeer sterke groei door die in de nabije toekomst ongetwijfeld zal doorzetten. Dientengevolge is ook de interesse voor de technologische produktie- en controleprocessen van deze devices en van de vele in ontwikkeling zijnde nieuwe devices sterk toegenomen. Met name het nat etsen van III-V materialen speelt een essentiële rol in diverse stadia van deze processen. Het grote aantal etsmiddelen in combinatie met de verschillende halfgeleidermaterialen maakt het noodzakelijk om via meer fundamenteel en systematisch onderzoek te komen tot een meer gerichte keuze van etsmiddelen en etsomstandigheden. Het in dit proefschrift beschreven onderzoek beoogt hieraan een bijdrage te leveren. Daartoe wordt op systematische wijze een experimentele studie beschreven naar het donkeretsgedrag van GaAs en InP in een groot aantal waterige etsoplossingen. Een onderscheid wordt gemaakt tussen enerzijds het karakteriseren van de verschillende etssystemen, in het eerste gedeelte van dit proefschrift, en anderzijds het meer praktisch gerichte toepassen van de verworven inzichten, in het tweede gedeelte.

De elektrochemie speelt een sleutelrol in het eerste, en tevens meest uitgebreide deel, dat gevormd wordt door de hoofdstukken 2 t/m 7. Door de combinatie van elektrochemische meetmethodieken met macroscopische etsexperimenten is duidelijk geworden dat het oplossen van III-V halfgeleidermaterialen in de onderzochte etsoplossingen kan verlopen via twee verschillende mechanismen : een zogenaamd 'electroless' mechanisme en een 'chemisch' etsmechanisme. Karakteristiek voor het electroless oplossen is dat het etsproces gescheiden kan worden in twee deelprocessen die tegelijkertijd aan hetzelfde oppervlak plaatsvinden: de anodische oxidatie van de halfgeleider en de kathodische reductie van een oxidatiemiddel in oplossing. Hierbij vindt overdracht plaats van vrij beweeglijke ladingdragers tussen de vaste stof en het oxidatiemiddel. Door de deelprocessen gescheiden te bestuderen is inzicht verkregen in de factoren die bepalend zijn voor beide reacties. Met name de invloed van de aangelegde potentiaal op de anodische oxidatie, en

dus op de oplosnelheid van de halfgeleider, is karakteristiek voor dit mechanisme. Kenmerkend voor het chemisch oplosmechanisme is daarentegen dat etssnelheid niet beïnvloed wordt door een op de halfgeleider aangelegde potentiaal. Markant is de bevinding dat chemische etsmiddelen bestaan uit bifunctionele moleculen of ionen. Een algemeen reactiemodel is gepresenteerd waarin een gelijktijdige verbreking van bindingen, zowel in de vaste stof als tussen de beide functionele groepen van het chemisch etsmiddel, gevolgd wordt door de onmiddellijke vorming van nieuwe oppervlaktebindingen. Hierdoor zijn er bij deze chemische processen geen vrije ladingdragers betrokken, hetgeen verklaart dat de aangelegde potentiaal geen invloed heeft op de oplosnelheid van III-V materialen.

Naast het etsmechanisme speelt de snelheid waarmee de oplosreacties verlopen een belangrijke rol. De etskinetiek voor de verschillende systemen is veelal ook op elektrochemische wijze onderzocht. De bestudering van het oplosmechanisme en de oploskinetiek heeft geleid tot een classificatie van de onderzochte etssystemen. In het tweede gedeelte van dit proefschrift (hoofdstuk 8), wordt aan de hand van deze classificatie beschreven welke invloed het mechanisme en de kinetiek uitoefenen op de vorm van geëtste structuren in deze halfgeleidermaterialen.

Alvorens te komen tot een beschrijving en interpretatie van het elektrochemisch gedrag van, en etsexperimenten aan, III-V materialen, worden in hoofdstuk 2 een aantal theoretische aspecten belicht, die van fundamenteel belang zijn voor het gedrag van halfgeleidermaterialen. Met name de potentiaalverdeling aan het halfgeleider/vloeistof grensvlak, die geheel anders is dan aan het metaal/vloeistof grensvlak, heeft een grote invloed op ladingoverdrachtsreacties die tussen de halfgeleider en redoxsystemen in de oplossing kunnen verlopen. De factoren die voor deze reacties van belang zijn, komen aan de orde. Naast een beschouwing over de principiële verschillen tussen het electroless en chemisch etsmechanisme wordt ook aandacht besteed aan de wijze waarop met behulp van roterende ring-schijf elektrodesystemen de kinetiek van etsreacties bepaald kan worden.

In hoofdstuk 3 wordt uiteengezet hoe en onder welke omstandigheden de diverse elektrochemische experimenten en etsexperimenten zijn uitgevoerd. Hierbij krijgen de 'flow-cell-experimenten' bijzondere aandacht. Voor een groot aantal etssystemen is met behulp van deze 'flow-cell' op direkte wijze de potentiaalafhankelijkheid gemeten van zowel de anodische oxydatie als de macroscopische oplosnelheid van de halfgeleider. Op grond van deze experimenten is voor de onderzochte systemen bepaald volgens welk mechanisme het oplossen plaatsvindt.

Met betrekking tot het anodische oplosgedrag van GaAs in zowel zure als

basische elektrolyten, wordt in hoofdstuk 4 geconcludeerd dat oxydevorming een zeer grote rol speelt. Wanneer de oxydatiesnelheid lager is dan de maximale oplossnelheid van het oxyde vindt oplossen plaats onder oxyde-vrije omstandigheden. Wanneer echter de maximale oplosbaarheid van het oxyde overschreden wordt, is aangetoond dat er een dun oxydelaagje op het oppervlak gevormd wordt. Impedantiemetingen hebben aangetoond dàt, als gevolg van het ontstaan van geladen intermediairen in de anodische oplosreactie, de potentiaalverdeling aan het grensvlak beduidend sterker beïnvloed wordt wanneer een oxydelaagje het oppervlak bedekt dan wanneer dit niet het geval is.

Dat deze verschijnselen het electroless etsen van GaAs in oplossingen die een oxydatiemiddel bevatten drastisch kunnen beïnvloeden, wordt in hoofdstuk 5 beschreven. Door het elektrochemische gedrag van deze etssystemen in het donker, maar ook tijdens belichting, te bestuderen, is duidelijk geworden dat ook de herverdeling van de potentiaal onder oxyde-vrije omstandigheden de oorzaak is van een verwaarloosbaar lage etssnelheid van GaAs in een groot aantal electroless etsmiddelen. De invloed van de anodische oxydevorming op de reductiekinetiek van het oxydatiemiddel is met name in alkalisch milieu bestudeerd. In dit milieu is de pH een belangrijke parameter gebleken bij de regulatie van de oxydevorming. Afhankelijk van de verhouding van de OH^- concentratie en de concentratie van het oxydatiemiddel is het electroless etsen kathodisch bepaald onder oxyde-vrije omstandigheden, dan wel anodisch bepaald onder oxyde-vormende omstandigheden. Naast het electroless oplossen van GaAs is aangetoond dat een aantal andere etsmiddelen dit materiaal oplossen via een chemisch mechanisme.

In hoofdstuk 6 worden de resultaten beschreven van een elektrochemische studie naar het gedrag van InP in een aantal eenvoudige redoxsystemen. Op grond van deze resultaten is geconcludeerd dat, in het onderzochte pH-gebied, de ladingsuitwisseling tussen de vaste stof en de vloeistof alleen mogelijk is via de geleidingsband van de halfgeleider. Als gevolg van een relatief dikke oxydelaag die tijdens de anodische oxydatie ontstaat, is uitwisseling via de valentieband geblokkeerd. Hierdoor zijn electroless systemen onbruikbaar voor het oplossen van InP en kunnen alleen chemische etsmiddelen aangewend worden. Dit is experimenteel voor een aantal etsmiddelen bevestigd.

Hoofdstuk 7 fungeert als afsluiting van het elektrochemische deel van dit proefschrift, waarin conclusies getrokken worden ten aanzien van het etsmechanisme en de macroscopische etskinetiek. Deze resultaten zijn samengevat in tabel IV.

Deze tabel wordt ook als uitgangspunt gehanteerd voor het op microsco-

pische schaal etsen van vormen in GaAs en InP, hetgeen beschreven wordt in hoofdstuk 8. Het blijkt dat de kinetiek van de etsreacties een zeer nadrukkelijke rol speelt bij de bepaling van de vorm van etsprofielen. Wanneer de snelheid van het etsen bepaald wordt door de oppervlaktereactie, worden alleen bepaalde kristallografische vlakken in deze één-kristallijne materialen geëtst. Wanneer echter de snelheid van deze reactie zeer groot is, zoals gevonden voor een groot aantal etssystemen, dan wordt de vorm bepaald door de aanvoersnelheid van etscomponenten vanuit de oplossing naar het halfgeleideroppervlak. Dit resulteert veelal in geheel ronde etsvormen. Karakteristiek voor deze profielen is dat, als gevolg van twee-dimensionale diffusie, de etsdiepte nabij de maskerranden sterk vergroot wordt. Tussenvormen waarbij de vorm gedeeltelijk door de oppervlaktereactie en gedeeltelijk door het massatransport bepaald wordt, zijn experimenteel ook waargenomen. Het is gebleken dat niet alleen de kinetiek maar ook het oplosmechanisme een grote invloed heeft op de vorm van etsprofielen, in het bijzonder onder transport-bepaalde omstandigheden. Geheel ronde vormen worden alleen geëtst met chemische en anodisch bepaalde electroless etsmiddelen. Met kathodisch bepaalde electroless systemen worden altijd tussenvormen gevonden. Een model is gepresenteerd waarin aangetoond wordt dat, ten gevolge van de vrije beweeglijkheid van lading in de halfgeleider, bepaalde 'edele' kristallografische vlakken in deze electroless systemen kathodisch worden beschermd door het naburige 'onedele' oppervlak. Bij anodisch gecontroleerde electroless systemen verhindert de oxydevorming het preferentieel etsen van deze onedele oppervlakken. Aangezien er geen vrije ladingdragers bij het chemisch etsen betrokken zijn, worden onder deze omstandigheden ook bij deze categorie van etsmiddelen altijd ronde vormen geëtst. Tot slot wordt in het laatste gedeelte van hoofdstuk 8 aandacht besteed aan het feit dat de microscopische oplossnelheid van bepaalde kristallografische vlakken niet in alle gevallen overeenkomt met de gemeten macroscopische snelheid. Een model is voorgesteld waarin het van nature op het oppervlak van de halfgeleider aanwezige oxyde de microscopische oplossnelheid aanzienlijk kan verhogen. Dit heeft uiteindelijk grote gevolgen voor de vorm van de profielen. De in hoofdstuk 8 beschreven resultaten die betrekking hebben op de mechanistische en kinetische afhankelijkheid van de profielvorm, zijn samengevat in tabel VIII.

Algemeen concluderend kan gesteld worden dat elektrochemisch onderzoek bij uitstek geschikt is om het etsen van halfgeleidermaterialen te bestuderen. In dit proefschrift is op deze wijze het oplosgedrag GaAs en InP in een groot aantal etsoplossingen gekarakteriseerd. Er is een verband gelegd tussen het oplosmechanisme en de macroscopische etskinetiek enerzijds

en anderzijds de in deze materialen op microscopische schaal te etsen vormen. De hoofdconclusies met betrekking tot het macroscopische etsen en de relatie met het microscopische etsen zijn respectievelijk terug te vinden in tabel IV en tabel VIII. Het lijkt aannemelijk dat het etsgedrag van andere halfgeleidermaterialen op soortelijke wijze gekarakteriseerd kan worden en dat het inzicht verkregen tijdens dit onderzoek ook bij deze materialen leidt tot een meer gerichte keuze van etsmiddelen en etsomstandigheden voor de diverse toepassingen.

List of symbols and abbreviations

A	electrode area	[cm^2]
a	variable resist width	[μm]˙
B	proportionality constant of oxide formation	[nm·V^{-1}]
C	constant for hole injection	
C_{H}	capacitance of the Helmholtz layer	[F·cm^{-2}]
C_{if}	capacitance of interface states	[F·cm^{-2}]
C_{ox}	capacitance of a surface oxide layer	[F·cm^{-2}]
C_{sc}	capacitance of the space-charge layer	[F·cm^{-2}]
C_{ss}	capacitance of surface states	[F·cm^{-2}]
C_{t}	total cell capacitance	[F·cm^{-2}]
CB	Conduction Band	
Ch	chemical etching species in solution	
$\mathscr{D}_i$	diffusion coefficient of species i in solution	[cm^2·s^{-1}]
D_{ox}	energy distribution function of Ox in solution	
D_{red}	energy distribution function of Red in solution	
d_{H}	thickness of the Helmholtz layer	[nm]
d_{ox}	thickness of a surface oxide layer	[nm]
d_{r}	thickness of resist layer	[nm]
d_{sc}	thickness of the space-charge layer	[nm]
E	energy	[eV]
E_{a}	activation energy	[J·mole^{-1}]
E_{c}	energy of the conduction band-edge	[eV]
$E_{\mathrm{c}}^{\mathrm{ox}}$	conduction band-edge of semiconducting oxide	[eV]
E_{F}	fermi level in the semiconductor	[eV]
$E_{\mathrm{F,el}}$	fermi level in solution	[eV]
E_{g}	energy band-gap of the semiconductor	[eV]
$E_{\mathrm{g}}^{\mathrm{ox}}$	energy band-gap of a semiconducting oxide	[eV]
E_{ox}	energy level of Ox in solution	[eV]
E_{red}	energy level of Red in solution	[eV]

E_{sc}	energy drop over the space-charge layer	[eV]
E_v	energy of the valence band-edge	[eV]
E_v^{ox}	valence band-edge of semiconducting oxide	[eV]
EDAX	Energy Dispersive Analysis of X-rays	
EOS	Electrolyte Oxide Semiconductor model	
e	electronic charge is 1.60×10^{-19} A·s	[A·s] or [mA·s]
e^-	mobile electron	
F	Faraday constant is 96485	[A·s·eq^{-1}]
f	frequency	[s^{-1}]
h^+	mobile hole	
hν	photon	
I	current	[mA]
I^+	partial anodic current	[mA]
I^-	partial cathodic current	[mA]
ICP	Inductively-Coupled-Plasma emission spectrometry	
i	current density	[mA·cm^{-2}]
i^+	partial anodic current density	[mA·cm^{-2}]
i^-	partial cathodic current density	[mA·cm^{-2}]
i_{form}^a	formation rate of an anodic oxide	[mA·cm^{-2}]
i_{max}^a	maximum anodic current density	[mA·cm^{-2}]
i_{lim}^c	limiting diffusion-controlled cathodic current density	[mA·cm^{-2}]
if	interface states	
j	$(-1)^{\frac{1}{2}}$	
K_a	dissociation constant of acid	
k	Boltzmann constant is 1.38×10^{-23}	[J·K^{-1}]
	or 8.62×10^{-5}	[eV·K^{-1}]
k	reaction rate constant	
k_n	rate constant for electron capture	
k_p	rate constant for hole capture	
L	penetration depth of light	[μm]
M_s	molecular weight of semiconductor	[g·mole^{-1}]
MOS	Metal Oxide Semiconductor model	
m	number of electroless etching species to dissolve one III-V 'molecule'	
N_A	acceptor density in the semiconductor	[cm^{-3}]

N_c	effective density of states in the conduction band	$[cm^{-3}]$
N_D	donor density in the semiconductor	$[cm^{-3}]$
N_v	effective density of states in the valence band	$[cm^{-3}]$
n	number of electrons to reduce Ox^{n+}	
n_o	bulk concentration of electrons in the conduction band	$[cm^{-3}]$
n_s	surface concentration of electrons in the conduction band	$[cm^{-3}]$
Ox^{n+}	oxidizing agent in solution	
PMMA	PolyMethylMethAcrylate	
p	number of chemical species to dissolve one III-V 'molecule'	
p_o	bulk concentration of holes in the valence band	$[cm^{-3}]$
p_s	surface concentration of holes in the valence band	$[cm^{-3}]$
Q_H	charge density in the Helmholtz layer	$[A \cdot s \cdot cm^{-2}]$
Q_{if}	interface charge density	$[A \cdot s \cdot cm^{-2}]$
Q_{sc}	charge density in the space-charge layer	$[A \cdot s \cdot cm^{-2}]$
Q_{ss}	surface state charge density	$[A \cdot s \cdot cm^{-2}]$
q	constant for the recombination reaction	
R	gas constant is 8.314	$[J \cdot mole^{-1} \cdot K^{-1}]$
R_e	resistance of electrolyte	$[\Omega \cdot cm^2]$
R_{rec}	recombination resistance	$[\Omega \cdot cm^2]$
R_t	total cell resistance	$[\Omega \cdot cm^2]$
RDE	Rotating Disk Electrode	
RRDE	Rotating Ring Disk Electrode	
Red	reduced species in solution	
r_i	various radii of RRDE	$[mm]$
rec	recombination	
rpm	revolutions per minute	$[min^{-1}]$
S	solid	
SCE	Saturated Calomel Electrode	
SEM	Scanning Electron Microscope	
Sh	Sherwood number (dimensionless)	
SS	Surface States	
T	temperature	$[K \text{ or } °C]$

T_e	probability of electron tunneling through an oxide layer	
T_e^o	probability of electron tunneling in absence of an oxide layer	
t	time	[s]
t_{dis}	time to dissolve an oxide layer	[s]
V	voltage (potential)	[V(SCE)]
V_a	anodic prepolarization potential	[V(SCE)]
V_{fb}^o	flat-band potential under standard conditions	[V(SCE)]
V_{fb}'	flat-band potential during surface charging	[V(SCE)]
V_H^o	potential drop over the Helmholtz layer under standard conditions	[V(SCE)]
V_H'	potential drop over the Helmholtz layer during surface charging	[V(SCE)]
V_{ox}	potential drop over surface oxide layer	[V(SCE)]
$V_{ox/red}^o$	standard redox potential	[V(SCE)]
V_r	open-circuit (rest) potential	[V(SCE)]
V_{sc}	potential drop over the space-charge layer	[V(SCE)]
VB	Valence Band	
v_{ch}	chemical etch rate	[nm·s^{-1}]
v_e	electroless etch rate	[nm·s^{-1}]
v_t	total etch rate	[nm·s^{-1}]
v_{sol}	solution flow rate	[ml·s^{-1}]
X^-	nucleophilic agent in solution	
X	dimensionless profile coordinate	
x_o	underetching resist edge	[μm]
Y	dimensionless profile coordinate	
y_b	etch depth at the deepest point of a diffusion-controlled profile	[μm]
Z	impedance	[Ω·cm^2]
Z_{im}	imaginary part of impedance	[Ω·cm^2]
Z_{re}	real part of impedance	[Ω·cm^2]
α	absorption coefficient of light	
β	dimensionless etching parameter	
γ	collection efficiency	

δ	difference (change)	
∂	diffusion layer thickness	[cm]
ε	dielectric constant	
ε_o	permittivity of free space is 8.86×10^{-14}	[F·cm^{-1}]
ε_{ox}	dielectric constant of oxide layer	
η	overpotential	[V]
$\varkappa$	rate constant of charge transfer	
λ	reorientation energy	[eV]
ν	kinematic viscosity	[cm^2·s^{-1}]
ξ	constant for electron tunneling	[nm^{-1}]
ϱ_s	density of the semiconductor	[g·cm^{-3}]
τ	dimensionless etching time	
ϕ	photon flux	[s^{-1}·cm^{-2}]
φ	constant potential drop at a reference electrode	[V]
ω	angular velocity of RDE or RRDE	[rad·s^{-1}]
ω_f	angular frequency = $2\pi f$	[rad·s^{-1}]

(001)	crystallographic plane	
[ ]	concentration	[mole·l^{-1}]
[ ]$_s$	concentration at the electrode surface	[mole·l^{-1}]
[ ]$_b$	concentration in the bulk of solution	[mole·l^{-1}]
[110]	crystallographic direction	
$\approx$	approximately	
$\propto$	proportional to	
∞	infinite	
$\oplus$	immobile positive charge	
$\ominus$	immobile negative charge	

Superscripts

a	anodic
c	cathodic

Subscripts

cb	reaction via the conduction band
vb	reaction via the valence band
ss	reaction via surface states

e	electroless
ch	chemical
d	dark
hν	under illumination

List of publications

Other publications of the author related to the subject of this thesis are:

* J.J. Kelly and P.H.L. Notten.
'Surface charging effects during photoanodic dissolution of n-GaAs electrodes'.
Journal of the Electrochemical Society, **130**, 2452, (1983).

* J.J. Kelly and P.H.L. Notten.
'Hole injection reactions and the potential distribution at the p-GaAs/ electrolyte interface under anodic polarization'.
Electrochimica Acta, **29**, 589, (1984).

* P.H.L. Notten.
'The etching of InP in HCl solutions: a chemical mechanism'.
Journal of the Electrochemical Society, **131**, 2641, (1984).

* J.E.A.M. van den Meerakker, J.J. Kelly and P.H.L. Notten.
'The minority carrier recombination resistance: a useful concept in semiconductor electrochemistry'.
Journal of the Electrochemical Society, **132**, 638, (1985).

* H.K. Kuiken, J.J. Kelly and P.H.L. Notten.
'Etching Profiles at resist edges. Part I; mathematical models for diffusion-controlled cases'.
Journal of the Electrochemical Society, **133**, 1217, (1986).

* P.H.L. Notten, J.J. Kelly and H.K. Kuiken.
'Etching profiles at resist edges. Part II; experimental confirmation of models using GaAs'.
Journal of the Electrochemical Society, **133**, 1226, (1986).

* D. Meissner, Ch. Sinn, R. Memming, P.H.L. Notten and J.J. Kelly.
'On the nature of the inhibition of electron transfer at illuminated p-type
semiconductor electrodes'.
'Homogeneous and heterogeneous photocatalysis', page 317, Eds. E. Peliz-
zetti and N. Serpone, D. Reidel Publishing Company, Dordrecht, (1986).

* J.J. Kelly, J.E.A.M. van den Meerakker and P.H.L. Notten.
'Electrochemistry of photoetching and defect-revealing in III-V materials'.
'Grundlagen von Elektrodenreaktionen', Dechema-Monographien,
Band 102, page 453, VCH-Verlagsgesellschaft, Ed. J.W. Schultze,
Frankfurt am Main, (1986).

* P.H.L. Notten and J.J. Kelly.
'Evidence for cathodic protection of crystallographic facets from GaAs
etching profiles'.
Journal of the Electrochemical Society, **134**, 444, (1987).

* P.H.L. Notten.
'The role of surface charging and potential redistribution on the kinetics
of hole injection reactions at n-GaAs'.
Electrochimica Acta, **32**, 575, (1987).

* P.H.L. Notten.
'Hypochlorite reduction at GaAs : a multifaceted reaction'.
Journal of Electroanalytical Chemistry and Interfacial Electrochemistry,
224, 211, (1987).

* P.H.L. Notten and A.A.J.M. Damen.
'The electrochemistry of InP in Br_2/HBr solutions and its relevance to
etching behaviour'.
Applied Surface Science, **28**, 331, (1987).

* J.J. Kelly, J.E.A.M. van den Meerakker, P.H.L. Notten and R.P. Tij-
burg.
'Wet-chemical etching of III-V semiconductors'.
Philips Technical Review, **44**, 61, (1988).

* P.H.L. Notten.
'The influence of native oxide layers on the shape of etching profiles at
resist edges'.
To be published.

Curriculum vitae

Peter Notten werd op 7 juni 1952 in Eindhoven geboren. Via een drie jarige HBS opleiding (Gemeentelijk Lyceum Eindhoven) en het voorbereidend jaar aan het Instituut voor Hoger Beroeps Onderwijs (IHBO; thans Hogeschool Eindhoven) behaalde hij in 1973 aan ditzelfde Instituut het HBO-A diploma (analytisch-chemische studierichting). Na het vervullen van zijn Militaire Dienstplicht (1973/1974) kwam hij in maart 1975 in dienst van het Philips Natuurkundig Laboratorium; de eerste jaren als wetenschappelijk assistent, later als wetenschappelijk medewerker. In 1976 werd door middel van avondstudie het HBO-B diploma, eveneens in de analytisch-chemische studierichting, behaald aan het IHBO Eindhoven. In de daarop volgende jaren werden diverse opleidingen aan verschillende Universiteiten en Instellingen met goed gevolg afgesloten: College 'Elektrochemie' aan de Technische Universiteit Eindhoven (1977); college 'Elektrochemisch-technologische aspecten van de energieproblematiek' aan de Technische Universiteit Eindhoven (1978); $1\frac{1}{2}$ jaar durende interne Philips opleiding 'Hogere Technische Opleiding Vaste Stoffen' met als gevolgd studieprogramma 'Thermodynamica en Fasenleer, Kristallografie en Structuuronderzoek, Chemische meetmethoden, Oppervlakteanalyse technieken en Grensvlakchemie'. Deze opleiding werd afgesloten met een literatuuronderzoek wat geresulteerd heeft in een scriptie getiteld 'The rechargeable Manganese Dioxide Electrode' (1979/1980). Verder is een opleiding gevolgd aan de Summer School 'Advanced Instrumental Methods in Electrode Kinetics' aan de University of Southampton (1982), evenals het college 'Statistiek' aan de Open Universiteit (1987).

Het onderzoek beschreven in dit proefschrift werd verricht op het Philips Natuurkundig Laboratorium in de groep Grensvlakchemie in de periode september 1980 - maart 1986. Vanaf begin 1986 onderzoekt de auteur het elektrochemische gedrag van hydride-vormende intermetallische verbindingen.

Dankwoord

zoek naar het etsen van microscopische vormen in halfgeleidermaterialen en het onderkennen van het belang van de elektrochemie daarbij, in een stroomversnelling geraakt. Zijn wiskundige beschrijvingen van de transportverschijnselen in de vloeistof zijn van onmisbare waarde gebleken. In dit verband wil ik ook Cees Vuik (T.U. Delft) noemen. Dankbaar heb ik gebruik gemaakt van het door hem ontwikkelde computerprogramma voor de berekening van etsvormen en van zijn hulp bij het gebruik van dit programma.

Een belangrijke bijdrage aan dit proefschrift hebben ook Dré Damen en Mark Cornelissen geleverd. Nauwgezet en met veel toewijding hebben zij in hun respectievelijke afstudeer- en stageperiode talloze elektrochemische- en etsexperimenten uitgevoerd, geïnterpreteerd en beschreven.

Veelvuldig en nooit tevergeefs heb ik een beroep gedaan op de verschillende dienstverlenende groepen binnen het Natuurkundig Laboratorium zoals de analytische-chemische afdeling onder leiding van Piet Rommers die het gallium- en indiumgehalte in de vele honderden monsteroplossingen altijd snel en met grote nauwkeurigheid heeft bepaald. Ook de hr. M. Renders van de fijnmechanische afdeling ben ik veel dank verschuldigd, zowel voor het aanpassen van de apparatuur t.b.v. ring-schijf metingen als voor de nauwkeurige fabricage van deze elektrodesystemen. De glastechnische afdeling onder leiding van de hr. J. Thijssen wil ik danken voor het vervaardigen van vele glazen meetcellen waarbij de micro-elektrochemische 'flowcell' zoals afgebeeld in Fig. 2.4 het meest in het oog springt. Chris Geenen voor de EDAX-analyses en voor de vele honderden etsprofielen die hij in de afgelopen jaren 'in zijn SEM' heeft bekeken en gefotografeerd. Daphne van Ake voor het typen van het manuscript en het veelvuldig aanpassen van de tekst als deze bijgeschaafd moest worden. Henny Alblas voor het tekenen van alle figuren in dit proefschrift. De Audio-Visuele Dienst voor de bewerking van de talloze foto's. Met name Theo Schoenmakers ben ik veel dank verschuldigd voor de vele nuttige adviezen en kritische opmerkingen met betrekking tot de lay-out van dit proefschrift.

Tot slot ben ik mij bewust van de grote aanslag die ik de afgelopen tijd op het geduld van Pascalle, Brechtje en Roel heb gedaan, en van de vele opofferingen die zij zich hebben moeten getroosten. In het bijzonder ben ik Pascalle meer dan dankbaar voor haar nimmer aflatende morele steun en haar aansporingen die onmisbaar zijn geweest in de achter ons liggende woelige periode waarin hoogte- en dieptepunten elkaar soms in hoog tempo afwisselden. Jij was er 'gewoon' altijd om het evenwicht in stand te houden of te herstellen als dat nodig was. Met erg veel waardering heb ik dit proefschrift dan ook aan hen opgedragen.

STELLINGEN

behorende bij het proefschrift

Electrochemical study of the etching
of III-V semiconductors

door

P.H.L. Notten

I

Naast de oploskinetiek wordt het belang van het oplosmechanisme voor de vormbepaling van de te etsen profielen in éénkristallijne materialen onvoldoende onderkend.

Dit proefschrift.

II

De invloed van niet-lineaire diffusie op zowel het etsen als het groeien van structuren onder transport-bepaalde omstandigheden wordt aanzienlijk groter naarmate de afmetingen van de structuren kleiner worden.

Dit proefschrift, hoofdstuk 8.
C.H.J. van den Brekel, Proefschrift K.U. Nijmegen, (1978).
J.W.M. Jacobs, Proefschrift R.U. Utrecht, (1988).

III

Het gebruik van de zogenaamde 'Volcano-relatie' om de elektrokatalytische eigenschappen van intermetallische verbindingen voor de waterstofreactie te verbeteren is niet altijd doeltreffend.

P.H.L. Notten and E. Brok, Extended Abstract no. 5.13, 38th ISE meeting, Maastricht, (1987).
M.M. Jakšić, Electrochim. Acta, **29**, 1539, (1984).

IV

Ten onrechte wordt er vaak vanuit gegaan dat de voortgang van de biologische evolutie eenzijdig in stand gehouden wordt door de veranderende fysisch-chemische omstandigheden.

V

In tegenstelling tot hypofosfiet dat in 'electroless' nikkelbaden rechtstreeks gereduceerd kan worden tot atomair fosfor, is de inbouw van atomair borium in nikkelbaden met boorhydride als reductiemiddel te wijten aan de reductie van het oxydatieproduct van boorhydride.

J.E.A.M. van den Meerakker, J. Appl. Electrochem., **11**, 395, (1981).

VI

Het verdient aanbeveling om niet alleen de kleur van de gebruikte etsoplossingen te vermelden in publikaties, maar ook hun chemische samenstelling.

S. Adachi and K. Oe, J. Electrochem. Soc., **131**, 126, (1984).

VII

Doordat de bandkanten van halfgeleidermaterialen onder wisselende om-
standigheden niet vastliggen, zijn conclusies uit eenvoudige elektrochemische
metingen omtrent de vraag welke halfgeleiderband bij de ladingover-
drachtsreactie is betrokken soms misleidend.

Dit proefschrift, hoofdstuk 5.
H. Gerischer and W. Mindt, Electrochim. Acta, **13**, 1329, (1968).

VIII

Het algemeen streven om giftige zware metalen uit het milieu te weren kan
voor een aanzienlijk deel gehonoreerd worden wanneer de cadmium-elek-
trode in herlaadbare nikkel-cadmium batterijen vervangen zou worden door
een hydridevormende elektrode.

IX

Door de wereldwijde afname van de biologische diversiteit wordt een grote
aanslag gedaan op het homeostatische vermogen van de aardse biosfeer.

J.E. Lovelock, 'Gaia', Oxford University Press, (1987).

X

Veel verwarring en frustratie zou voorkomen kunnen worden wanneer bij
de bekendmaking van een nieuwe vinding via de media, de desbetreffende
wetenschappelijke publikatie gelijktijdig zou verschijnen.

NOS Journaal 24-3-1989.

XI

Het waarnemen van spanningen is, in het algemeen, veel eenvoudiger dan
deze te interpreteren.

Dit proefschrift.
A.L. Hodgkin and A.F. Huxley, J. Physiol. (London), **117**, 500, (1952).